Space Weather Prediction Using Ground-Based Observations

地上望遠鏡による宇宙天気予報

関　大吉

京都大学大学院　総合生存学館

2021 年 3 月

Contents

Abstract

Solar flares, explosive phenomena filled with magnetised plasma on the solar surface, release energy in the amount of 10^{21}–10^{25} J in various forms such as radiative energy, kinetic energy, and thermal and non-thermal energy. Associated with solar flares, various other forms of phenomena including filament eruptions and coronal mass ejections (CMEs) often take place on the solar surface. Filaments, dense cooler plasma floating in the solar corona supported by magnetic fields, often become unstable at the end of their lives and finally erupt. CMEs are the huge bulk of plasma observed by coronagraphs with a mass of 10^{11}–10^{13} kg.

It has been pointed out that the solar flares and other accompanied eruptions (hereafter, solar eruptions) cause adverse impacts on human society. Solar eruptions can disturb the plasma environment in the near-Earth space and the Earth's upper atmosphere, which is called "space weather." CMEs are known as major drivers of severe geomagnetic disturbances, resulting in a damaged transformers and huge blackouts (e.g., blackout throughout Quebec province, Canada, in March 1989). The electrons and protons in the near-Earth space are known to cause various satellite malfunctions. Therefore, for the purpose of mitigating adverse effects on human society, it is crucially important to monitor solar activity and predict solar eruptions.

In the main part of this dissertation, the author focuses on space-weather prediction, especially the prediction of filament eruptions and their CME association, by using a ground-based telescope, Solar Dynamics Doppler Imager (SDDI) at Hida Observatory, Kyoto University. Filament eruptions are often accompanied by CMEs, and the core of CMEs is believed to originate from the filament material. Investigating the predictability of filament eruptions in advance and their CME associations should be benefit in predicting solar eruptions. Moreover, space-weather prediction by ground-based telescopes can benefit us from the viewpoint of disaster risk management. Compared to artificial satellites, which provide us the valuable data for the prediction and monitoring of solar eruptions and are, however, vulnerable to space weather, ground-based telescopes experience very few malfunctions due to solar eruptions. In order to build a resilient space-weather-prediction operation, they should be used as backup for the prediction and

monitoring of solar eruptions.

To achieve this goal, the author and co-researchers first conducted a case study to investigate the predictability of a filament eruption on November 5, 2016. By leveraging the SDDI observation, which enables us to obtain an unprecedented detailed line-of-sight (LOS) velocity distribution of a filament with a high time cadence (15 sec[†]), we found that the standard deviation of the LOS velocity distribution increased to 3–4 km s^{-1} 6 h prior to the eruption, compared with 2–3 km s^{-1} observed 21 h[††] before the eruption. Therefore, we concluded that the standard deviation of LOS velocity distribution could be used as the precursor of a filament eruption (Chapter 2).

On the basis of the results of the case study, we further analysed other 11 events in the catalogue in the same manner and found that 9 out of 12 events exhibited Phase 1, during which the standard deviation of LOS velocity increased without significant changes in its average. Limited to robust estimations, our results suggest that we could predict the clearly observed filament eruptions with the lead time of 1.3 ± 0.47 h (Chapter 3).

In Chapter 4, we provided descriptions of "SMART/SDDI Filament Disappearance Catalogue," in which we listed almost all the filament eruptions observed by the SDDI from May 2016 to June 2019, and some statistical properties of the data compiled in the catalogue. The catalogue compiles miscellaneous information related to filament eruptions, including their flare associations, CME associations, neighbouring active regions, three-dimensional trajectory of erupting filaments, detection in Interplanetary Scintillation (IPS), occurrence of interplanetary CME, and geomagnetic activities.

In Chapter 5, we investigated the relationships between several physical parameters of filament eruptions and their CME associations on the basis of the catalogue in Chapter 4. The association between filament eruptions and CMEs has been widely argued, and the proportion of filament eruptions associated with CMEs is still under debate (10–90%). For the accurate prediction of a CME occurrence, it is important to reveal what physical parameters of filament eruptions control their association with CMEs. We found that if the product of the maximum radial velocity normalised by 100 km s^{-1} and the filament length normalised by 100 Mm to the power of 0.96 is larger than 0.80, the filament will become a CME with a probability of 93%. Our findings suggest the importance of measuring the three-dimensional velocity of filament eruptions for the better prediction of CME occurrence.

In Chapter 6, we showed the importance of the prediction of solar eruptive phenomena based on ground-based telescopes. We put an emphasis on the operational aspect of space-weather prediction and presented its feasibility by introducing the Continuous H-Alpha

---

[†]seconds

[††]hour

Imaging Network (CHAIN) project, which aims to create a world-wide observational network with ground-based solar telescopes in multiple wavelengths for 24-hour continuous observation.

In the succeeding chapters, the author focused on the potential space-weather impacts on artificial satellites. Compared to Chapter 2–6, in which the prediction of solar eruptive phenomena was emphasised, the subsequent chapters paid more attention to the possible consequence of space weather including the vulnerability of artificial satellites to space weather, and the benefit of artificial satellites to human society.

In Chapter 7, we assessed the potential impact on the artificial satellites in case of a disastrous solar flare. By taking simple linear regressions, we found that the 6-days averaged proton flux with its energy above 100 MeV showed a remarkably good correlation (R2 > 0.9) to the anomaly rate (the number of anomalies per satellite per flare event) of GEO satellites. This result implied that in case of 1-in-100-years and 1-in-1000-years solar flares, the GEO-satellite-anomaly rates should be ∼8 (1-in-100-years case) and ∼55 (1-in-1000-years case) times larger than the worst case ever observed.

In Chapter 8, the author reported the following two projects, which are conducted to understand the benefit of satellites' observation to human society; (1) Earth-observation data (EO data) for multidisciplinary research & consulting work, and (2) R&D for space-weather-prediction business. The achievements are summarised that (1) a list of 184 publicly available EO data was compiled, made available on the website, and used to plan a study of economic-activity estimation and a consulting business, and (2) we developed an algorithm that can predict geophysical quantity X related to space weather, which is crucial for satellite operations, 24 hours ahead with an error of 6.9%, through joint fundamental R&D with Company A.

Chapter 1

General Introduction

The Sun, which looks stable and inactive in the visible light, often produces eruptive phenomena called solar flares. Solar flares are explosive phenomena filled with magnetised plasma on the solar surface. They are triggered by the reconnections of opposite-polarity magnetic fields (called magnetic reconnections) and release the energy of 10^{21}–10^{25} J in the various forms such as radiative energy, kinetic energy, and thermal and non-thermal energy [1]. Figure 1.1 shows one of the largest solar flares ever observed, X17.4-class flare, on 2003 October 28. This event is also known as "Halloween event". Conventionally, solar flares are classified with regard to its peak soft X-ray (SXR) flux, which is commonly used as a proxy for the severity of flares. The peak fluxes above 10^{-6}, 10^{-5}, and 10^{-4} W m^{-2} are called C-class, M-class, and X-class, respectively. The digits next to the alphabet, C, M, or X, represent the value of the peak flux divided by 10^{-6}, 10^{-5}, or 10^{-4}, respectively. So, X17.4-class flare means that the peak flux of the flare was 17.4×10^{-4} W m^{-2}. The top panel in Figure 1.1 shows the solar full-disk extreme-ultraviolet (EUV) intensity image observed the Extreme-ultraviolet Imaging Telescope (EIT) [2] onboard the Solar and Heliospheric Observatory (SOHO) on 2003 October 28 at 11:12 UT. The bottom panel shows SXR fluxes between 1.0–8.0 Å* (black) and 0.5–4.0 Å (grey) observed by the Geostationary Operational Environmental Satellite (GOES) October 27 to 31 during 2003. One can recognise a significant bright feature in the vicinity of the solar centre in the top panel and a proliferation in the SXR flux in the bottom panel at the corresponding time.

Accompanied by solar flares, various forms of eruptive phenomena often take place. The intense electromagnetic waves in various wavelengths ranging from 10^{-1} Å (X-rays) to 10^{10} Å (radio) are emitted with an initiation of solar flares [3]. Figure 1.2 shows M4.4-class flare observed in Hα line centre (6562.8 Å) by Solar Dynamics Doppler Imager (SDDI) installed on Solar Magnetic Activity Research Telescope (SMART) on September 5 at 01:08 UT in 2017. One can observe the strong enhancement in Hα line emission in the

---

*Å is equivalent to 10^{-10} m.
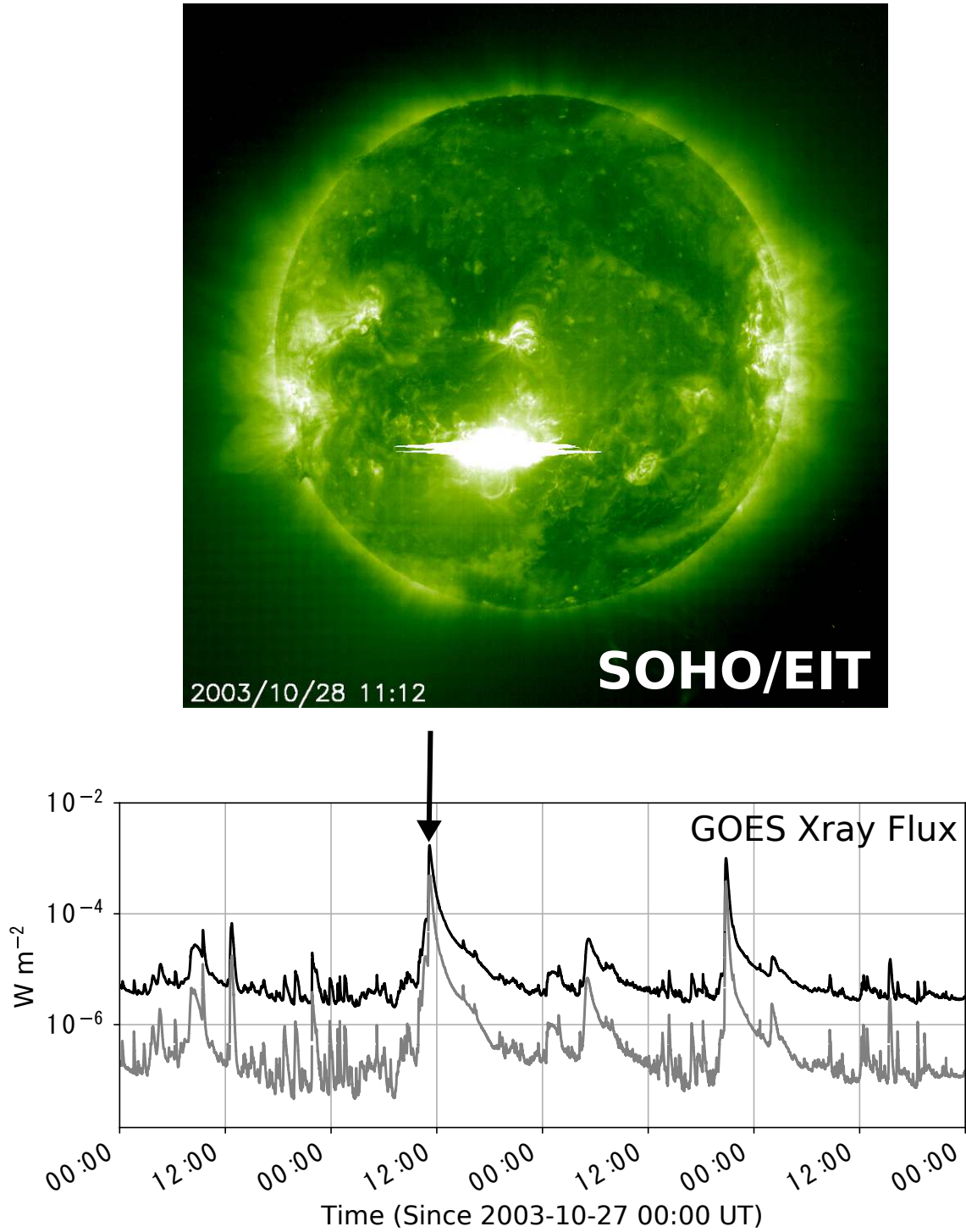
Figure 1.1: *Top*: The solar full-disk extreme-ultraviolet (EUV) intensity image observed by the SOHO/EIT on 2003 October 28. The bright part in the vicinity of the solar centre represents the solar flare. *Bottom*: Soft X-ray (SXR) fluxes between 1.0–8.0 Å (black) and 0.5–4.0 Å (grey) observed by the GOES from 2003 October 27 to 31. The SXR flux is commonly used for the proxy of the severity of a flare. The peak pointed by a black arrow corresponds to the flare event shown in the top panel (X17.4-class flare).

2
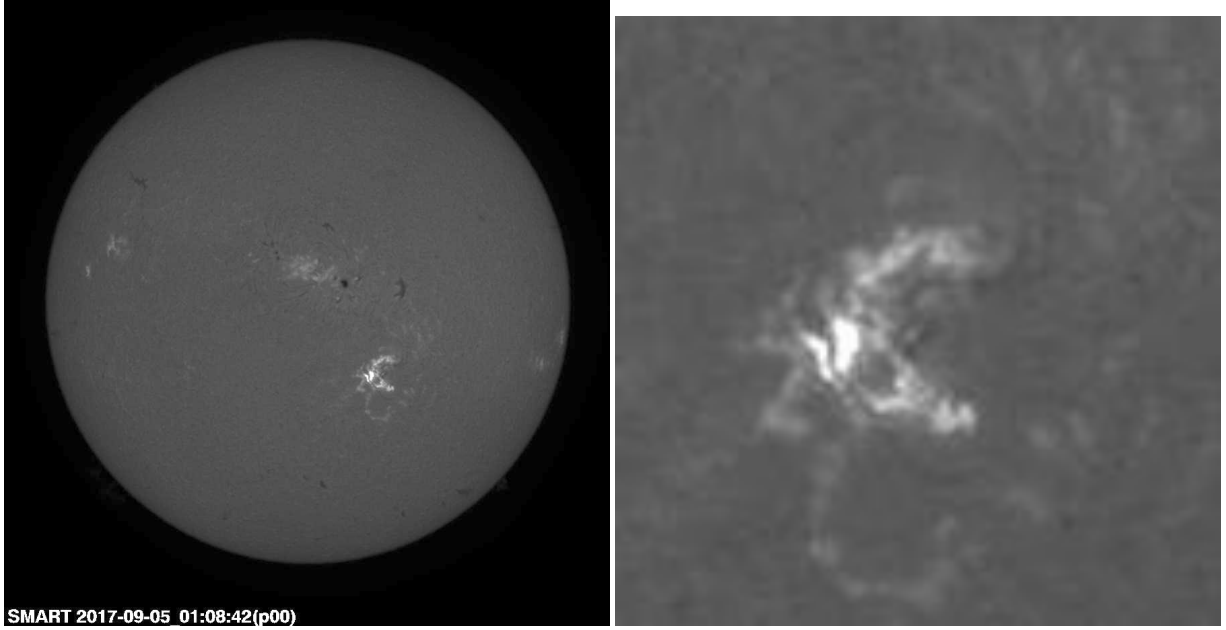
Figure 1.2: *Left*: The solar full-disk image in Hα line centre observed by the SMART/SDDI on 2017 September 5. The bright part in the vicinity of the solar centre represents the solar flare. *Right*: Part of the left panel.

vicinity of the centre of the Sun. The huge bulk of plasma called Coronal Mass Ejection (CME) with its mass of 10^{11}–10^{13} kg [4] can be observed in coronagraph as a white feature. The energetic electrons and protons almost in the speed of light called Solar Energetic Particle (SEP) are frequently produced as well. These ejecta and emissions can disturb the plasma environment around the near-Earth space and the Earth's upper atmosphere. Such severe disturbances of interplanetary and near-Earth plasma environment mainly driven by the magnetic activity of the Sun is called "space weather" [5]. Despite the diversity in size and morphology, these eruptive phenomena are considered different aspects of the common magnetohydrodynamic process, and hereafter, we call them as "solar eruptive phenomena" in this dissertation.

Recently, it is pointed out that solar flares could bring various adverse effects on human society, and it is of a great importance to monitor the solar activity and predict solar eruptive phenomena. X-ray and EUV radiations affect the electron density of the Earth's upper atmosphere due to the enhanced ionisation and interfere high frequency (HF) radio communications as well as satellite communications [6]. CMEs are known as a major driver of the severe disturbance of geomagnetic fields called geomagnetic disturbance. It can produce the geomagnetically induced current through the ground and the electric power grid, which could initiate a damage in transformers (Oughton et al. [7] and the references therein). In March 1989, there was a huge blackout throughout Quebec province in Canada, and electricity supply had ceased for 9 hours because of the severe

3

geomagnetic storm caused by two successive CMEs [8–10]. Note that those detected by in-situ observations near the Earth are often called by a different name, Interplanetary CME (ICME). SEPs are the proton or electron whose energy ranges from a few keV to a few GeV driven by a magnetic reconnection during a solar flare (called Impulsive SEP event) or by a fast-large-scale CME shock wave (called Gradual SEP event) [11]. The electrons and protons in the near-Earth space are known to cause the various satellite malfunctions including electrostatic discharge, surface and internal charging and single event upsets. For example, in Halloween event (between October 23 and November 6 in 2003), during which the successive severe solar eruptive phenomena took place, 47 satellites reported malfunctions, 1 satellite (Midori 2) suffered a total loss, and more that 10 satellites stopped their services more than 1 day [12]. For the more intensive review of satellite-anomaly events, see Horne et al. (2013) [13] and Cannon et al. (2013) [14]. Additionally, highly-energetic protons can pose astronauts to the risk of radiation exposure. Therefore, for the purpose of mitigating adverse socioeconomic impacts, it is crucially important to monitor the solar activity and predict these solar eruptive phenomena.

Similar to other terrestrial disasters like an earthquake, a low-frequency-high-impact solar disaster could also be anticipated. Maehara et al. and their colleagues [15–17] found that a "superflare", a flare whose energy is 10–1000 times larger than that ever observed on the Sun, could also occur on the solar-type or sun-like stars by surveying stellar activities. They also found that the stellar superflares follow the similar power-law distribution between frequency and severity to the Sun. According to their studies, the expected frequency of X100 and X1000-class flares might be once in 200 and 1000 years, respectively. The recent statistical study on superflares with the up-to-date information on the physical quantities of stars [18] showed that X5000-class superflares could occur even on the physically quite similar stars to the Sun (the G-type, slowly rotating, single stars) approximately once in 2000–3000 years. The most recent work by this group [19] showed that the Sun could produce ∼X700-class and ∼X1000-class flares once in ∼3000 and ∼6000 years, respectively.

Moreover, indirect evidences of solar superflares have been reported and discussed in many studies from the theoretical and observational perspectives. Shibata et al. (2013) [20] conducted a simple theoretical calculation to assess the possibility whether the Sun can generate a large-enough sunspot to produce a superflare and concluded that it is possible to produce such a large sunspot that can initiate a X1000-class flare within one solar cycle (∼11 years).

From the observational point of view, Miyake et al. (2012, 2013) [21, 22] investigated the content of carbon-14 (^{14}C), the isotope of carbon-12, inside a Japanese tree ring. ^{14}C content in tree rings reflects its value in the atmosphere, and thus if its increase is

observed, it should be the strong evidence of the enhancement of cosmic ray flux around the Earth. As a result, they found spiky sudden increases of ^{14}C content in 774 and in 994. Given that the origins of these proliferation are superflares, the former and latter events produced 50 times and 30 times larger amount of SEPs than one of the largest solar particle events on February 23, 1956, respectively [23]. Note that 1956 event corresponds to X1–X10-class flare, taking into account the good correlation (R = 0.65) between SXR peak flux and Hα brightening area [24] and the observed Hα total brightening area [25]. According to Takahashi et al. (2016) [26], there is a theoretical scaling relationship between the upper limit of SEP flux, F_p, and SXR peak flux, F_{sxr}, in a certain flare event (see Figure 7.5). Assuming that this largest SEP flux in 1956 was almost the upper limit flux, we can roughly estimate 774 and 994 events correspond to X109–X1090-class and X59–X590-class flares, respectively.

Furthermore, many descriptions of auroras have been found in the ancient literature all over the world including low latitudinal regions. If the severe geomagnetic storm happens, it can be observed even at the low latitudes, where usually we cannot observe auroras. Hayakawa et al. (2016) [27] found the historical auroral records around the world including the low-latitude area, Korea, during 990–994. The evaluated Dst index of the geomagnetic storm was -970 nT, indicating that this geomagnetic storm was much severer than that during one of the largest events on March 1989 (-589 nT). The survey of historical records has also successfully shown the indirect evidences of other extreme space weather events in 1770 [28], 1872 [29], and 1909 [30].

However, in spite of intensive studies for the possibility of disastrous solar flares and the reports of the vulnerability among the space assets, the current predictions of solar eruptive phenomena majorly rely on the space-borne data. Since they can provide us valuable information of magnetic fields (such as EUV and SXR observations) that cannot be obtained from the ground, the studies to predict solar eruptive phenomena have been making use of the observations by artificial satellites. However, artificial satellites are vulnerable to space weather. In case that a superflare should happen and almost all the satellites lost their services, the predictability of the succeeding solar flares should be greatly lessened in the current situation. On the other hand, compared with artificial satellites, ground-based telescopes have few malfunctions due to space weather and should be more robust to solar eruptive phenomena. Thus, from the viewpoint of a disaster risk management, the possibility and limitation of predicting the solar eruptive phenomena and monitoring the solar activity fully by ground-based telescopes should be more intensively studied. And ground-based telescopes should be used as a backup for the prediction and monitoring of solar eruptive phenomena in order to build a resilient space-weather-prediction system.

In the main part of this dissertation (Chapter 2–6), the author focused on a space-weather prediction, especially the prediction of filament eruptions and their CME associations, by using the ground-based telescope called Solar Dynamics Doppler Imager (SDDI) installed on the Solar Magnetic Activity Research Telescope (SMART) at Hida Observatory, Kyoto University. Filaments are dense (10^9–10^{11} cm^{-3}) cooler (10^4 K) plasma floating in the solar corona (density $\sim 10^8$ cm^{-3} and temperature $\sim 10^6$ K) supported by magnetic fields. Filaments can be observed as a dark feature in Hα line. They usually become unstable at the end of their lives and finally erupt, which is called filament eruptions. Filament eruptions are often accompanied by CMEs, and the core of CMEs is believed to originate from the filament material if they exhibit the so-called three-part structure (leading edge, faint coronal cavity, and dense core). Thus, investigating the predictability of filament eruptions in advance and their CME associations should be a benefit in predicting the solar eruptive phenomena.

To achieve this goal, the author and co-researchers first conducted a case study to investigate the predictability of a filament eruption on November 5, 2016. By leveraging the SDDI observation, which enables us to obtain an unprecedented detailed line-of-sight (LOS) velocity distribution of a filament with a high time cadence (15 sec[†]), we found that the standard deviation of the LOS velocity distribution increased to 3–4 km s^{-1} 6 h prior to the eruption, compared with 2–3 km s^{-1} observed 21 h[††] before the eruption. Therefore, we concluded that the standard deviation of LOS velocity distribution could be used as the precursor of a filament eruption (Chapter 2).

On the basis of the results of the case study, we further analysed other 11 events (12 events in total) in a similar manner and found that;

1. 9 out of 12 events exhibited Phase 1, during which the standard deviation of LOS velocity increases without significant changes in its average, regardless of the types of filaments and their CME associations,

2. the duration of Phase 1 widely ranged from 0.18 to 42 h, and limited to robust estimations, a quiescent filament has a $\sim$10 times longer Phase-1 duration than the other types of filaments, and

3. in all the cases of the intermediate and quiescent filaments, the standard deviation during Phase 1 generally changed from 2–3 km s^{-1} to 4–5 km s^{-1}.

According to these results, we could predict the clearly observed filament eruptions with the lead time of 1.3 ± 0.47 h, which suggests a strong feasibility of the prediction of filament eruptions using the SDDI (Chapter 3).

[†]seconds

[††]hour

In the succeeding chapters, Chapter 4 and 5, we focused on the prediction of CME occurrence based on the kinematics of filament eruptions. It is widely recognised that filament eruptions are frequently associated with CMEs. Since CMEs are a major source of disturbances of the space environment surrounding the Earth, it is important to investigate these associations in detail for the better prediction of CME occurrence. However, the proportion of filament eruptions associated with CMEs is under debate. The estimates range from $\sim 10\%$ to $\sim 90\%$ in studies and could be affected by the manners to select the events. For the accurate prediction of a CME occurrence, it is important to reveal what physical parameters of filament eruptions control their association with CMEs.

To clarify these relationships, we first constructed "SMART/SDDI Filament Disappearance Catalogue", in which we listed almost all the filament eruptions observed by the SDDI from May 2016 to June 2019. In total, we collected 43 events. The catalogue compiles miscellaneous information related to filament eruptions, including their flare associations, CME associations, neighbouring active regions, three-dimensional trajectory of erupting filaments, detection in Interplanetary Scintillation (IPS), occurrence of interplanetary CME, and geomagnetic activities. In Chapter 4, we provided a description of the catalogue and some statistical properties of the data compiled in the catalogue.

In Chapter 5, we investigated the relationships between several physical parameters of filament eruptions and their CME associations. In contrast to the previous Chapter, the present study aims to improve the predictability of CME association by combining those parameters. Selecting 28 events in the catalogue which are credibly associated with CMEs and investigating the relationships between the parameters including the length, velocity during eruption, and direction of eruption, and the CME association, we found that the product of the maximum radial velocity normalised by 100 km s^{-1} and the filament length normalised by 100 Mm to the power of 0.96 can well classify the CME occurrence. If the product is larger than 0.80, the filament will become a CME with a probability of 93%, and if the product is smaller than 0.80, it will not become a CME with a probability of 100%. Our findings suggest the importance of measuring the three-dimensional velocity of filament eruptions for the better prediction of CME occurrence.

In Chapter 6, we showed the importance and feasibility of the prediction of solar eruptive phenomena based on ground-based telescopes. Compared to the previous Chapters that mainly focused on their scientific aspects of the prediction of solar eruptive phenomena, this Chapter put more emphasis on its operational aspect. We presented its feasibility by introducing the Continuous H-Alpha Imaging Network (CHAIN) project, which aims to create a world-wide observational network with ground-based solar telescopes in multiple wavelengths for 24-hour continuous observation. We also provided the recent progress of CHAIN project and challenges which should be tackled to realise a

ground-based space-weather prediction.

In the succeeding chapters, the author concentrated on the potential space-weather impacts on artificial satellites. Compared to Chapters 2–6, in which the scientific and operational aspects of the prediction of solar eruptive phenomena were emphasised, the subsequent Chapters paid more attention to the possible consequence of space weather including the vulnerability of artificial satellites to solar eruptive phenomena and the benefit of artificial satellites to human society.

In Chapter 7, we assessed the potential impact on the artificial satellites in case of a disastrous solar flare. Though the vulnerability of satellites to solar eruptions has been widely reported, little study has been conducted to evaluate the damages by a disastrous solar flare. For the objective of recognising the necessity of the prediction of solar eruptive phenomena by ground-based telescopes, it is of a great importance to quantitatively assess it. By taking simple linear regression between the satellite-anomaly rate (defined as the number of anomalies per satellite per flare event) and 19 space-weather related physical parameters individually, we found that the 6-days averaged proton flux with its energy above 100 MeV showed a remarkably good correlation ($R^2 > 0.9$) to the anomaly rate of GEO satellites. This result implied that in case of 1-in-100-years and 1-in-1000-years events, the GEO-satellite-anomaly rates should be 4.62 and 31.3, respectively. These rates are ∼8 (1-in-100-years case) and ∼55 (1-in-1000-years case) times larger than the worst case ever observed.

In Chapter 8, the author reported the following two projects, which are conducted to understand the benefit of satellites' observation to human society and undertaken at Special Research Project II and III in Graduate School of Advanced Integrated Studies in Human Survivability, Kyoto University; (1) Earth-observation data (EO data) for multidisciplinary research & consulting work, and (2) R&D for space-weather-prediction business. The achievements are summarised as below;

1. A list of 184 publicly available EO data was compiled and made available on the website. We used them to plan a study of economic-activity estimation. In addition, the application to the consulting business was examined, and it was found to be difficult to apply in cases lacking spatial and geographical information.

2. We developed an algorithm that can predict geophysical quantity X related to space weather, which is crucial for satellite operations, 24 hours ahead with an error of 6.9%, through joint fundamental R&D with Company A.

Sun

filament

Ch. 2 and 3
Is it possible to quantify a filament activation and use it as a precursor of a filament eruption?

Coronal
Mass
Ejection
(CME)

Ch. 4 and 5
What physical parameters of filament eruptions control their CME associations?

Ch. 7
How severe malfunctions would satellites suffer in case of a disastrous solar flare?

Ch. 6
The feasibility of a prediction of filament eruptions by ground-based telescopes

Ch. 8
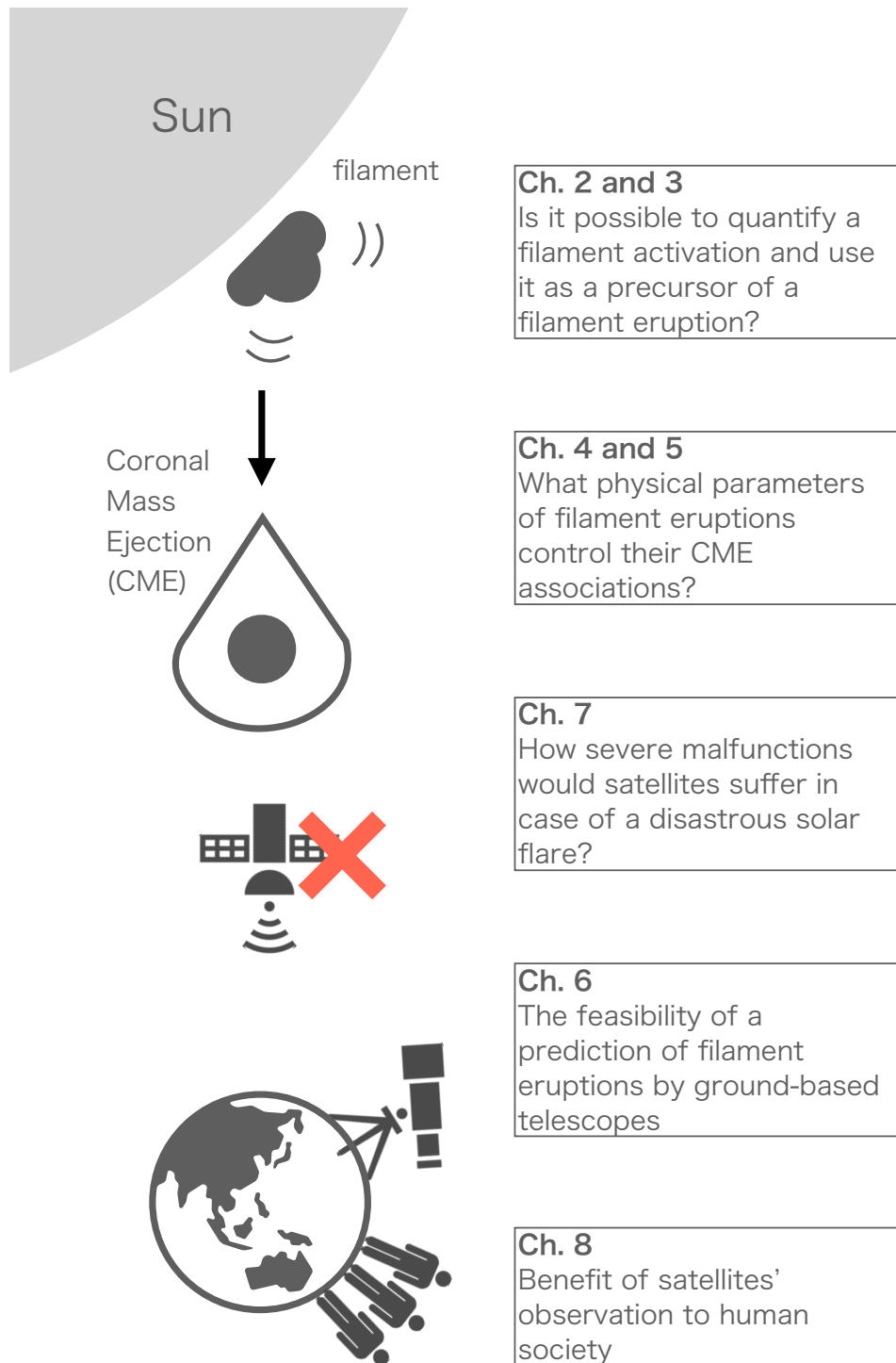Benefit of satellites' observation to human society

Figure 1.3: The graphical abstract of this dissertation.

Chapter 2

Small-scale Turbulent Motion of the Plasma in a Solar Filament as the Precursor of Eruption

This Chapter[*][†] presents a case study to investigate the predictability of a filament eruption on November 5, 2016 We derived the LOS velocity and micro-turbulence at each pixel in the filament using the Becker's cloud model. Especially, the standard deviation of the LOS velocity distribution can be regarded as a measure for the amplitude of the small-scale motion in the filament. We also conducted observational analysis in coronal emission lines and the extrapolation of the surrounding potential fields. We found that the standard deviation on the previous day of the eruption was mostly constant around 2–3 km s^{-1}, and it slightly increased to 3–4 km s^{-1} on the day of the eruption. We also found that both the spatially averaged micro-turbulence inside the filament and the nearby coronal line emission increased 6 (micro-turbulence) and 10 (coronal line emission) h prior to eruption, respectively. In this event, we could not find any significant changes in the global potential-field configuration preceding the eruption, which indicates that there is a case in which it is difficult to predict the eruption only by tracking the extrapolated global magnetic fields. From this result we suggest that the increase in the amplitude of the small-scale motions in a filament can be regarded as a useful precursor of a filament eruption.

A filament eruption, a spectacular erupting phenomenon of dense cooler plasma, often

---

[*]Seki, D., Otsuji, K., Isobe, H., Ishii, T. T., Sakaue, T., Hirose, K., "Increase in the amplitude of line-of-sight velocities of the small-scale motions in a solar filament before eruption", The Astrophysical Journal Letters, 843(2), L24(5pp), 2017

[†]Seki, D., Otsuji, K., Isobe, H., Del Zanna, G., Ishii, T. T., Sakaue, T., Ichimoto, K., Shibata, K., "Small-scale Turbulent Motion of the Plasma in a Solar Filament as the Precursor of Eruption", The Astrophysical Journal, under review

Sun

filament

Ch. 2 and 3
Is it possible to quantify a filament activation and use it as a precursor of a filament eruption?

Coronal
Mass
Ejection
(CME)

Ch. 4 and 5
What physical parameters of filament eruptions control their CME associations?

Ch. 7
How severe malfunctions would satellites suffer in case of a disastrous solar flare?

Ch. 6
The feasibility of a prediction of filament eruptions by ground-based telescopes

Ch. 8
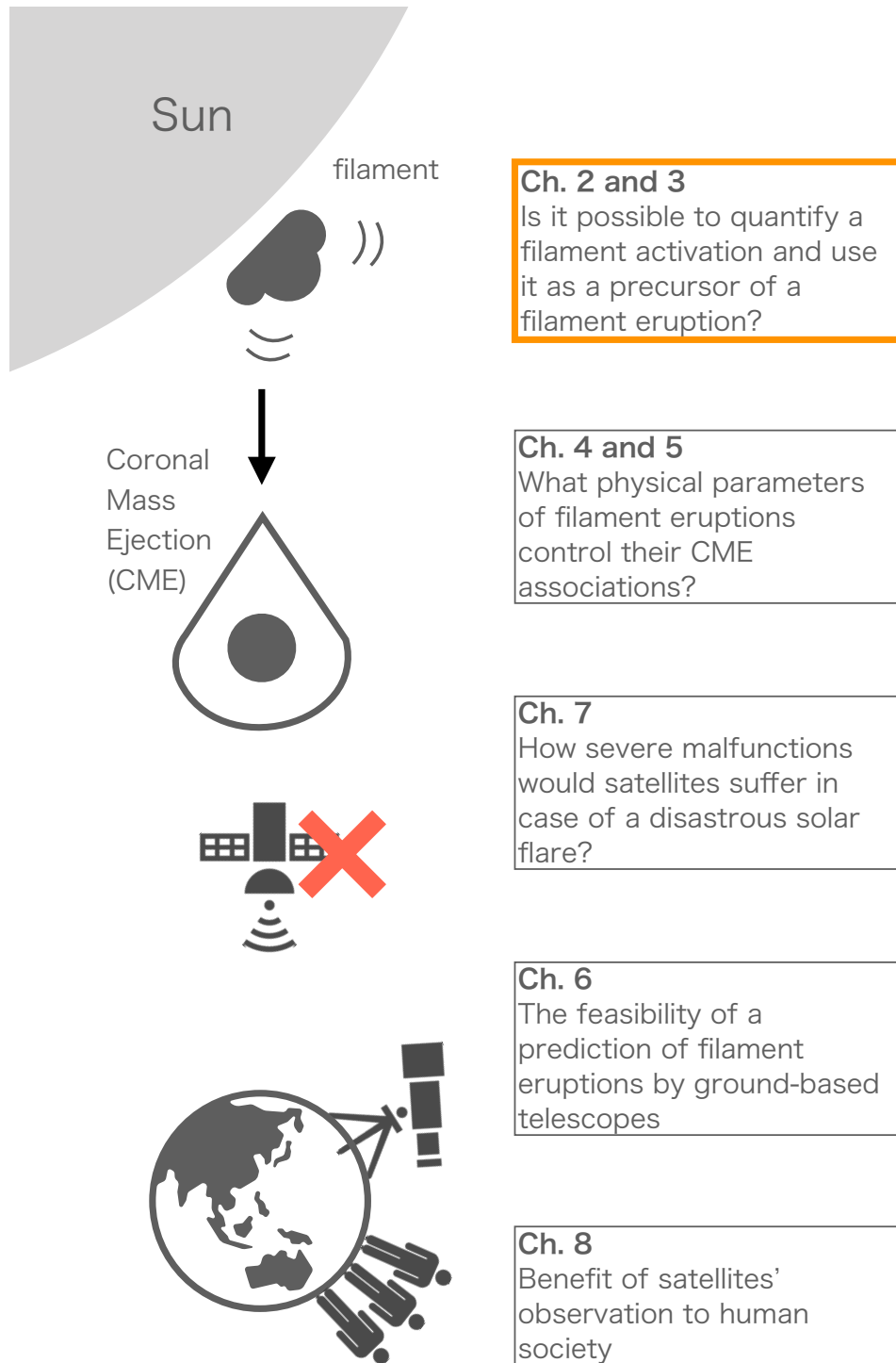Benefit of satellites' observation to human society

Figure 2.1: The graphical abstract of this dissertation (the orange rectangle corresponds to this Chapter).

initiates on the solar surface. A filament is dense (10^9–10^{11} cm^{-3}) and cooler (10^4 K) plasma floating in the solar corona (its density $\sim 10^8$ cm^{-3}, and its temperature $\sim 10^6$ K) supported by magnetic fields. The plasma is believed to be in equilibrium state due to the balance between gravitational force and Lorentz force. The models of the supporting magnetic-field configuration can be roughly classified into two types: the so-called Kippenhahn-Schulüter (KS) model first proposed by Kippehhahn & Schlüter (1957) [31] in which the magnetic-field topology has a concave-upward shape where the dense plasma is condensed and the model called Kuperus-Raadu (KR) model first proposed by Kuperus & Raadu (1974) [32] in which the magnetic field has a helical configuration similar to a flux rope. In KR model, the plasma is condensed at the bottom of the flux rope [33]. For more information on observational aspects of filaments, see Parenti (2014) [34].

A filament eruption is often preceded by dynamical motion called filament activations [34–37]. Slow ascending motion of a filament, typically with a velocity of a few km s^{-1} and a duration time of tens of minutes for active region filament and hours for quiescent filament, has been reported in many studies as a precursor of eruption. A turbulent motion was reported as well prior to a filament eruption [36] and more generally, a solar flare. Harra et al. (2001) [38] observed that non-thermal velocity inside an active region increased prior to the flare on 1993 October 3 and suggested that this is the indicator of turbulent changes in the active region.

In this Chapter, we report that the standard deviation of line-of-sight-velocity (LOSV) distribution of small-scale plasma motions inside a filament increased as the filament was reaching the eruption. By using the Solar Dynamics Doppler Imager (SDDI) [39] onboard the Solar Magnetic Activity Research Telescope (SMART) [40] at the Hida Observatory, we monitored the doppler velocity map of the filament from 29 h before the onset of the eruption. For more details of the instrument, see Ichimoto et al. (2017) [39]. As a result, we determined that the standard deviation increased to 3–4 km s^{-1} 6 h prior to the eruption, whilst it was 2–3 km s^{-1} from 29 to 21 h prior to the eruption. The average LOS velocity was approximately constant around 0 km s^{-1}. Thus, we concluded that this broadening LOSV distribution (increase of the standard deviation) could reflect the information on the preceding turbulent plasma motion inside a filament.

In the rest of this Chapter, we present further analysis on this event including the extrapolation of the surrounding potential fields and multi-wavelengths observation. Kliem & Török (2006) [41] investigated one of the the ideal magnetohydrodynamic (MHD) instabilities called Torus instability first proposed in Bateman (1978) [42] in the situation of low-beta magnetised plasma. They found that critical conditions to favour the instability were related to the so-called "decay index", which is defined as the minus gradient of the unsigned horizontal component of the overlying magnetic field with respect to a height.

In addition, we performed an observational analysis using the SDO/AIA 94, 211, 171, 193 and 304 bands to investigate the increasing intensity in the coronal emission lines. The destabilisation of a flux rope containing a filament by magnetic reconnections plays a key role in initiation of its eruption [43, 44]. If there exists small-scale magnetic reconnections preceding the eruption, the rising intensity in the coronal (high-temperature) emission line should be observable. Those SDO/AIA bands enable us to estimate high-temperature emissions such as Fe XIV 211 Å ($\sim$ a few 10^6 K) and Fe XVIII ($\sim$ a few 10^7 K) [45].

2.1 Observations and Methods

2.1.1 Data

We used multi-wavelengths observations of the Sun by the Atmospheric Imaging Assembly [46] installed on the Solar Dynamics Observatory (SDO). The SDO/AIA captures the full-disk Sun routinely in 10 wavelengths including 94 Å and 304 Å with a time cadence of 12 sec and a spatial sampling of 0.6 arcsec per pixel.

LOS magnetograms of the Sun taken by the Helioseismic and Magnetic Imager (HMI) [47] onboard the SDO and a synoptic chart of the photospheric radial magnetic fields imputed by HMI LOS magnetograms were also used. The SDO/HMI observes the solar full-disk line-of-sight magnetogram with a time cadence of 45 sec and a spatial sampling of 0.5 arcsec per pixel. Synoptic HMI charts are remapped "radial" component of magnetograms onto the Carrington coordinate grid. Here, "radial" means that the observed HMI LOS magnetograms are assumed to be the LOS component of purely radial magnetic fields. Thus, for the computation of this imputed radial magnetic-field component, the HMI LOS magnetograms are divided by the cosine of the angle from the disk centre. For each Carrington longitude, the values from 20 remapped magnetograms closest in time to the central meridian passage of that longitude are averaged.

The full-disk images in Hα line centre and its wings captured by the SDDI and the Global Oscillation Network Group (GONG) were also used to see the morphology of the target filament and to compute its LOS velocity. The SDDI on the SMART at the Hida Observatory, Kyoto University, has been conducting a routine observation since 2016 May 1. It captures the solar full-disk images in 73 channels at steps of 0.25 Å from Hα line centre - 9.0 Å to Hα line centre + 9.0 Å i.e., at 36 positions in the blue wing, Hα line centre, and 36 positions in the Hα red wing. Each observation is conducted with a time cadence of 15 sec and a spatial sampling of 1.23 arcsec per pixel. A part of daily observational data (Hα centre, $\pm$ 2.0, $\pm$ 1.25, $\pm$ 0.5, and +3.5 Å) is always available on our website (`https://www.hida.kyoto-u.ac.jp/SMART/T1.html`) from 2016 May 1 to

14

the present.‡ The GONG is a community-based program managed by the National Solar Observatory which enables us to conduct 24-hour routine observation of the Sun in Hα line centre with 6 ground stations all over the world [48].

2.1.2 Overview

Top two panels in Figure 2.2 shows the solar full-disk images captured by the SDDI (Hα line centre) and by the SDO/AIA 304 around 02:14 UT on 2016 November 5. This filament first appeared from the solar east limb on October 28 as a prominence. Bottom panel shows the highest height of its spine measured as 33 Mm above the limb. It was located at the latitude of N27 degree and in the vicinity of an active region NOAA AR 12605, and was tilted by an angle of approximately 45 degree with respect to the south-north direction. Its length was about 112 Mm measured in Hα centre. Figure 2.3 shows the configuration of the potential fields at 00:00 UT on November 4.

This filament dynamically changed its morphology for the last 16 h of its life. Figure 2.4 shows the temporal evolution of the target filament from 12:00 UT on November 4 (16 h prior to eruption) to 00:00 UT on November 5 (4 h prior to eruption). All the panels except for the bottom right panel were captured by the GONG program managed by the National Solar Observatory [48], and the bottom right panel was by the SDDI at the Hida Observatory. The filament was stable for a while on October 28–November 3 with its shape like the top left panel in Figure 2.4. On 12:47 UT, a B2.2-class flare in the GOES soft X-ray occurred in the vicinity of NOAA AR 12605, and the filament started to move to the northeast. In the helioprojective-cartesian coordinates, the filament lay between 300 and 450 arcsec in y-axis at 12:00 UT, whilst it moved to the higher latitude approximately between 400 and 500 arcsec in y-axis 12 h afterward.

The filament started to erupt around 03:00 UT to the north and totally disappeared in Hα line centre around 03:40 UT on November 5. Two-ribbon brightening was also observed in both Hα line centre and the SDO/AIA 304 in the vicinity of the filament location after eruption. This filament eruption was associated with a small flare (B1.1-class) in the GOES soft X-ray, which peaked at 04:30 UT (see the bottom panel in Figure 2.5). Top panel in Figure 2.5 shows a two-ribbon flare observed by the SDO/AIA 304 at 04:30 UT (white arrows). The field of view is the same as the white rectangles in both the top panels in Figure 2.2. We can recognise that a two-ribbon flare was observed at the south-west of the filament location.

A CME was observed at 04:36 UT in the SOHO/LASCO C2 [49] with a linear speed of 403 km s^{-1}. A moderate geomagnetic disturbance on November 10–11, which peaked

---

‡The full version of the data (73 wavelengths) is also available. Please contact us (data_info@kwasan.kyoto-u.ac.jp), if you would like to use it.
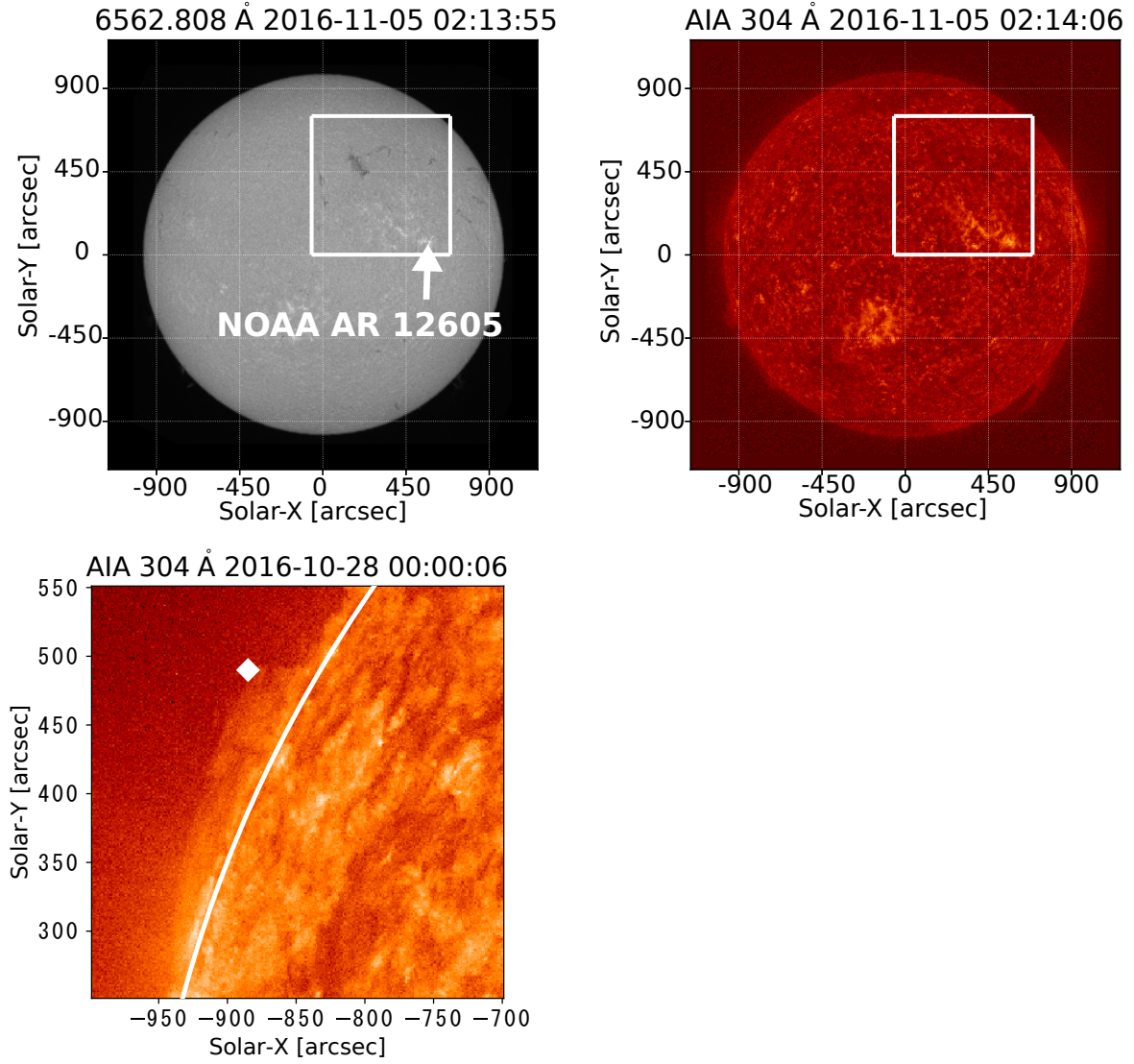
Figure 2.2: *Top*: Hα centre observed by the SMART/SDDI (left) and the SDO/AIA 304 images (right) of the full-disk Sun around 02:14 UT on 2016 November 5. White box in each image is equivalent to frames in Figure 2.4. *Bottom*: Sub-image of the solar east limb taken by the SDO/AIA 304 at 00:00 UT on October 28. The white line and diamond indicate the solar limb and the highest point of the target prominence, respectively.
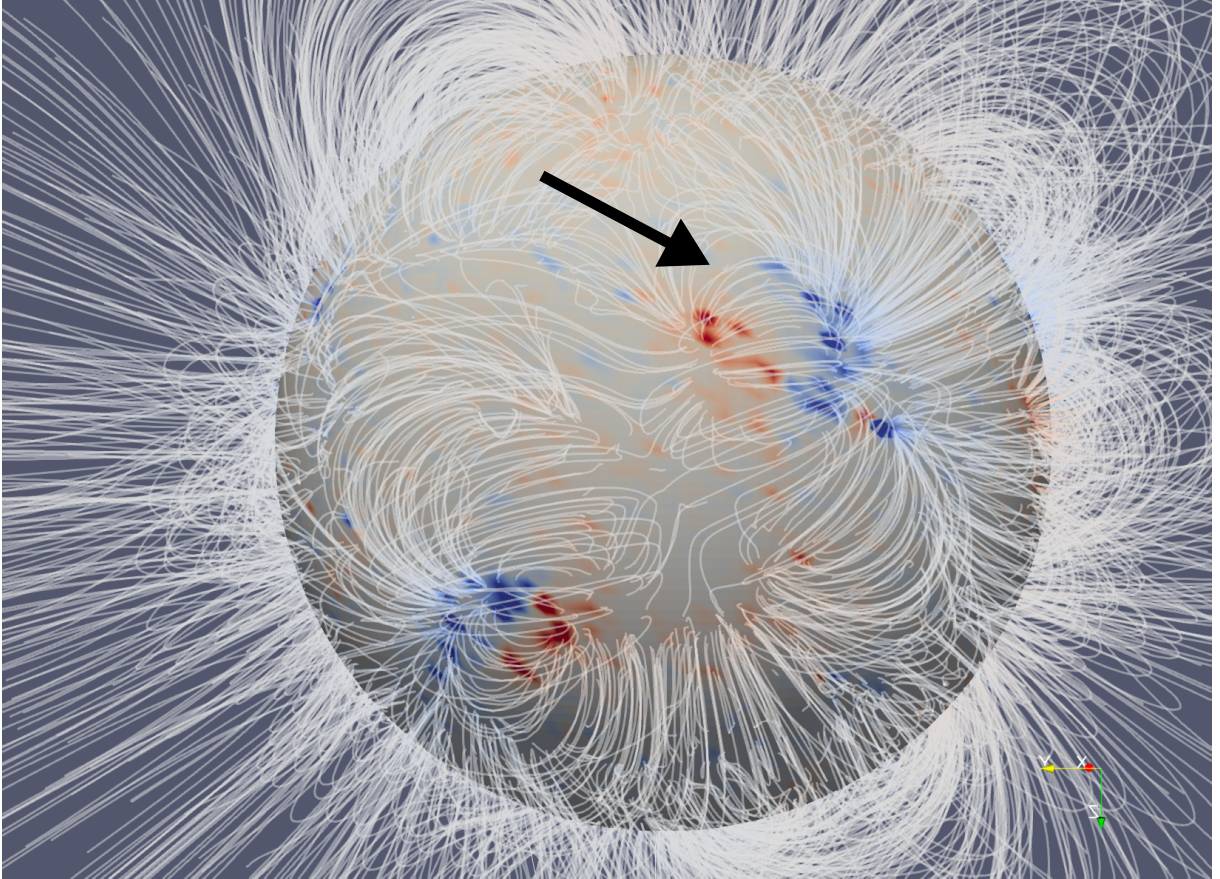
Figure 2.3: The extrapolated potential fields at 00:00 UT on November 4. The blue and red surfaces show the negative and positive radial components of the potential fields on the sphere surface, respectively. To aid visualisation, they are shown with a scale of lower and upper limits of $\pm$ 50 G. Black arrow points the rough location of the filament.
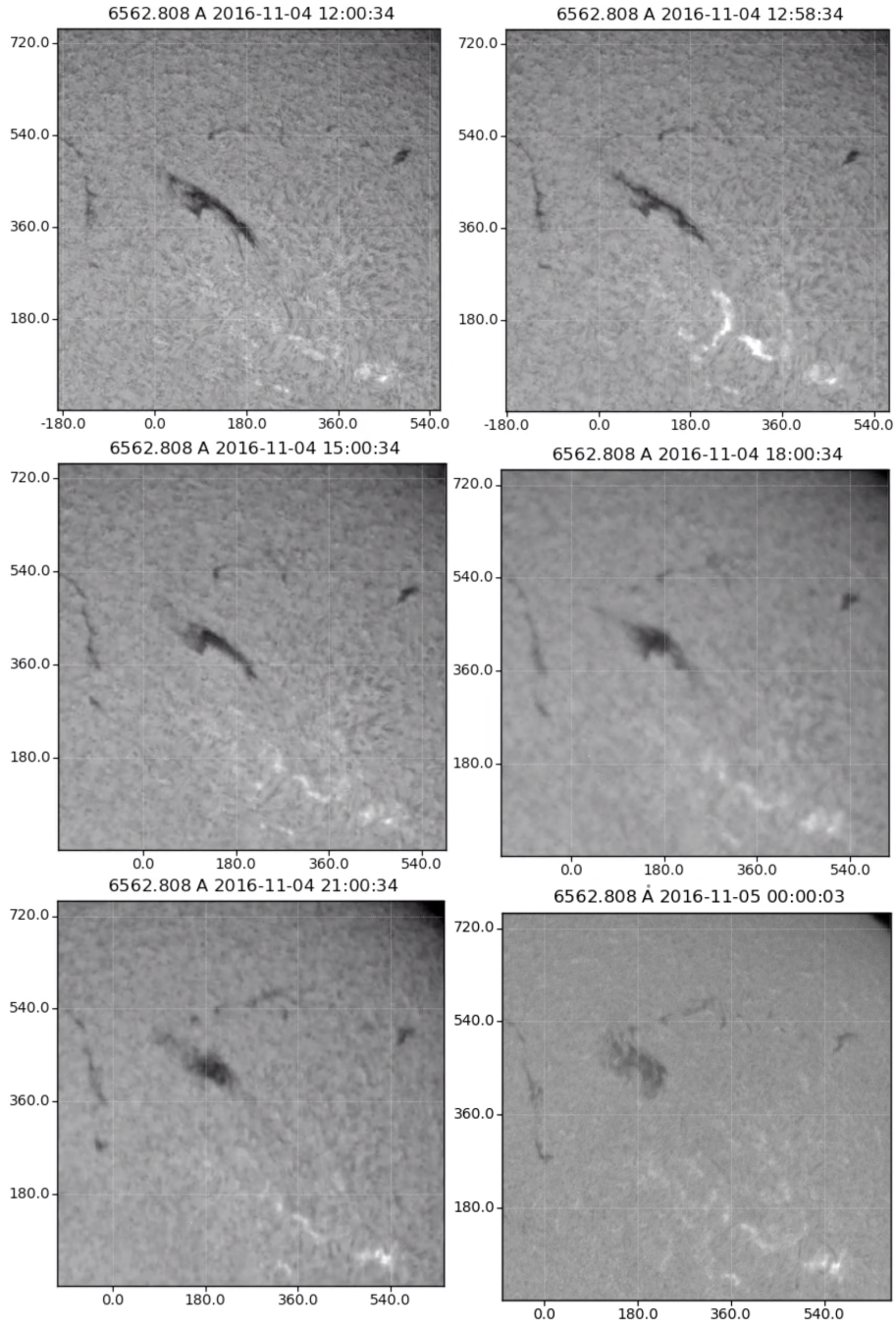
Figure 2.4: Temporal evolution of the target filament from 12:00 UT on November 4 (16 h prior to eruption) to 00:00 UT on November 5 (4 h prior to eruption). All the panels except for the bottom right panel were captured by the GONG program, and the bottom right panel was by the SDDI at the Hida Observatory.

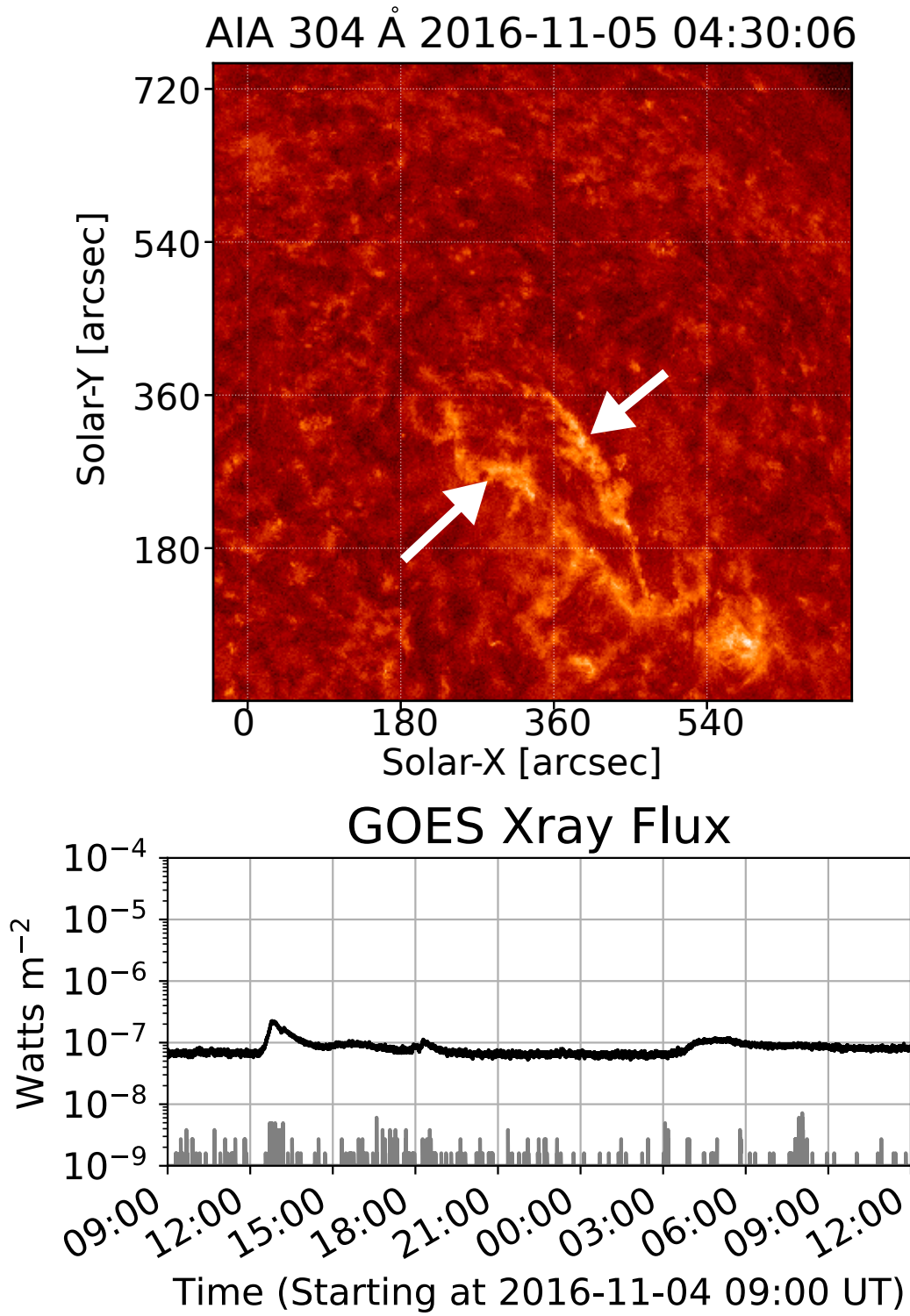Figure 2.5: *Top*: The SDO/AIA 304 sub-image at 04:30 UT on November 5, when the associated B1.1-class flare peaked. A two-ribbon flare (white arrows) was observed at the south-west of the filament location. *Bottom*: Soft X-ray fluxes between 1.0–8.0 Å(black) and 0.5–4.0 Å(grey) observed by the GOES. The gradual peak around 04:00 UT on November 5 is associated with the target filament eruption.

at -59 nT in Dst [50] around 18:00 UT on November 10, was also observed. According to Richardson & Cane Catalogue [51], an interplanetary CME shock was first detected on 2016 November 9 at 06:04UT, which is consistent with the estimated arrival time of the CME (2016 November 9 11:44UT) derived from the simple empirical model provided by Gopalswamy et al. (2000) [52]. After the arrival of the shock, the interplanetary CME plasma and the magnetic fields were observed from 2016 November 10 00:00UT to 2016 November 10 16:00UT on the basis of the occurrence of abnormally low proton temperature and the reduced fluctuations and organisation in the interplanetary magnetic fields [51]. Thus, this geomagnetic disturbance can be attributed to the CME driven by the filament eruption. Figure 2.6 shows an image captured by the SOHO/LASCO C2 and the geomagnetic disturbance on 2016 November measured in Dst index.

2.1.3 Extrapolation of magnetic fields

To investigate the decay index surrounding the filament, we computed potential fields from the imputed radial magnetic-field components of the photosphere. The decay index calculated from potential fields is commonly used for the stability analysis [53–56]. In this study, we set the critical decay index, above which Torus instability is considered to be more favourable, as 1, following previous observational studies [53,54]

It should be noted that it was necessary to compute potential fields for the whole Sun unlike other decay-index analyses in which potential fields are extrapolated only for the subregion of the Sun (e.g. Filippov (2013) [53]), because the region to be considered in this study (white rectangle in Figure 2.2) was too large to ignore the sphericity of the Sun. Moreover, for the purpose of tracking the temporal evolution of the global magnetic fields with a time cadence of 1 day, a synoptic chart is not suitable for the boundary condition of potential-field-source-surface (PFSS) extrapolation, because it is provided once in $\sim$ 27 days (rotation period of the Sun). Therefore, assuming that the unobservable hemisphere was equivalent to the HMI synoptic map, we used "patched HMI synoptic charts" described in Figure 2.7 as a boundary condition for conducting PFSS extrapolation.

Figure 2.7 shows how we constructed a boundary image used for extrapolation. There are three steps; first, we imputed the radial component of magnetic fields from HMI LOS magnetogram, assuming that HMI measures the line-of-sight component of a purely radial magnetic field (Figure 2.7 (a)). Secondly, we extracted the subregion of a magnetogram between heliocentric latitudes and longitudes of $\pm$ 60 degree (inside the white contour in Figure 2.7 (a)). Thirdly, we patched it in the form of a heliocentric spherical coordinate to the HMI synoptic chart for Carrington Rotation 2183 (Figure 2.7 (c)).

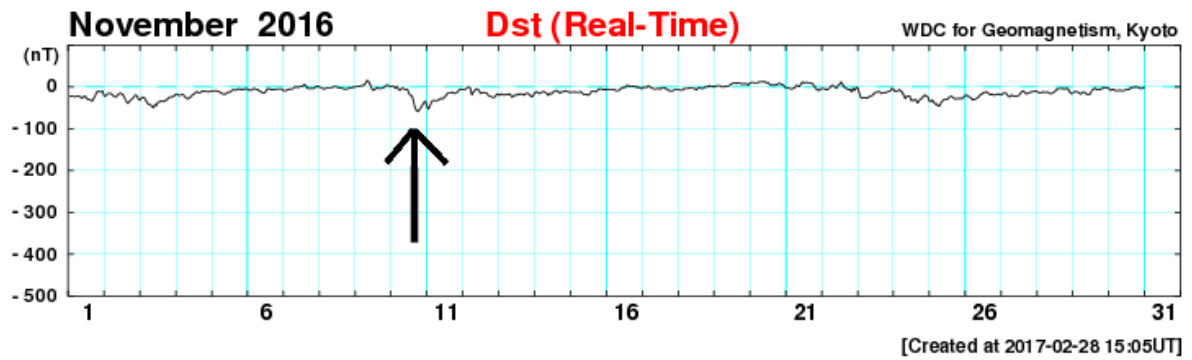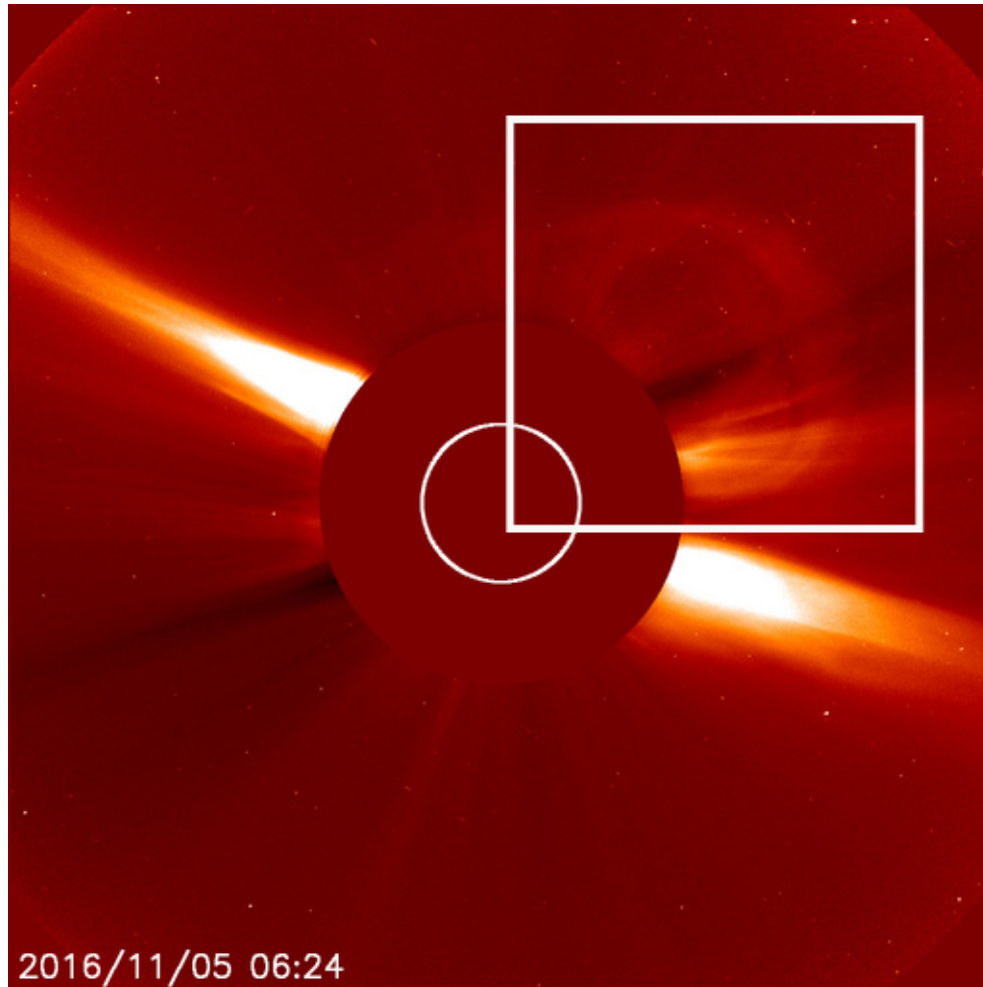We used Potential Field Source Surface Solver provided by Yeates, A. R. [57] to ex-

Figure 2.6: *Top*: CME associated with the target filament eruption observed by the SOHO/LASCO C2 (white rectangle). *Bottom*: The geomagnetic activity during 2016 November. The associated moderate geomagnetic disturbance was observed on 2016 November 10 with its peak value of -59 nT in Dst [50] at 18:00 UT on November 10 (black arrow).

2016-11-05 00:00 UT
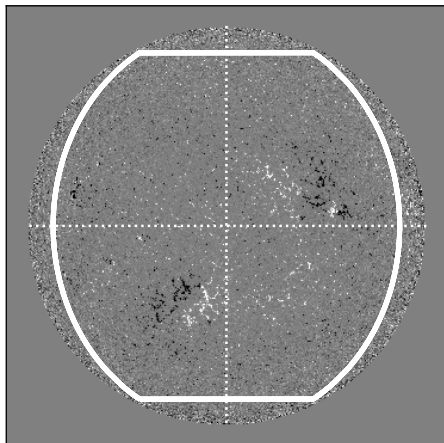
HMI Synoptic Chart for CR 2183
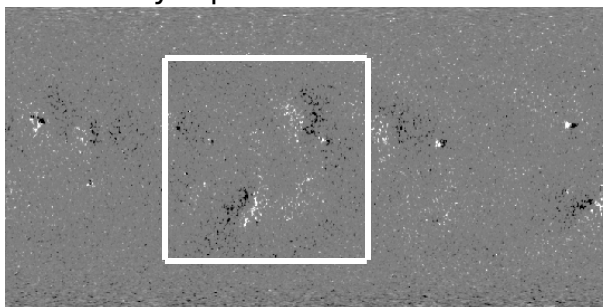
Patched Synoptic Chart for CR 2183
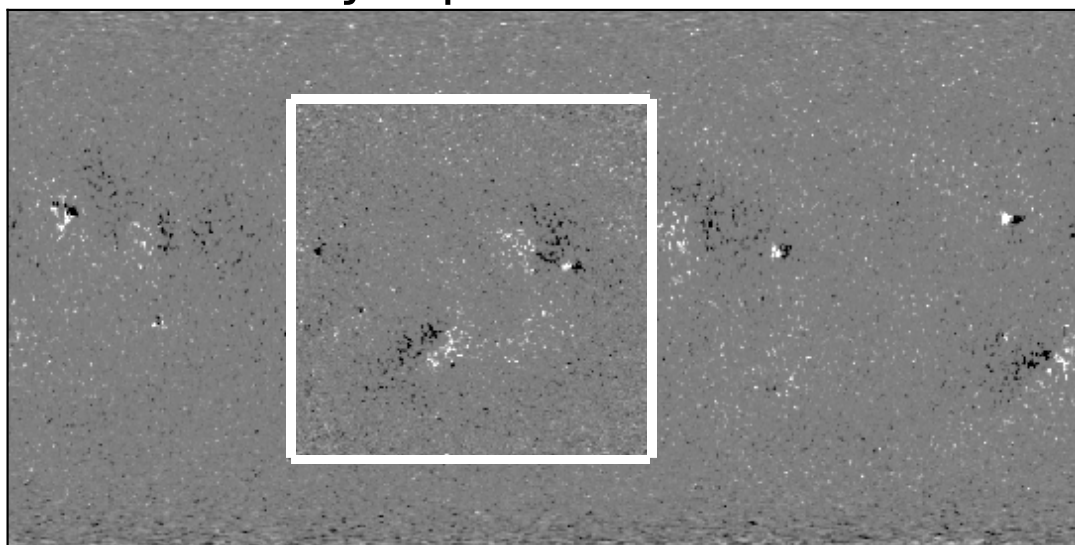
Figure 2.7: *Top Left*: The imputed radial component of magnetic fields converted from HMI LOS magnetogram observed at 00:00 UT on 2016 November 5. Horizontal and vertical dotted lines correspond to where the heliocentric latitude and longitude are 0, respectively. *Top Right*: Synoptic chart for Carrington rotation 2186 converted from observations of the SDO/HMI. *Bottom*: The patched synoptic chart. Inside the white rectangle is the subregion of HMI magnetogram (white contour in the top left panel) in the form of a heliocentric spherical coordinate.

trapolate potential fields [58]. This Python-based code solves the basic equations for magnetic fields by using a finite-difference method with an assumption that the electric currents are negligible in a spherical shell. For more details, see `https://github.com/antyeates1983/pfss`. We chose 2.0 solar radius above the photosphere and 7 Mm as the height of source surface and the grid size of radius (height), respectively. Grid sizes of zenith and azimuth angle were taken to be 0.5 degree.

2.1.4 Cloud model

To compute the LOS velocity and micro-turbulence inside a filament, we utilised cloud model first proposed by Beckers 1964 [59]. Assuming that (1) the source function is constant along the wavelengths and (2) along the LOS direction and that (3) the line absorption coefficient is a Gaussian shape, this model enables us to determine four physical parameters of the plasma cloud, the source function, the Doppler width, the Doppler shift, and the optical depth [60–66]. By virtue of wide wavelength coverage and high spectral, spatial, and temporal resolution of the SDDI, we can track these four physical parameters in unprecedented detail. The LOS velocity (v_{los}) and the micro-turbulence (ξ) at each pixel were calculated from the Doppler shift ($\Delta\lambda_S$) and the Doppler width ($\Delta\lambda_D$), respectively, based on the equations [60];

$$v_{los} = c\frac{\Delta\lambda_S}{\lambda_0}, \tag{2.1}$$

$$\Delta\lambda_D = \frac{\lambda_0}{c}\sqrt{\xi^2 + \frac{2k_B T}{m_p}}, \tag{2.2}$$

where c, λ_0, k_B, T, and m_p are the velocity of light, the wavelength of Hα line centre (6562.808 Å), Boltzmann constant, a fixed temperature of 10^4 K in the filament, and the mass of proton, respectively.

Figure 2.8 shows the flow chart of our analysis. Here, we present more detailed explanation of our method. In the first step (grey arrows in Figure 2.8), we produced a so-called "mask", a binary image to cover only the target filament. Since the cloud model can be applied only to the plasma cloud area above the chromosphere, this process was essential to determine where four physical parameters were to be calculated. In the first grey arrow pointing right, we selected the positions of dark features in a subregion for each wavelength full-disk image. The produced image has one for the positions of dark features and zero for the other positions. Dark features were defined as the positions where the intensity, $I(\lambda)$, is lower than $\bar{I}(\lambda) - 2\sigma_{I(\lambda)}$, in which $\bar{I}(\lambda)$ and $\sigma_{I(\lambda)}$ are the mean and standard deviation of the intensity, respectively. In the second grey arrow pointing
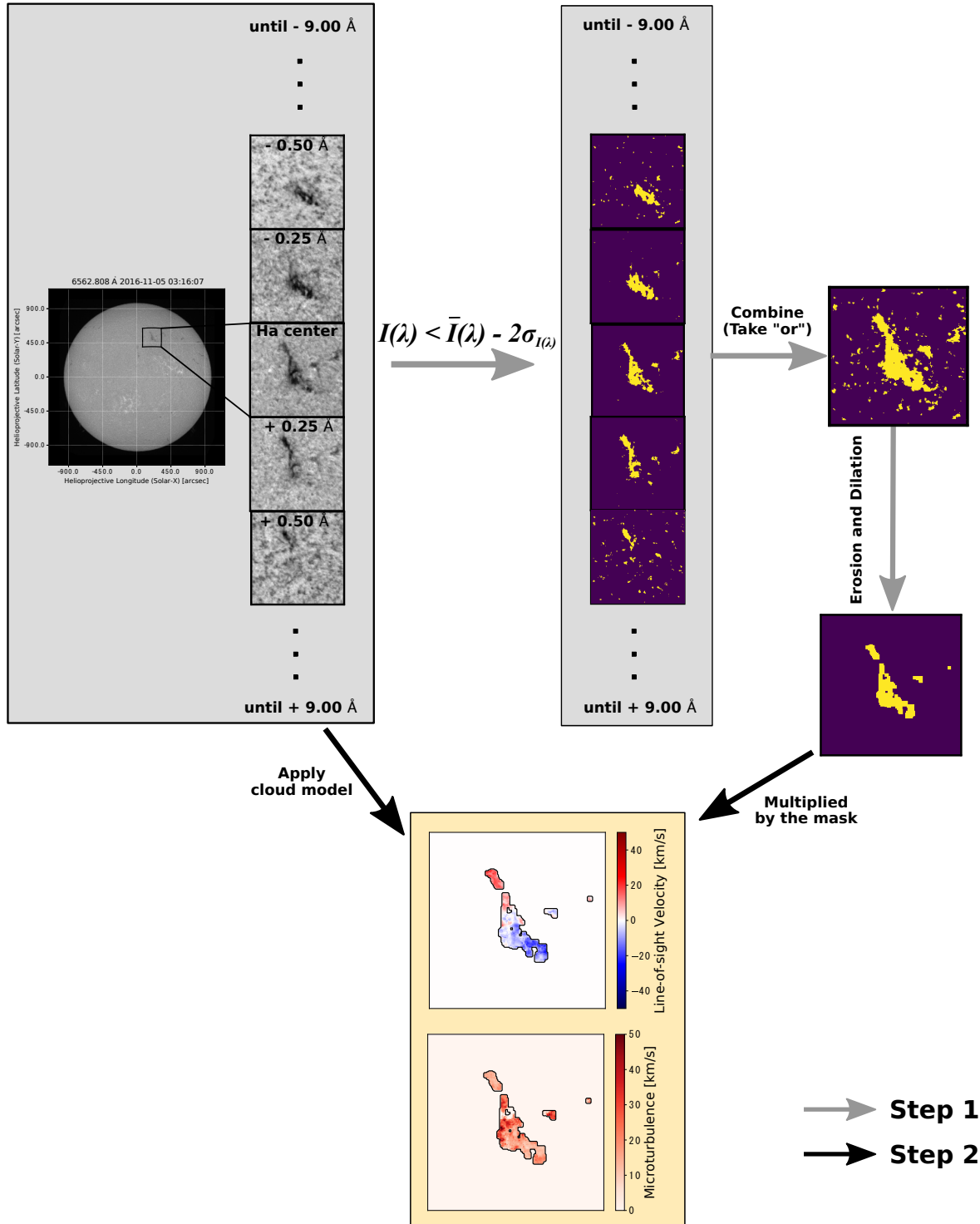
Figure 2.8: Flow chart of our analysis. Grey and black arrows indicate Step 1 and Step 2, respectively. The black lines on the LOSV and micro-turbulence maps contour the mask where the cloud model was applied.

right, we took "or" for all the 73 binary masks; i.e. the produced image has one for the positions where there is a dark feature in at least one wavelength image and zero for those where no dark features existed in 73 wavelengths. In the third grey arrow pointing bottom, we applied standard image processing methods called "erosion" and "dilation". These processes are conduced for all the pixels in the combined binary mask. Erosion is a process by which a certain pixel becomes one only if all the surrounding eight pixels are one, whilst dilation is an opposite process; i.e. a certain pixel becomes zero only if all the surrounding eight pixels are zero. Erosion and dilation are typically used to remove tiny noises in a binary image and to extract comparatively large features in the image. This erosion-dilation process is essential to select only the dark feature originated from a filament, as one can see the contaminated granular dark features such as spicules in the combined image. We applied two times of dilation processes after three times of erosion processes. The number of processes were determined by trial and error.

After producing the mask image, we moved on to the further step. Black arrows in Figure 2.8 show the second step of calculation of the LOS velocity and the micro-turbulence of the filament. By applying the cloud model only to where the binary mask image has one, we obtained the doppler shift, doppler width, source function, and optical depth inside the main body of the filament. The doppler shift and doppler width were converted to the LOS velocity and the micro-turbulence, respectively.

2.2 Results

2.2.1 LOS velocity distribution

Figure 2.9 shows the time series of the SDDI images. From the top to the bottom, the observations in Hα centre, +0.5 Å, -0.5 Å, -1.0 Å, and the LOS velocity are displayed. The filament was stable and only the small portions were barely visible at $\pm$ 0.5 Å, before 00:00UT on Nov. 5. However, from $\sim$ 00:30UT the small scale motions in the filament became noticeable in the wing images as well as the LOS velocity. The amplitude of the small scale motion showed further increase after $\sim$ 2:30UT, and finally the filament erupted around 3:30UT.

In order to quantify the small-scale motions in the filament prior to the eruption, we made the histograms of the LOS velocity. Figure 2.10 shows the examples of the histograms and the corresponding LOS velocity images at 22:49UT on Nov. 4, 1:05UT, 3:07UT and 3:22UT on Nov. 5. The mean velocity and the standard deviation are also shown in the figure. One can recognise that the histograms are quite symmetric before the eruption, but the standard deviation increases with time and the histograms themselves
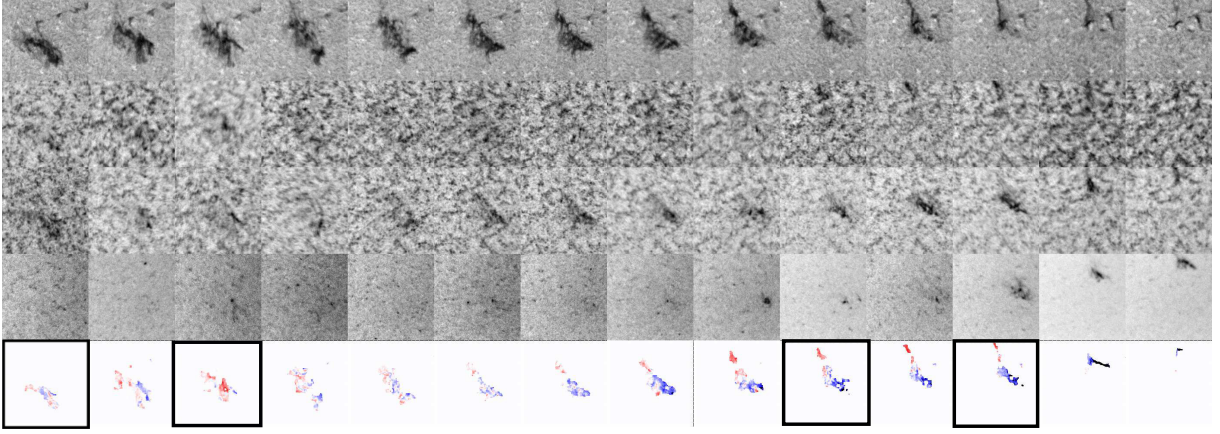
Figure 2.9: Time series of Hα images at the line centre, at + 0.5 Å, at - 0.5 Å, and at - 1.0 Å(the top three row) and of the images of LOS velocity of the filament (bottom row). The velocity scale of the bottom images are identical to the right images of Figure 2.10.

become asymmetric.

Figure 2.11 shows the temporal profile of the standard deviation of the histogram and the mean LOS velocity. For the standard deviation, the data from the previous day is also shown (from 23:00UT on November 3 to 7:00UT on November 4). The standard deviation stays almost constant around 2–3 km s^{-1} on the previous day (23:00UT on November 3 – 7:00UT on November 4). At the beginning of the observation on the next day (22:00UT on November 4), the standard deviation slightly increases to 3–4 km s^{-1}. It stays constant until $\sim$ 0:30UT and then gradually increase with a rate of 1.1 m s^{-2} until it peaks at around 1:10UT. This peak in the standard deviation is associated with a positive peak of the mean velocity. Then, the standard deviation starts to increase again at around 2:30UT with a rate of 2.8 m s^{-2}, and at around 3:10UT both the standard deviation increases sharply and also the mean velocity decreases sharply, leading to the onset of the eruption.

2.2.2 Micro-turbulence

Figure 2.12 shows the temporal evolution of the spatially averaged micro-turbulence of the filament during the same period as Figure 2.11. The horizontal dotted line indicates the micro-turbulence of 15 km s^{-1}. Although the mean micro-turbulence had been around 12 km s^{-1} until 21 h prior to eruption, it increased to around 14 km s^{-1} at 22:00 UT on November 4 (6 h prior to eruption) and continued increasing to around 25 km s^{-1} until the onset of the eruption.
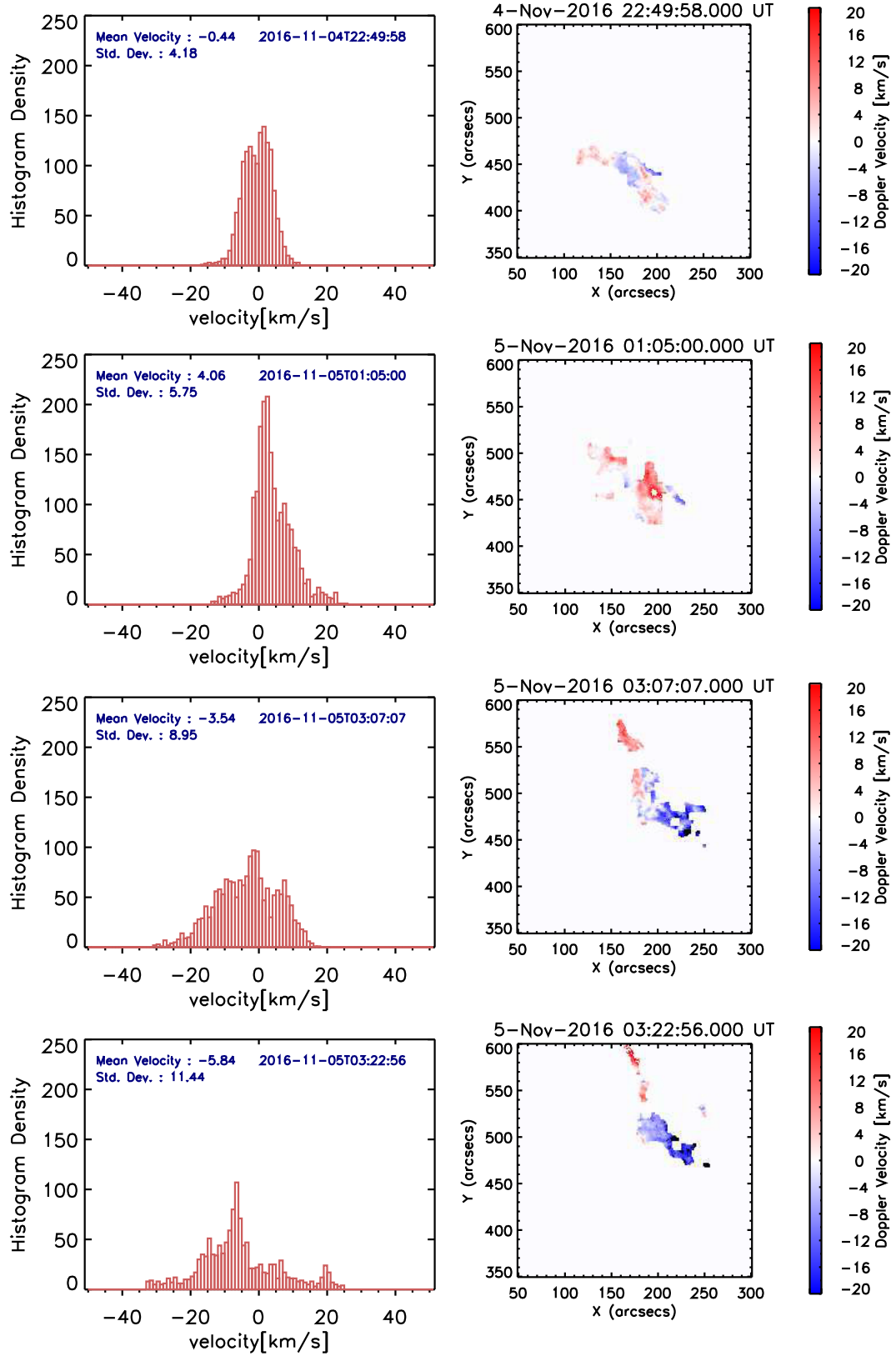
Figure 2.10: *Left*: The histograms of the LOS velocity images. Each histogram corresponds to the right image. The word "Std. Dev." means standard deviation. *Right*: 4 LOS velocity images inside the black squares of Fig.2.9.
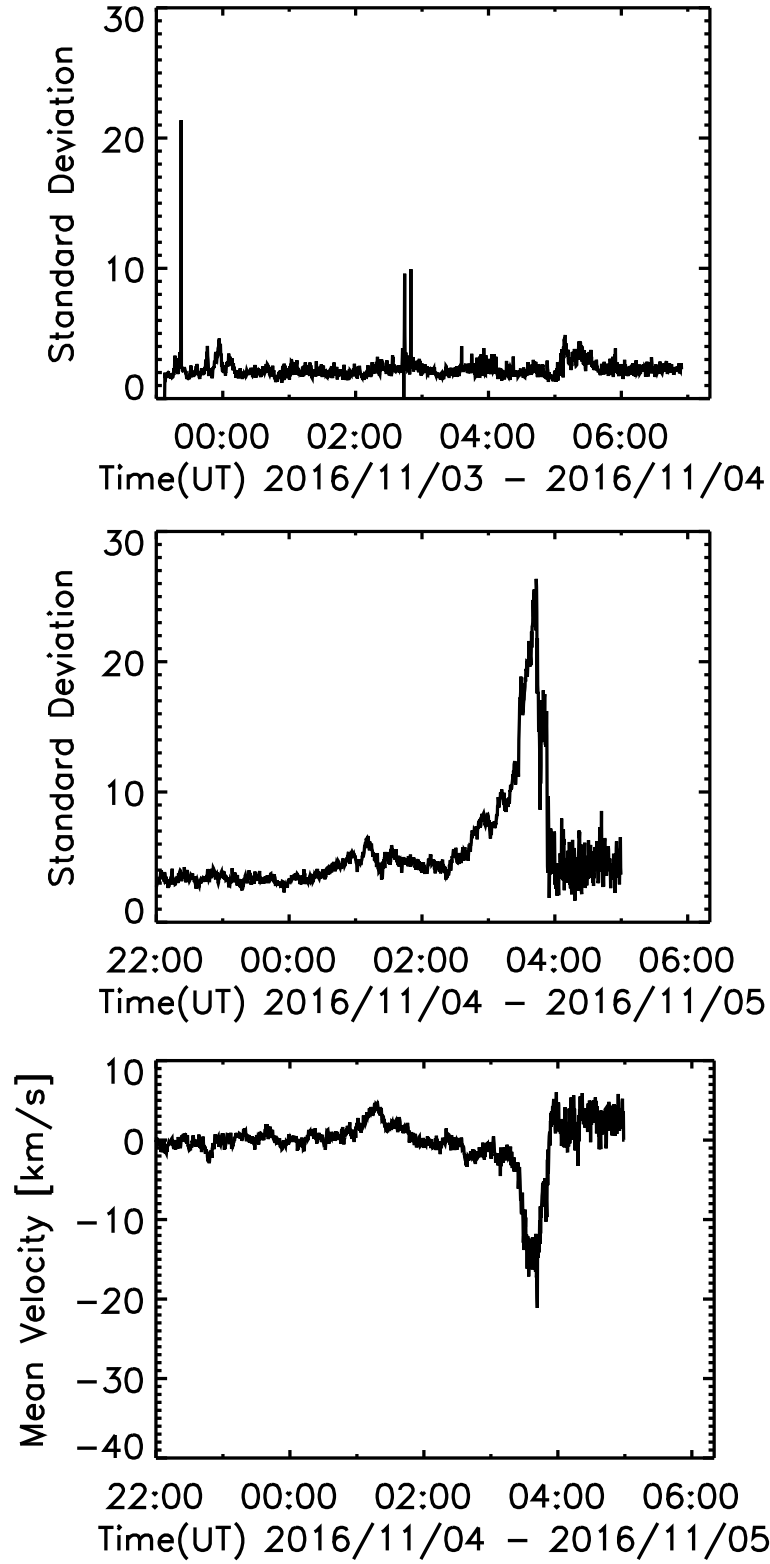
Figure 2.11: *Top and Middle* : Temporal evolution of the standard deviation of LOS velocity from 23:00UT on November 3 to 7:00UT on November 4 and from 22:00UT on November 4 to 5:00UT on November 5. *Bottom* : Temporal evolution of the average LOS velocity.
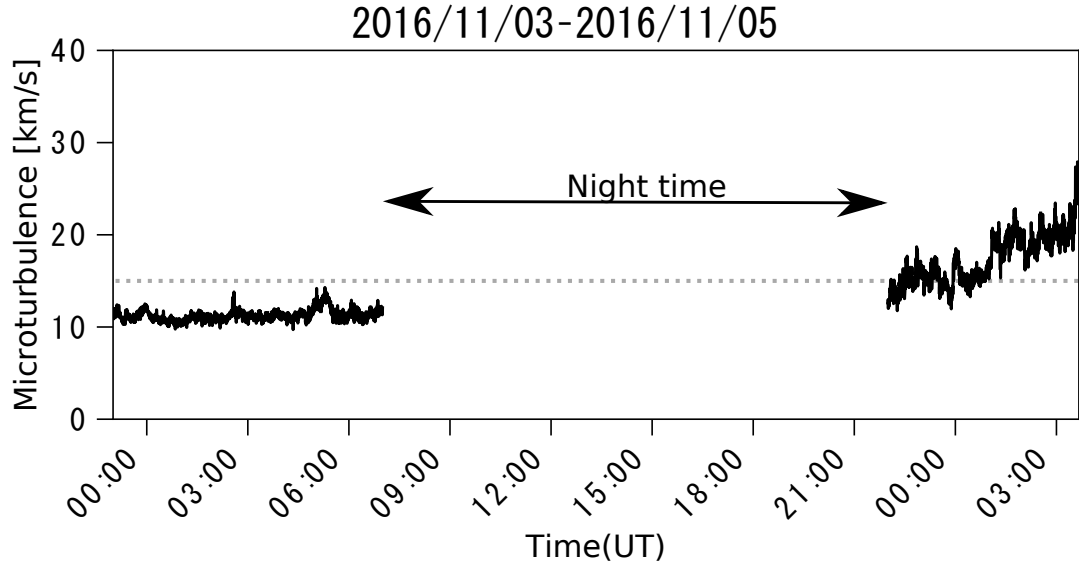
Figure 2.12: The spatial average of the micro-turbulence of the filament from November 3 on 23:00 UT (around 29 h prior to eruption) to November 5 on 03:40 UT (the eruption time). The horizontal dotted line indicates 15 km s^{-1}.

2.2.3 Decay index

Figure 2.13 demonstrates the decay-index distribution in the vicinity of the filament on November 3, 4 and 5 at 00:00 UT. Left panels show Hα images superimposed by the photospheric polarity inversion lines (PILs) denoted by red lines and the cross sections of the right panels depicted as cyan lines. Each right panel exhibits the side view of the three-dimensional decay index along the cyan line in the left panel. From top to bottom, we can recognise a similar decay-index distribution with time. Generally, the decay index took higher value in the higher location. In the vicinity of the filament, the decay index was always below one. Note that the filament in Hα laid between the positions 2 and 3 on November 3 and 4, whilst it was located between 1 and 2 on November 5. The emerging flux region (EFR; see Figure 2.16) appeared in the vicinity of the position 3. It was difficult to derive the height of the filament from LOS velocity due to the lack of data (night time).

2.2.4 Coronal line emission

Figure 2.14 shows the temporal evolution of the spatially averaged count per pixel in Fe XIV (a few 10^6 K) from a linear combination of AIA 211, 171 and 193 passbands [45] estimated by;

$$I(\text{Fe XIV}) = I(211\mathring{A}) - I(171\mathring{A})/17 - I(193\mathring{A})/5. \tag{2.3}$$

29
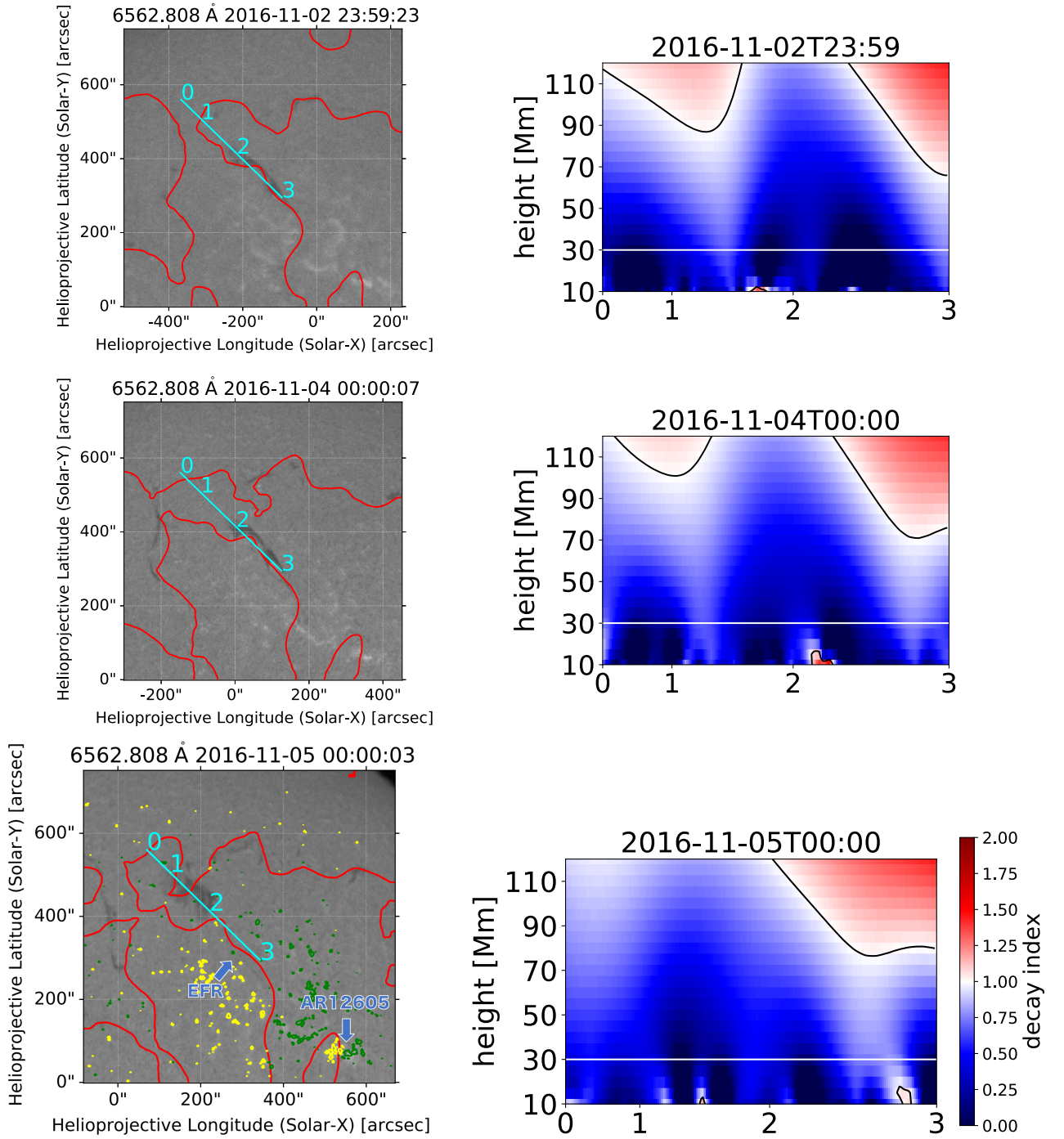
Figure 2.13: *Left*: Hα centre images observed by SDDI at three different times superimposed by photospheric PIL (red line). Cyan line in each panel corresponds to the cross section of the right panel. Yellow and green contours indicate the HMI LOS magnetogram at ±100 G. For EFR, see Figure 2.16. *Right*: Side view of three-dimensional distribution of decay index. Each digit at the bottom axis corresponds to the digit on the left panel. White and black lines corresponds to the approximate height of the filament (30 Mm) and the contour where decay index is 1, respectively.

White rectangles are located between the two ribbons. These locations were in the vicinity of the stable filament seen in Hα centre. To remove the noises, we temporally averaged every AIA intensity for 5 minutes. We can observe rising intensities inside the rectangles 3 and 4 approximately from 18:00 UT, while those in the other regions did not exhibit such an ascent. Note that the location of EFR in Figure 2.16 corresponds to the rectangle 2.

Figure 2.15 exhibits the same temporal evolution except the emission line of Fe XVIII (a few 10^7 K) estimated by the equation [45];

$$I(\text{Fe XVIII}) = I(94\text{\AA}) - I(211\text{\AA})/120 - I(171\text{\AA})/450. \qquad (2.4)$$

Inside any rectangles, the counts did not exhibit the rising feature except the sudden increase around 13:00 UT. This is due to a B-class flare taken place at NOAA AR 12605.

2.3 Discussion

2.3.1 Turbulent motion

The increase of the standard deviation with a rate of 2.8 m s^{-2} during 2:30–3:10UT before the eruption may correspond to the slow-rise phase commonly observed before filament eruptions [67,68]. By investigating the Hα centre images in Figure 2.9, one can recognise the global drift of the filament toward north-west in the plane of the sky. On the other hand, the weaker (1.1 m s^{-2}) increase in the standard deviation starting around 00:00UT is not associated with a global drift of the filament. This may be regarded as the precursor of the onset of the slow-rise phase.

It should be also noted that, the standard deviation during 22:00–00:00UT is almost constant, but its absolute value is slightly larger than that in the previous day. Moreover, as seen in Figure 2.12, the average micro-turbulence inside the filament also demonstrated an increase with time. These results might reflect the preceding turbulent motion of the plasma inside a filament. The difference between the standard deviation of the LOSV distribution and the average micro-turbulence is the assumed blobs taken into account. LOS velocity only assumes one moving component of plasma blob along line of sight, whereas the micro-turbulence considers the actual unresolved plasma motion. To derive more realistic LOSV distribution, we need further investigation to improve the model, but that is not the focus of this study.

Here, we suggest two possible origins for the preceding turbulent motions; one is the magnetic Rayleigh-Taylor (RT) instability, and the other is small-scale reconnections. The small-scale vertical motions of plasma are often observed in quiescent prominences
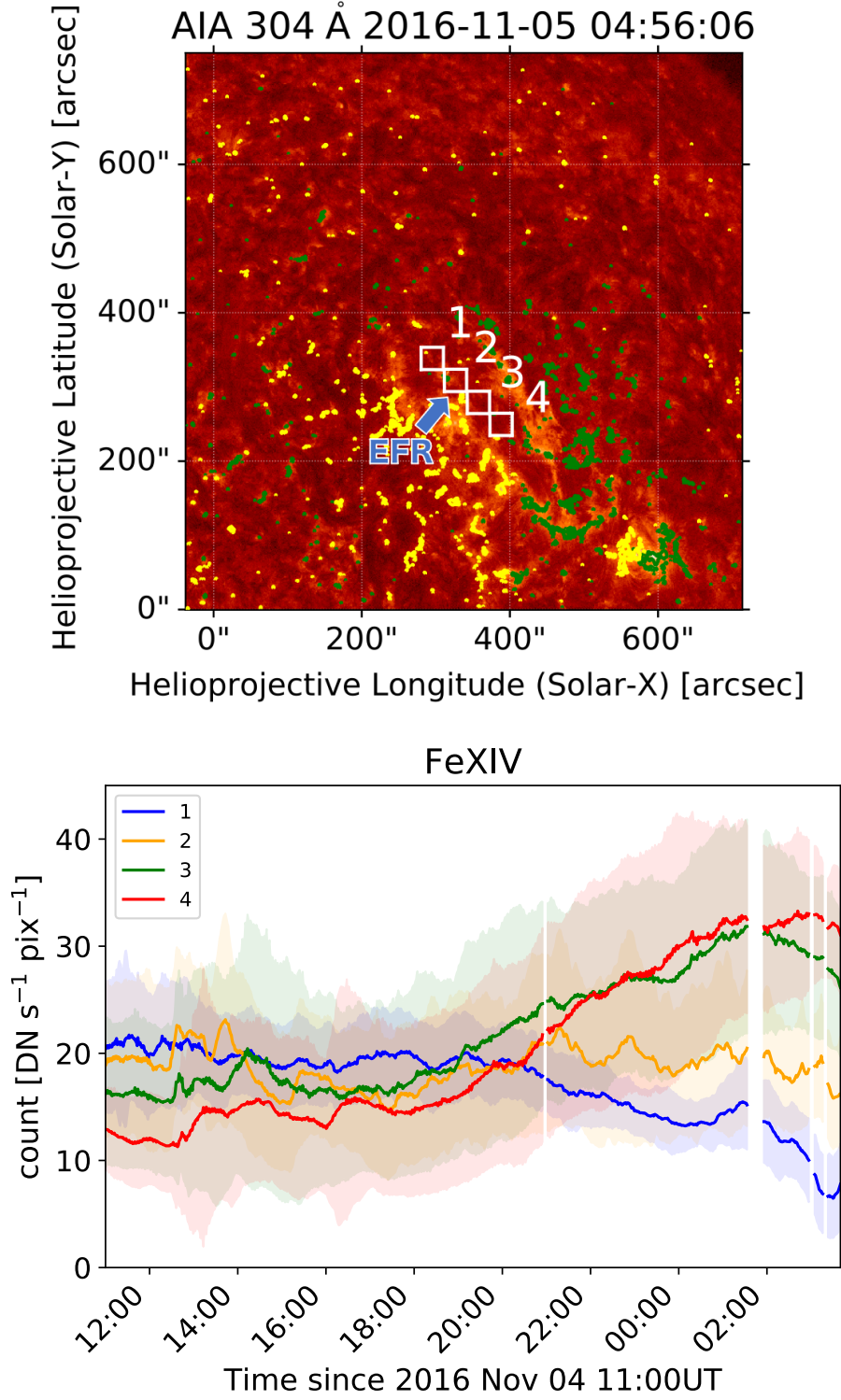
Figure 2.14: *Top*: The areas to calculate average counts are depicted as white rectangles on SDO/AIA 304 image. For the coloured contours in yellow and green and EFR, see Figure 2.16. *Bottom*: Temporal evolution of spatially averaged counts per pixel in Fe XIV emission inside four different areas, 1, 2, 3, and 4. Each number corresponds to the rectangle in the panel (a). The effect of the solar rotation was corrected for determining the white rectangles. The shaded area indicates $\pm 1\sigma$ counts inside each rectangle.
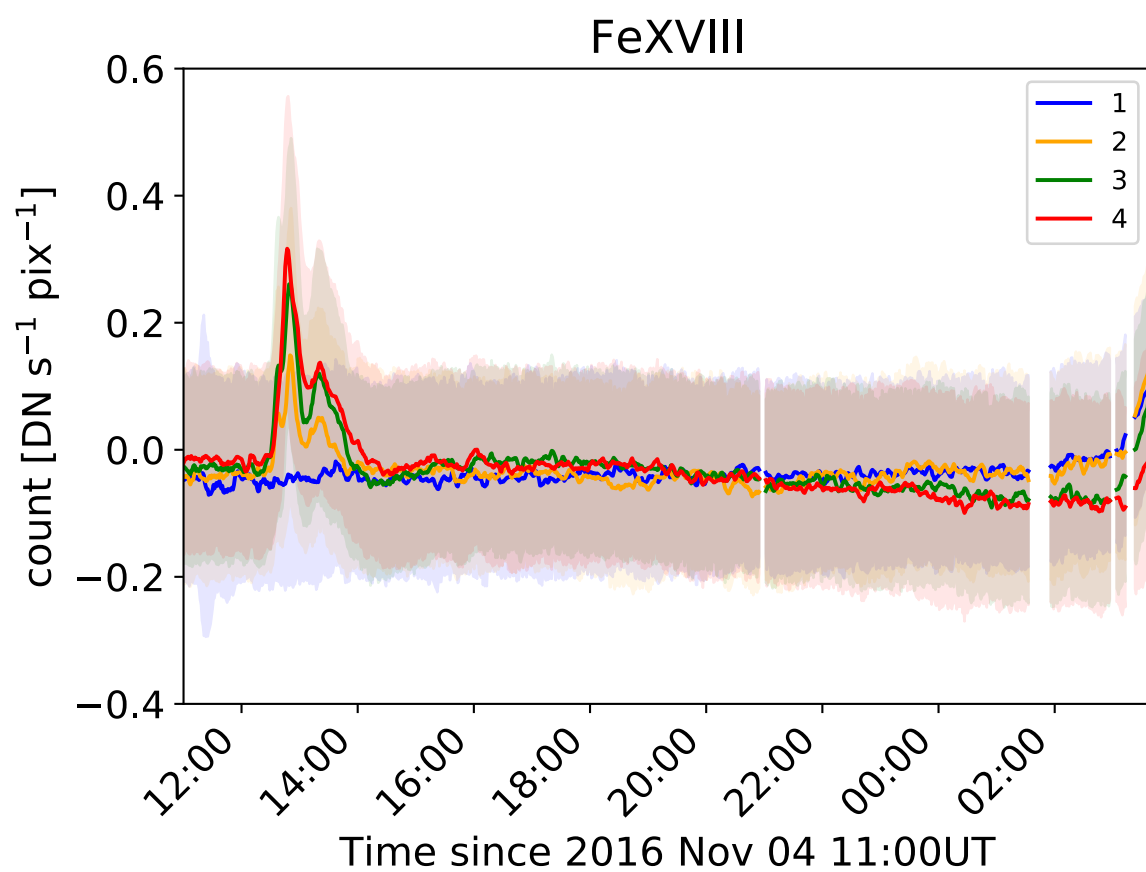
Figure 2.15: Same plot as Figure 2.14 (bottom) except the emission line of Fe XVIII.

with high-resolution observation [69, 70]. Its physical origin is still uncertain, but one promising mechanism is the magnetic RT instability [71, 72]. Hillier et al. (2011) [71] curried out three-dimensional magnetohydrodynamic (MHD) simulations to analyse how the magnetic flux rope (KS model) is stable to the magnetic RT instability, and reconstructed the up-flows of the plasma with constant velocities. The dependences between initial parameters of the ideal MHD simulations and the evolution of the instability were also discussed in Hillier et al. (2012) [72]. In their studies, the maximum velocity of a rising plume reached 5.9 and 2.5 km s^{-1} under the conditions of plasma $\beta = 0.5$ and 0.2, respectively. The terminal velocity of the rising plasma plume is determined by the balance among the Lorentz force, the gravitational force, and the gas pressure gradient at the top of the plume. At the beginning of the rising, the plume experiences an acceleration due to the buoyancy dominant force. It continues until the magnetic fields are transported by the flow and sufficiently accumulated at the top of the plume to balance the gravitational force, the magnetic tension, and the magnetic and gas pressures. As a magnetic flux rope containing a filament is reaching eruption, it should be expected that the flux rope expands, and the magnetic fields become weaker. Thus, it should take more time to realise the force balance at the top of the plume, resulting in the faster terminal velocity of the plume and the more active small-scale motions in the filament.

The other possibility is due to the small-scale reconnections below the filament. In this study, we observed rising intensities in the coronal line (a few 10^6 K) in the vicinity of the filament (see Figure 2.14). These increasing profiles could denote the continuous occurrence of small-scale reconnections below the flux rope, which could lead to destabilising it and result in a disturbance of the small-scale plasma inside the filament. Chifor et al. (2006) [73] observed a EUV brightening feature ($\sim10^6$ K) at the footpoint of a prominence $\sim$20 min prior to the eruption. In their study, they concluded that this suggestive brightening denoted the onset of "tether-cutting reconnection", in which once reconnections below a flux rope are initiated, it will ascend due to cutting off the anchoring magnetic fields, and more reconnections will be induced (e.g. Moore et al. (2001) [74]). The observation of the continuous enhancement in Fe XIV could be attributable to this positive feedback loop process, and the evolution of this event could be explained by this scenario. Note that during this period there was no increase in Fe XVIII line (see Figure 2.15), which indicates that there might not be substantial flares to increase the high-temperature line.

2.3.2 Trigger and evolution of the eruption

An emerging flux was observed around 9 h before eruption, and this emerging flux could be the trigger of the eruption. The studies showed that the existence of EFR plays a key
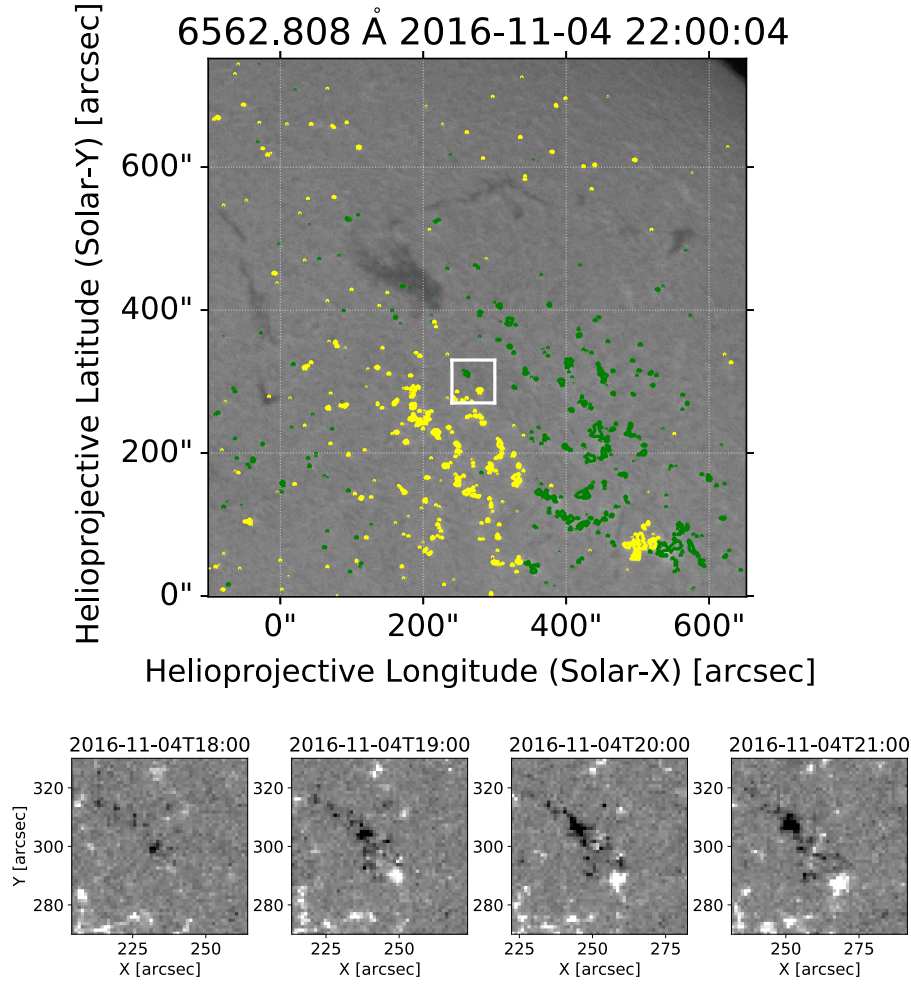
Figure 2.16: *Top*: Hα image taken by the SDDI superimposed by the contours of +100 G (yellow) and −100 G (green) of the HMI LOS magnetorgram. *Bottom*: The HMI LOS magnetograms inside the white rectangle in the top panel at four different times. To enhance visualisation, the magnetograms are shown with a scale of lower and upper limits of ± 100 G.

role in the initiation of a filament eruption from the observational and theoretical points of view [43, 44, 75]. Figure 2.16 shows that the location of a bipole in comparison with that of the filament and the snapshots of EFR observed by the HMI. One can recognise that from 19:00 UT on November 4 the bipole evolved with time. The two polarities were separated with time, which is characteristic of an emerging flux. Kusano et al. (2012) [75] found that there are several types of small magnetic structures which should appear in the vicinity of the PIL in order to favour the onset of solar eruptions. Especially, one of them is called reversed-shear-type (RS-type), in which small-scale magnetic field (such as emerging flux) is injected to pre-existing large-scale sheared magnetic field with a certain rotation angle with respect to large-scale potential field (see Figure 1 and 5 in [75]).

Figure 2.17 shows solar sub-images observed by the AIA 304 and the HMI at 03:41 UT on November 5 superimposed by the blue dotted line indicating the edge of the two ribbons (left and middle). We can notice that the large-scale magnetic field surrounding the filament was sheared in clockwise. Right panel shows the schematic diagram of top view of the large-scale and small-scale magnetic structures. This magnetic-filed configuration corresponds to RS-type configuration for negative shear (clockwise rotation) introduced in Kusano et al. (2012) [75]. Thus, we concluded that the filament eruption could be triggered by the emerging flux observed at 18:00UT.

Figure 2.13 shows that the decay index nearby the filament was smaller than one, meaning that the flux rope was Torus stable. It should be noted that in Kliem & Török (2006) [41], they assumed the shape of flux rope as a ring. On the other hand, Ishiguro & Kusano (2017) [76] found that the ideal MHD instability can be initiated even in the Torus-stable condition, i.e., decay index is less than one, if the magnetic loop has a double-arc-shape configuration. They called this critical condition for the eruption under a certain geometry as Double arc instability (DAI). The DAI-favoured magnetic configuration can be produced in the "tether-cutting" reconnection scenario [74]. Additionally, this scenario agrees with the result of Kusano et al. (2012) [75] The evolution of this event could be explained by this scenario (see the previous section), and the magnetic-field configuration could be the DAI-favoured one.

2.3.3 Implication for space-weather prediction

Quiescent filament eruptions sometimes drive large CMEs and cause severe geomagnetic disturbances. Thus, in terms fo a space-weather prediction, it is also of a great importance to predict filament eruptions. McAllister et al. (1996) [77] reported a large polar crown filament eruption on 1994 April 14. Although this event was not associated with any significant flares, we experienced a severe geomagnetic disturbance with Dst is approximately -200 nT in a few days of the eruption. Isobe et al. (2019) [78] investigated the records of aurora displayed in the middle magnetic latitudes (China and Japan) during the Maunder minimum in 1653, which indicates the presence of a great geomagnetic disturbance although the solar activity at that time must have been very quiet. With a simple theoretical discussion, they concluded that this geomagnetic storm was extremely intense (Dst < -300 nT) and can be driven by a quiescent filament eruption.

Our result implies that it is hardly possible to predict the filament eruption only from the photospheric magnetic fields and the extrapolated potential fields in this event because the photospheric magnetic fields scarcely changed over the past several days of the eruption. From Figure **??**, we cannot recognise any significant changes in the global magnetic-field configuration which lead to the onset of the eruption. Moreover, the region
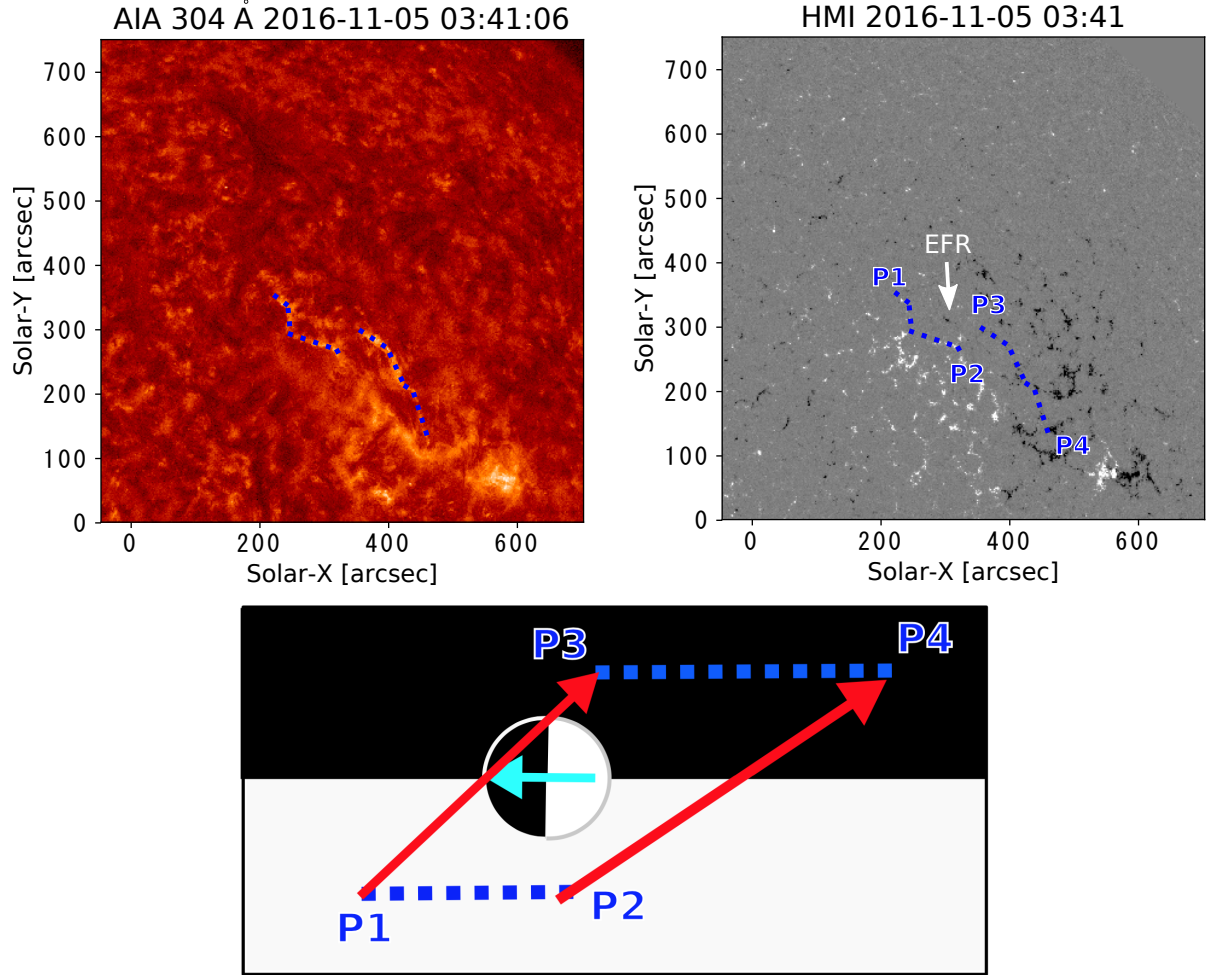
Figure 2.17: *Top*: Solar sub-images observed by SDO/AIA 304 and SDO/HMI at 03:41 UT on November 5. The blue dotted line corresponds to the edge of the flare ribbon. White arrow indicates the emerging flux region. To enhance visualisation, the magnetogram is shown with a scale of lower and upper limits of $\pm$ 200 G. *Bottom*: The schematic diagram of top view of the large-scale and small-scale magnetic structures. Cyan and red arrows indicate the small-scale magnetic field and the possible large-scale field, and white and black regions correspond to the positive and negative polarity regions, respectively. Blue dotted lines and P1-4 are simple expression of those in the middle panel. This magnetic-filed configuration corresponds to RS-type configuration for negative shear (clockwise rotation) introduced in Kusano et al. (2012) [75]

to be considered around the filament is a global quiet one, and we can hardly expect to obtain precise vector-magnetic-field data. That is why it is difficult to extrapolate more realistic magnetic fields such non-linear force free fields for this event. This illustrates that there is a case in which it is difficult to predict and monitor when a filament will erupt only from the global magnetic-field configuration. Thus, we suggests that the internal turbulent motion in a filament can also provide useful clues to predict filament eruptions

Chapter 3

Statistical Study of Small-scale Motions in Solar Filaments as the Precursors of Eruptions

Since it is still unclear whether the increase in the standard deviation of LOS velocity prior to the eruption found in the previous Chapter, is common in filament eruptions, other 11 filaments that vanished in Hα line centre images were further analysed in a similar manner; these included two quiescent filaments, four active region filaments, and six intermediate filaments. This study[*] showed that in all the 12 events, the standard deviation of the LOS velocities increased before the filaments vanished. It is also found that; (1) 9 out of 12 events exhibited Phase 1, during which the standard deviation of LOS velocity increases without significant changes in its average, (2) the duration of Phase 1 widely ranged from 0.18 to 42 h, and limiting to not-overestimated events, a quiescent filament has a 10 times longer Phase-1 duration than the other types of filaments, and (3) in all the cases of the intermediate and quiescent filaments, the standard deviation during Phase 1 generally changed from 2–3 km s^{-1} to 4–5 km s^{-1}. According these results, we could predict the clearly observed filament eruptions with the lead time of 1.3 ± 0.47 h. Thus, we concluded that the standard deviation of the LOS velocities of the small-scale motions in a filament can potentially be used as the precursor of filament eruptions.

A dark filament, or a prominence, is the dense and cool plasma supported by magnetic fields in the solar corona, with a plasma density of 10^9–10^{10} cm^{-3} and a temperature of 10^4 K. In general, a filament is globally stable; however, at the end of its life, it generally becomes unstable and erupts [34]. A filament eruption is generally associated

---

[*]Seki, D., Otsuji, K., Isobe, H., Ishii, T. T., Ichimoto, K., Shibata, K., "Small-scale motions in the solar filaments as the precursors of the eruptions", Publications of the Astronomical Society of Japan, 71(3), 56(18pp), 2019
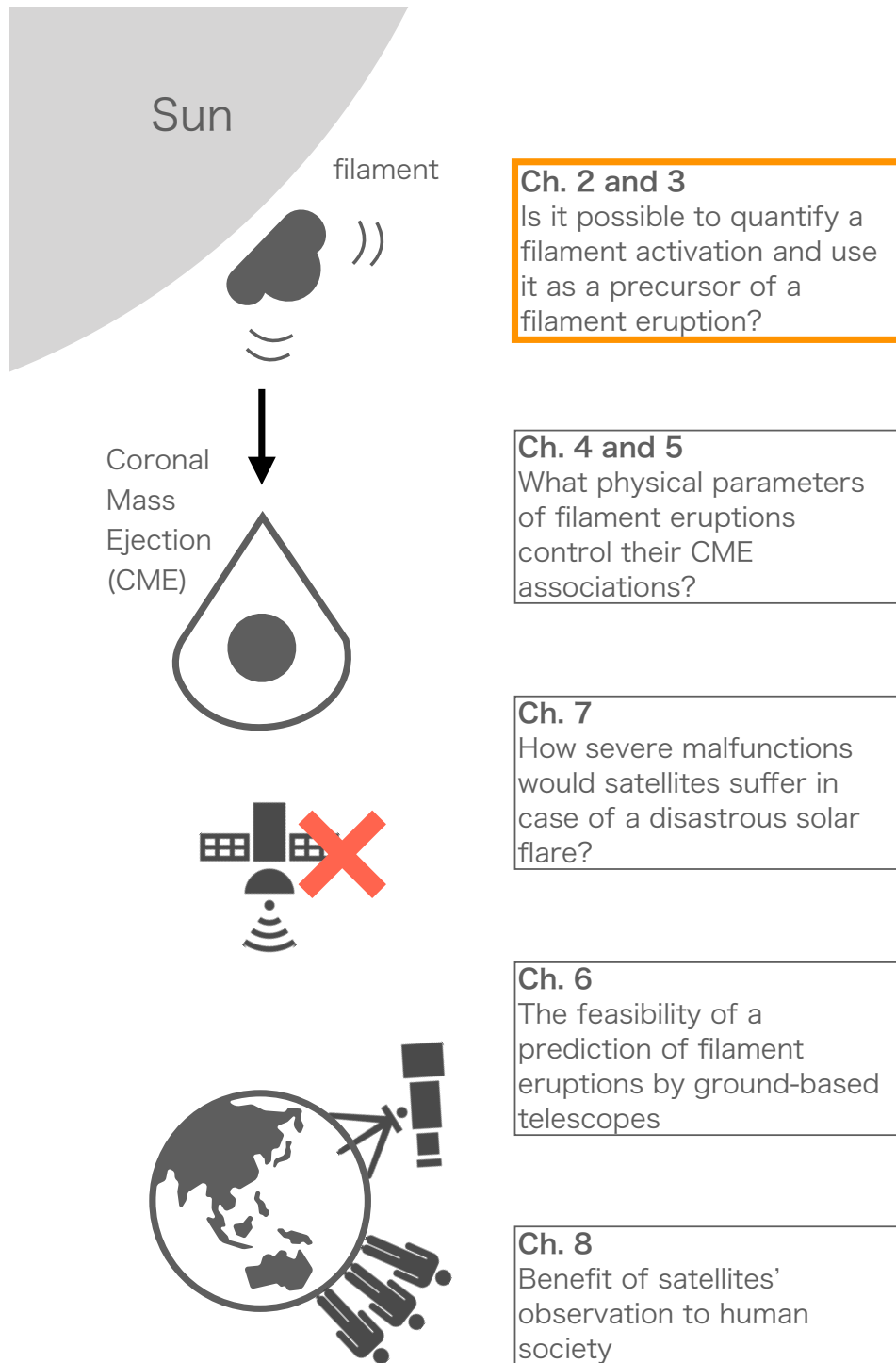
Figure 3.1: The graphical abstract of this dissertation (the orange rectangle corresponds to this Chapter).

with various solar eruptive phenomena such as flare, coronal mass ejections (CMEs), and very large arcade formation on the quiet Sun. Although they are diverse in size, morphology, and emitting radiation spectrum, they are considered to be the different aspects of a common magnetohydrodynamic process that involves plasma ejection and magnetic reconnection [1].

Filament eruptions are generally preceded by filament activations [34,35] such as slow rise [67,79], twisting and rotational motions [80], fragmentary brightenings [81], weak heating [73], oscillatory plasma motions [68], and active internal motions [36,65] in the filaments.

In the more general context of solar eruptions, various types of "triggers" have been proposed, including emerging magnetic flux [43,44,75], magnetic reconnection at various magnetic configurations [74,82], and helicity injection [83,84]. Among others, an increase in the non-thermal velocity prior to the onset of a flare is discussed in [38]. By spectroscopic observation of the coronal lines, [38] identified a non-thermal line broadening prior to an increase in the X-ray flux and electron temperature, indicating an increase in the turbulent motion occurring prior to the onset of the flare.

In our previous study, we analysed an intermediate filament near NOAA 12605, which erupted on November 5, 2016. The data were captured by the Solar Dynamics Doppler Imager (SDDI) [39] newly installed on the Solar Magnetic Activity Research Telescope (SMART) [40] at the Hida Observatory. The SDDI captures solar full-disk images in wavelengths from Hα - 9.0 Å to Hα + 9.0 Å at steps of 0.25 Å. It permits us to monitor the Hα line profile and thus determine the line-of-sight (LOS) velocity map (such as the bottom panels in Figure 3.2) prior to and during the eruption of a filament. From the velocity map, we prepared a histogram of the LOS velocity and calculated the standard deviation of the velocity distribution to quantify the small-scale motions in the filament. We determined that

1. although the standard deviation was almost constant at approximately 2–3 km s^{-1} from 29 to 21 h prior to the eruption, it had increased to 4–5 km s^{-1} 6 h prior to the eruption, whereas the mean LOS velocity was constant at 0 km s^{-1}. We also determined that

2. approximately 1 h prior to eruption, the average of the LOS velocity distribution assumed a negative value; this implies that the filament started to move toward the Earth globally, whereas the standard deviation increased to 10 km s^{-1}.

The second observation is likely to correspond to the commonly observed slow-rise phase [67,68]; meanwhile, the first observation indicates an increase in the turbulent motion of the filament prior to the onset of the slow-rise phase and may be regarded as an indication that

the filament was approaching an unstable state or a loss of equilibrium, which impelled the eruption. Hereafter, we call such a pre-slow-rise period with increasing standard deviation but without significant change in the mean LOS velocity, as "Phase 1." "Phase 2" is defined as the period from the time when both the increase in the standard deviation and the systematic change in the mean LOS velocity start, to the time when the filament vanishes. Phase 1 can be regarded as a gradual increase in the turbulent motion a significant time prior to the onset of the slow rise; Phase 2 includes the slow-rise phase as well as the eruption phase (with a further increase in the turbulent motion).

The objective of this study is to examine whether these two observations of [65] generally hold for other filament eruptions. For this purpose, we examined 17 filament disappearance events observed by the SDDI from the beginning of its routine observation in May 2016, to May 2017. After removing low-quality data sets, we analysed 12 filaments, which included two quiescent filaments, four active region filaments, and six intermediate filaments, similarly as in Seki et al. (2017) [65]. We present our event list and method in Section 2, and the results are presented in Section 3. In Section 4, we summarise and discuss our results.

3.1 Observations

3.1.1 Event List

The SDDI installed on the SMART at Hida Observatory has been conducting routine observations since May 1, 2016. It captures solar full-disk images in 73 wavelengths: from Hα line centre $-$ 9.0 Å to Hα line centre $+$ 9.0 Å at steps of 0.25 Å, i.e., 36 positions in the blue wing, Hα line centre, and 36 positions in the red wing. A set of the images in the 73 wavelengths is obtained with a time cadence of 15 sec and spatial sampling of 1.23 arcsec per pixel [39]. When the weather permitted, the SDDI could continuously monitor the Sun during the daytime in Hida.

We selected 12 events, which are presented in Table 3.1. With regard to "CME [UT]" in Table 3.1, we identified the CME associated with a filament eruption by considering its first appearance time, central position angle, and linear speed reported in the SOHO/LASCO CME catalogue [85, 86]. The obtained 12 filament disappearance events includes two quiescent filaments, four active region filaments, and six intermediate filaments.

Table 3.1: Filament disappearance events analysed in this study (May 2016–May 2017)

id[a]	Date and time[b] [UT]	Type[c]	Flare time[d] [UT] & Class	CME[e] [UT]	Figure
1	2016 May 4 01:20	AF (NOAA 12541)	01:20 (B 6.9)	—	Fig. 3.12
9	2016 Jul 7 07:58	AF (NOAA 12561)	07:55 (C 5.0)	—	Fig. 3.13
17	2016 Sep 4 03:37	IF (NOAA 12586)	—	—	Fig. 3.6
18	2016 Sep 9 05:44	IF (NOAA 12588)	—	—	Fig. 3.7
19	2016 Sep 9 22:27	AF (NOAA 12588)	22:29 (B 4.0)	—	Fig. 3.14
23	2016 Nov 4 04:47	QF	—	08:00	Fig. 3.4
24	2016 Nov 5 03:40	IF (NOAA 12605)	04:30 (B 1.1)	04:36	Fig. 3.8
27	2017 Feb 19 05:40	IF (NOAA 12636)	05:47 (B 3.1)	—	Fig. 3.2, 3.3, 3.9
31	2017 Apr 23 05:40	IF (NOAA 12652)	05:50 (B 1.7)	06:00	Fig. 3.10
32	2017 Apr 23 04:52	AF (NOAA 12651)	—	—	Fig. 3.15
33	2017 Apr 24 02:06	QF	—	05:34	Fig. 3.5
34	2017 Apr 30 00:38	IF (NOAA 12653)	01:00 (B 3.0)	02:36	Fig. 3.11

[a] The id number in the SMART/SDDI Filament Disappearance Catalogue (see Chapter 4).

[b] The time when a filament completely vanished in Hα line centre as observed by the SDDI.

[c] The type of filament; AF, QF, and IF correspond to active region filament, quiescent filament, and intermediate filament, respectively.

[d] The peak time and the class of a flare determined by soft X-ray flux in the GOES 1.0–8.0 Å channel.

[e] The time when the associated CME was first observed by SOHO/LASCO C2.
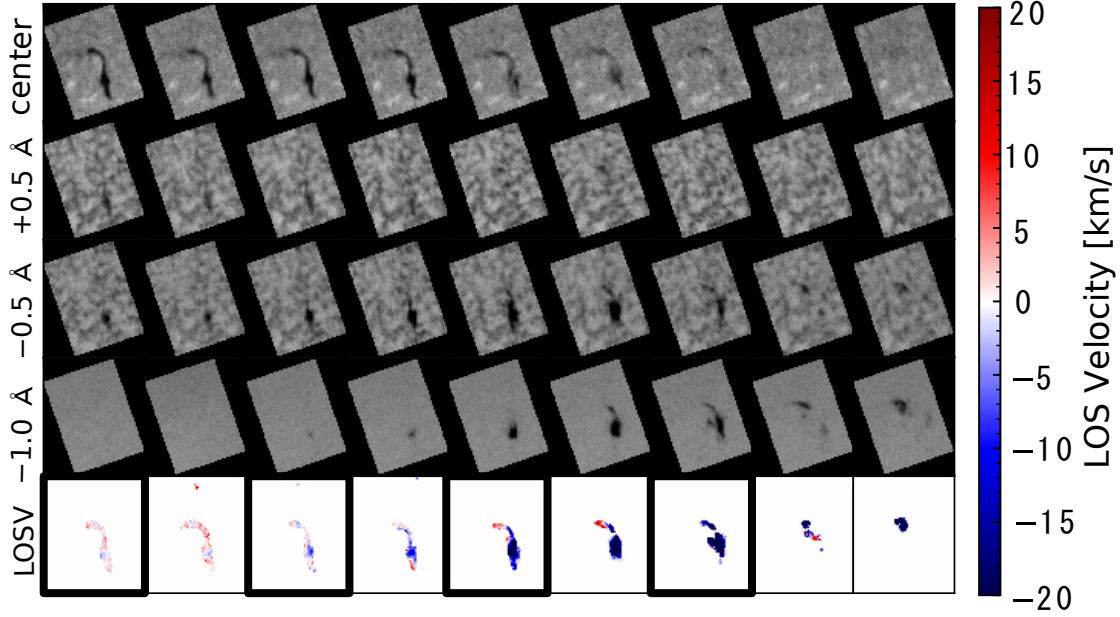
Figure 3.2: *From top to bottom*: Time series of Hα images at the line centre , + 0.5 Å, − 0.5 Å, and − 1.0 Åand of the LOS velocity map of the filament on February 19, 2017 (Event 27).

3.1.2 Analysis

We used Beckers' cloud model [59] to calculate the LOS velocity. By applying the model to the 73 images captured at the multiple wavelengths around Hα, we determined the source function, Doppler width, Doppler shift, and optical depth of each filament; we assumed that the source function is constant along the wavelengths and along the LOS direction and that the line absorption coefficient is a Gaussian [60–66]. Then, the LOS velocity at each pixel was calculated from the Doppler shift. The advantages of the SDDI are the wide wavelength coverage around Hα and the high spectral and temporal resolution; these enable us to obtain the LOS velocity distribution in unprecedented detail. Figure 3.2 shows examples of the data. These images were obtained on February 19, 2017.

Our data analysis is composed of three steps: development of a mask to obtain the form of a target filament, calculation of the LOS velocity of the filament using the cloud model, and the data selection. In the first step, we developed a "mask", a binary image that covered an entire target filament. Because Becker's cloud model can be applied only where a "cloud" (= filament) is present above the top of the chromosphere, this process was necessary to determine the pixels where the LOS velocity was to be calculated. We cropped a sub-image from the full-disk image that covered the entire filament prior to

44

and during disappearance. Then, we determined the positions of the pixels where the intensities were lower than $\bar{I}(\lambda) - 2\sigma_{I(\lambda)}$; here, λ is one of the 73 wavelengths, $\bar{I}(\lambda)$ is the average of the intensities inside the sub-image in λ, and $\sigma_{I(\lambda)}$ is their standard deviation. This position-determination procedure was conducted for all the 73 wavelengths. Bringing all the positions together, we finally obtained a binary image whose pixels at the same position have one and the other pixels have zero. However, the mask image developed in this manner covers other dark features such as spicules as well as the main body of the filament. To remove such noises, we applied a standard image processing called "erosion and dilation." Dilation is a process wherein if at least one of the surrounding pixels is one for a pixel, it will be set to one. That is, a pixel is set to zero only if all the eight pixels around it are zero. Erosion is the opposite process wherein a pixel is set to one only if all the surrounding eight pixels are one. By executing the dilation process several times after several erosion processes (e.g., executing erosion–erosion–erosion–dilation–dilation in order), we obtained a clean mask image covering only most of the target filament. The number of repetitions, which was determined by trial and error, was different for different events.

After the mask image was produced, we proceeded to the second step—calculation of the LOS velocity of the filament using the cloud model. All the 73 images in the different channels were multiplied by the binary-mask image, and Becker's cloud model was applied to the nonzero pixels. This step yielded the images of the source function, the Doppler width, the Doppler shift, and the optical depth of the filament at a specified time. We applied these two steps for all the data to obtain a time series of these four physical parameters. The Doppler shift was converted to the LOS velocity; in the following, we use only the LOS velocity.

After carrying out these two steps, as the third step, we manually removed the data unsuitable for our analysis. Terrestrial clouds sometimes covered the Sun, resulting in incorrect calculation of the Doppler shift. Because we need to deduce the standard deviation and the average of the LOS velocity, these can significantly affect our result. In addition to this, small high-speed features that were apparently not associated to the filament were occasionally included in the mask and also significantly affected the average and standard deviation calculation. Therefore, we visually examined all the Hα line centre images and the LOS velocity maps and removed the data contaminated by terrestrial clouds and small high-speed features, from our analysis.

To quantify the small-scale-plasma motion in each filament, we calculated the standard deviation and average of the LOS velocity distribution. The standard deviation can be regarded as a measure of the enhancement of the turbulent small-scale-plasma motion. Figure 3.3 shows four representative snapshots of the filament on 2017 February 19, man-

ifesting the increase in standard deviation with time owing to the filament activation and eruption.

3.2 Results

3.2.1 Quiescent Filaments

Event 23

Figure 3.4 shows snapshots of Event 23 in Hα line centre and SDO/AIA 304 [46]; it also shows the time evolution of the average and standard deviation of the LOS velocity of a filament. This filament was a typical large quiescent filament without active regions in its vicinity. It gradually erupted to the solar west and was accompanied by a slow CME with a linear speed of 147 km s^{-1} as revealed by the SOHO/LASCO C2/3. Approximately 45 h prior to the eruption, the standard deviation was approximately 2–3 km s^{-1}; it marginally increased to 3–4 km s^{-1} 17 h later. Approximately 5 h prior to eruption, it was about 4 km s^{-1} (Phase 1). From 01:24 UT, the standard deviation started to increase to approximately 5 km s^{-1} and the mean velocity became marginally negative; this manifested the start of the slow-rise phase, i.e., Phase 2. Finally, it disappeared at approximately 04:47 UT (dash-dotted line).

Note that even after the eruption, both the standard deviation and average of the LOS velocity exhibited the values in the right panel of Figure 3.8. This originated from the statistical summary of the LOS velocity of patchy features such as remnants of the filament and spicules. Although our masking method described in section 3.1.2 can remove most of the noises originating from them, marginal amounts of such features remained. As stated in Section 3.1.2, our method cannot distinguish the target plasma from other dark features in Hα line centre and its wings. However, compared to the main body of the filament, the total amounts of such features were so small prior to and during the eruption that it is highly likely that our result was negligibly affected.

Event 33

Figure 3.5 shows snapshots of Event 33 in Hα line centre and SDO/AIA 304; it also shows the time evolution of the average and standard deviation of the LOS velocity of a filament. This filament was a typical large quiescent filament without active regions in its vicinity; it erupted on April 24, 2017 02:06 UT to the solar north-east, accompanied by a rapid dynamic CME with a linear speed of 854 km s^{-1}. There was no notable geomagnetic storm within a few days after the eruption. Approximately 23 h prior to eruption, the standard deviation was 2–3 km s^{-1}; from 03:30 UT on April 23, it started
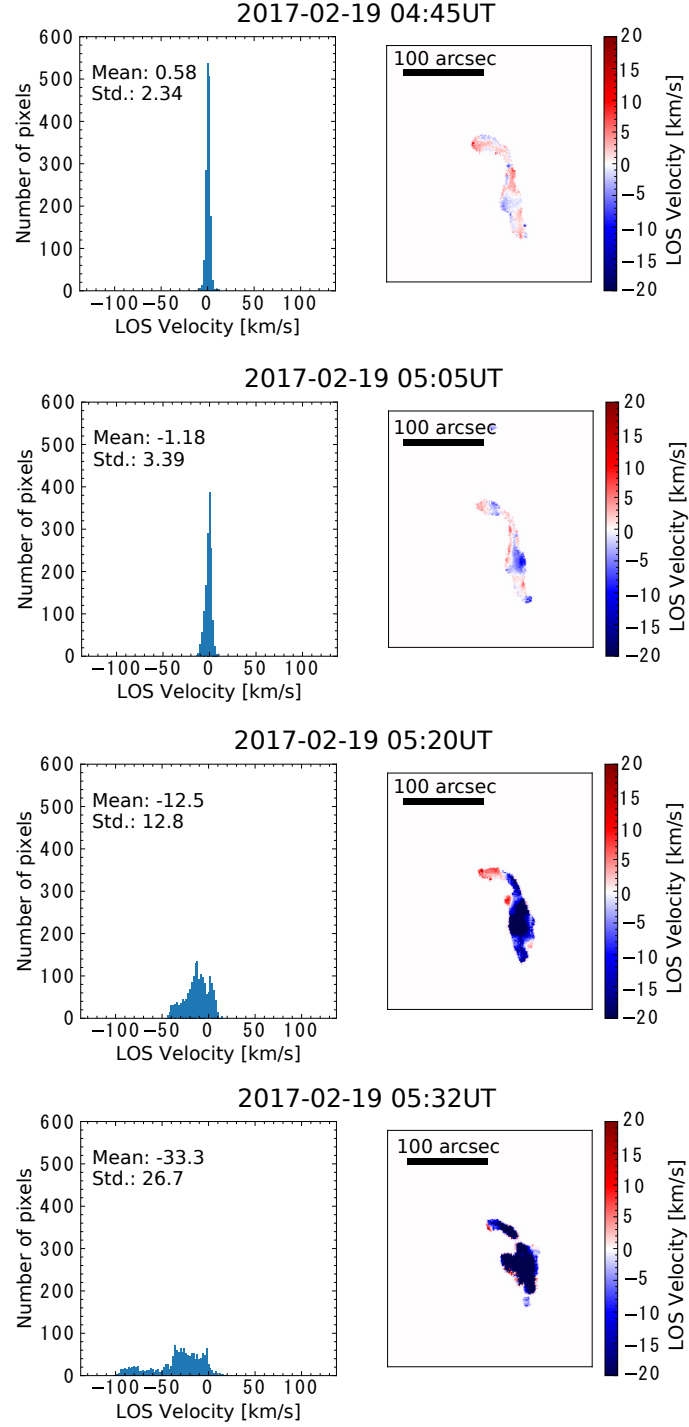
Figure 3.3: *Left*: Histograms of the LOS velocity images. Each histogram corresponds to the right image. The mean and standard deviation of the LOS velocity are written on the upper left. Each bin represents 2 km s^{-1}. *Right*: Four LOS velocity images from Figure 3.2 (the thick rectangles in the bottom panels of Figure 3.2). Note that the LOS velocity map on each right panel is shown with a scale of lower and upper limits of $\pm$ 20 km s^{-1}.

47
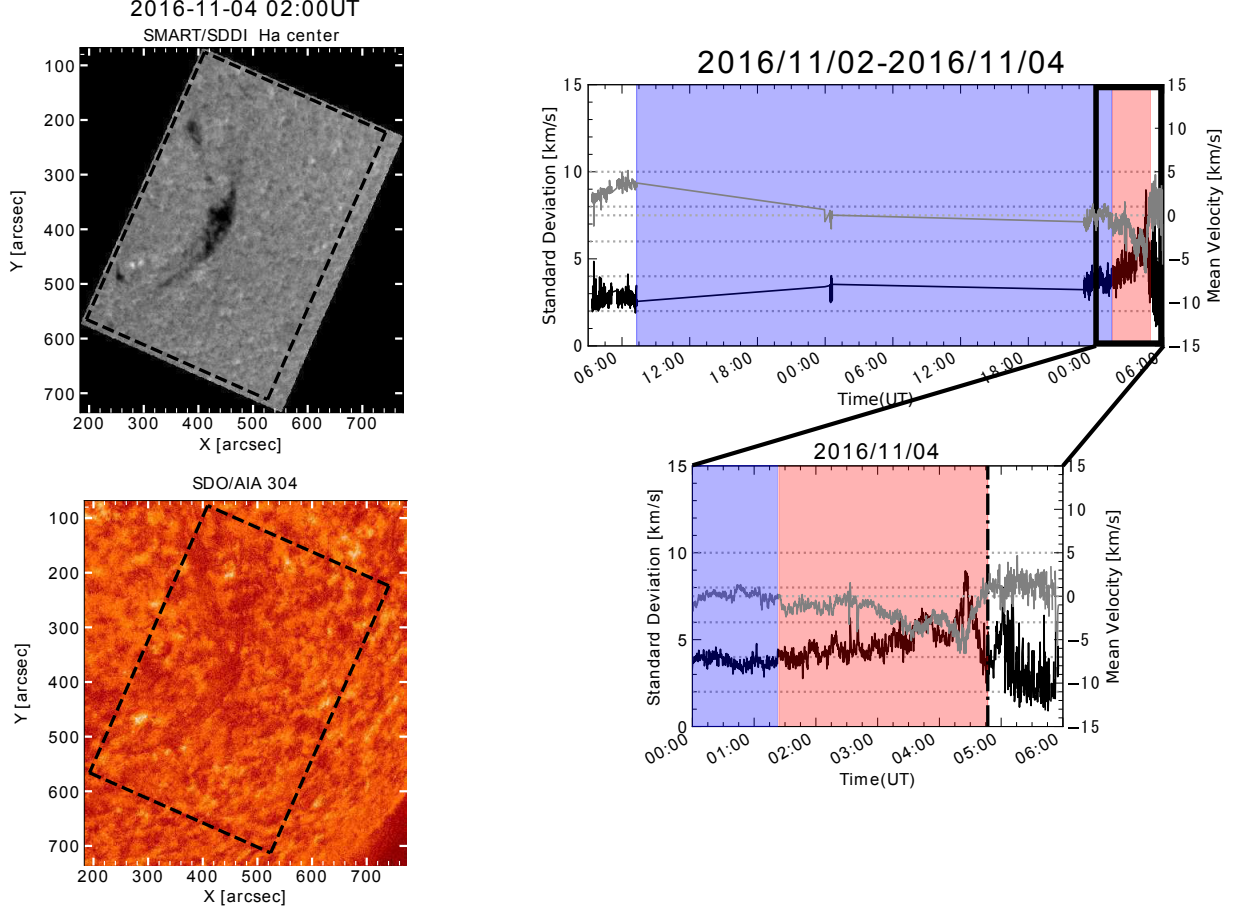
Figure 3.4: *Left*: Hα line centre and SDO/AIA 304 images showing the target filament of Event 10. A black dashed rectangle on each image is the area within which we determined the standard deviation and mean of the LOS velocity. *Right*: Standard deviation (black line, left axis) and average (grey line, right axis) of LOS velocity of filament. The bottom panel is an enlargement of the black rectangle in the top panel. The vertical dash-dotted line in the bottom panel is the time when the filament vanished completely in Hα line centre. The blue and red shaded areas correspond to Phases 1 and 2, respectively. The horizontal dotted lines are shown where the standard deviations are 2, 4, 6, 8, and 10 km s^{-1}, and the average is 0 km s^{-1}.

to increase to approximately 4 km s^{-1}, i.e., Phase 1 started. The increases in both the standard deviation and average were observed from 23:00 UT; however, both the values started to decrease in approximately 30 min. The standard deviation increased again from approximately 01:30 UT on April 24; finally, the filament completely vanished at 02:06 UT.

The increases and decreases in both the values 2.5 h prior to eruption were also observed in our previous work (see Figure 2.11). It was challenging to verify Phase 2 in this case. The possible reason for the absence of Phase 2 is that this filament moved and erupted in an almost perpendicular direction to the LOS direction.
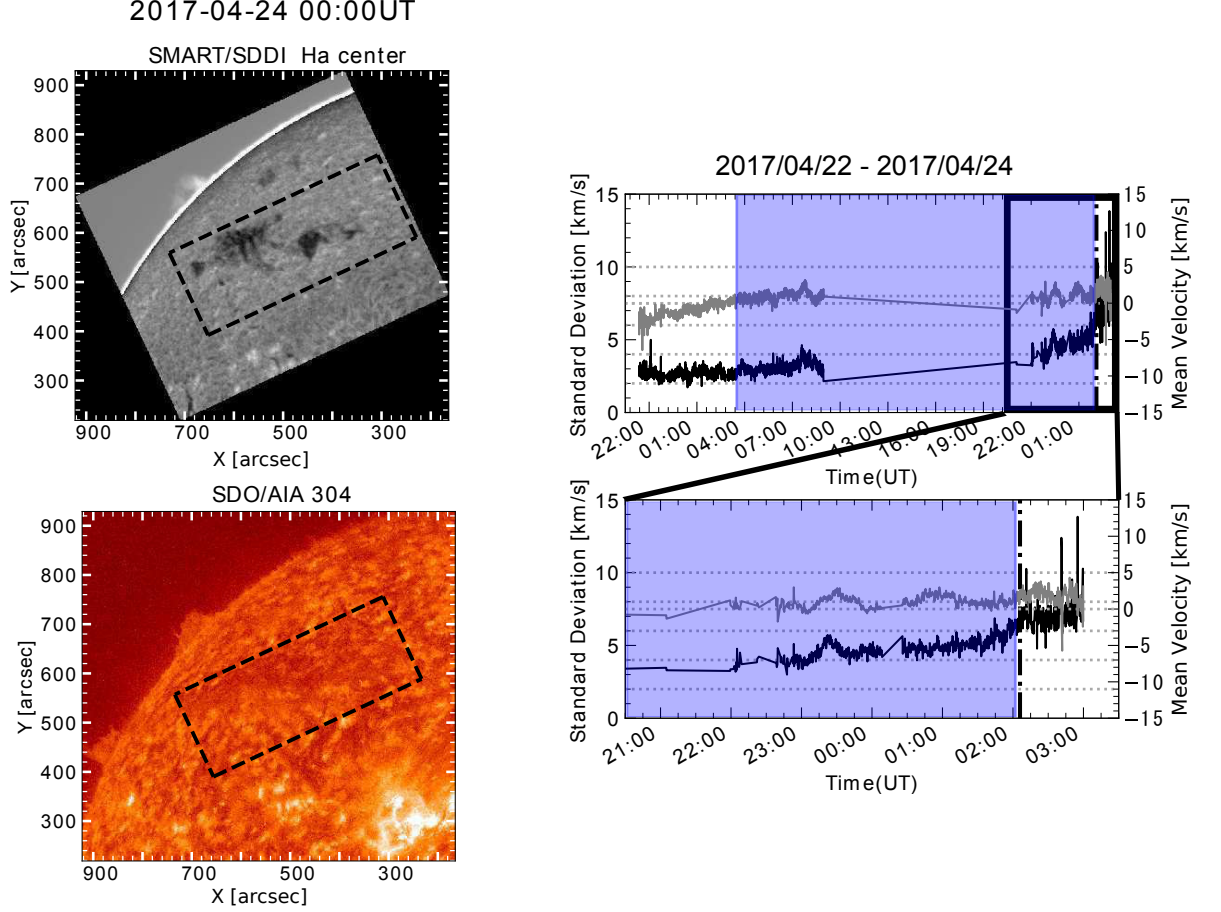
Figure 3.5: *Left*: Hα line centre and SDO/AIA 304 images showing the target filament of Event 16. The definition of the black dashed rectangles is identical to that in Figure 3.4. *Right*: Standard deviation (black line, left axis) and average (grey line, right axis) of LOS velocity of filament. The bottom panel is an enlargement of the black rectangle in the top panel. The definitions of the blue shaded area, vertical black dash-dotted line, and horizontal grey dotted lines are identical to those in Figure 3.4. In this case, we could not clearly identify a Phase-2 period (see text), and therefore, red shaded area is absent.

3.2.2 Intermediate Filaments

Event 17

Figure 3.6 shows snapshots of Event 17 in Hα line centre and SDO/AIA 304; it also shows the time evolution of the average and standard deviation of the LOS velocity of a filament. This filament was located in the vicinity of the active region NOAA 12586 and not on it; therefore, we classified it as an intermediate filament. This filament disappeared on September 4, 2016 03:37 UT in both Hα line centre and SDO/AIA 304; moreover, a possible CME associated with this event was not observed by SOHO/LASCO C2/3. At approximately 21:00 UT on September 2, 2016 (approximately 31 h prior to eruption), the standard deviation was approximately 4 km s^{-1}. From approximately 00:00 UT on

September 4 (approximately 4 h prior to eruption), both the standard deviation and average of the LOS velocity started to change; the former increased to above 4–5 km s^{-1} with a large fluctuation until the eruption, whereas the latter recovered to 0 km s^{-1} approximately 1 h later. Then, this filament vanished at 03:37 UT. There was no signature of Phase 1 in this case. It might be possible that Phase 1 had already occurred before approximately 09:00 UT on September 2, 2016.

With regard to Phase 2 (red shaded area in Figure 3.6), except the difference in sign, the profile was similar to that of Events 24 [65] and 33. Furthermore, in a few wavelengths of the SDO including 304, 193, and 211, this filament displayed an upward motion, i.e., moved toward the solar west in the radial direction; this coincided with the dynamic changes in both the statistical values. This coincidence is consistent with our interpretation of Phase 2, including the slow-rise phase. Note that there was a data gap from 02:55 UT to 03:37 UT on September 4, 2016 because of unfavourable weather condition.

Event 18

Figure 3.7 shows snapshots of Event 18 in Hα line centre and SDO/AIA 304; it also shows the time evolution of the average and standard deviation of the LOS velocity of a filament. This filament was located in the vicinity of the active region NOAA 12588 and vanished on September 9, 2016 in both Hα line centre and the SDO/AIA 304. A possible accompanying CME was not observed. From 03:00 UT to 03:45 UT, the standard deviation of the LOS velocity was almost constant at 2 km s^{-1}, and the average was also almost constant. Then, only the standard deviation started to increase to 3–4 km s^{-1} (Phase 1) from 03:45 UT to 05:00 UT, whereas the mean LOS velocity was still almost constant at approximately 2 km s^{-1}. From 05:10 UT, the filament started to vanish, and at 05:44 UT, it disappeared almost entirely.

Approximately 2.5 h prior to disappearance (approximately 03:14 UT), a B7.9 class flare was observed in NOAA AR 12588; then, the disruption in the loops approximately located in the right-half of the dashed box in Figure 3.7 was observed at the SDO/AIA 304, 171, 193, and 211. It might be possible that the preceding flare or the disruption was related to the disappearance of the filament.

Event 24

Figure 3.8 shows snapshots of Event 24 in Hα line centre and SDO/AIA 304; it also shows the time evolution of the average and standard deviation of the LOS velocity of a filament. This filament was located in the vicinity of the active region NOAA 12605. It

Figure 3.6: *Left*: Hα line centre and SDO/AIA 304 images of Event 17. The plage indicated by the white arrow is NOAA AR 12588. The definition of the black dashed rectangles is identical to that in Figure 3.4. *Right*: Standard deviation (black line, left axis) and average (grey line, right axis) of LOS velocity of the filament. The bottom panel is an enlargement of the black rectangle in the top panel. The definitions of the red shaded area, vertical black dash-dotted line, and horizontal grey dotted lines are similar to those in Figure 3.4. In this case, we could not clearly identify a Phase-1 period (see text); therefore, blue shaded area is absent.

erupted dynamically to the solar north-east on November 5, 2016 04:00 UT, accompanied by a moderate CME with a linear speed of 403 km s^{-1}. This CME probably caused the moderate geomagnetic disturbance during November 9–10, 2016. A two-ribbon flare was observed in both Hα line centre and SDO/AIA 304, in the vicinity of the filament location immediately after the eruption; this was accompanied by a B1.1-class event in the GOES soft X-ray, which peaked at 04:30 UT. For further details, refer to [65]. The standard deviation was approximately 2–3 km s^{-1} until approximately 07:00 UT on November 4, 2016; however, at 22:00 UT on November 5, 2016, it was 4–5 km s^{-1}, with an average velocity of 0 km s^{-1}. Therefore, Phase 1 started during the data-gap period. It gradually increased until 02:30 UT; then, both the standard deviation and mean of LOS velocity

Figure 3.7: *Top*: Hα line centre and SDO/AIA 304 images of Event 7. The plage indicated by the white arrow is NOAA AR 12588. The definition of black dashed rectangles is identical to that in Figure 3.4. *Bottom*: Standard deviation (black line, left axis) and average (grey line, right axis) of the LOS velocity of the filament. The definitions of the blue and red shaded areas, vertical black dash-dotted line, and horizontal grey dotted lines are identical to those in Figure 3.4.

started to change more dramatically, i.e., Phase 2 started.

Event 27

Figure 3.9 shows snapshots of Event 27 in Hα line centre and SDO/AIA 304; it also shows the time evolution of the average and standard deviation of the LOS velocity of a filament.

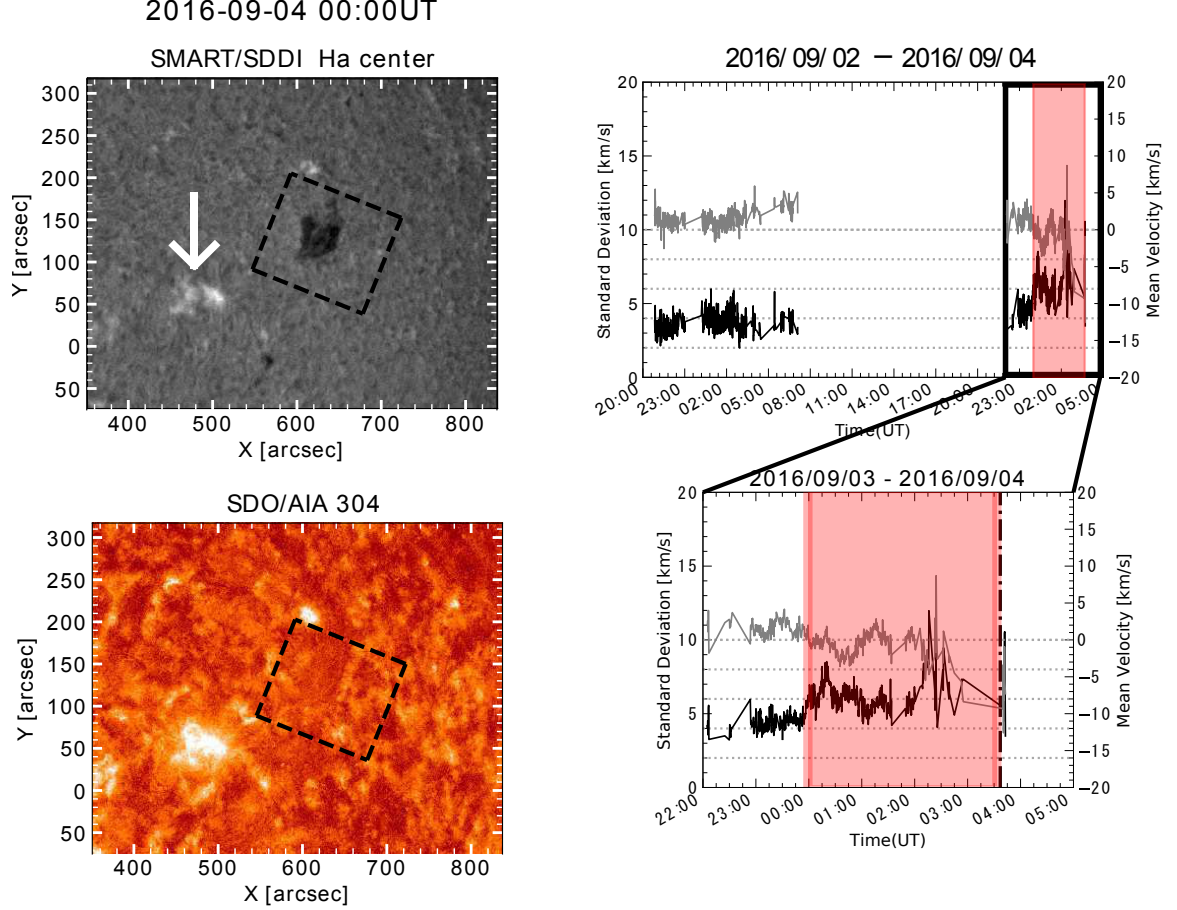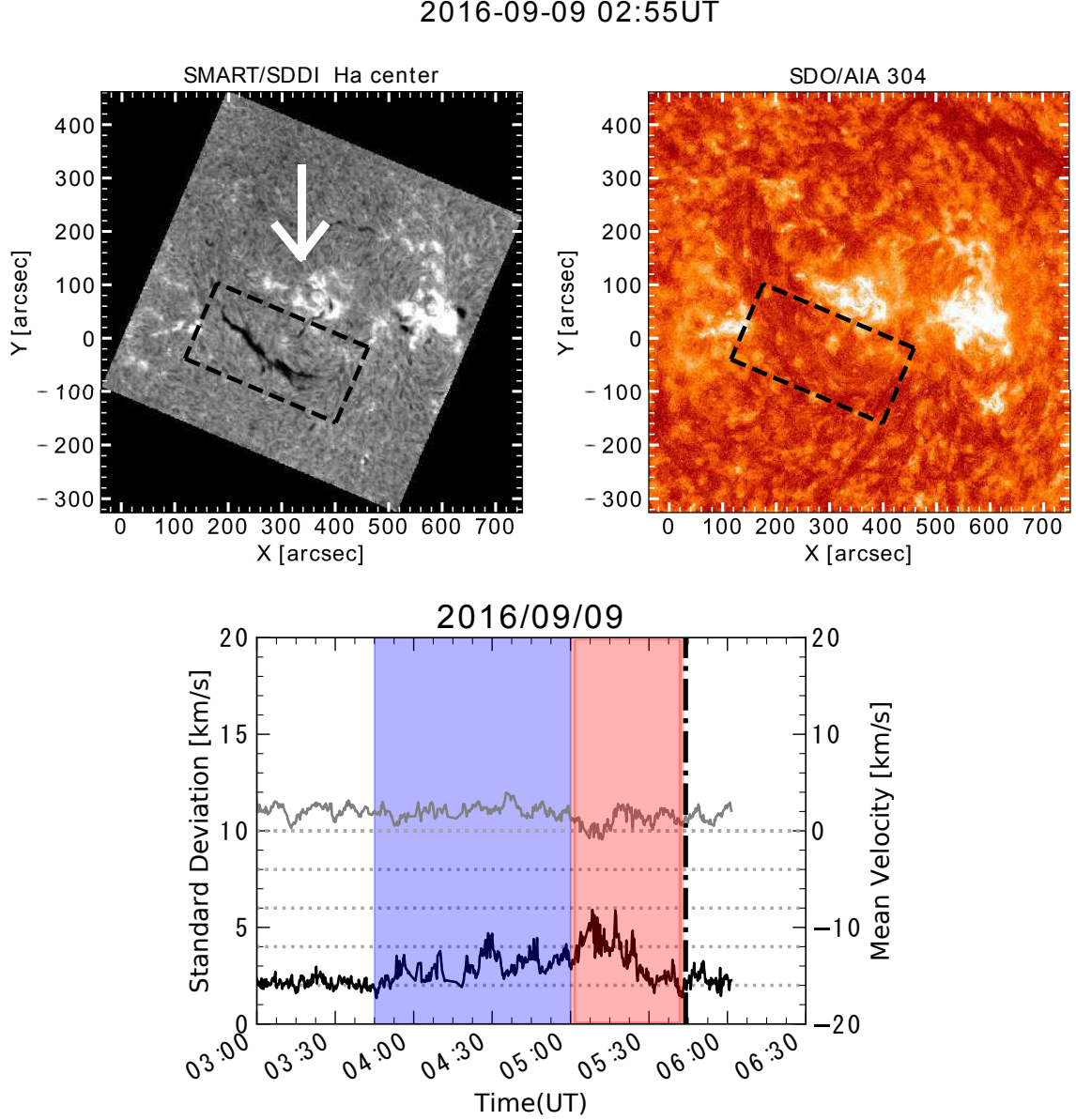Figure 3.8: *Left*: Hα line centre and SDO/AIA 304 images of Event 11. The plage indicated by the white arrow is NOAA AR 12605. The definition of black dashed rectangles is identical to that in Figure 3.4. *Right*: Standard deviation (black line, left axis) and average (grey line, right axis) of LOS velocity of the filament. The bottom panel is an enlargement of the black rectangle in the top panel. The definitions of the blue and red shaded areas, vertical black dash-dotted line, and horizontal grey dotted lines are identical to those in Figure 3.4.

This filament was located in the vicinity of the active region NOAA 12636. It erupted rapidly to the solar north on February 19, 2017; however, a possible CME associated with this event was not observed by SOHO/LASCO C2/3. A two-ribbon flare was observed in the vicinity of the filament location immediately after eruption; this was accompanied by a B3.1-class event in the GOES soft X-ray, which peaked at 05:47 UT. From 04:50 UT to 05:10 UT, the standard deviation gradually increased from 2–3 km s^{-1} to 4–5 km s^{-1}. The mean LOS velocity was almost constant at approximately 0 km s^{-1} during this period; thus, this increase represents Phase 1. Then, the standard deviation increased more sharply than before, and the average LOS velocity exhibited the gradual decrease. This phase corresponds to Phase 2. From approximately 05:28 UT, both values started to change more dramatically, and finally, it erupted.
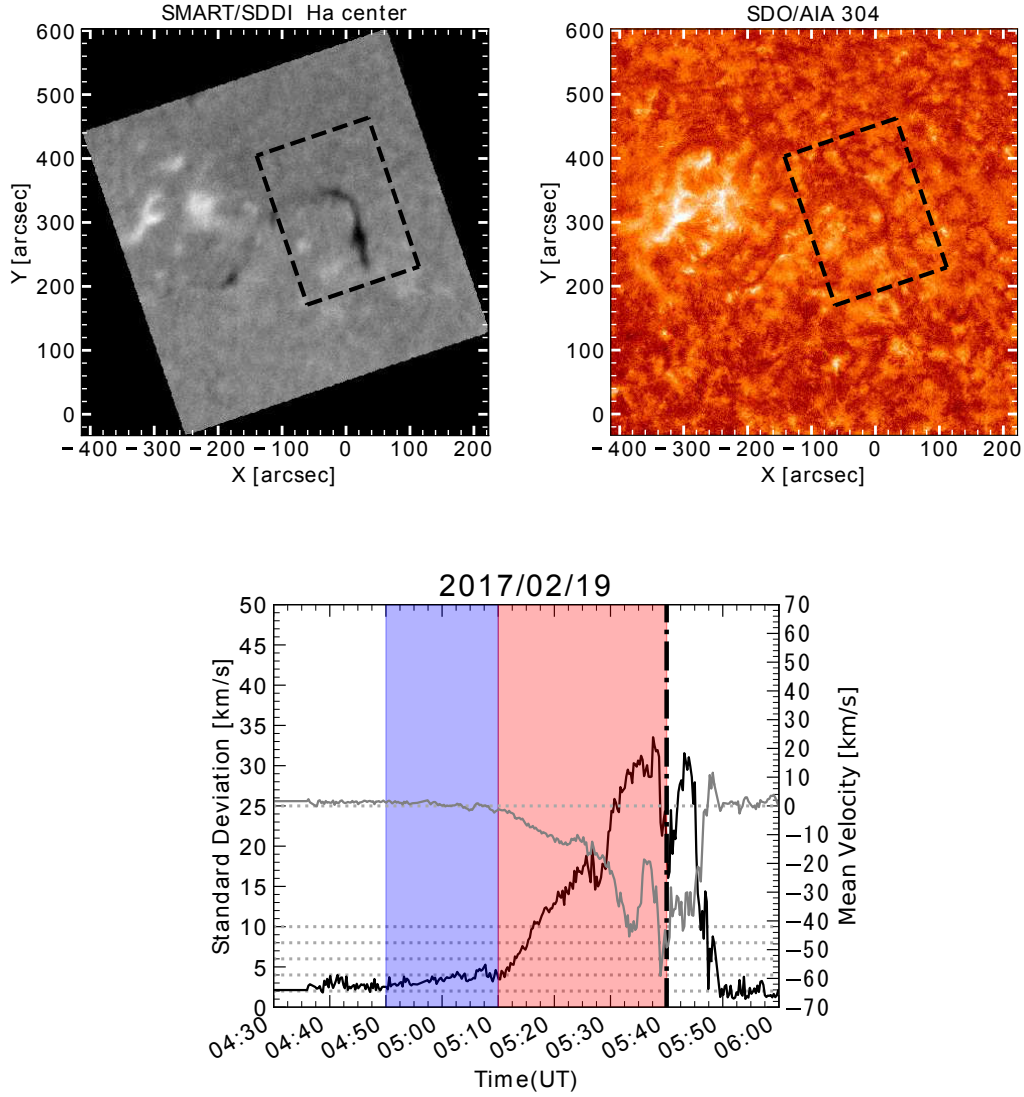
Figure 3.9: *Top*: Hα line centre and SDO/AIA 304 images of Event 12. The plage on the left side of the filament corresponds to NOAA AR 12636. The definition of black dashed rectangles is identical to that in Figure 3.4. *Bottom*: Standard deviation (black line, left axis) and average (grey line, right axis) of LOS velocity of filament. The definitions of the blue and red shaded areas, vertical black dash-dotted line, and horizontal grey dotted lines are identical to those in Figure 3.4.

Event 31

Figure 3.10 shows snapshots of Event 31 in Hα line centre and SDO/AIA 304; it also shows the time evolution of the avera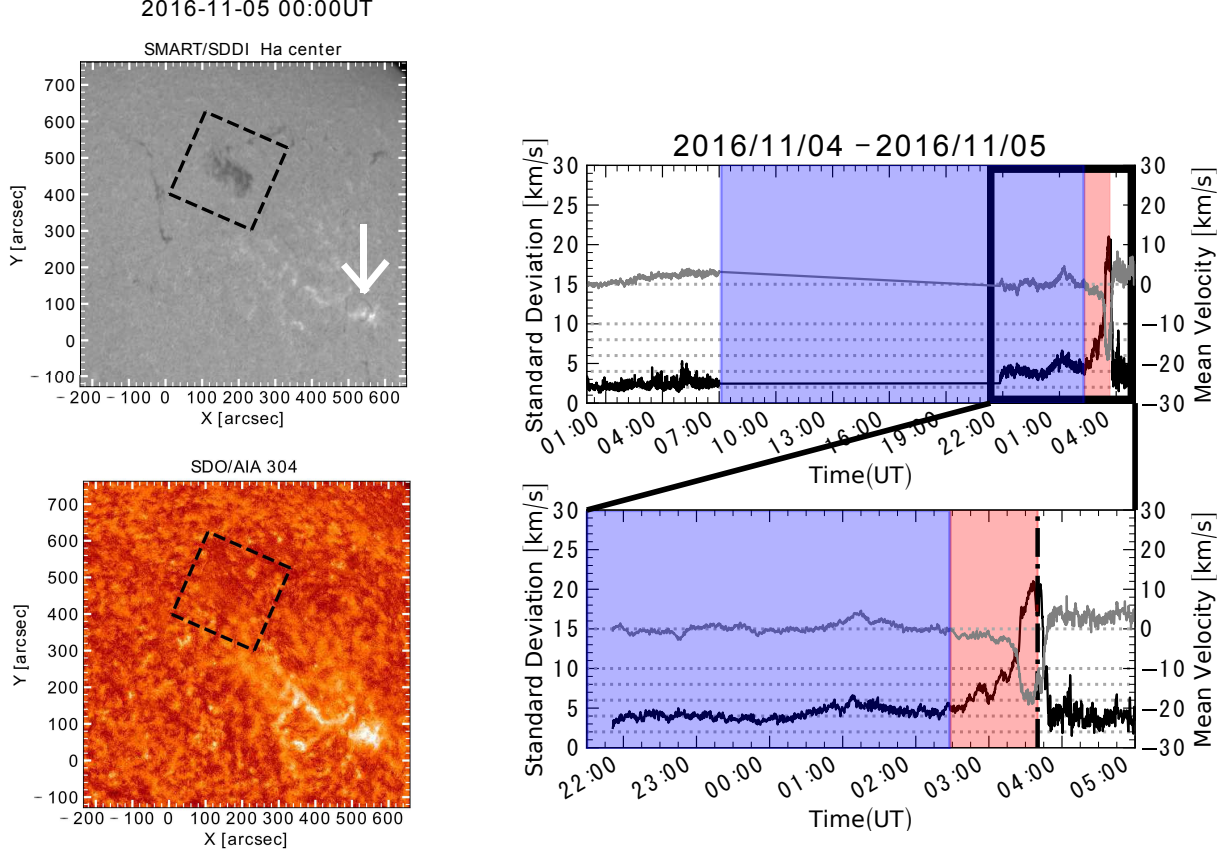ge and standard deviation of the LOS velocity of a filament. This filament was located in the vicinity of the active region NOAA 12652. It erupted rapidly to the solar south-east on April 23, 2017 accompanied by a rapid and

dynamic CME with a linear speed of 955 km s^{-1}. A two-ribbon flare was observed in both Hα line centre and SDO/AIA 304, in the vicinity of the filament location immediately after eruption; this was accompanied by a B1.7-class event in the GOES soft X-ray, which peaked at 05:50 UT. From 04:15 UT to 04:51 UT (the blue shaded area in Figure 3.10), the standard deviation gradually increased from 2–3 km s^{-1} to 4–5 km s^{-1}. Because the mean LOS velocity was almost constant at approximately 0 km s^{-1} during this period, the period represents Phase 1. Then, the standard deviation increased more sharply than before, and the average of the LOS velocity exhibited the gradual decrease. From approximately 05:18 UT, both values started to change more dramatically, and finally, it erupted.

Figure 3.10: *Top*: Hα line centre and SDO/AIA 304 images of Event 15. The plage indicated by the white arrow is NOAA AR 12652. The definition of the black dashed rectangles is identical to that in Figure 3.4. *Bottom*: Standard deviation (black line, left axis) and average (grey line, right axis) of LOS velocity of filament. The definitions of the blue and red shaded areas, vertical black dash-dotted line, and horizontal grey dotted lines are identical to those in Figure 3.4.

Event 34

Figure 3.11 shows snapshots of Event 34 in Hα line centre and SDO/AIA 304; it also shows the time evolution of the average and standard deviation of the LOS velocity of a filament. This filament was located in the vicinity of the active region NOAA 12653. It moved dynamically to the solar west and vanished on April 30, 2017, accompanied by a gradual CME with a linear speed of 282 km s^{-1}. A two-ribbon flare was observed in both Hα line centre and SDO/AIA 304, in the vicinity of the filament location immediately after eruption; this was accompanied by a B3.0-class event in the GOES soft X-ray, which peaked at 01:00 UT. From 23:24 UT to 00:00 UT, the standard deviation gradually increased from 2 km s^{-1} to 4–6 km s^{-1}. Because the mean LOS velocity was almost constant during this period, it can be regarded as Phase 1. Then, the standard deviation increased more sharply, and the average of the LOS velocity decreased dramatically.

3.2.3 Active Region Filaments

We obtained four active-region-filament-disappearance events. In general, the plasma of active region filaments is highly dynamic. This is apparent from the larger amplitudes of both the standard deviation and mean of the LOS velocity compared to those of quiescent and intermediate filaments.

Event 1

Figure 3.12 shows snapshots of Event 1 in Hα line centre and SDO/AIA 304; it also shows the time evolution of the average and standard deviation of the LOS velocity of a filament. This filament was located at NOAA AR 12541. It erupted to the solar west on May 4, 2016; moreover, a possible CME associated with this event was not observed by SOHO/LASCO C2/3. A two-ribbon flare was observed in both Hα line centre and SDO/AIA 304, in the vicinity of the filament location immediately after eruption; this was accompanied by a B6.9-class event in the GOES soft X-ray, which peaked at 01:20 UT. From 00:11 UT to 00:20 UT, the standard deviation started to increase from 4 km s^{-1} to 8 km s^{-1}, with the mean LOS velocity almost constant (Phase 1). Then, both the statistical values started to proliferate, and the filament erupted at 01:20 UT.

Event 9

Figure 3.13 shows snapshots of Event 9 in Hα line centre and SDO/AIA 304; it also shows the time evolution of the average and standard deviation of the LOS velocity of a filament. This filament was located at the active region NOAA 12561. This filament
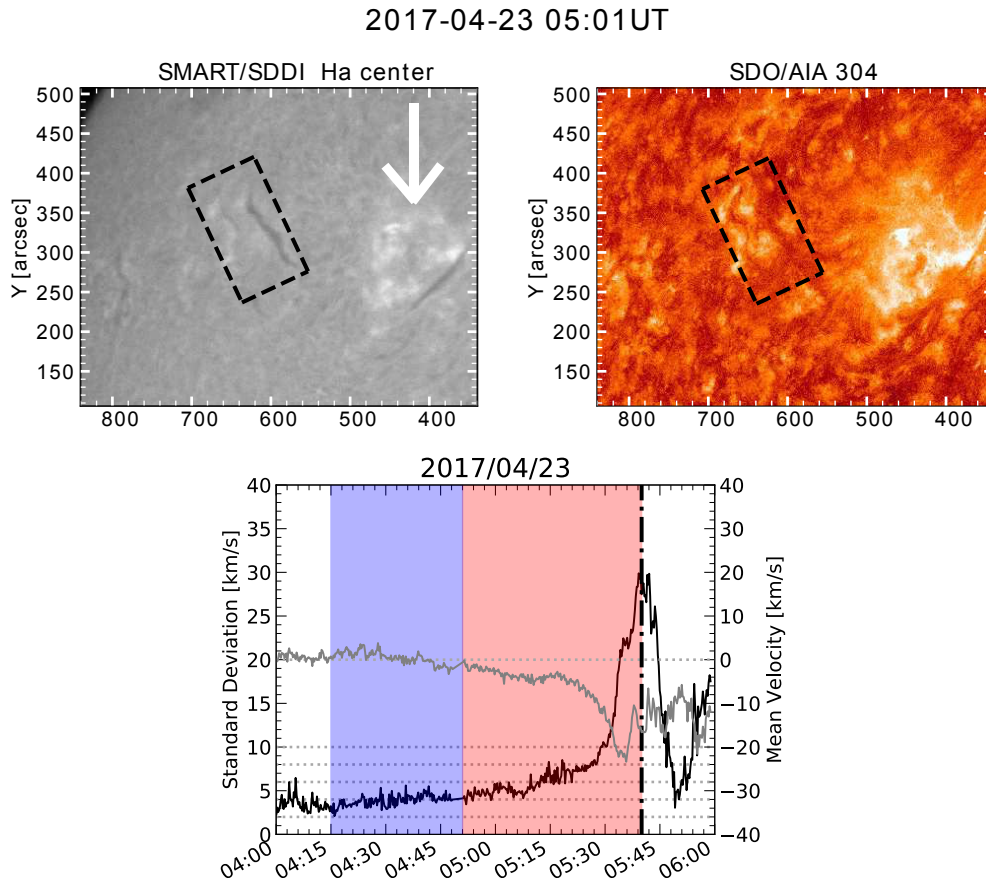
Figure 3.11: *Top*: Hα centre and SDO/AIA 304 images of Event 17. The plage indicated by the white arrow is NOAA AR 12652. The definition of the black dashed rectangles is identical to that in Figure 3.4. *Bottom*: Standard deviation (black line, left axis) and average (grey line, right axis) of LOS velocity of filament. The definitions of the blue and red shaded areas, vertical black dash-dotted line, and horizontal grey dotted lines are identical to those in Figure 3.4.

erupted to the solar south-west on July 7, 2016; however, a possible CME associated with this event was not observed by SOHO/LASCO C2/3. A two-ribbon flare was observed in the vicinity of the filament location immediately after eruption; this was accompanied by a C5.0-class event in the GOES soft X-ray, which peaked at 07:58 UT. From 07:47 UT, the filament showed the initiation of Phase 2 as the standard deviation started to increase from approximately 6 km s^{-1} to 8–10 km s^{-1}, and the average became negative. From 07:52 UT, both the values manifested more dramatic changes, and finally, it erupted.

It should be noted that this filament vanished in Hα between approximately 02:00 UT and 07:40 UT (the data gap in the upper right panel), and it appeared again at 07:40. Furthermore, Phase 1 was not detected probably because the plasma of the active region

Figure 3.12: *Top*: Hα line centre and SDO/AIA 304 images of Event 1. The active region where the filament is located is NOAA AR 12542. The definition of the black dashed rectangles is identical to that in Figure 3.4. *Bottom*: Standard deviation (black line, left axis) and average (grey line, right axis) of LOS velocity of filament. The definitions of the blue and red shaded areas, vertical black dash-dotted line, and horizontal grey dotted lines are identical to those in Figure 3.4.

filament moves dynamically, and it was unfeasible to recognise the marginal and gradual change in the LOS velocity.

Event 19

Figure 3.14 shows snapshots of Event 19 in Hα line centre and SDO/AIA 304; it also shows the time evolution of the average and standard deviation of the LOS velocity of a filament. This filament was located at the active region NOAA 12588. It erupted to the sol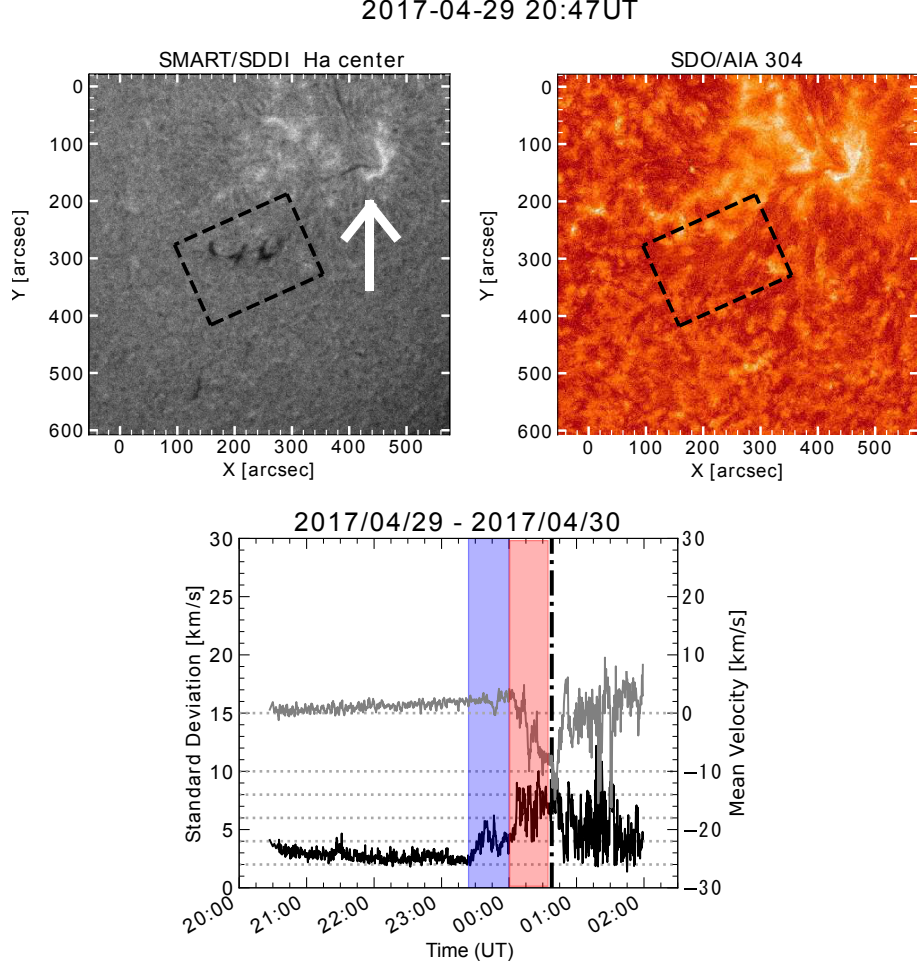ar north-east on September 9, 2016; however, a possible CME associated with this event was not observed by SOHO/LASCO C2/3. A two-ribbon flare was observed in the vicinity of the filament location immediately after eruption; this was accompanied by
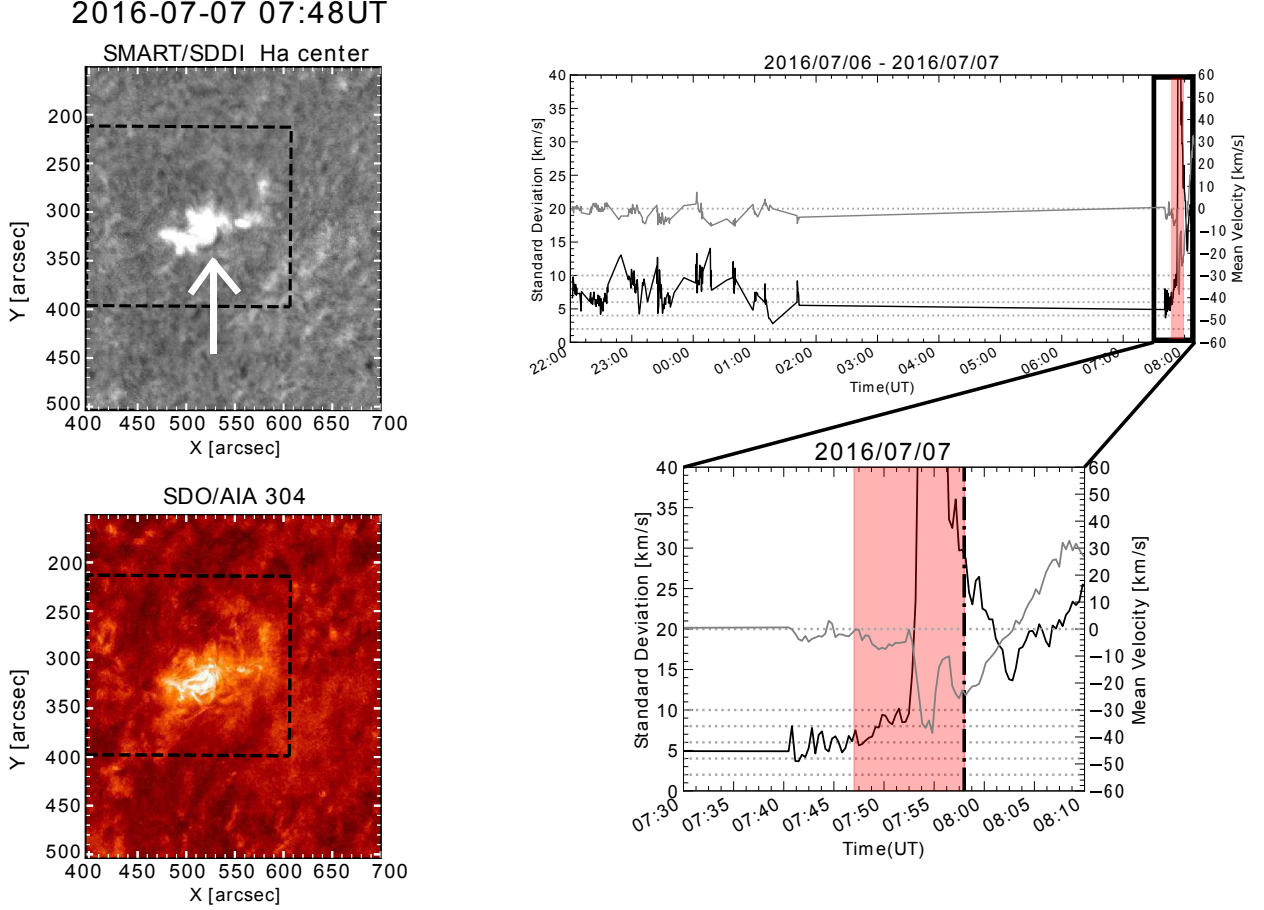
Figure 3.13: *Left*: Hα line centre and SDO/AIA 304 images showing the filament on NOAA AR 12561 (Event 4). The white arrow indicates the target active region filament, and a black rectangle on each image is the area inside which we calculated the standard deviation and mean of LOS velocity. *Right*: Standard deviation (black line, left axis) and average (grey line, right axis) of LOS velocity of filament. The bottom panel is an enlargement of the black rectangle in the top panel. The definitions of the red shaded area, horizontal dotted lines, and vertical dashed and dash-dotted lines are identical to those in Figure 3.4. In this case, we could not clearly identify a Phase-1 period (see text); therefore, blue shaded area is absent.

a B4.0-class event in the GOES soft X-ray, which peaked at 22:29 UT. From 17 to 14 h prior to eruption, the standard deviation became 4–8 km s^{-1} with large fluctuations. However, 35 min prior to eruption, it became very high (17 km s^{-1}), whereas the average was approximately 0 km s^{-1} until 22:06 UT. Thus, Phase 1 probably started during the data-gap period. From 22:06 UT, the average of the LOS velocity started to decrease and became negative, whereas the standard deviation remained more or less high; thus, Phase 2 was initiated.

59
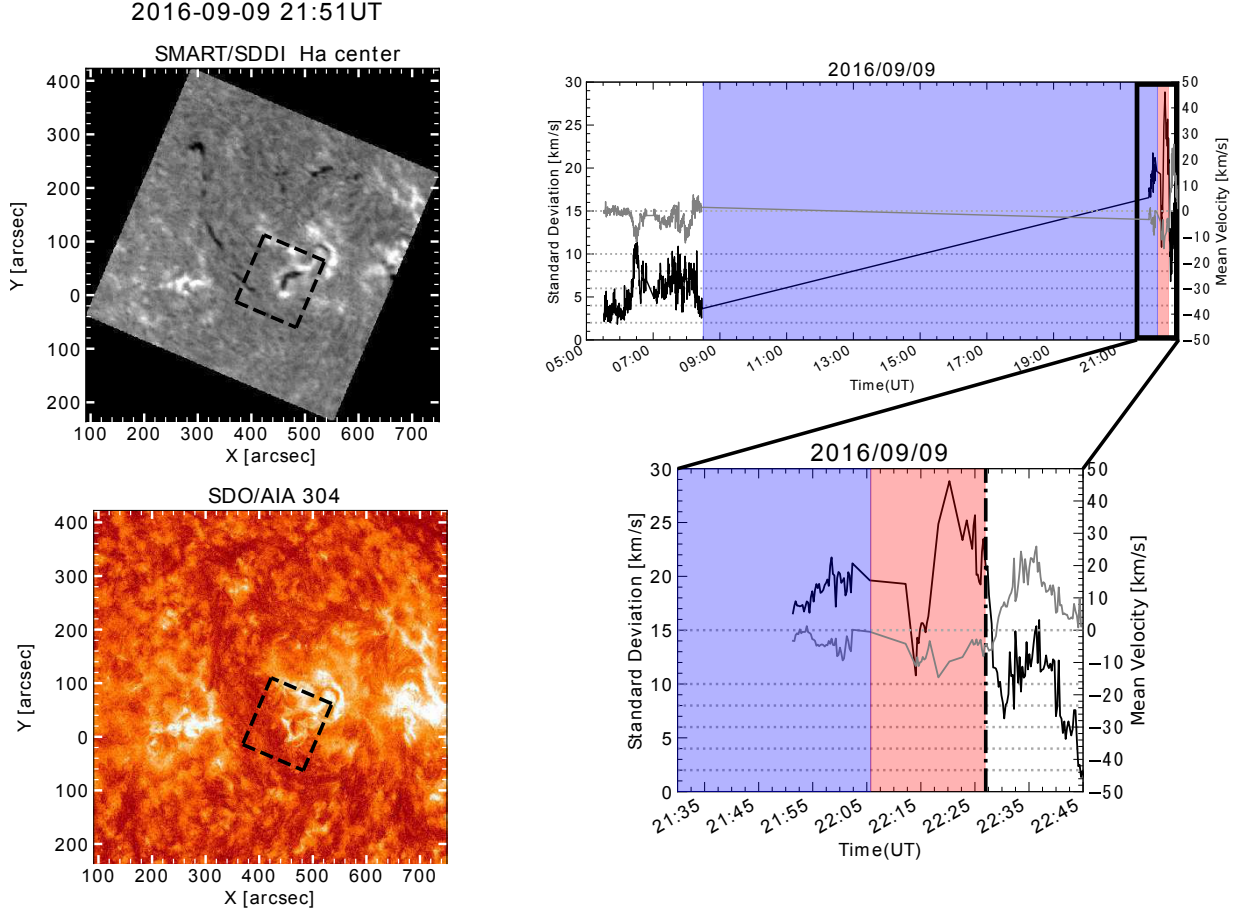
Figure 3.14: *Left*: Hα line centre and SDO/AIA 304 images of the filament on NOAA AR 12588 (Event 8). The definition of the black dashed rectangles is identical to that in Figure 3.4. *Right*: Standard deviation (black line, left axis) and average (grey line, right axis) of LOS velocity of filament. The bottom panel is an enlargement of the black rectangle in the top panel. The definitions of the blue and red shaded areas, vertical black dash-dotted line, and horizontal grey dotted lines are identical to those in Figure 3.4.

Event 32

Figure 3.15 shows snapshots of Event 32 in Hα line centre and SDO/AIA 304; it also shows the time evolution of the average and standard deviation of the LOS velocity of a filament. This filament was located at the active region NOAA 12651 and vanished on April 23, 2017; moreover, a possible CME associated with this event was not observed by SOHO/LASCO C2/3. In this event, a B3.8-class flare in the GOES soft X-ray, which peaked at 03:06 UT, was observed at NOAA AR 12651 approximately 1.8 h prior to disappearance. Within a short period after this flare, the filament started to vanish, and the dynamic changes in both the standard deviation and average of the LOS velocity began. In this case, Phase 1 was difficult to confirm.

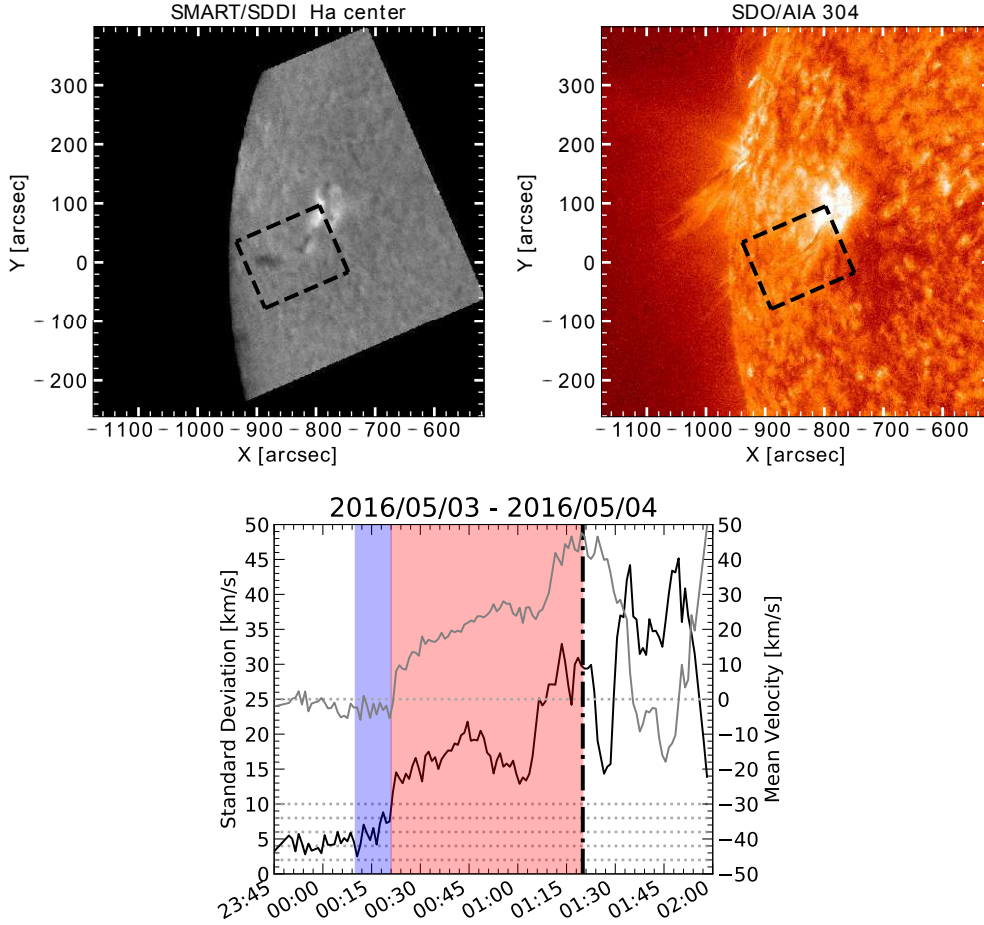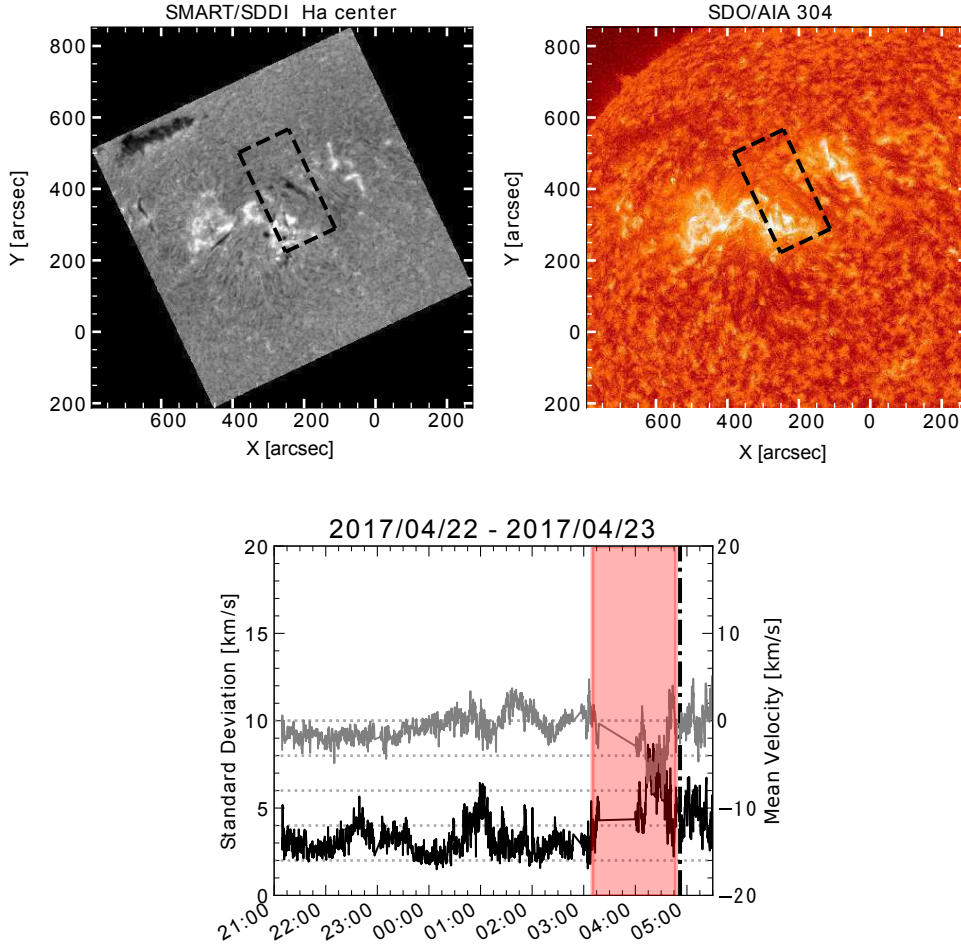Figure 3.15: *Top*: Hα line centre and SDO/AIA 304 images of Event 14. The active region where the filament was located is NOAA AR 12651. The definition of the black dashed rectangles is identical to that in Figure 3.4. *Bottom*: Standard deviation (black line, left axis) and average (grey line, right axis) of LOS velocity of filament. The definitions of the red shade area, vertical black dash-dotted line, and horizontal grey dotted lines are identical to those in Figure 3.4. In this case, we could not clearly identify a Phase-1 period; therefore, blue shaded area is absent.

3.3   Summary and Discussion

In this study, we analysed 12 filament-disappearance events observed by the SMART/SDDI in Hida Observatory from May 2016 to May 2017 in the same manner as that in Seki et al. (2017) [65] with the purpose of clarifying whether the precursor of a filament eruption indicated in Seki et al. (2017) [65] could be detected as a common feature prior to other filament-disappearance events. Owing to the narrow passband width around Hα line centre and the high time cadence of the SDDI, we succeeded in obtaining the unprecedented detailed LOS velocity maps of filaments. Moreover, by tracking the average and standard

deviation of the LOS velocity of each filament, we investigated the existence of Phase 1 (the period during which the standard deviation increases while the average is almost constant) and Phase 2 (from the time of initiation of the systematic changes of both the statistical values to the time of a filament eruption). The summary of the results is presented in Table 3.2.

Table 3.2: Properties and durations of Phases 1 and 2

id	Type	Phase 1 [hours]	Phase 2 [hours]	CME [UT]	t_A [sec]	Phase 1 / t_A	Figure
1	AF (NOAA 12541)	0.18	1.0	–	~230	~3	Fig. 3.12
9	AF (NOAA 12561)	–	0.17	–	–	–	Fig. 3.13
17	IF (NOAA 12586)	–	3.5	–	–	–	Fig. 3.6
18	IF (NOAA 12588)	1.2	0.75	–	~230	~19	Fig. 3.7
19	AF (NOAA 12588)	14*	0.27	–	–	–	Fig. 3.14
23	QF	25–42	3.5	08:00	~1400	~65–110	Fig. 3.4
24	IF (NOAA 12605)	4.7–20	1.2	04:36	~230	~74–310	Fig. 3.8
27	IF (NOAA 12636)	0.33	0.50	–	~230	~5	Fig. 3.2, 3.3, 3.9
31	AF (NOAA 12651)	–	1.7	–	–	–	Fig. 3.15
32	IF (NOAA 12652)	0.60	0.82	06:00	~230	~9	Fig. 3.10
33	QF	23	–	05:34	~1400	~60	Fig. 3.5
34	IF (NOAA 12653)	0.60	0.63	02:36	~230	~9	Fig. 3.11

The value with an asterisk (Phase-1 duration of Event 19) could be overestimated because of the lack of data. t_A corresponds to an Alfvén time on the assumption that (1) the length of a filament is 300 Mm (QF) or 150 Mm (IF, AF), (2) the magnitude of magnetic field is 10 G (QF) or 30 G (IF, AF), and (3) the electron number density is 10^{10} cm^{-3}.

In all the 12 events except Event 33, Phase 2 was detected prior to the disappearance of the filament, regardless of the filament types and whether the disappearance was associated with a CME or not. In addition, it should be noted that in Event 33, the filament moved and erupted perpendicularly to the LOS direction in appearance so that the LOS component of its velocity was marginal. Therefore, we conclude from this study that in general, the Phase-2 period is observed prior to filament disappearance.

Now, we present three other findings of this study. First, our results also reveal wide variations in Phase 1 and Phase 2, ranging from 0.18 to 42 h and 0.17 to 3.5 h, respectively. Omitting the possibly overestimated durations of Phase 1 (Events 19 and 24), we observe that a quiescent filament has a longer Phase-1 duration than the other two types of filaments by one or two orders of magnitude. This difference is probably owing to the difference in the Alfven time of a filament, although further study is required to verify this. Meanwhile, although the Phase-2 duration also varies among the events by an order, such a relation between the types of filaments and the duration is not evident.

Secondly, in all the cases of the intermediate and quiescent filaments, the standard deviation during Phase 1 generally changed from 2–3 km s^{-1} to 4–5 km s^{-1}. This common transition was observed regardless of the CME association and the size and types of filament. In addition, Kubota & Uesugi (1986) [87] reported that approximately 24 h prior to disappearance, the mean and standard deviation of the LOS velocity of the quiescent filament that disappeared at 04:10 UT on May 8, 1984, were 0.92 km s^{-1} and 2.1 km s^{-1}, respectively.

Thirdly, in Events 24 and 33, both the standard deviation and average of the LOS velocity manifested temporary, significant, and systematic increases in a specific period (from 00:30 UT to 01:30 UT in Event 24 and from 23:00 UT to 00:00 UT in Event 33). The similar temporary change in both the statistical values is also evident in Event 17 from 00:00 UT to 01:00 UT; the only exception is that the average of the LOS velocity decreased. The possible interpretation of these temporary disturbances is that they reflect the intermittent disruptions such as emerging flux and magnetic reconnection that contribute to the global evolution of the equilibrium of the magnetic flux system.

In terms of space weather, filament eruptions exhibit a potential risk of disturbing it. McAllister et al. (1996) [77] reported the event of a polar crown filament, which erupted on 1994 April 14. This eruption displayed a very large coronal arcade in a soft X-ray image; finally, a very large geomagnetic storm (Dst $\sim$ -200 nT) occurred three days after the eruption. Severe geomagnetic storm produced by a quiescent filament eruption is also reported by Cliver et al. (2009) [88]. Joselyn & McIntosh (1981) [89] revealed that 42 geomagnetic storms out of 65 were associated with filament disappearances and argued that a filament disappearance could be used as a useful predictor of geomagnetic storms.

From this perspective, our present study, which demonstrated the general appearance of Phase 2 prior to filament eruptions, proposes a new method to predict filament eruptions by utilising Phase 2 as an effective precursor. Considering our results, this method enables us to predict filament eruptions 1.3 h on an average prior to onsets. Furthermore, it should be emphasised that this method is currently based only on data captured by ground-based telescopes. Although space-borne data are indispensable for space weather prediction, artificial satellites are vulnerable to space weather effects [5]. In this context, the prediction of solar eruptive phenomena based only on the data of ground-based telescopes as in our method is highly likely to be valuable for supporting the current space weather prediction system.

However, in order to realise the operational prediction, further studies, including on how to distinguish Phase 2 from temporary significant increase in both the statistical values (see the previous paragraph), how to address terrestrial clouds contaminating observed images, and how to speed computation, should be conducted. With regard to the infrastructure, a network of ground-based telescopes that monitor Hα line centre as well as its blue and red wings, such as CHAIN project [90], can play a significant role in the operation [91].

Chapter 4

SMART/SDDI Filament Disappearance Catalogue

This Chapter* describes "SMART/SDDI Filament Disappearance Catalogue," in which we listed almost all the filament disappearance events that the Solar Dynamics Doppler Imager (SDDI) has observed since its installation on the Solar Magnetic Activity Research Telescope (SMART) in May 2016. Our aim is to build a database that can help predict the occurrence and severity of coronal mass ejections (CMEs). The catalogue contains miscellaneous information associated with filament disappearance such as flare, CME, active region, three-dimensional trajectory of erupting filaments, detection in Interplanetary Scintillation (IPS), occurrence of interplanetary CME (ICME) and Dst index. We also provide statistical information on the catalogue data. The catalogue is available from the following website.

https://www.kwasan.kyoto-u.ac.jp/observation/event/sddi-catalogue/

Dark filaments observed on the solar disk (or prominences on the solar limb) are comprised of dense cool plasma floating in the solar corona supported by a magnetic field. Their electron densities and temperatures are estimated as 10^9–10^{10} cm^{-3} and around 10^4 K, respectively [34]. At the end of their lives, filaments sometimes disappear (known as "disparition brusque") or dynamically erupt, which is associated with a coronal mass ejection (CME). In this Chapter, we define "filament disappearance" as an event in which a filament disappears completely in an Hα line observation. An eruption is believed to be triggered by magnetic reconnection, ideal magnetohydrodynamic (MHD) instability or loss of equilibrium [92]. The reconnection-induced triggering mechanism includes magnetic reconnection between the pre-existing flux rope containing the filament

---

Sun

filament

Ch. 2 and 3
Is it possible to quantify a filament activation and use it as a precursor of a filament eruption?

Coronal
Mass
Ejection
(CME)

Ch. 4 and 5
What physical parameters of filament eruptions control their CME associations?

Ch. 7
How severe malfunctions would satellites suffer in case of a disastrous solar flare?

Ch. 6
The feasibility of a prediction of filament eruptions by ground-based telescopes

Ch. 8
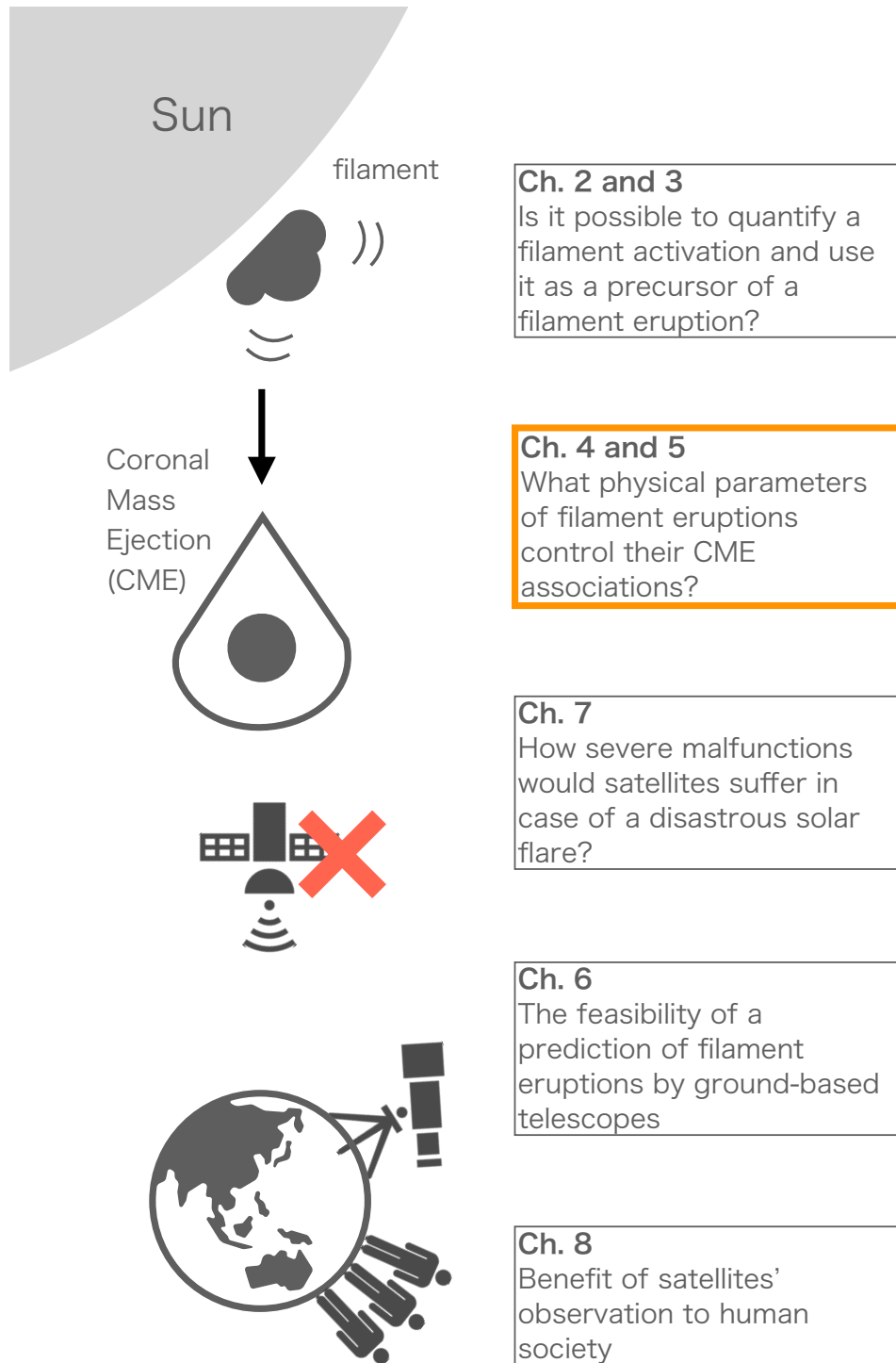Benefit of satellites' observation to human society

Figure 4.1: The graphical abstract of this dissertation (the orange rectangle corresponds to this Chapter).

and the nearby emerging magnetic flux [43, 44, 75], the overlying fields above the flux rope [82] or the underlying sheared fields below the filament [74]. As for the instability-induced triggering mechanism, several MHD instabilities including Torus instability [41] and Kink instability [93, 94] have been proposed.

Space weather is a plasma disturbance in the interplanetary medium and near-Earth space caused by solar magnetic activity. Recently, space weather has attracted much attention due to its potential societal and economic impacts [5, 14]. Since filaments often erupt and become a part of CMEs, they can also be a major cause of space weather. McAllister et al.(1996) [77] reported a polar crown filament eruption on 1994 April 4 and its associated geomagnetic storm (Dst ~ -200 nT) three days later. Cliver et al.(2009) [88] also reported a quiescent filament eruption event on 1991 November 9, which caused a significant geomagnetic storm (Dst ~ -354 nT) around three days after the eruption.

To mitigate the impacts of geomagnetic storms, a number of studies have sought to predict CME arrival times and the occurrence of severe geomagnetic storms [52, 95, 96] using coronagraphs, such as Large Angle and Spectrometric Coronagraph (LASCO; Brueckner et al.(1995) [49]) onboard the Solar and Heliospheric Observatory (SOHO; Domingo et al.(1995) [97]). However, coronagraphs only provide the information on the plane-of-sky velocity of CMEs (i.e., they lack information on the line-of-sight velocity (LOSV)).

In an effort to compensate for the LOSV information of CMEs, in this Chapter, we present a catalogue of filament disappearances observed by the Solar Dynamics Doppler Imager (SDDI; Ichimoto et al.(2017) [39]) installed on the Solar Magnetic Activity Research Telescope (SMART; UeNo et al.(2004) [40]) at Hida Observatory, which is called the "SMART/SDDI Filament Disappearance Catalogue." Hereafter, we refer to it as "the Catalogue" throughout this dissertation. SDDI has been used to observe the solar full-disk image since 2016 May 1 in 73 wavelengths around the Hα absorption line at 656.28 nm. The time cadence is 15 sec, and the spatial sampling is 1.23 arcsec pix^{-1}. SDDI's key benefits are its continuous full-disk observation of the Sun and its wide coverage of observing wavelengths. It captures the full-disk Sun from Hα centre $- 9.0$ Å(blue shift) to Hα centre $+ 9.0$ Å(red shift) every 0.25 Å. The high resolution in wavelengths and the wide coverage around Hα line enables us to determine the LOSV of filaments in unprecedented detail due to its dynamic range of ± 400 km s^{-1}. For more details on SDDI, see Ichimoto et al.(2017) [39].

4.1 Overview of the Catalogue

The Catalogue webpage can be accessed at `https://www.kwasan.kyoto-u.ac.jp/observation/event/sddi-catalogue/`. Figure 4.2 provides the layout of the Catalogue webpage. The

SMART/SDDI Filament Disappearance Catalogue

This is the cataolgue of filament disappearance (or disparition brusque) observed by the SMART/SDDI (Ichimoto et al. 2017, SolPhys)

To download the entire catalogue (excel file), click HERE.

id & obs_date	event_reports	flare_class	flare_peak_time	noaa_ar	ar_location	ar_size	CME	central_PA	angular_width	linear_speed	credibility
No.001 2016.05.04	#20160504	B6.9	2016-05-04 01:22:00	12541	N04E38	1.3521e+04	-	-	-	-	2
No.002 2016.05.14	#20160514	B5.2	2016-05-13 22:31:00	12544	N20E07	1.1377e+04	-	-	-	-	2
No.003 2016.05.14	#20160514	-	-	-	-	-	-	-	-	-	2
No.004 2016.05.23	#20160523	-	-	-	-	-	2016-05-23 07:48:00	65	9	260	1
No.005 2016.05.24	#20160524	-	-	-	-	-	2016-05-24 05:12:00	268	11	524	3
No.006 2016.06.02	#20160602	B7.9	2016-06-01 22:35:00	-	-	-	2016-06-01 23:12:00	48	13	217	3
No.007 2016.06.20	#20160620	B5.0	2016-06-19 23:47:00	12555	S09W90	-	2016-06-19 23:36:00	248	54	1065	3
No.008 2016.06.20	#20160620	B2.2	2016-06-20 08:26:00	12555	S09W90	-	2016-06-20 07:48:00	259	80	826	3
No.009 2016.07.07	#20160707	C5.1	2016-07-07 07:56:00	12561	S15W45	4174.5	-	-	-	-	3
No.010 2016.07.19	#20160719	-	-	-	-	-	-	-	-	-	3
No.011 2016.07.20	#20160720	C1.4	2016-07-20 01:26:00	12565	N05W35	7983.7	2016-07-20 03:12:00	294	25	331	2

Figure 4.2: The layout of the Catalogue webpage

table lists all the filament-disappearance events observed by SDDI from 2016 May 1 to 2019 June 18. To identify events, we first searched for the word of "filament" in the daily observation logs created by human operators. Then, if eruptive events were reported on a particular day, we investigated whether there was a filament disappearance in the Hα centre on that day by investigating the daily quick-look movie. The catalogue contains 36 columns related to flare association, CME association, filament disappearance dynamics, interplanetary conditions and geomagnetic activity. Each column is described in the following section.

4.2   Column descriptions

The first two columns, "id & obs_date" and "event_reports," identify filament disappearance events with a number and observing date. Clicking the id number takes to a full-disk image of the Sun taken in the Hα line centre (see Figure 4.3). Clicking the observation date takes to the webpage for SDDI daily observations, which include a java movie and fits files of the day's observations.

The next five columns, "flare_class," "flare_peak_time," "noaa_ar," "ar_location" and "ar_size," provide information on the associated flare. "Flare_class" and "flare_peak_time" correspond to the soft X-ray flare class peak time from the Geostationary Operational Environmental Satellite (GOES) observations. Clicking these values reveals the soft X-ray light curve. The "noaa_ar," "ar_location" and "ar_size" are the NOAA Active Region (AR) number, the AR location in heliographic coordinates, and the rough AR size, respectively. Note that the AR size is measured as the size of the rectangle containing the entire AR, corrected for projection effects due to sphericity. Clicking these values takes to the corresponding webpage in the Solar Monitor https://www.solarmonitor.org.

The next five columns, "CME," "central_PA," "angular_width," "linear_speed" and "credibility," provide information on the associated CME. "CME," "central_PA," "angular_width" and "linear_speed" correspond to the date and time of the CME's first appearance in the LASCO C2 field of view, the central position angle, the angular width and the CME's linearly estimated speed, listed in the SOHO/LASCO CME Catalog [85,86] (hereafter the "CME Catalog"). As the CMEs in the CME Catalog were manually tracked, some CMEs (particularly very poor events) were not listed in the CME Catalog. In such cases, we tracked the LASCO images by ourselves. In the "CME" column, we added a comment "-" if there was no CME candidate, and "nan" if there was no investigation into associated CMEs mainly due to a lack of LASCO data. Clicking these four values takes to the corresponding webpage in the CME Catalog. "Credibility" denotes the subjective credibility of the CME association. Higher values indicate higher credibility; events with
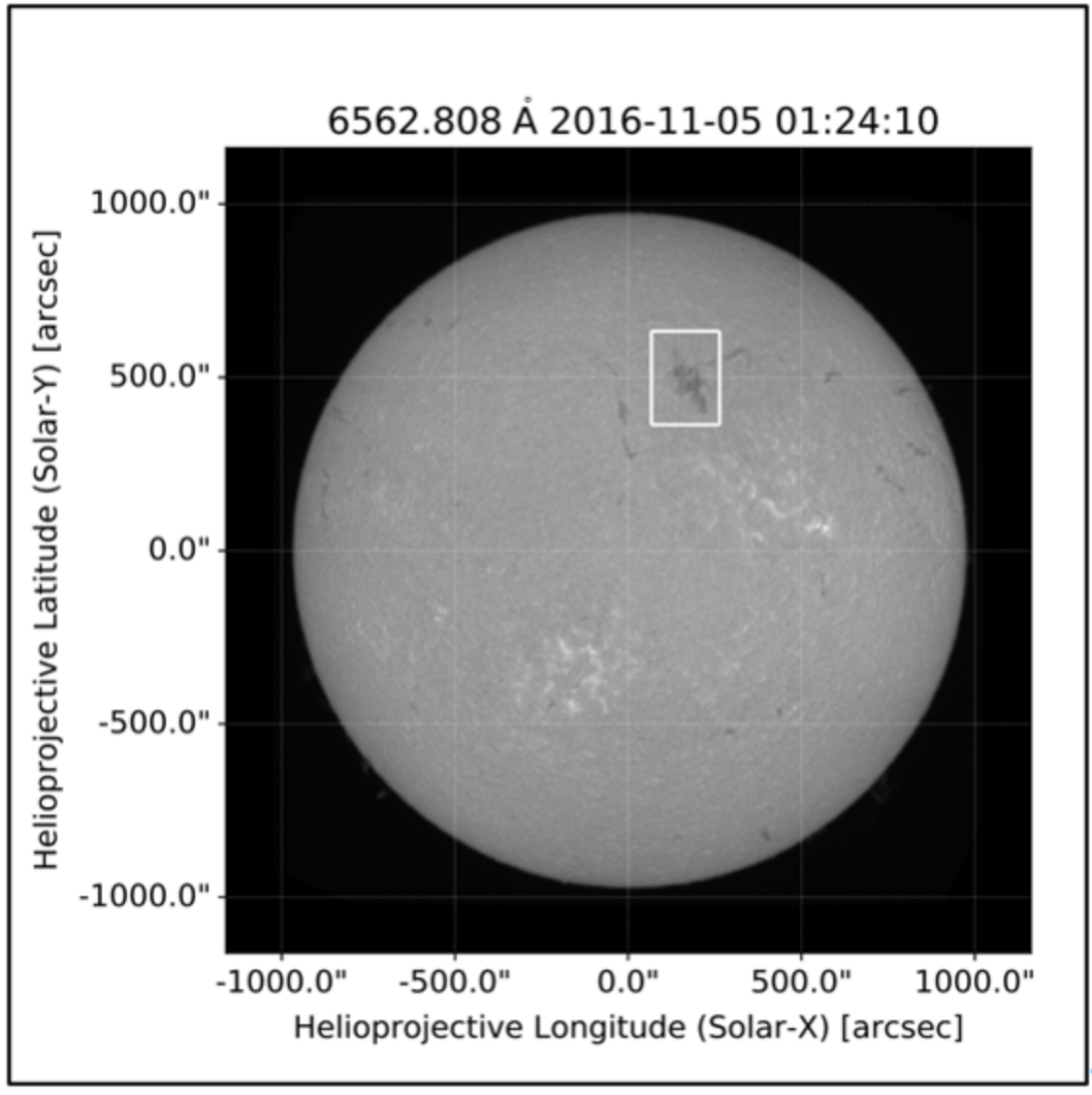
Figure 4.3: A full-disk image of the Sun in the Hα line centre captured when a filament started to disappear (same as "FD_start_time"). The white rectangle encloses the target filament.
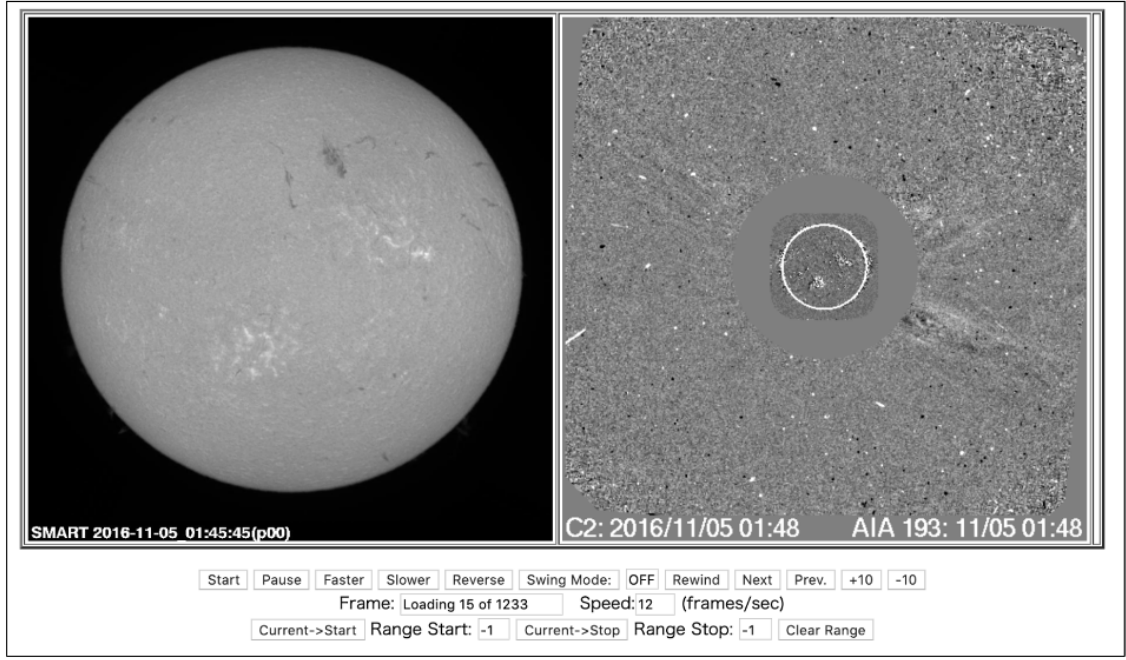
Figure 4.4: A snapshot of the two movies that were utilised to investigate the association between a filament disappearance and a CME.

a credibility of 1 may be controversial. Clicking the credibility shows the actual movies that were used to investigate the CME association (see Figure 4.4): the solar full-disk movie in Hα (for most of the events) or in 304 Å captured by the Atmospheric Imaging Assembly [46] onboard the Solar Dynamics Observatory [98] and the running difference movie of SOHO/LASCO C2 are shown.

The next sixteen columns, "FD_start_time," "FD_end_time," "x," "y," "longitude," "latitude," "Vx," "Vy," "Vz," "Vr_max_time," "Vr_max," "Vr_fin," "tracked_data," "phi," "theta" and "inclination_angle," pertain to filament dynamics. "FD_start_time" and "FD_end_time" correspond to the start and end times of a filament disappearance, which are defined as the time when the filament appeared in the Hα line centre − 0.5 Å and the time when the filament totally disappeared from all observed wavelengths, respectively. Clicking these two values takes to the corresponding movie, a snapshot of which is shown in Figure 4.5. The black dashed line indicates the trajectory of the filament, along which we measured the X and Y positions of the filament. The small green rectangle corresponds to the measured position at that time. The measured position was determined as the apex point observed in "weighted averaged contrast (WAC)" image, which is the average contrast through SDDI wavelengths (Hα centre − 9.0 Åto the Hα centre + 9.0

73
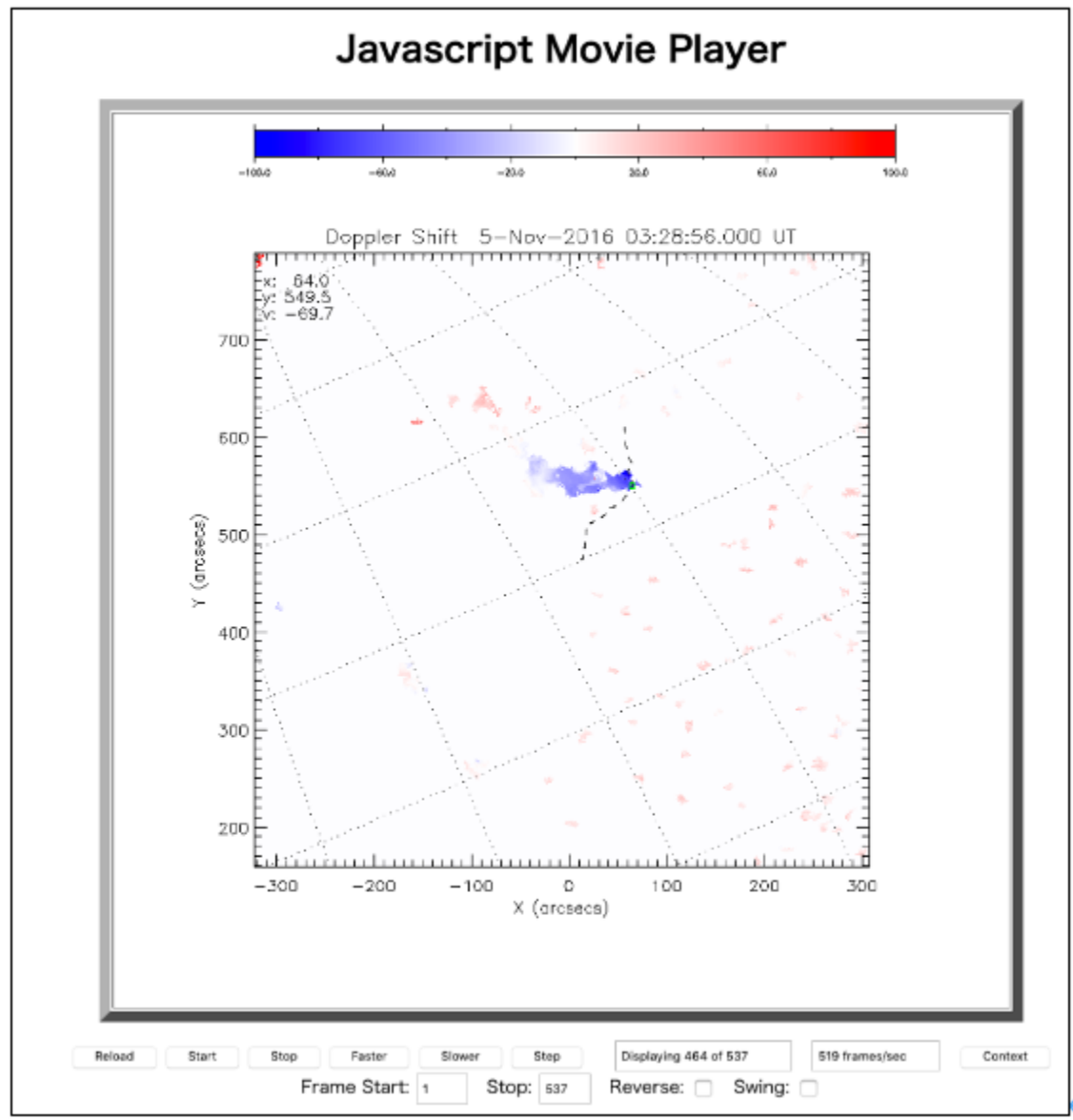
Figure 4.5: A snapshot of the LOSV movie and the trajectory of a filament. The black dashed line denotes the trajectory of the filament.
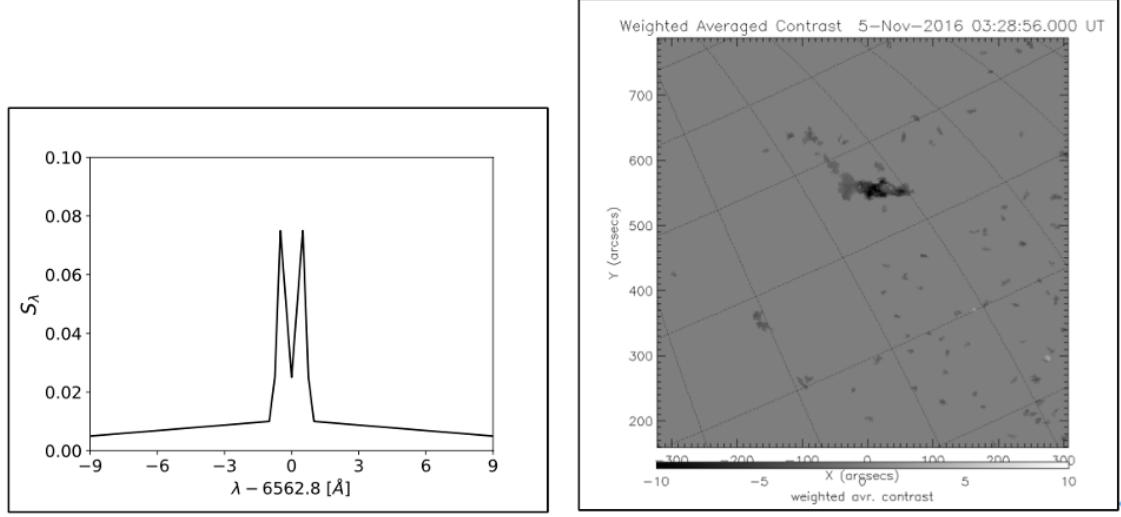
Figure 4.6: *Left*: Weight value S_λ along wavelengths. *Right*: A snapshot of WAC movie on 2016 November 5. (https://www.kwasan.kyoto-u.ac.jp/∼otsuji/trajectory_data/20161105012400/proc0/movie.html)

Å) with specific weights. The value of WAC, Iwac, was calculated by

$$I_{wac} = \frac{1}{N} \sum_{\widehat{C_\lambda} > 3.0} \widehat{C_\lambda} \tag{4.1}$$

$$\widehat{C_\lambda} = \frac{C_\lambda}{S_\lambda} \tag{4.2}$$

$$C_\lambda = \frac{I_\lambda - I_{0\lambda}}{I_{0\lambda}} \tag{4.3}$$

where N is the number of wavelengths in which $\widehat{C_\lambda}$ is larger than 3.0, I_λ, and $I_{0\lambda}$ are intensities of the target filament and background evaluated from the surrounding regions at the wavelength, λ, and S_λ is the weight value shown in Figure 4.6, which empirically corresponds to the standard deviation of contrast, C_λ. The WAC image can collect the darker features from all wavelengths, which allows tracking the target filament, regardless of the Doppler shift (for more details, in Otsuji et al.(in prep).) Figure 4.6 is a snapshot of an actual WAC movie constructed from SDDI observations on 2016 November 5. Note that links to WAC movies are not included in the catalogue. The WAC movie can be accessed at `https://www.kwasan.kyoto-u.ac.jp/~otsuji/trajectory_data/` `{'FD_start_time'inYYYYMMDDHHmm00}/proc0/movie.html` (see Figure 4.6). "X," "y," "longitude" and "latitude" indicate the position of the approximate centre of the filament at "FD_start_time". Clicking these four values shows the solar full-disk image and the target filament (same as clicking "id"). Note that the height of a filament was assumed to be 40 arcsec ($\sim$ 29 Mm), leading to a few degrees of uncertainty in "longitude," "latitude"

and "inclination angle" due to the projection effects. "Vx," "Vy," "Vz," "Vr_max_time," "Vr_max" and "Vr_fin" correspond to the representative velocity components of the filament and measured time. Firstly, we manually measured the filament's X- and Y-positions and LOSV. Then, assuming the three components of its position were 0 Mm at the beginning of measurement (same as "FD_start_time") and determining the LOS location by integrating its LOS velocity with the time, we constructed its position in the heliocentric Cartesian coordinates (see Figure A in the webpage). We also transformed and obtained the position in the local Cartesian coordinates as well, in which three orthogonal base vectors were directed along the solar normal, latitudinal direction and longitudinal direction. The maximum radial velocity component was obtained as the maximum derivative of the interpolated spline from the radial positions. It was listed as "Vr_max" and its measured time was "Vr_max_time." Three velocity components in the heliocentric Cartesian coordinates at that time, "Vx," "Vy" and "Vz," were derived in the same manner. "Vr_fin" corresponds to the radial velocity at the "FD_end_time." Clicking these values shows the time-distance plots in two different coordinates (see Figure 4.7), the heliocentric Cartesian coordinates and the local Cartesian coordinates. "Tracked_data" contains the actual tracked locations in csv format. For more details on how to measure these velocity components, see Otsuji et al. (in prep). "Phi" and "theta" indicate the velocity angles in spherical coordinates. "inclination_angle" shows the angle between the local solar normal and the velocity (see Figure A and B in the webpage). Clicking these angles demonstrates the filament's three-dimensional trajectory (see Figure 4.8)

The three columns, "length," "length_csv" and "Type," are related to the filament's length and type before its disappearance. The length was measured manually as shown in Figure 4.9. Clicking the "length" displays the same image for each event. The time series of the measured positions is stored in the csv file, "length_csv". Each filament or prominence was classified as one of the following three types, based on the connectivity to the active regions; active region filament (AF), intermediate filament (IF) and quiescent filament (QF). If the filament was entirely in the active region, it was classified as AF. If there was no nearby active region, it was QF. If the filament was neither AF nor QF, it was categorised as IF.

The next column, "IPS," corresponds to the g-values of the associated enhancement of the interplanetary scintillation (IPS) and its observed date. IPS is the disturbance of the radio wave from a distant source caused by the interplanetary plasma, such as from the solar wind or CMEs. The g-value is defined as the ratio of the IPS disturbance at the observed time to its annual average. For more details about IPS and g-value, see Gapper et al. (1982) [99] and Iju et al. (2013) [100]. For all CME-associated events, we investigated whether the g-value was greater than 1.5 around the equivalent position angle
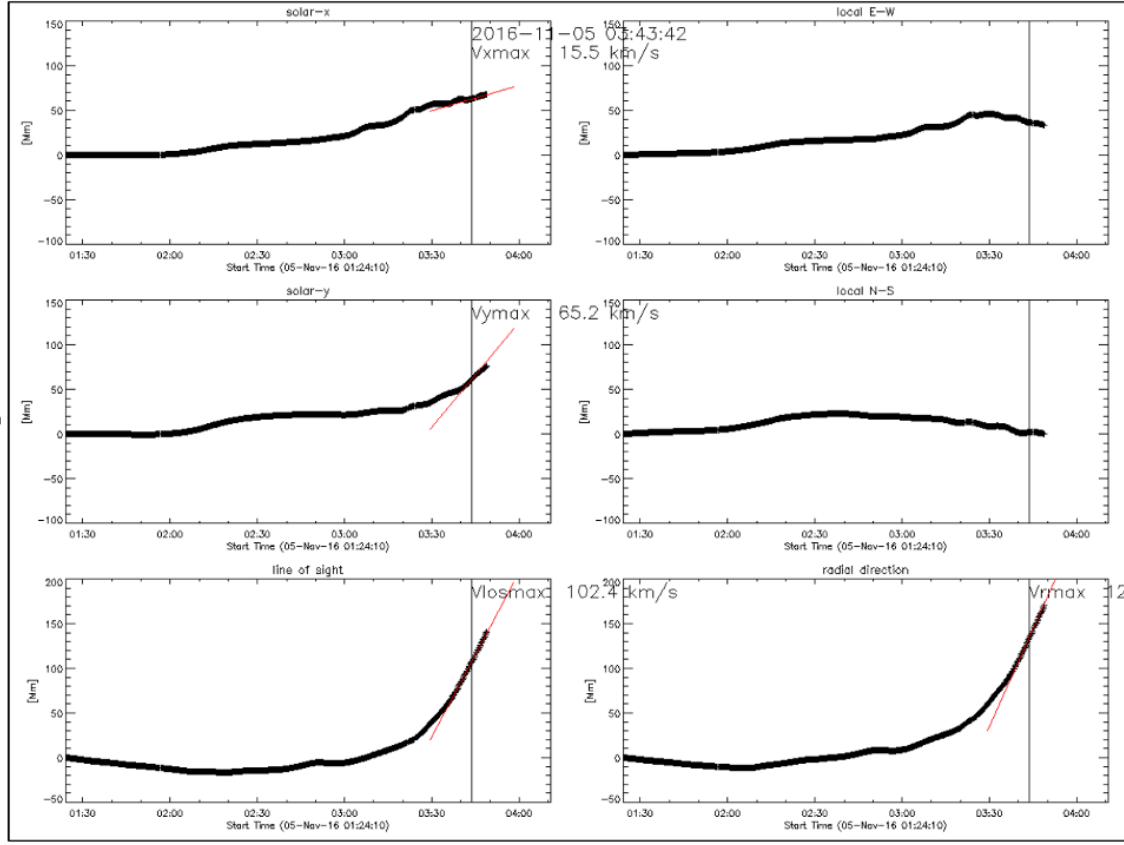
Figure 4.7: *Left*: Time-distance plots in heliocentric Cartesian coordinates, in which x- and y-axis are directed to the solar west and north, respectively. Z-axis points toward the Earth along the line-of-sight direction. *Right*: Same plots in local Cartesian coordinates. Local E-W and local N-S indicate the longitudinal and latitudinal directions on the solar surface, respectively. The black and red lines indicate the time when the radial velocity was maximum and the tangent of the height-time plot, respectively.
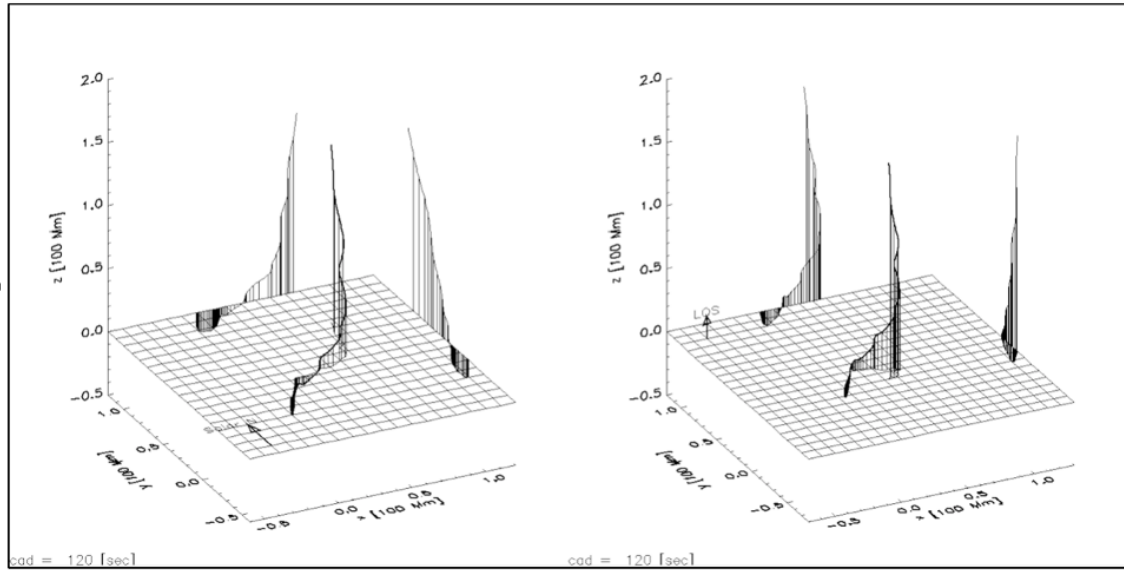
Figure 4.8: Three-dimensional trajectory of the filament. The left and right panels exhibit the trajectories in the heliocentric Cartesian coordinates (z-direction is LOS) and the local Cartesian coordinates (z-direction is the solar normal). The arrows in the left and right panels point to the solar north and to the Earth, respectively. The black vertical lines between three-dimensional trajectories and the horizontal planes (z = 0) are drawn every two minutes.

of the CME. The statistical mean and standard deviation of all the g-values, observed from 1997 to 2009, were 1.07 and 0.47, respectively. Thus, we regarded a g-value greater than 1.5 as indicating the presence of interplanetary plasma cloud. Placing a cursor on the date shows the g-values greater than 1.5. Clicking the date displays the daily chart of the IPS observation, as shown in Figure 4.10.

The column "ICME" lists the arrival time of the associated interplanetary CME registered in the Richardson & Cane ICME Catalog (`http://www.srl.caltech.edu/ACE/ASC/DATA/level3/icmetable2.html`). Interplanetary CMEs (ICMEs) were detected as an abnormally low temperature plasma, which is commonly observed for most of CMEs. For more details, see Cane and Richardson (2003) [51]. The two columns, "Dst_peak_time" and "Dst_peak_value," indicate the time and peak of the Dst index 1–7 days after the filament disappeared. Note that this peak value is not necessarily associated with the filament disappearance. Users should be careful when considering the causes of geomagnetic disturbance. Clicking these values shows the monthly plot of the Dst index at the World Data Center for Geomagnetism, Kyoto. The last column notes a comment. Placing a cursor over the word, "note," shows it as a popover.
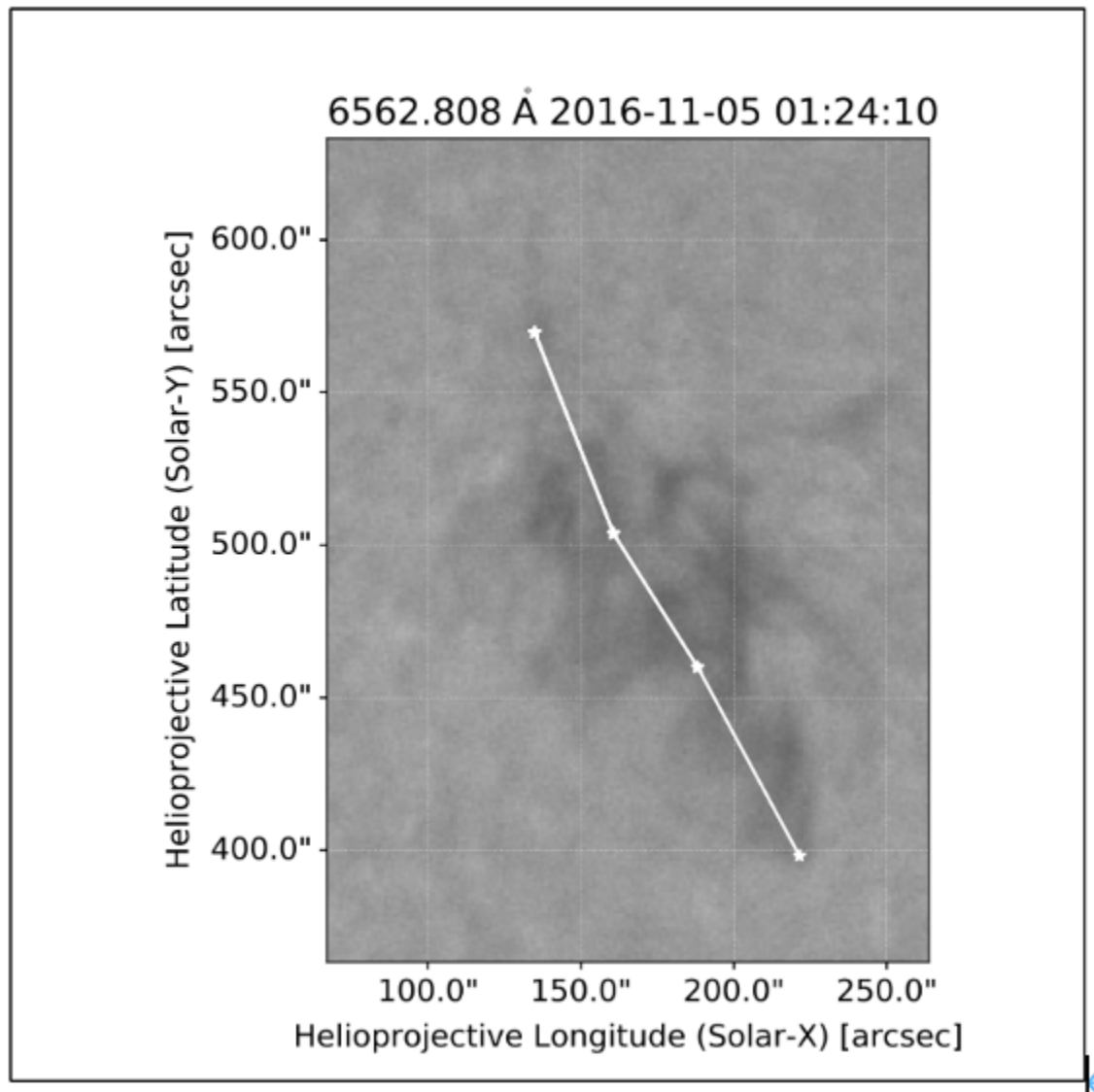
Figure 4.9: Close-up image of the target filament. This white line indicates trace of the filament when the length was measured.
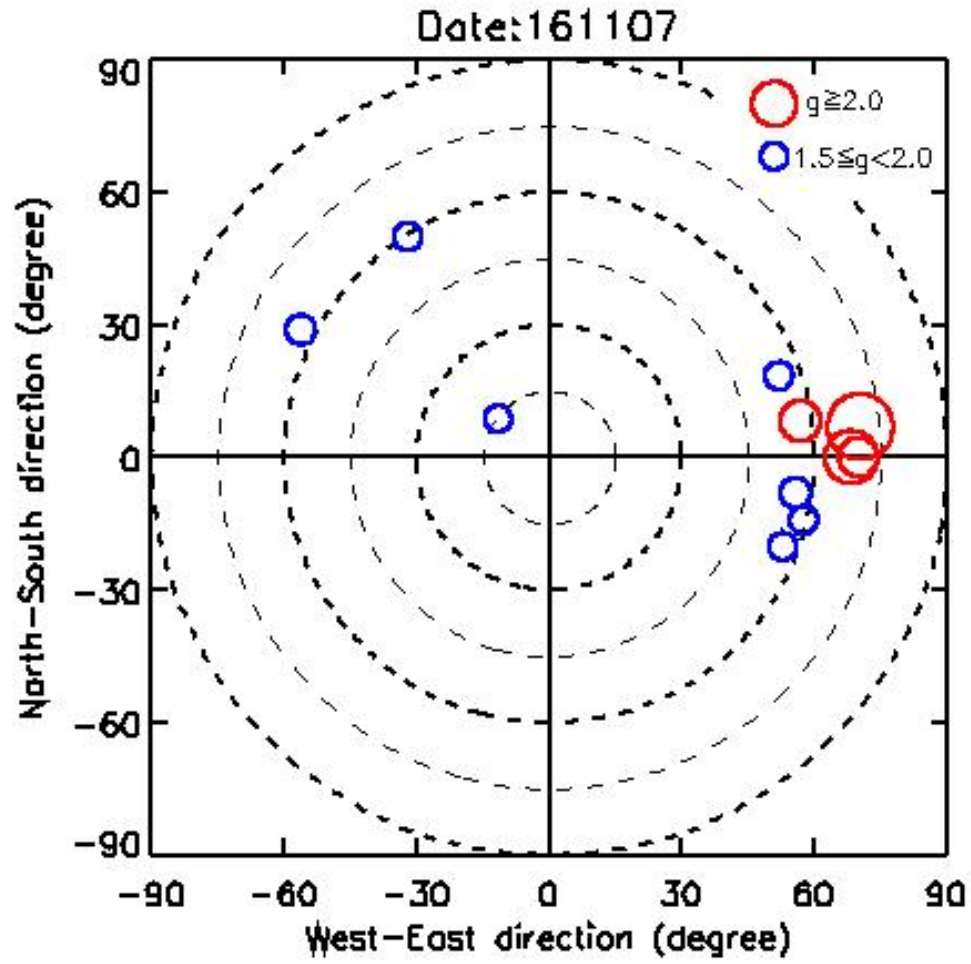
Figure 4.10: Daily IPS observation. The blue and red circles point to the positions where g-values are 1.5–2.0 and $\geq$ 2.0, respectively. The centre of the map corresponds to the Sun.
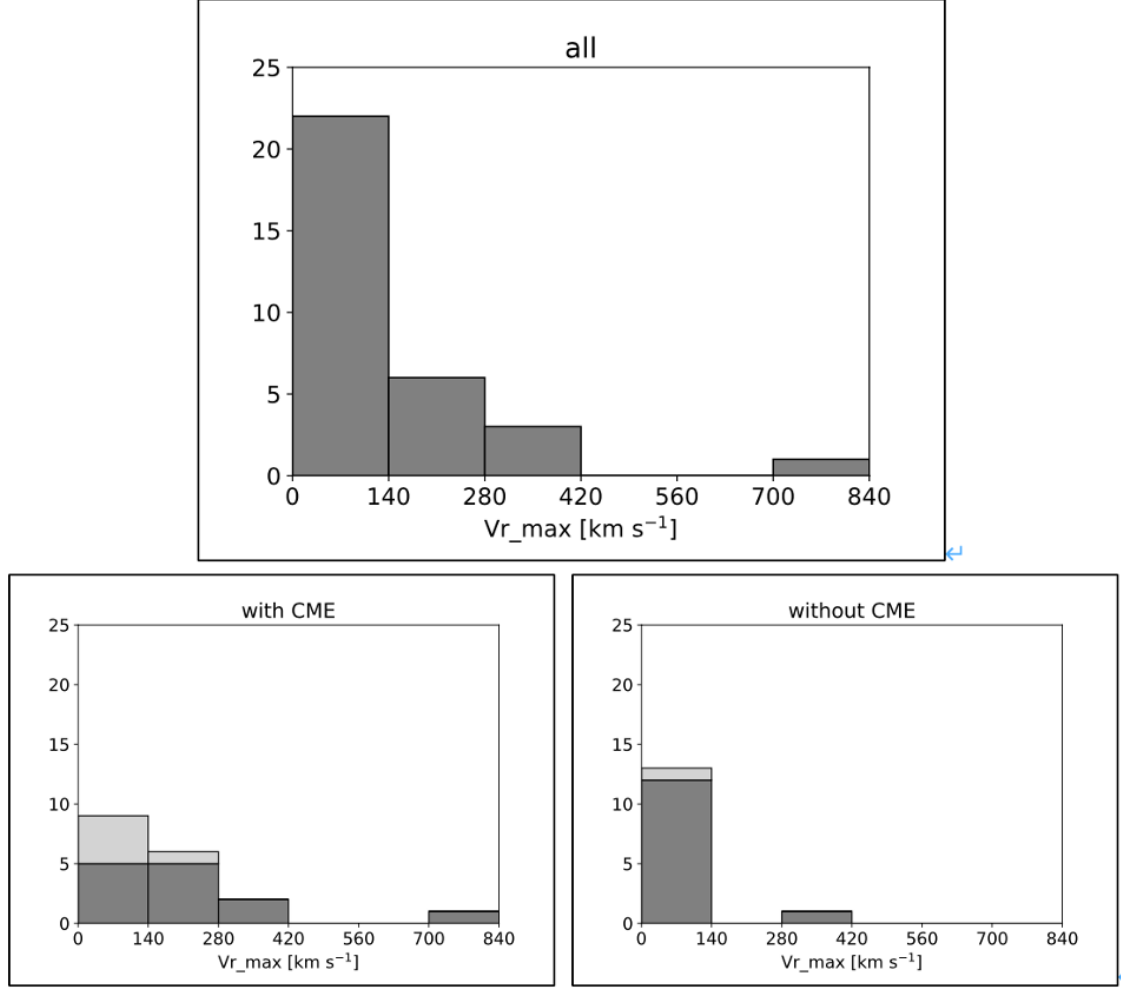
Figure 4.11: *Top*: Distribution of maximum radial velocities of all the filament disappearances (top) *Bottom left*: only for the events associated with CMEs *Bottom right*: only for the events without CMEs. Light grey bins correspond to the events whose values of "credibility" are 1 (i.e., ambiguous events).

4.3   Statistical properties

In this section, we provide information on the statistical properties of the filament disappearance events in our table. Figure 4.11 demonstrates the distribution of the maximum radial velocities. The averages for all the filament disappearances, CME-associated and CME-unassociated disappearances were 124, 177 and 55.6 km s^{-1}, respectively. 59% of the filament disappearances with their maximum radial velocities < 140 km s^{-1} were not associated with CMEs and 90% of the filament disappearances with their maximum radial velocities > 140 km s^{-1} were associated with CMEs. The faster the filaments disappeared in the radial direction, the more likely they are associated with CMEs. Table vrmaxnum summarises statistical properties of Figure 4.11. The value in a parenthesis corresponds to the number of the clear events whose values of "credibility" are 2 or 3.
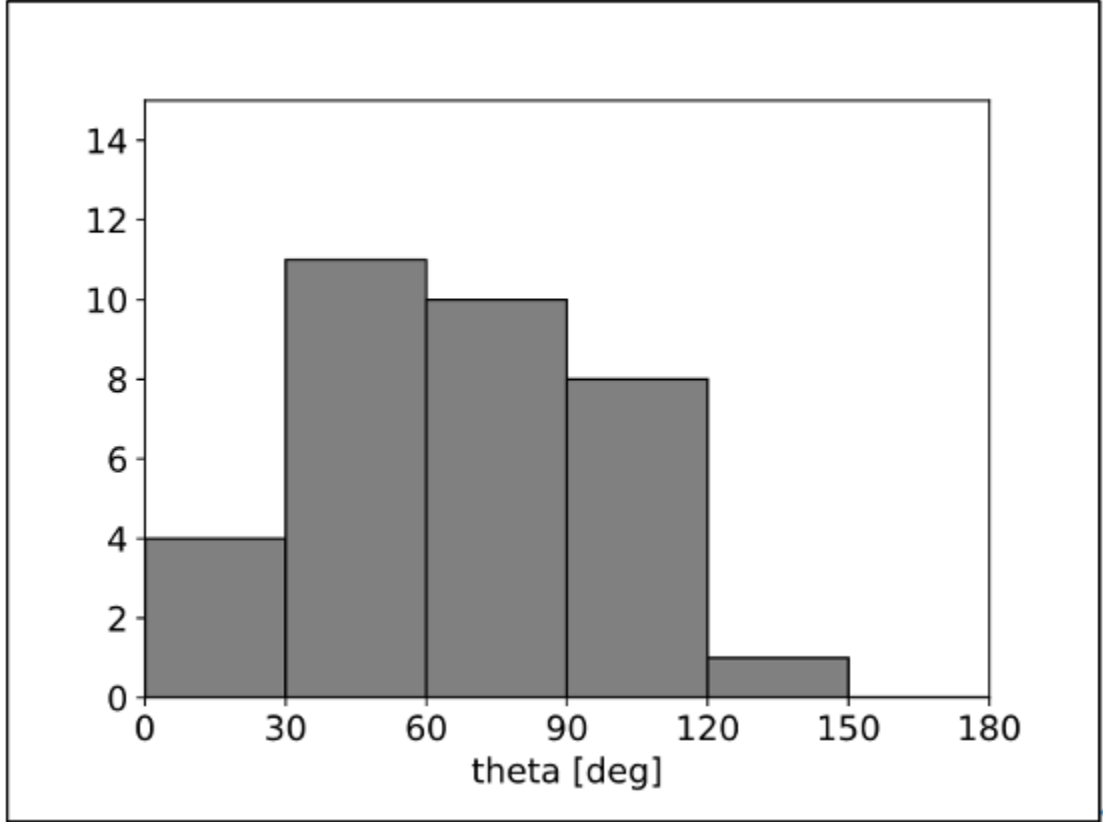
Figure 4.12: Distribution of theta angles of filament disappearances with respect to the LOS direction.

Table 4.1: Statistical properties of the maximum radial velocities.

	all events	with CME	without CME
< 140 km s^{-1}	22	9 (5)	13 (12)
> 140 km s^{-1}	10	9 (8)	1 (1)
total	32	18 (13)	14 (13)

Figure 4.12 shows the distribution of the inclinations between the maximum velocity of erupting filaments and LOS direction. The average theta angle was 64.4 deg. For 26% of the events, the theta angles were larger than 90 deg, which corresponds to an opposite direction to the Earth.

Figure 4.13 demonstrates the distributions of the inclinations between the direction of an eruption and the solar normal. The histogram is displayed in terms of the solid angle derived by "inclination_angle" in the catalogue. The average solid angle is 2.10 str which corresponds to 48.2 deg in terms of "inclination_angle". For the events whose solid
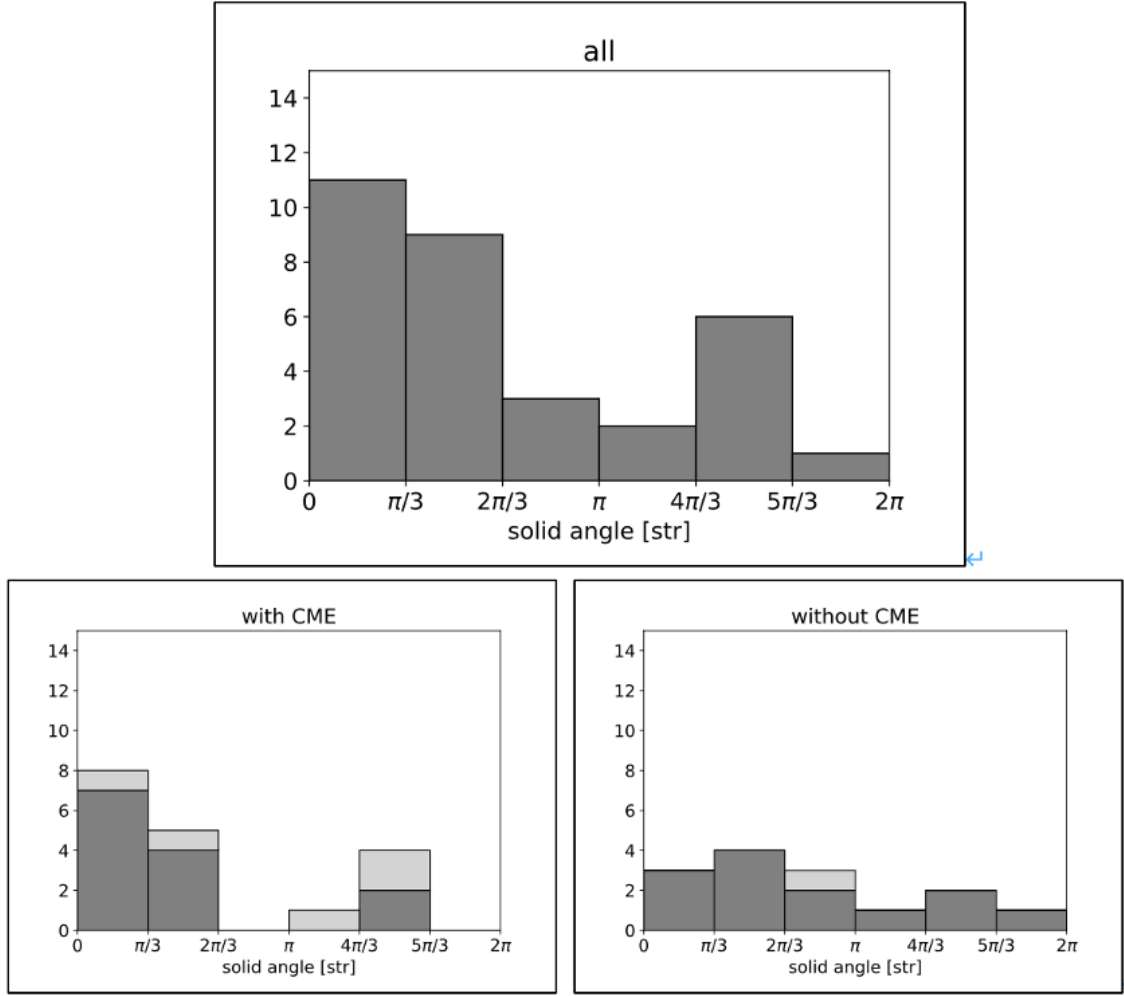
Figure 4.13: *Top*: Distribution of inclinations of filament disappearances in terms of solid angle derived by "inclination_angle". *Bottom left*: only for the events associated with CMEs. *Bottom right*: only for the events without CMEs.

angles are less than $2\pi / 3$, 65% of filament disappearances are associated with CMEs. For those with their solid angles more than $2\pi / 3$, 58% of filament disappearances are not associated with any CMEs. Only taking the clear events into account, we can see that 75% of filament disappearances are not associated. This result is consistent with Gopalswamy et al. (2003) [101], in which transverse events, whose solid angles are expected to be large, are less associated with CMEs than radial events, whose solid angles should be small. Table 4.2 summarises statistical properties of Figure 4.13. The value in a parenthesis corresponds to the number of clear events.

Table 4.2: Statistical properties of the solid angles.

	all events	with CME	without CME
$< 2\pi/3$	20	13 (11)	7 (7)
$> 2\pi/3$	12	5 (2)	7 (6)
total	32	18 (13)	14 (13)

Figure 4.14 shows the distributions of the apparent lengths of filaments at the beginning of their disappearances ("FD_start_time" in the catalogue). The average length was 139 Mm. 63% of the filaments whose lengths are less than 150 Mm are not associated with CMEs during their disappearances. On the other hand, 67% of those with their lengths of more than 150 Mm disappeared with CMEs. We can see that the longer the filaments, the more likely they are to be associated with CMEs. Table 4.3 summarises the statistical properties of Figure 4.14. The value in a parenthesis corresponds to the number of clear events. It must be noted that some narrow CMEs from close to the disk centre may not be observed by LASCO, so the lack of association may be due to this visibility effect in at least some cases.

Table 4.3: Statistical properties of the lengths.

	all events	with CME	without CME
< 150 Mm	24	9 (8)	15 (13)
> 150 Mm	15	10 (6)	5 (5)
total	39	19 (14)	20 (18)

4.4   Summary

This paper presented the "SMART/SDDI Filament Disappearance Catalogue" that aims to investigate essential parameters for predicting CME associations, CMEs' arrival times, and the potential geomagnetic impacts. The catalogue listed 43 filament-disappearance events observed by SDDI since the beginning of its operation (2016 May 1) with miscellaneous information, including the associated flare; active region; CME; the position, dynamics and properties of the filaments; IPS; and geomagnetic disturbance. Statistical properties were provided as well and we recognise that the faster filaments disappeared, the less inclined to the solar normal their direction of disappearance is and the longer filaments are, the more CMEs tend to be associated with them. As a future work, we will aim to complement the catalogue by using data from the CHAIN project [91,102], because
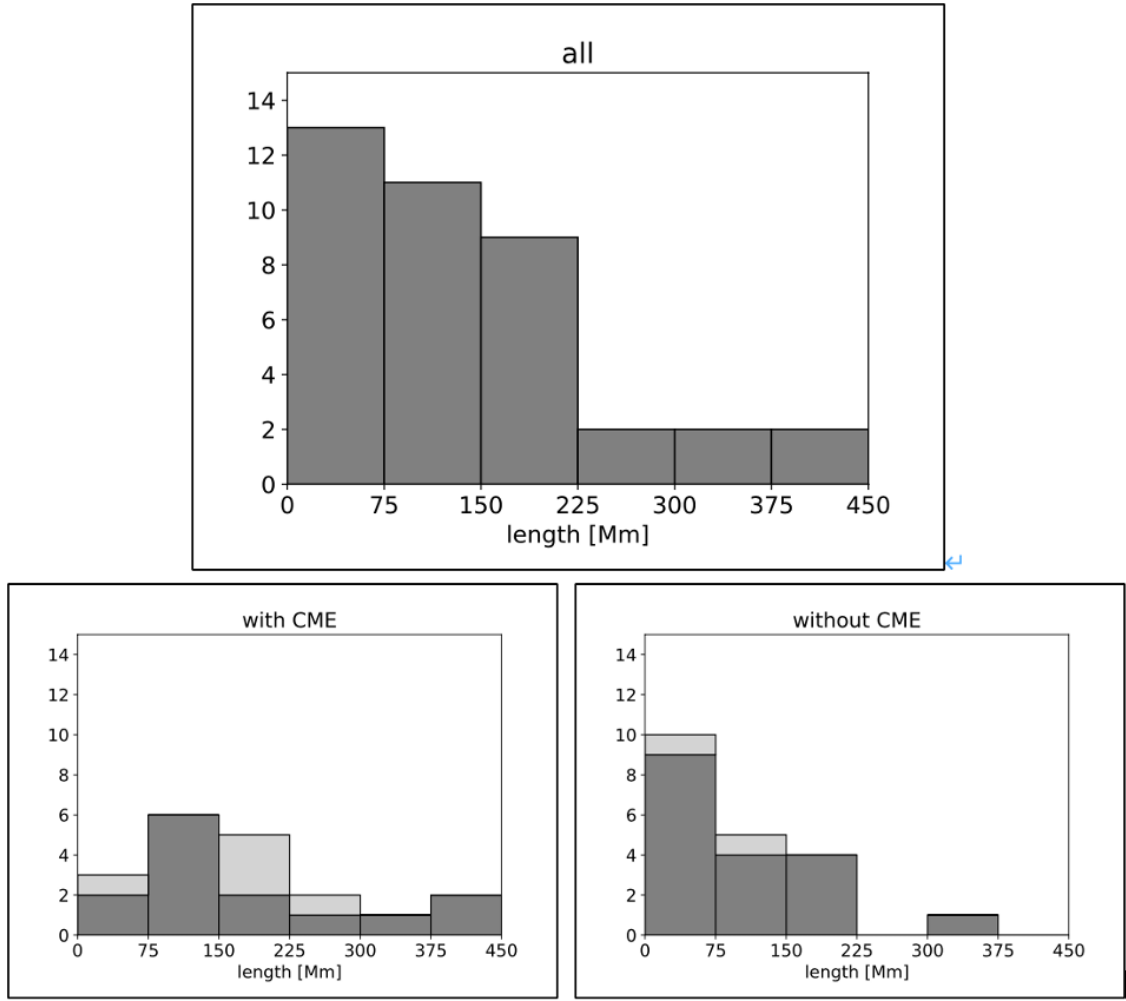
Figure 4.14: *Top*: Distribution of apparent lengths of all the filaments. *Bottom left*: only for those associated with CMEs. *Bottom right*: only for those without CMEs.

it archives the solar full-disk observation in the Hα line centre, red wing and blue wing during the night in Japan (i.e., during which SDDI is unable to conduct observation).

Chapter 5

Relationship between Three-dimensional Velocity of Filament Eruptions and CME Association

It is widely recognised that filament disappearances or eruptions are frequently associated with CMEs. Since CMEs are a major source of disturbances of the space environment surrounding the Earth, it is important to investigate these associations in detail for the better prediction of CME occurrence. However, the proportion of filament disappearances associated with CMEs is under debate. The estimates range from ∼10% to ∼90% and could be affected by the manners to select the events. This study[*] aims to reveal what parameters control the association between filament eruptions and CMEs. We analysed the relationships between CME associations and the physical parameters of filaments including their length, maximum ascending velocity, and direction of eruptions using 28 events of filament eruptions observed in Hα. We found that the product of the maximum radial velocity normalised by 100 km s^{-1} and the filament length normalised by 100 Mm to the power of 0.96 is well correlated with the CME occurrence. If the product is larger than 8.0×10^6 km^2 s^{-1}, the filament will become a CME with a probability of 93%, and if the product is smaller than this value, it will not become a CME with a probability of 100%. We suggest a kinetic-energy threshold above which filament eruptions are associated with CMEs. Our findings suggest the importance of measuring the velocity vector of filament eruption in three-dimensional space for the better prediction of CME occurrence.

Filaments are regions of dense cool plasma floating in the corona that are supported

---

[*]Seki, D., Otsuji, K., Ishii, T. T., Asai, A., Ichimoto, K., "Relationship between three-dimensional velocity of filament eruptions and CME association", Earth, Planets and Space, under review

Sun

filament

Ch. 2 and 3
Is it possible to quantify a filament activation and use it as a precursor of a filament eruption?

Coronal
Mass
Ejection
(CME)

Ch. 4 and 5
What physical parameters of filament eruptions control their CME associations?

Ch. 7
How severe malfunctions would satellites suffer in case of a disastrous solar flare?

Ch. 6
The feasibility of a prediction of filament eruptions by ground-based telescopes

Ch. 8
Benefit of satellites' observation to human society

Figure 5.1: The graphical abstract of this dissertation (the orange rectangle corresponds to this Chapter).

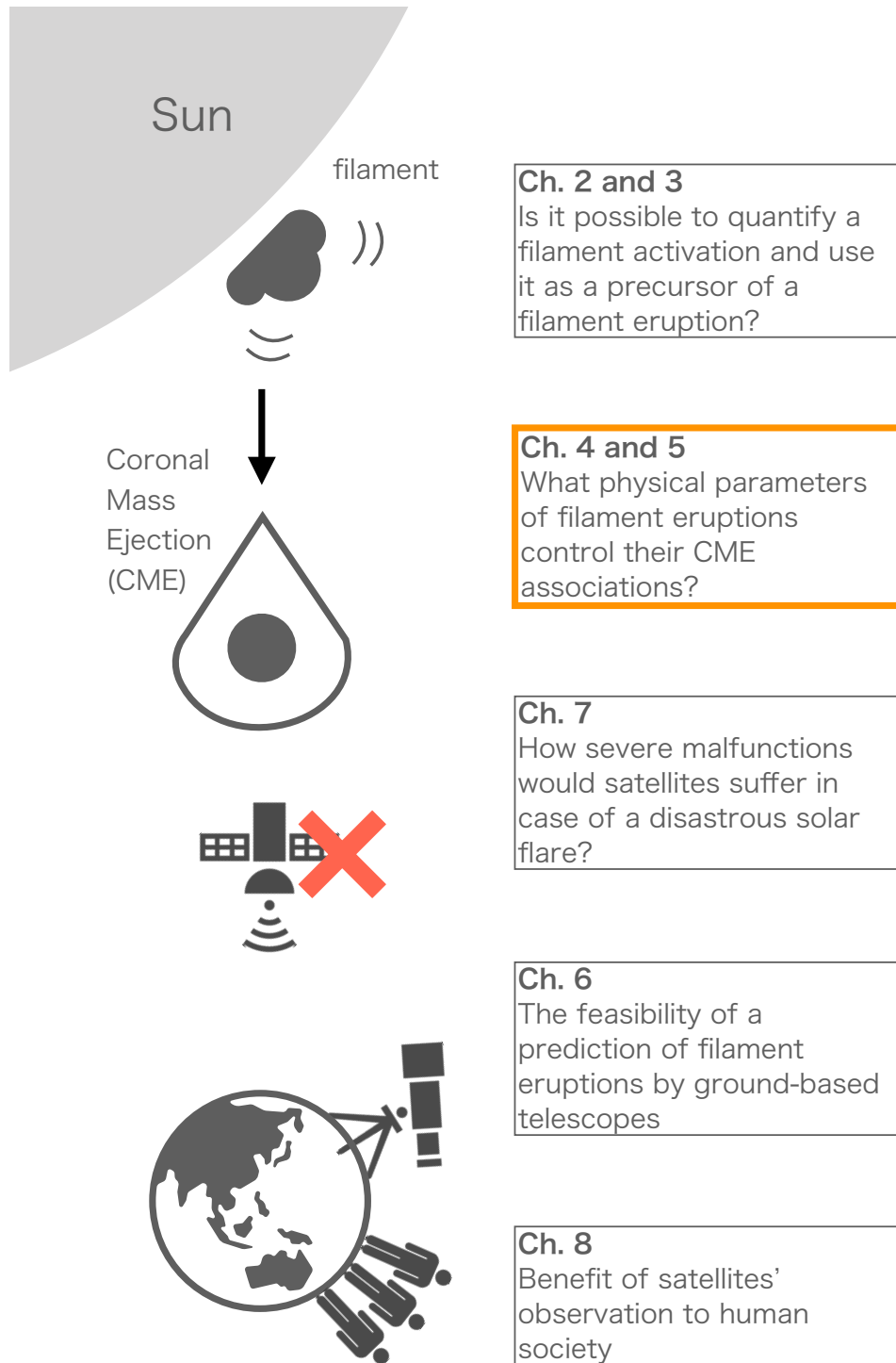by magnetic fields. They are observed in absorption as dark features on the solar disk in Hα (6562.8 Å) and in emission as prominences above the solar limb. At the end of its life, a filament disappears by slow fading or exhibits a transient eruption. Before it disappears or erupts, small-scale blobs observed in Hα in a filament often show a larger standard deviation of the line-of-sight (LOS) velocity [65, 66]. During eruption phase, the entire body of a filament ascends at a velocity of 100–1000 km s^{-1} [34].

Filament eruptions are often associated with coronal mass ejections (CMEs), which are observed by coronagraphs such as the Large Angle and Spectrometric Coronagraph (LASCO) [49]. Some CMEs exhibit a three-part structure [103] consisting of a leading edge, faint coronal cavity, and dense core. Others exhibit more complex forms, appearing as narrow jets or global eruptions, which are called halo CMEs [104]. The core of a CME is believed to originate from the filament mass if the CME is associated with a filament eruption. Because the Sun is concealed by an occulting disk in coronagraph observations of CMEs, it is difficult to observe the early evolution of CMEs. Investigations of the evolution of filament eruptions and their association with CMEs are expected to clarify the early evolution of CMEs.

CMEs often produce severe geomagnetic storms, which expose the Earth to a potential risk of adverse socioeconomic impacts such as a widespread blackout [8]. A CME associated with a polar crown filament eruption reportedly caused a severe geomagnetic disturbance (Dst ∼ −200 nT) three days after the eruption [77, 105]. Therefore, to mitigate the socioeconomic impacts of geomagnetic disturbances, it is essential to predict the occurrence of CMEs and their arrival to the Earth. And to reveal the relationship between CMEs and the eruption or disappearance of filaments is important for the better prediction.

However, the reported proportion of filament disappearances or eruptions that are associated with CMEs ranges from ∼10% to ∼90%. Hori & Culhane (2002) [106] studied 50 prominence eruptions observed at 17 GHz by the Nobeyama Radioheliograph [107] and found that 92% of them were associated with CMEs. Seki et al. (2019b) [108] investigated 43 filament disappearances in Hα data observed by the Solar Dynamics Doppler Imager (SDDI) [39] on the Solar Magnetic Activity Research Telescope (SMART) [109] at Hida Observatory, Kyoto University, and found that 50% of them were associated with CMEs. McCauley et al. (2015) [110] studied 904 filament and prominence eruptions observed in He II (304 Å) by the Atmospheric Imaging Assembly (AIA) [46] and found that 73% of them were associated with CMEs. In contrast, Al-Omari et al. (2010) [111] automatically classified 7332 filament/prominence eruptions reported by the National Centers for Environmental Information[†] as events associated or not associated with CMEs and found that

---

[†]ftp://ftp.ngdc.noaa.gov/STP/SOLAR_DATA/SOLAR_FILAMENTS/ accessed in 2008

only 17% of them were associated with CMEs. (For a more detailed summary of previous studies on the filament–CME association, see Table 1 in Al-Omari et al. (2010) [111]). It is supposed that the discrepancy among these results could depend on how to select the events.

In this study, we aim to reveal what parameters control the association between the filament eruptions and CMEs. We investigate the relationships between physical parameters that characterise filament eruptions, i.e., the length, velocity during eruption, and direction of eruption, and the CME association. Several studies have shown that these parameters are well correlated with the CME association of filament eruptions [61, 108, 112]. Gilbert at al. (2000) [112] studied 54 prominence eruptions observed above the limb in Hα. They defined "eruptive prominences" as those in which all or part of the material escaped from the solar gravitational field and "active prominences" as those in which none of the material appeared to escape. They found that eruptive prominences clearly had a larger apparent velocity (the velocity projected on the plane of the sky) above 1.10 solar radii than active prominences did and that eruptive prominences were more strongly associated with CMEs (94%) than active ones (46%). Our previous study [108] found that filament eruptions are more likely to be associated with CMEs if the filament length exceeds 150 Mm, the maximum radial velocity exceeds 140 km s^{-1}, or their direction is inclined by less than 48 deg with respect to the solar normal. Thus, in the present study, we focus on these three parameters of filament eruptions and investigate how the association rate varies with respect to them. Note that, in contrast to our previous work that we investigated the tendency of CME association with respect to individual physical parameters, the present study aims to improve the predictability of CME association by combining those parameters. In Section 5.1, we provide a description of the data we utilised. In the succeeding sections, the results will be provided, followed by summary and discussion.

5.1   Data and Methods

5.1.1   Data

We selected events from the SMART/SDDI Filament Disappearance Catalogue[‡] [108]. The unique advantage of the SDDI is its wide wavelength coverage, which makes it possible to determine the LOS velocity of erupting filaments up to 400 km s^{-1}. The Catalogue lists 43 filament/prominence disappearances observed by SDDI from 2016 May 1 to 2019 June 18, in which filaments/prominences totally disappeared at the Hα line centre. We selected 28 of these events that had a credibility value of 2 or 3 for CME association in

---

[‡]https://www.kwasan.kyoto-u.ac.jp/observation/event/sddi-catalogue/

the catalogue (description of "credibility" will be provided later). That is, we used only events whose CME association or non-association is fairly clear. Note that some of the events were excluded from our analysis, even though their credibility was 2 or 3, because (1) terrestrial clouds covered the target filaments, and it was impossible to estimate their precise LOS velocities (No.001, 007, 018, 021, 022, 035, and 043), or (2) the length of the target filament could not be measured due to the lack of observation (No.029). Most of the selected events (26 of 28) are filament eruptions, and two events (on May 24 and June 20 in 2016) are prominence eruptions observed on the solar limb. Hereafter, we refer to these 24 events simply as filament eruptions.

The credibility value indicates how credible the CME association of an event is. We made a movie containing solar full-disk images of each event in the Hα line centre or in 304Å and LASCO C2 running difference images. While watching each movie, we examined the directional and temporal association of each filament eruption with the CME and assigned a credibility value based on our judgement. The actual movies used for examination can be accessed at the catalogue webpage (click the credibility column). Our judgement is based on (1)ΔT, which is the difference between the time when a CME was first observed in LASCO and the time of total disappearance of the filament in Hα centre (same as FD_end_time in the catalogue), and (2)$\Delta\phi$, which is the difference between the position angle of the filament and the central position angle of the CME. Table 5.1 describes how we determined the credibility 2 or 3 of the CME association on the basis of ΔT and $\Delta\phi$. The credibility 1 was labeled to events which were difficult to determine one-to-one correspondence. More specifically, we labeled the credibility 1 (1) if two filaments disappeared within one hour, the difference between their $\Delta\phi$'s was within 15 deg, and they were diagnosed as being associated with the same CME, or (2) if there were flares located within 30 deg from the central position angle of the CME and within a few hours prior to CME occurrence. For example, the events No.002 and No.003 in the catalogue were categorised as the credibility of 1 because two filaments disappeared within one hour, and it was ambiguous which of these events was actually associated with one CME. Another example is No.012, in which a CME could be attributable to a C-class flare occurred in an active region rather than to the filament eruption of the interest, and thus we concluded the credibility of this event as 1.

Table 5.1: Criteria for determining the credibility of a CME association on the basis of ΔT and $\Delta \phi$. The units of ΔT and $\Delta \phi$ are hour and deg, respectively.

	$\Delta T < 2$	$2 < \Delta T < 6$	$6 < \Delta T < 9$	$9 < \Delta T$
$\Delta \phi < 30$	with CME credibility 3	with CME credibility 2	without CME credibility 2	without CME credibility 3
$30 < \Delta \phi < 70$	with CME credibility 2	with CME credibility 2	without CME credibility 2	without CME credibility 3
$70 < \Delta \phi < 100$	without CME credibility 2	without CME credibility 2	without CME credibility 2	without CME credibility 3
$100 < \Delta \phi$	without CME credibility 3	without CME credibility 3	without CME credibility 3	without CME credibility 3

Table 5.2 shows the selected 24 events with their CME associations and physical parameters.

Table 5.2: Filament eruptions used in this study. Data are taken from the SMART/SDDI Filament Disappearance Catalogue [108].

date & time (UT)	CME	Cred. [a]	V_{r_max} (km s^{-1})	V_{r_fin} (km s^{-1})	V_{pos} [b] (km s^{-1})	V_{max} (km s^{-1})	L (Mm)	Θ [c] (deg)
2016-05-24 01:00	Yes	3	134	36.4	134	175	137	11.8
2016-06-01 21:00	Yes	3	173	50.8	189	226	151	25.7
2016-06-20 05:30	Yes	3	215	41.3	223	224	63.6	16.6
2016-07-07 07:19	Yes	3	359	189	272	365	35.6	9.67
2016-07-19 05:30	No	3	30.8	−3.80	27.0	93.1	31.7	53.9
2016-07-20 01:00	Yes	3	122	−6.40	101	199	99.8	43.9
2016-08-09 23:30	Yes	3	149	51.3	130	155	449	15.0
2016-08-11 22:00	No	2	9.40	2.00	38.2	52.0	153	75.9
2016-08-13 02:30	No	3	34.8	−18.0	108	234	139	71.3
2016-08-19 02:00	No	2	3.60	2.20	18.1	22.3	341	78.5
2016-09-03 23:53	No	3	15.7	15.0	9.35	52.7	52.5	7.89
2016-09-09 21:51	No	3	51.6	25.8	22.3	154	41.7	35.2
2016-11-04 01:32	Yes	2	38.4	26.8	39.6	44.3	312	29.1
2016-11-05 01:24	Yes	3	121	109	67.0	123	112	7.26
2017-02-10 04:00	No	2	4.90	−1.40	11.5	14.2	154	64.9
2017-02-19 04:44	Yes	2	161	143	185	218	112	42.2
2017-03-05 01:30	No	3	68.1	40.9	74.4	81.0	42.7	32.7
2017-04-23 04:30	Yes	3	456	436	497	523	113	29.4
2017-04-23 03:05	No	3	18.9	−25.0	18.1	324	73.9	45.5
2017-04-23 23:08	Yes	3	80.3	36.5	110	112	293	44.4
2017-04-29 23:30	Yes	2	44.2	−10.6	151	154	271	73.0
2017-09-25 21:24	Yes	2	172	7.70	530	555	164	72.0
2017-12-07 02:15	No	3	2.30	−43.3	63.8	246	69.8	88.0
2018-04-03 02:30	No	3	82.7	−2.77	139	183	160	59.0
2018-04-20 05:00	No	2	0.100	−23.4	0.141	46.7	59.3	72.5
2018-07-16 06:00	No	3	40.0	−5.00	52.8	75.6	77.4	43.9
2018-07-31 03:00	No	3	3.70	3.30	0.412	13.5	99.6	26.1
2019-02-23 22:30	Yes	3	47.6	28.2	45.1	66.6	285	43.6

[a] The credibility of the association between a CME and a filament eruption. $3 > 2 > 1$. Events with a credibility of 1 are excluded from this study.
[b] The apparent velocity of a filament. It is defined as $\sqrt{V_x^2 + V_y^2}$, where V_x and V_y are the east–west and south–north velocities projected on the plane of the sky, respectively.
[c] The inclination angle of a filament eruption with respect to the solar normal.

'Date & time' is the start time of a filament eruption and is defined as the first observation of a dark feature in Hα − 0.5 Å. It is equivalent to 'FD_start_time' in the catalogue. 'CME' indicates whether a filament eruption is associated with a CME. V_{r_max}, V_{r_fin}, V_{pos}, and

V_{max} are determined as follows. We manually tracked and measured the position and LOS velocity of a blob at the apex of the filament that was present until its total disappearance in Hα. Then, we constructed its three-dimensional velocity as a function of time. V_{r_max} is the maximum radial (or ascending) velocity during the eruption, whilst V_{max} is the maximum magnitude of three-dimensional velocity. V_{pos} is equal to $\sqrt{V_x^2 + V_x^2}$, where V_x and V_y are the velocities of the filament in the east–west and south–north directions on the plane of the sky, at the time of V_{r_max}, respectively. V_{r_fin} is the radial velocity at the last observation of a filament in Hα. L is the length of a filament measured at the same time as 'date & time'. The projection effect is corrected according to the location of the filament on the solar disk. Θ is the inclination angle between the direction of the filament velocity at the time of V_{r_max} and the solar normal (see Figure B on the catalogue webpage). For further details of how these values were determined, see our previous paper [108].

5.1.2 Methods

We utilised Linear Support Vector Classification (LSVC), which is one of the popular machine-learning methods for classification, to estimate the CME association from the observation of filaments. Our goal is to obtain the coefficients of the solid lines in Figure 5.3, which successfully separate the events associated with CMEs from those without CMEs in accordance with the velocity and length of filaments. These lines can be expressed as

$$\boldsymbol{w}^T\boldsymbol{x} = w_0 + w_1 x_1 + w_2 x_2 = 0, \tag{5.1}$$

where $\boldsymbol{w} = (w_0, w_1, w_2)^T$ is a coefficient vector to be optimised, and $\boldsymbol{x} = (1, x_1, x_2)^T$ is a feature vector, which corresponds to the observation. In our case, x_1 is a common log of a normalised velocity (V_{r_max}, V_{max}, or V_{pos} divided by V_0), and x_2 is a common log of a normalised length (L divided by L_0).

We optimised $\boldsymbol{w}$ by minimising the loss, l, defined as

$$l = \frac{1}{2}\boldsymbol{w}^T\boldsymbol{w} + C\sum_{i=1}^{N}(\max(1 - y^i\boldsymbol{w}^T\boldsymbol{x}^i, 0))^2, \tag{5.2}$$

where i and N are the index and the number of our selected events, $y^i \in \{-1, 1\}$ is the label of the CME association for the event i (-1: without CME, 1: with CME), $\boldsymbol{x}^i = (1, x_1^i, x_2^i)^T$ is an actual observed values for the event i, and C is a constant (in our case, set to be 100). The first term in Equation (5.2) is a penalty term, which prevents the classifier from overfitting to the sample. As for the second term, intuitively, to minimise
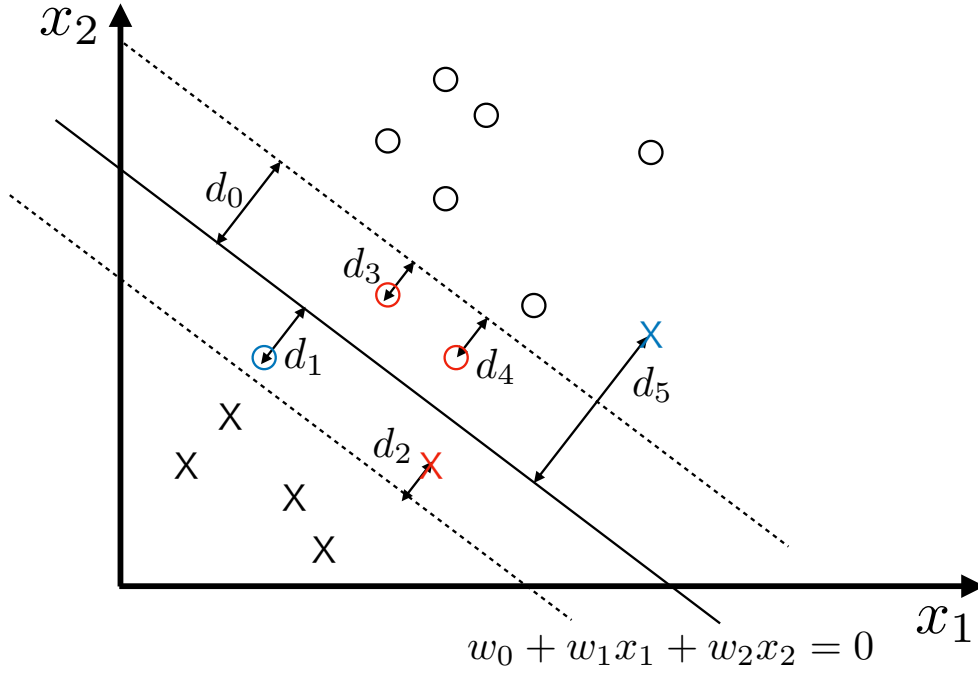
Figure 5.2: The schematic view of the meaning of the second term in equation 5.2.

it corresponds to (1) maximising the sum of the distances to the line from the correctly classified "near" data points and, simultaneously, (2) minimising the sum of the distances to the line from the misclassified data points.

Here, we describe the meaning of the second term in more detail. Figure 5.2 displays the schematic view of our analysis. Suppose that we aim to divide open circles and crosses according to two variables, x_1 and x_2. On the basis of the present $\boldsymbol{w}$, we can calculate d_0 defined as

$$d_0 = \frac{1}{\sqrt{w_1^2 + w_2^2}}, \tag{5.3}$$

and select the correctly classified "near" data points whose distances to the line are smaller than d_0, i.e., the correctly classified data points between the dashed lines in the figure (coloured in red). We also select the misclassified data points regardless of their distances to the line (coloured in blue). Then, Equation (5.2) should be written as

$$l = \frac{1}{2}\boldsymbol{w}^T\boldsymbol{w} + \frac{C}{d_0}\{(d_1 + d_5 + 2d_0) + (d_2 + d_3 + d_4)\}. \tag{5.4}$$

The first parenthesis in Equation (5.4) corresponds to the sum of the distances to the solid line from the misclassified events (and d_0 multiplied by the number of them). The second

parenthesis sums up the distances to the nearest dashed line from the correctly classified "near" data points. Finally, by solving the minimisation of l for $\boldsymbol{w}$, we obtained the well separable lines shown in Figure 5.3. For further details, see Fan et al. (2008) [113].

5.2 Results

Figure 5.3 displays the CME associations according to L (vertical axis) and V_{r_max} (top left), V_{max} (top right), or V_{pos} (bottom left) on a logarithmic scale. Here, the length and velocities are normalised by $L_0 = 100$ Mm and $V_0 = 100$ km s^{-1}, respectively. We can see the tendency that the longer and faster filaments are more likely to be associated with CMEs. The solid lines in the panels are drawn by the following relationships;

$$\left(\frac{V_{r\_max}}{V_0}\right) \times \left(\frac{L}{L_0}\right)^{0.96} = 0.80 \tag{5.5}$$

$$\left(\frac{V_{max}}{V_0}\right) \times \left(\frac{L}{L_0}\right)^{1.1} = 1.4 \tag{5.6}$$

$$\left(\frac{V_{pos}}{V_0}\right) \times \left(\frac{L}{L_0}\right)^{0.72} = 0.85 \tag{5.7}$$

They were determined by using the algorithm of Linear Support Vector Classification implemented in LIBLINEAR [113]. In the top left panel (V_{r_max}), 27 events out of 28 (96%) were correctly classified into the two groups of filament eruptions with (open circles) and without (crosses) CMEs, whilst in the other cases, 21 (for V_{max}) and 25 (V_{pos}) events were correctly separated. If we make a separation so that the number of correctly classified events can be maximised, 27 (V_{r_max}), 24 (V_{max}), and 26 (V_{pos}) events will be correctly classified (the separations not shown in the figure). Thus, a better prediction of the CME association could be obtained by using V_{r_max} rather than using V_{max} or V_{pos} at least with our limited number of the events, 28. This result suggests the advantage of measuring the radial velocity of filament eruptions. It also suggests that measuring both the velocity and the length of filaments should contribute to the better prediction of CME occurrence. The three-dimensional velocity observation provides a better capability for predicting the occurrence of CMEs, whilst the Hα imaging observations without Doppler measurements (V_{pos}) can still contribute to it.

Figure 5.4 displays histograms of events with (grey) and without (black) CMEs with respect to the left-hand sides (LHS) of Equation (5.5)–(5.7). These histograms also demonstrate that the CME association is better identified when V_{r_max} is used than when V_{max} or V_{pos} is used. In the top left panel, we see a clear bimodal distribution, which is less clear in the other cases. To confirm the bimodality quantitatively, we introduced a statistic,
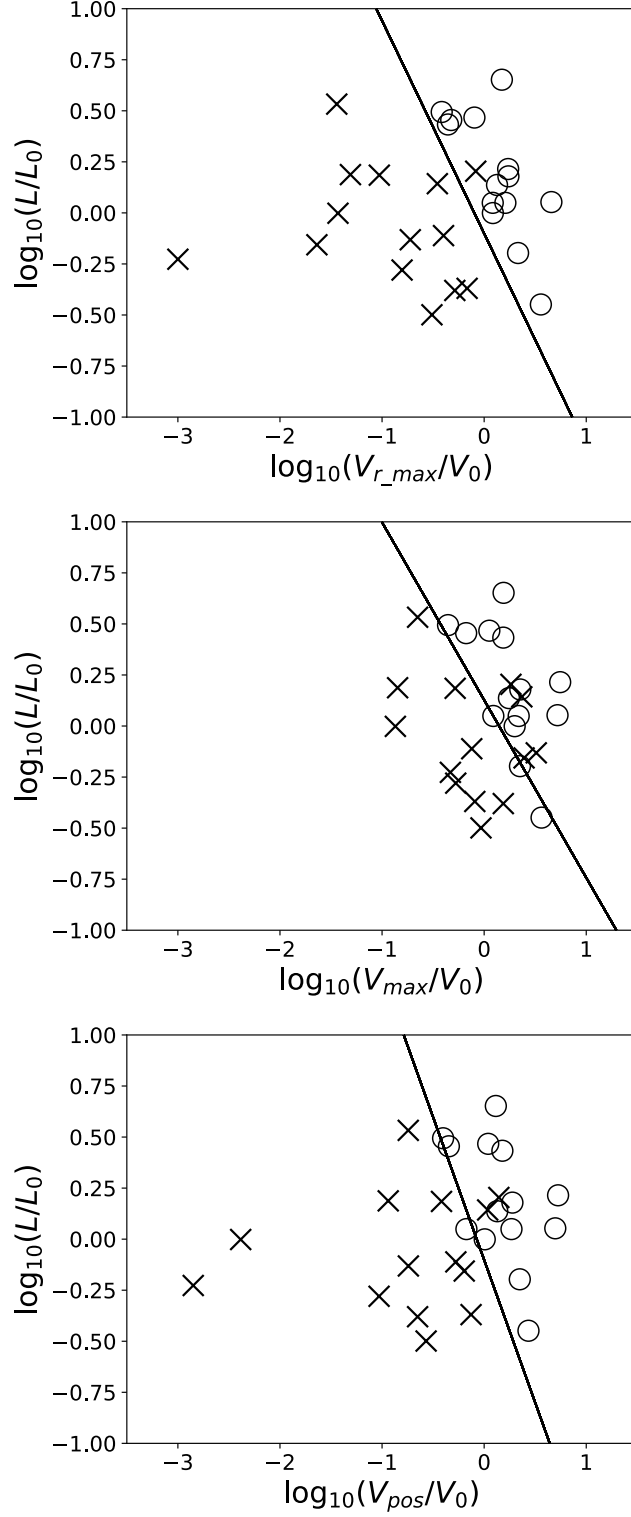
Figure 5.3: Plots of filament eruptions according to V_{r_max} (top left), V_{max} (top right), or V_{pos} (bottom left) and filament length, L, on a common logarithmic scale. V_0 and L_0 correspond to the typical velocity (100 km s^{-1}) and typical length (100 Mm) of filaments, respectively. Open circles and crosses represent events with and without CMEs, respectively. The solid line is described in the text.

97
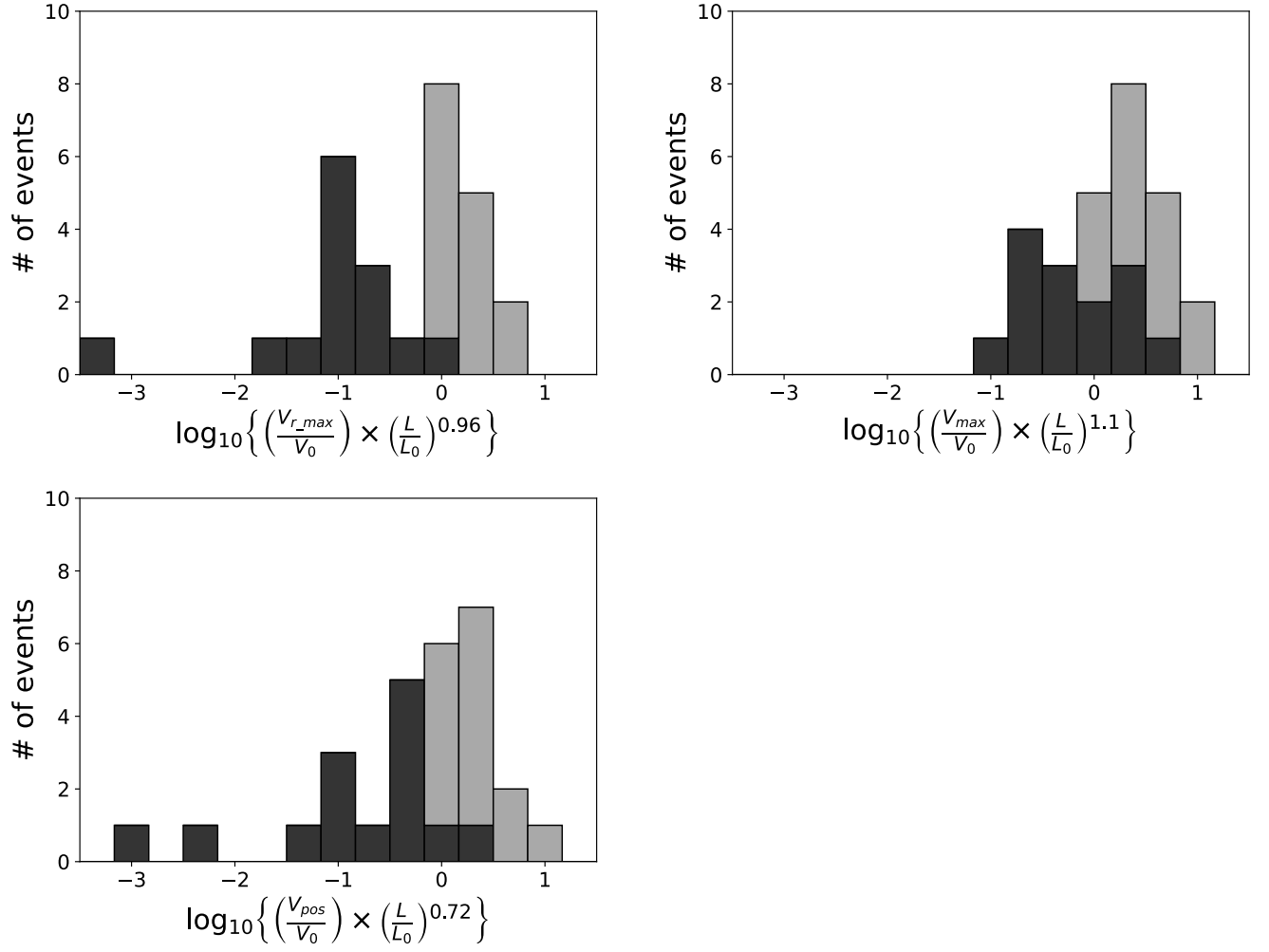
Figure 5.4: Histograms of the LHS of Equation (5.5)–(5.7) on a common logarithmic scale. The dark and light grey bars correspond to the events without and with CMEs, respectively. The bars are stacked. The size of a bin is 0.33

D-value, which is defined as

$$D \equiv \frac{|\mu_1 - \mu_2|}{\sigma}, \tag{5.8}$$

where μ_1 and μ_2 are the averages of the two normal distributions fitted to the events with and without CMEs, and σ is equivalent to

$$\sigma = \sqrt{\frac{\sigma_1^2 + \sigma_2^2}{2}}, \tag{5.9}$$

where σ_1 and σ_2 are their standard deviations. The D-value represents the distance between the means of two normal distributions relative to their standard deviations. These distributions can be regarded as being separated if the D-value is larger than 2 [114–116]. The means and standard deviations of two normal distributions (with and without CMEs) for each case of Equation (5.5)–(5.7) are summarised in Table 5.3 together with the D-values. We obtained D values of 2.3, 1.8, and 1.7 for V_{r_max}, V_{max}, and V_{pos}, respectively. Only V_{r_max} exhibits the D-value larger than 2. The better bimodality when V_{r_max} is used is confirmed quantitatively.

Table 5.3: Summary statistics of the fitted normal distributions and the corresponding D values.

| | with CMEs | | without CMEs | | |
	μ_1	σ_1	μ_2	σ_2	D
V_{r_max} (Eq. (5.5))	0.28	0.23	-1.0	0.76	2.3
V_{max} (Eq. (5.6))	0.46	0.28	-0.20	0.44	1.8
V_{pos} (Eq. (5.7))	0.29	0.29	-0.81	0.88	1.7

Figure 5.5 shows the CME association with respect to the radial velocity of the last observation (V_{r_fin}) and L (left panel) or a common log of the LHS of Equation (5.5) (right panel) for each filament eruption. Open circles and crosses denote events with and without CMEs, respectively. Most of the filament eruptions (80%) with negative V_{r_fin} (grey area), i.e., events in which the filaments fall back to the Sun, were not associated with CMEs. In addition, 77% of the filament eruptions with positive V_{r_fin} and L larger than 70 Mm were associated with CMEs. Note that the filaments with the smaller (larger) value of the LHS of Equation (5.5) similarly tend to have smaller (larger) V_{r_fin} (see the right panel).

From Figure 5.5, we can also recognise that there are exceptional events that were associated with CMEs despite their negative V_{r_fin}'s (-6.40 km s^{-1} and -10.6 km s^{-1}).
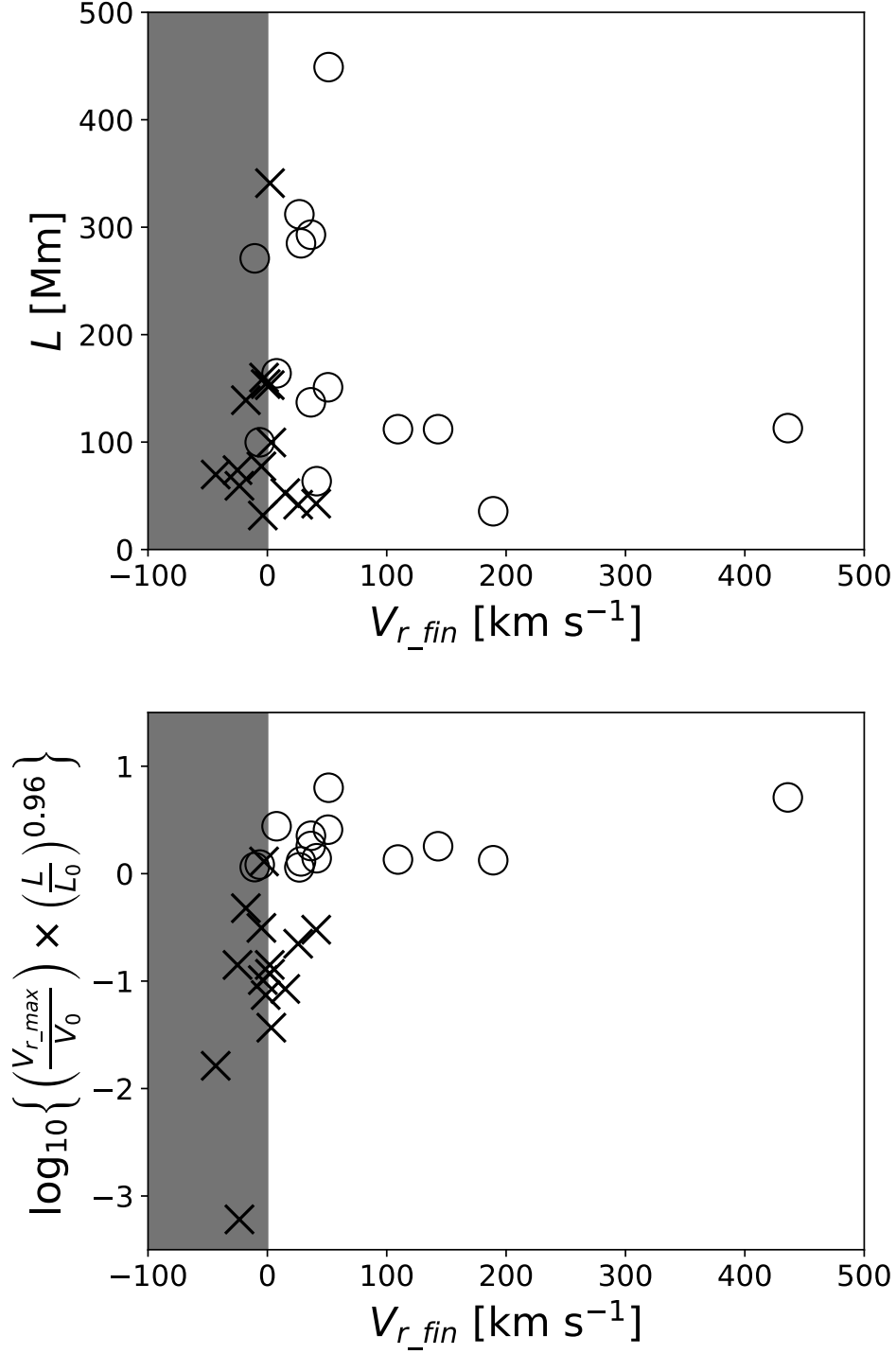
Figure 5.5: Plot of filament eruptions according to V_{r_fin} and filament length (left) or common log of the product of normalised V_{r_max} and normalised L to the power of 0.92 (right). Open circles and crosses have the same meaning as in Figure 5.3. Grey area corresponds to negative V_{r_fin}.
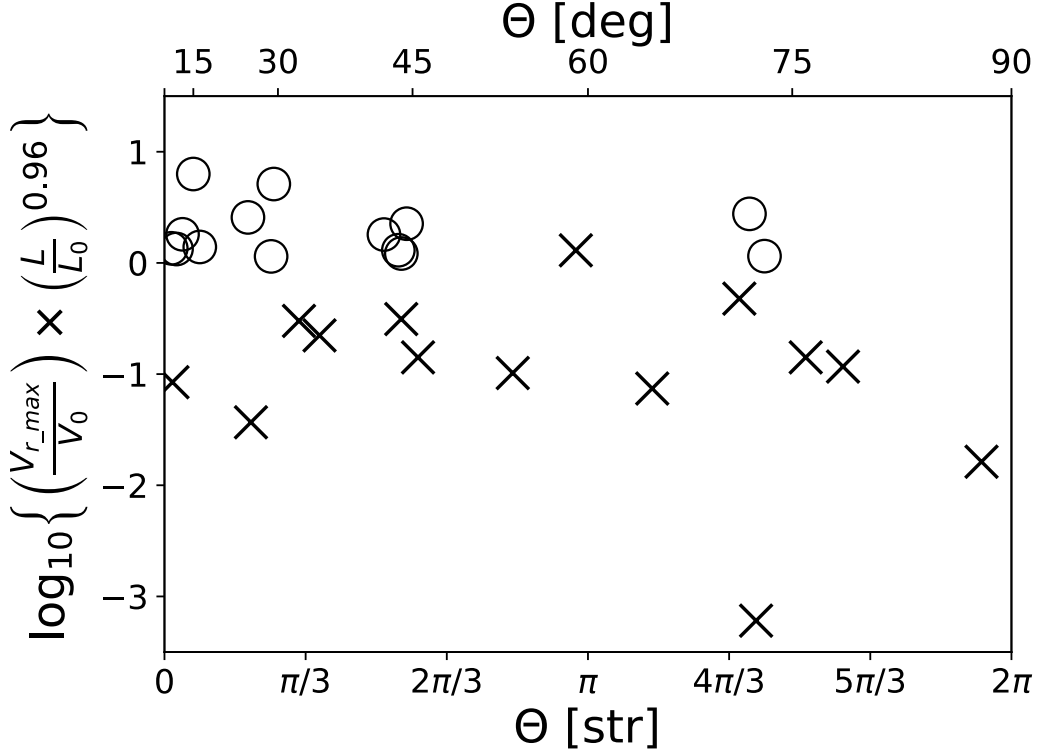
Figure 5.6: Plot of filament eruptions according to Θ (inclination angle in steradians and degrees) and a common log of the LHS of Equation (5.5). The symbols have the same meaning as in Figure 5.3.

We speculate that the blobs which escaped the solar gravity and erupted into the interplanetary space became invisible in Hα, and we tracked a part of the filament that fell back to the solar surface.

Figure 5.6 shows the CME association according to the LHS of Equation (5.5) (vertical axis) and Θ, the inclination angle (angle from the solar normal) of the velocities (horizontal axis). We found that 82% of the filament eruptions with directions that were inclined by more than 45 deg from the solar normal were not associated with CMEs, and 71% of those with their Θ's smaller than 45 deg were associated with CMEs. Thus, the inclination angle of eruptions will provide a clue for forecasting the CME occurrence. Note that the LHS of Equation (5.5) of the filament eruptions with their Θ's larger than 45 deg seldom exceeds −0.097 (= log10(0.80)). Figure 5.6 also shows that 86% of the events associated with CMEs have their Θ's smaller than 45 deg, while only 36% of the non-associated ones have Θ smaller than 45 deg. These results are consistent with the work of Gopalswamy et al. (2003) [101], in which they defined two types of prominence eruptions, radial and transverse events, according to the eruptive motion of the prominence observed on the solar limb. In their statistical study, they found that 94% of the prominence eruptions associated with CMEs were radial events (86% in our study) and that 76% of
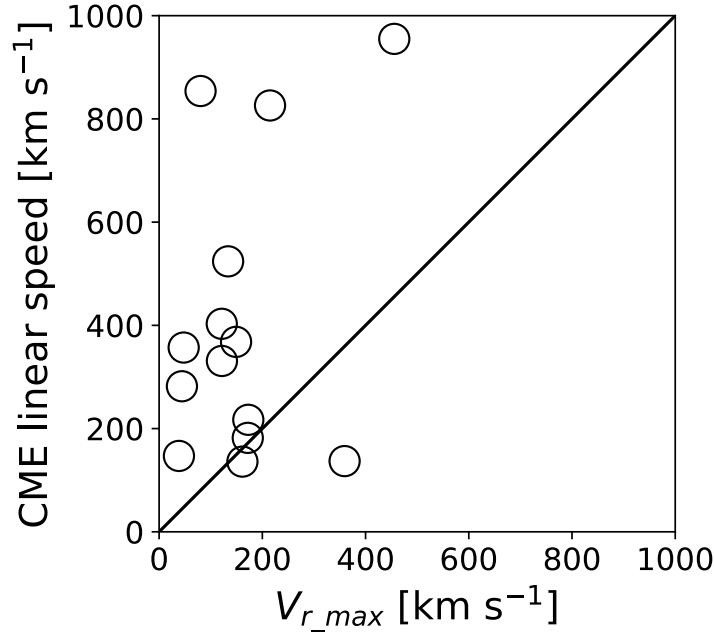
Figure 5.7: Plot of filament eruptions according to V_{r_max} and CME linear speed. The black line corresponds to equal speeds.

the transverse events were not associated with CMEs (82% in our study).

Figure 5.7 shows the linear speed of the CMEs in the SOHO/LASCO CME Catalog [86] against V_{r_max}. The CME speed is expected to be larger than the velocity of the associated filament eruption [101]. The black line indicates equal speeds. All the data points but one ($V_{r\_max} = 359$ km s^{-1}) are above or close to the black line, as expected. However, since there is a large scatter in the ratio of CME linear speed to V_{r_max}, it is difficult to predict CME linear speeds from the maximum radial velocity.

5.3 Summary and Discussion

In this study, we investigated the relationships between the physical parameters of filament eruptions (three-dimensional velocity, filament length, and direction of eruption) and their CME associations using 28 events observed by SDDI at Hida Observatory. We found that the filament eruptions are well separated into two groups of events, one with and the other without CMEs, according to the product of the normalised maximum ascending velocity (V_{r_max}/V_0) and the normalised filament length (L/L_0) to the power of 0.96, and that among the filament eruptions with $\left(\frac{V_{r\_max}}{V_0}\right) \times \left(\frac{L}{L_0}\right)^{0.96} > 0.80$, 93% are associated with CMEs, and 100% of filament eruptions with the product < 0.80 are not associated with

CMEs. The apparent velocity and the length of filaments measured in Hα observation could also provide a good measure for predicting the occurrence of CMEs, though the accuracy of the prediction using the apparent velocity is worse than that using the radial velocity. Our results suggest that the three-dimensional velocity, or more specifically the radial velocity derived from it, and the length of the erupting filament are the notable parameters for improving the predictability of CME association. And thus, we suggests the importance of observations of the three-dimensional velocity of filament eruptions for the prediction of CMEs. It should be noted, however, that improvement of statistics, i.e., studies with a larger number of examples, are strongly required to confirm these results.

Here, we propose a possible physical interpretation for the solid line in the top left panel of Figure 5.3. This line, which is represented by Equation (5.5), successfully separates events into those with and without CMEs. We assume that (1) the cross section of filaments, A, follows the relationship of

$$\left(\frac{A}{A_0}\right) = \left(\frac{L}{L_0}\right),\tag{5.10}$$

where A_0 is the typical cross section of filaments (100 Mm^2), and that (2) the average hydrogen density is common among filaments, i.e., 10^{11} cm^{-3}, which is a typical value for quiescent prominences [117]. Then, if we regard Equation (5.5) as

$$\left(\frac{V_{r\_max}}{V_0}\right) \times \left(\frac{L}{L_0}\right) \sim 0.80,\tag{5.11}$$

its square represents the kinetic energy of an erupting filament, i.e., $\frac{1}{2} \times$ proton mass $\times$ density $\times$ volume $\times$ Vr_max$^2 = 5.4 \times 10^{28}$ erg. This relationship could be regarded as the kinetic-energy threshold above which filament eruptions are associated with CMEs. Note that if the length of a filament is 100 Mm, the deduced mass gets 1.7×10^{15} g. Gilbert et al. (2006) [118] reported the masses of 18 prominences, which ranged from $(1.08 \pm 0.52) \times 10^{14}$ to $(2.09 \pm 0.80) \times 10^{15}$ g. Our assumed "typical" mass is consistent with the reported values.

As mentioned in Section 1, the CME association rates of filament eruptions reported to date range from ∼10% to ∼90%. Here, we provide a possible interpretation of this wide range based on our results. We showed that the product of the normalised radial velocity of eruptions and the normalised filament length makes a key contribution to the CME association. The high association rates of 80%–90% in the past studies might be attributable to the criteria they used to select the events, under which the prominences have a predominantly large radial velocity and a large size. Gilbert et al. (2000) [112] reported that 94% of eruptive prominences (for the definition, see Section 1) were associated

with CMEs. Gopalswamy et al. (2003) [101] also reported that 83% of radial prominence eruptions were associated with CMEs. Their selected prominence eruptions should have had a predominant radial velocity. Gopalswamy et al. (2003) [101] and Hori & Culhane (2002) [106] detected prominences with the NoRH that have its spatial resolution of 10 arcsec [107], which is worse than the spatial sampling of the SDDI (1.23 arcsec pixel^{-1}). Therefore, the selected prominences in these studies seem to have a larger size (e.g., larger than 70 Mm, because 75% of the filaments smaller than 70 Mm were not associated with CMEs).

The association rate could also depend on whether studies include disk events (filament disappearances) in the records. In contrast to the high association rates (80 to 90%) reported in the studies taking into account only limb events (prominence disappearances) [101, 106, 112], some studies [108, 119, 120] in which both disk and limb events were considered manifested the association rate of approximately 40–50%. Pojoga & Huang (2003) [119] reported that 39% of filament and prominence eruptions observed in Hα were associated with CMEs. Jing et al. (2004) [120] reported that 56% of filament eruptions were associated with CMEs by automatically detecting filament disappearances in Hα. In our study, considering only credible events, we found that 50% of filament eruptions in Hα were associated with CMEs.

Additionally, the observational wavelengths at which filaments or prominences are detected could also affect the association rate. In Hα, as mentioned in the previous paragraph, approximately 40 to 50% of disappearance events were associated with CMEs. By contrast, McCauley et al. (2015) [110] used full-disk solar images in the 171, 193, and 304 Å AIA passbands and reported an association rate of 72%.

The low association rate (17%, Al-Omari et al. (2010) [111]) might be attributable to the fact that the authors include ejecta such as surges in addition to filament eruptions in their sample. Among their 7332 events, they introduced 15 "filament types", including coronal rain, sprays, and surges. In our study, we did not refer to these ejecta as filaments, and we excluded them from our list. Thus, the definition of filaments in that study was different from ours. Moreover, most of their events ($\sim$80%) were smaller than $\sim$70 Mm (see Figure 8 in [111]). According to our result (see Figure 5.3 or 5.5), 75% of the eruptions of filaments with lengths smaller than 70 Mm were not associated with CMEs. Assuming that this relation holds for coronal rain, surges, and sprays, $\sim$60% (80% $\times$ 75%) of all their selected events may not be associated with CMEs in our criteria. Therefore, the low association rate in their study can also be attributed to the event selection criteria; i.e., a significant portion of their events is thought to be located below the threshold line proposed in this paper.

The results of this study can be used to develop a methodology to predict the oc-

currence of CMEs by measuring the three-dimensional velocities of filament eruptions. Moreover, our previous works suggest that the occurrence of filament eruptions can be predicted prior to their initiation by 1.3 ± 0.47 h for intermediate filaments and 28 ± 3.5 h for quiescent filaments, on the basis of the standard deviation of the LOS velocity distribution in filaments [65, 66]. Hence, by using SDDI data and measuring the LOS velocity of filaments, we could predict the occurrence of filament eruptions ∼1 to ∼10 h in advance and also, during eruptions, estimate the possibility of CME association before coronagraph observations.

Chapter 6

Continuous H-Alpha Imaging Network (CHAIN) Project

In this Chapter*, we show the importance of the prediction of solar eruptions based on the ground-based telescopes and presented its feasibility by introducing the Continuous H-Alpha Imaging Network (CHAIN) project, which aims to create a world-wide observational network with ground-based solar telescopes observing in multiple wavelengths, including Hα line centre, red wing, and blue wing for 24-hour continuous observation of the three-dimensional velocity fields of filament eruptions.

Space weather is the disturbances in the interplanetary plasma and magnetic fields mainly caused by the solar activity. It is known that space weather has potential risks to damage human technologies in forms of satellite anomalies, satellite air drag, single events, radiation exposure, and huge blackout [121]. As a global navigation satellite system like GPS is now one of the essential social infrastructures, human beings will be getting more and more dependent on space technology in future. Therefore, in order to mitigate and prevent space weather disaster, it is highly significant to predict when and how large space weather events will happen.

Currently, space weather prediction is mainly done by using space-borne instruments such as the Atmospheric Imaging Assembly [46] and the Helioseismic and Magnetic Imager [47] on the Solar Dynamics Observatory [98], the Large Angle Spectroscopic Coronagraph [49] on the Solar and Heliospheric Observatory [97], and Geostationary Operational Environmental Satellite (GOES) series. There are basically two advantages to use space-borne data compared to ground-based telescopes' data. One is that they can see the sun in soft and hard X-ray and extreme ultraviolet in which we can never observe from the ground due to the air and which are essential to see the magnetic fields, giving us essen-
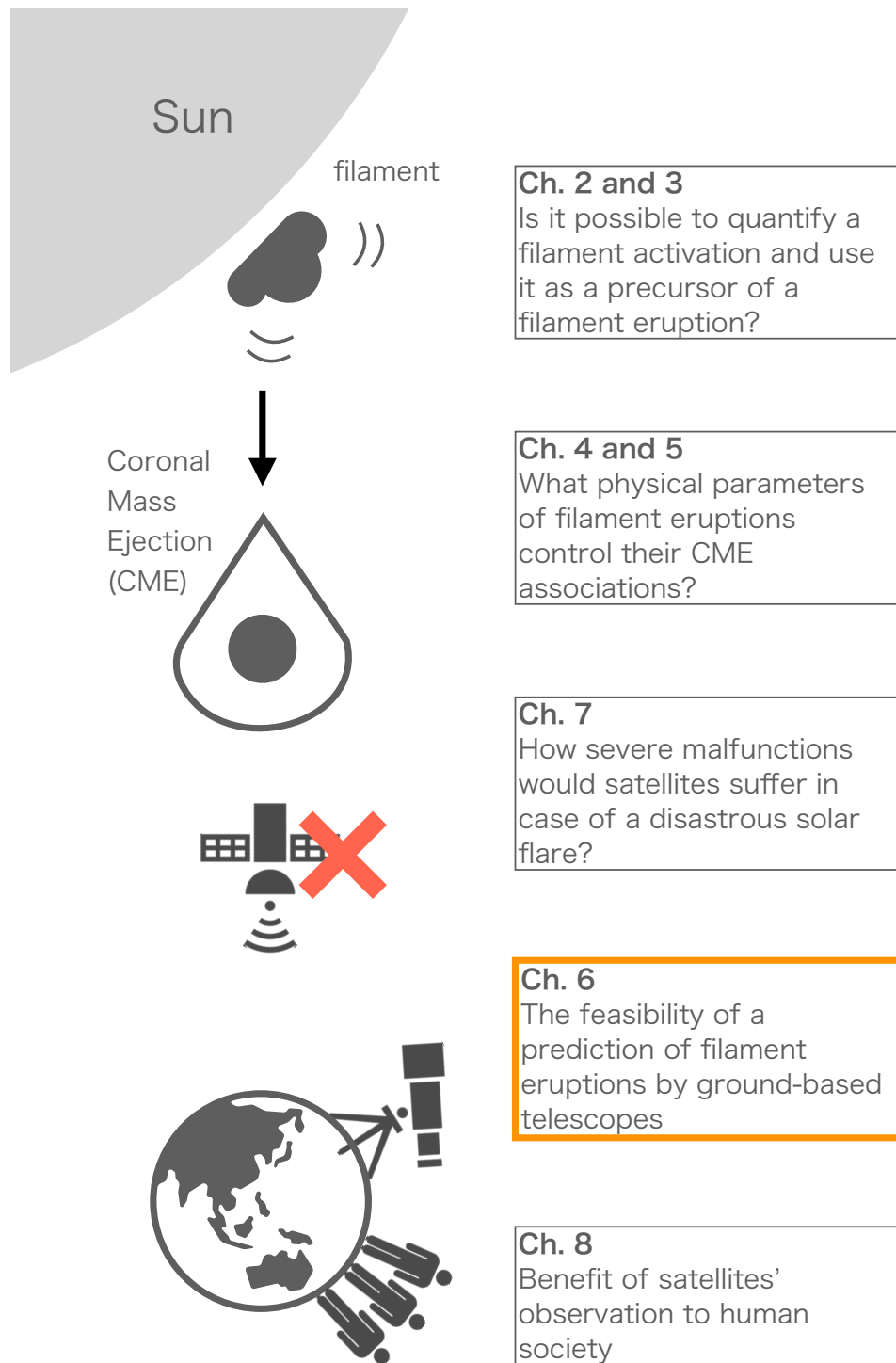

Figure 6.1: The graphical abstract of this dissertation (the orange rectangle corresponds to this Chapter).

tial information to predict solar flares. The other is that they can continue observation regardless of time and terrestrial weather.

However, it does not mean that the ground-based telescopes are no longer useful in terms of space weather prediction. Firstly, compared to the satellites, the ground-based telescopes are cheap, and developing countries can also introduce the instruments. Secondly, the ground-based telescopes do not have any effects of space weather, while artificial satellites could be damaged by severe space weather events. Therefore, ground-based telescopes can be used as backup, and even if a satellite observing in Hα and its wings should launch, they would still have some complementary roles in case of satellites' failure by a huge solar flare.

In this Chapter, we present the possibility of space weather prediction, especially of predicting solar explosive phenomena, by the ground-based telescopes, with reference to the recent progress of the Continuous H-Alpha Imaging Network (CHAIN) project [90] worked by Kyoto University. In the first section, we will give a method of prediction with reference to the recent suggestion in Seki et al. (2017) [65], and in the second section, from a hardware point of view the recent progress of CHAIN will be reported. And three challenges we are facing will be mentioned in the last section.

6.1 Prediction by Hα Image

At Hida Observatory in Kyoto University, there is a powerful instrument observing the sun in Hα line centre and its wings called Solar Dynamics Doppler Imager (SDDI) installed on Solar Magnetic Activity Research Telescope (SMART) [39].

6.1.1 Prediction of a Filament Eruption by Hα Images

SDDI has been conducting a routine observation since 2016 May 1. It takes the solar full-disk images of 73 channels at every 0.25 Åfrom the Hα line centre -9.0 Åto the Hα line centre $+9.0$ Å, i.e., at 36 positions in the blue wing, the Hα line centre, and 36 positions in the Hα red wing. Its time cadence is 15 sec, and the spatial sampling is 1.23 arcsec pix^{-1} [39]. When the weather permits, it continuously monitors the Sun during the daytime in Japan for approximately 10 h.

Making the most of the small gap between channels of 0.25 Åand the good time cadence of 15 sec, Seki et al. (2017) [65] deduced automatically the unprecedented detailed line-of-sight velocities of the filament which erupted around 4:00UT on 2016 November 5th by utilising Beckers' cloud model [59–61] (See Chapter 2). As a result, by tracking the standard deviation of line-of-sight velocities for each velocity map, we found that it

increased sharply around 1 hour before eruption. Figure 2.11 shows the time transition of the standard deviation. On the previous day of the eruption, the standard deviation was almost constant around 2–3 km s^{-1}. However, on the next day (the day of the eruption) it slightly increases to 3–4 km s^{-1} and stays constant until around 0:30 UT. Then it gradually increases at a rate of 1.1 m s^{-2} until it peaks around 1:10 UT, and it starts to increase again sharply at a rate of 2.8 m s^{-2} around 2:30 UT, which corresponds to around 1 hour before eruption. In this case, accompanied by a filament eruption, B-class flare started around 4:00 UT and the X-ray flux peaked around 4:40 UT, and also weak CME occurred. Therefore, this work suggests that if we track the standard deviation of the line-of-sight velocities of a filament, we may be able to predict solar explosive phenomena around 1 hour before it happens only by using ground-based telescopes' data.

From the operational point of view, it should be noted that in 2017 September we started the automatic detection and calculation of line-of-sight velocity of a filament during the observation every day. The deduced data has been stored at Hida Observatory and everyone can access it via its web site `http://www.hida.kyoto-u.ac.jp/SMART/SDDI/cloudmodel/`. Combining this system and the result of Seki et al. (2017), it could be possible to monitor filaments during observation and to create an automatic alerting system of filament eruptions.

6.1.2 CHAIN project

Introduction to CHAIN

We have been working Continuous H-Alpha Imaging Network (CHAIN) project, which is to create a world-wide observational network with ground-based solar telescopes observing in multiple wavelengths including Hα line centre, red wing and blue wing. Its purpose is to conduct 24-hour continuous observation of the three-dimensional-velocity fields of filament eruptions and the shock-wave structures on the whole solar surface (See No.6 of List of ISWI Projects at `http://www.iswi-secretariat.org`) [102]. Unlike other Hα networks such as the Global Oscillation Network Group (GONG) [48] and the Global H-alpha Network (GHN) [122], the strength of this observational network is to observe the Sun in not only Hα centre but also its red and blue wings.

There are 3 purposes for this project;

1. reinforcement of observations of the solar activity by formation of an international network of ground-based solar observations for 24 hours continuously,

2. observation and study of filament eruptions, shock waves (Moreton waves) with solar flares and variation of UV radiation on the full-disk of the Sun in order to

understand and predict the change of space-weather environment from the Sun to the Earth,

3. international spread, academic exchange and promotion of the space-weather research including developing countries.

From the space weather point of view, there are 2 important aspects of CHAIN project, (1) constructing ground-based 24-hour space weather prediction system by creating an international solar observational network with ground-based telescopes and (2) capacity building including technical and scientific training and space weather education through installing and operating the ground-based solar telescopes.

Outcomes of CHAIN

As the outcomes of CHAIN until 2017, 3 countries including Japan, Peru, and Saudi Arabia have been cooperating, and 17 papers related to CHAIN have been published (see Table 6.1 and 6.2). The contents of 7 papers are related to CHAIN project itself. The brief summaries of the contents are as follows;

- UeNo et al. (2007) [90]: It is the first paper related to CHAIN, and they explained about the project and their plan.

- Ishitsuka et al. (2007) [123]: They introduced their plan to refurbish solar observing stations in Peru and mentioned about installing FMT from Kyoto University in that context.

- UeNo et al. (2009) [124]: This paper published in Data Science Journal is explaining about data archive and observing system of CHAIN, and they claimed the necessity of improving the information technology.

- UeNo et al. (2010) [125]: With the introduction of CHAIN project, they mentioned that Algeria is one of the best candidates of this project and explained their plan of investigation.

- Seghouani (2010) [126]: He claimed the necessity of a new astronomical observatory in Algeria and mentioned about Dr. UeNo's visit and investigation.

- Ishitsuka et al. (2014) [127]: They showed the summaries of capacity building, observed data, and scientific results brought by the FMT installed in Peru as part of CHAIN project.

- UeNo et al. (2014) [102]: They showed the progresses about international collaboration and academic exchange of CHAIN from 2010 to 2013.

111

In the other 10 papers, CHAIN data are used for their scientific researches (see Table 6.1 and 6.2). Brief explanations are shown below;

- Nagashima et al. (2007) [128]: They used SMART Hα data to investigate the position and the active motion of 2 filaments.

- Narukage et al. (2008) [129]: SMART data were used to discover 3 Moreton waves on 2005 August 3.

- Asai et al. (2009) [130]: SMART data were used to show the temporal evolution of the AR NOAA 10798 in Hα.

- Zhang et al. (2011) [131]: FMT multi-wavelengths data were used to study the statistical properties of propagating Moreton waves.

- Asai et al. (2012) [132]: SMART data were used to detect a Moreton wave on 2011 August 9 and associated filament/prominence oscillations.

- Ishii et al. (2013) [133]: A new high-speed imaging system for solar flares installed on SMART was introduced.

- Shen et al. (2014) [134]: SMART data were used to calculate the Doppler velocity of a filament to investigate its oscillation property.

- Ichimoto et al. (2017) [39]: A new Hα and its wings imaging instrument, the Solar Dynamics Doppler Imager, was introduced.

- Cabezas et al. (2017) [63]: FMT data obtained at the National University San Luis Gonzaga of Ica, Peru, were used to derive the 3-dimensional velocity field of a filament eruption associated with a M-class flare on 2011 February 16.

- Seki et al. (2017) [65]: SMART/SDDI data were used for analysing the amplitude of the small-scale motion of the filament which erupted on 2016 November 5.

As for the capacity building, 7 lectures, 4 scientific educations, 2 technical trainings, and 5 data-analysis workshops have been held (see Table 6.3) for these 10 years.

6.2 Challenges for this Trial

One of the weak points of the ground-based telescopes is the influence of terrestrial weather and climate. As for CHAIN in the current situation, if one of the institutions cannot observe the sun, there is no other observatory that can compliment the data. Moreover,

Table 6.1: Published papers from 2007 to 2017

Year	Title	Authors	Journal
2007	CHAIN-Project and Installation of the Flare Monitoring Telescopes in Developing Countries	UeNo, S., Shibata, K., Kimura, G. et al.	Bulletin of the Astronomical Society of India, 35, 697.
2007	Triggering Mechanism for the Filament Eruption on 2005 September 13 in NOAA Active Region 10808	Nagashima, K., Isobe, H., Yokoyama, T. et al.	Astrophysical Journal, 668, 533.
2007	A Solar Observing Station for Education and Research in Peru	Ishitsuka, J., Ishitsuka, M., Avilés H. T. et al.	Bulletin of the Astronomical Society of India, 35, 709.
2008	Three Successive and Interacting Shock Waves Generated by a Solar Flare	Narukage, N., Ishii, T. T., Nagata, S. et al.	Astrophysical Journal, 684, L45
2009	The CHAIN-Project and Installation of Flare Monitoring Telescopes in Developing Countries	UeNo, S., Shibata, K., Kitai, R. et al.	Data Science Journal, 8, 30
2009	Evolution of Anemone AR NOAA 10798 and the Related Geo-Effective Flares and CMEs	Asai, A., Shibata,K., Ishii, T. T. et al.	Journal of Geophysical Research, 114, A00A21
2010	Continuous Hα Imaging Network Project (CHAIN) with Ground-based Solar Telescopes for Space Weather Research	UeNo, S., Shibata, K., Ichimoto, K. et al.	African Skies, 14, 17
2010	Un Observatoire dans la Région de Aurès	Seghouani, N.	African Skies, 14, 44
2011	Propagation of Moreton Waves	Zhang, Y., Kitai, R., Narukage, N. et al.	Publications of the Astronomical Society of Japan, 63, 685
2012	First Simultaneous Observation of an Hα Moreton Wave, EUV Wave, and Filament/Prominence Oscillations	Asai, A., Ishii, T. T., Isobe, H. et al.	Astrophysical Journal, 745, L18
2013	High-Speed Imaging System for Solar-FlareResearch at Hida Observatory	Ishii, T. T., Kawate, T., Nakatani, Y. et al.	Publications of the Astronomical Society of Japan, 65, 39
2014	Within the International Collaboration CHAIN: a Summary of Events Observed with Flare Monitoring Telescope (FMT) in Peru	Ishitsuka, J., Asai, A., Morita, S. et al.	Sun and Geosphere, 9, 85
2014	International Collaboration and Academic Exchange of the CHAIN Project in this Three Years (ISWI Period)	UeNo, S., Shibata, K., Morita, S. et al.	Sun and Geosphere, 9, 97

FMT in Saudi Arabia has another effect from its nature. Because of its high air temperature, it reaches approximately 50 degrees Celsius in the observation dome in the noon on summer. It is not expected for the filter installed on the telescope to become over 45 degrees Celsius so that it makes errors in observing wavelengths.

Another challenge to realise fully ground-based space weather prediction in case of CHAIN is accessibility of data. Internet speed is significantly slow, and approximately it takes more than 10 h to collect the observation data for one day. Because of slow data-sending speed by internet, we have been gathering the data from Saudi Arabia and Peru and storing them at Japan by manually carrying Hard Disk Drives.

The last challenge is the applicability of the new prediction method presented by Seki et al. (2017) [65] to FMT data. To use CHAIN as the data source of the prediction, we should confirm whether FMT data can be used for the prediction method, because the less amount of observing wavelengths leads to the less accurate estimation of line-of-sight velocities. SDDI has been observing at every 0.25 Å from Hα line $-$ 9.0 Å to Hα line $+$ 9.0 Å every 15 sec, while FMTs have been observing at 3 or 5 wavelengths, Hα line centre and Hα line $\pm$ 0.8 Å in Peru, or Hα line centre, Hα line $\pm$ 0.6 Å, and Hα line $\pm$ 1.2 Å in Saudi Arabia, in every 20 sec. Therefore, it should be checked whether the suggested precursor can also be detected from FMT data or not.

Table 6.2: Published papers from 2007 to 2017 (continued)

Year	Title	Authors	Journal
2014	A Chain of Winking (Oscillating) Filaments Triggered by an Invisible Etreme-ultraviolet Wave	Shen, Y., Ichimoto, K., Otsuji, K. et al.	Astrophysical Journal, 786, 151
2017	A New Solar Imaging System for Observing High-Speed Eruptions: Solar Dynamics Doppler Imager (SDDI)	Ichimoto, K., Ishii, T. T., Otsuji, K. et al.	Solar Physics, 292, 63
2017	"Dandelion" Filament Eruption and Coronal Waves Associated with a Solar Flare on 2011 February 16	Cabezas, D. P., Martínez, L. M., Buleje Y. J. et al.	Astrophysical Journal, 836, 33
2017	Increase in the Amplitude of Line-of-sight Velocities of the Small-scale Motions in a Solar Filament before Eruption	Seki, D., Otsuji, K., Isobe, H. et al.	Astrophysical Journal, 843, L24

Table 6.3: Capacity Building Activities from 2007 to 2017

Type	Date	Place	Country
Lecture	January 2007	Ica (National Ica University)	Peru
	January 2007	Lima(Instituto Geofísico del Perú)	Peru
	May 2008	Bouzaréah (Centre de Recherche en Astronomie, Astrophysique et Geophysique)	Algeria
	June 2008	Ica	Peru
	March 2010	Ica	Peru
	May 2011	Riyadh	Saudi Arabia
	August 2015	Riyadh	Saudi Arabia
Scientific Education	June 2010	Ica (National Ica University)	Peru
	October 2010	Ica (National Ica University)	Peru
	November 2010	Ica (National Ica University)	Peru
	October 2015	Riyadh (King Saud University)	Saudi Arabia
Technical Training	January 2007	Ica (National Ica University)	Peru
	July 2009	Hida (Hida Observatory)	Japan
Data-analysis Workshop	November 2010	Ica	Peru
	July 2011	Hida (Hida Observatory)	Japan
	July 2011	Mitaka (National Astronomical Observatory of Japan)	Japan
	March 2013	Hida (Hida Observatory)	Japan
	March 2015	Kyoto (Kwasan Observatory)	Japan
	February 2017	Kyoto (Kyoto University & Kwasan Observatory)	Japan

Chapter 7

Statistical Analysis on the Satellite Anomalies and its Implication in case of a Disastrous Solar Flare

Solar flares disturb the interplanetary and near-Earth plasma environment, and often cause miscellaneous adverse effects on artificial satellites. Recently, it was revealed that so-called "superflare" which has 10–100 times larger energy than the largest flare ever observed could occur on the Sun once in 100–1000 years. However, though there are several studies to analyse the relationships between the probability of satellite anomalies and various physical quantities related to the solar disturbances, little study has been conducted to assess the potential impact by a "disastrous" solar flare. This Chapter[*] shows the first impact assessment of satellite anomalies in case of a superflare. By taking simple linear regressions between the satellite-anomaly rate defined as the number of anomalies per satellite per flare event and 19 solar-disturbance-related physical parameters, the authors found that the 6-days averaged proton flux with its energy above 100 MeV had a remarkably good correlation (R^2 score > 0.9) to the anomaly rate of GEO and GPS satellites. Its extrapolation showed that in case of 1-in-100-years and 1-in-1000-years events, the GPS-satellite-anomaly rates should be 6.34 and 43.2, respectively. These rates are $\sim$8 (1-in-100-years case) and $\sim$50 (1-in-1000-years case) times larger than the worst case ever observed. We suggest that in cases of 1-in-100-years and 1-in-1000-years superflares, all the satellites could suffer from the anomalies, and the damages could be $\sim$8 and $\sim$50 times severer than the worst case ever observed.

Solar flares are explosive phenomena filled with magnetised plasma on the solar surface. They are triggered by the reconnections of opposite-polarity magnetic fields (called

---

[*]Seki, D., Isobe, H., Takara, K., "Statistical Analysis on the Satellite Anomalies and Its Implication in Case of a Disastrous Solar Flare", in prep

Sun

filament

Ch. 2 and 3
Is it possible to quantify a
filament activation and use
it as a precursor of a
filament eruption?

Coronal
Mass
Ejection
(CME)

Ch. 4 and 5
What physical parameters
of filament eruptions
control their CME
associations?

Ch. 7
How severe malfunctions
would satellites suffer in
case of a disastrous solar
flare?

Ch. 6
The feasibility of a
prediction of filament
eruptions by ground-based
telescopes

Ch. 8
Benefit of satellites'
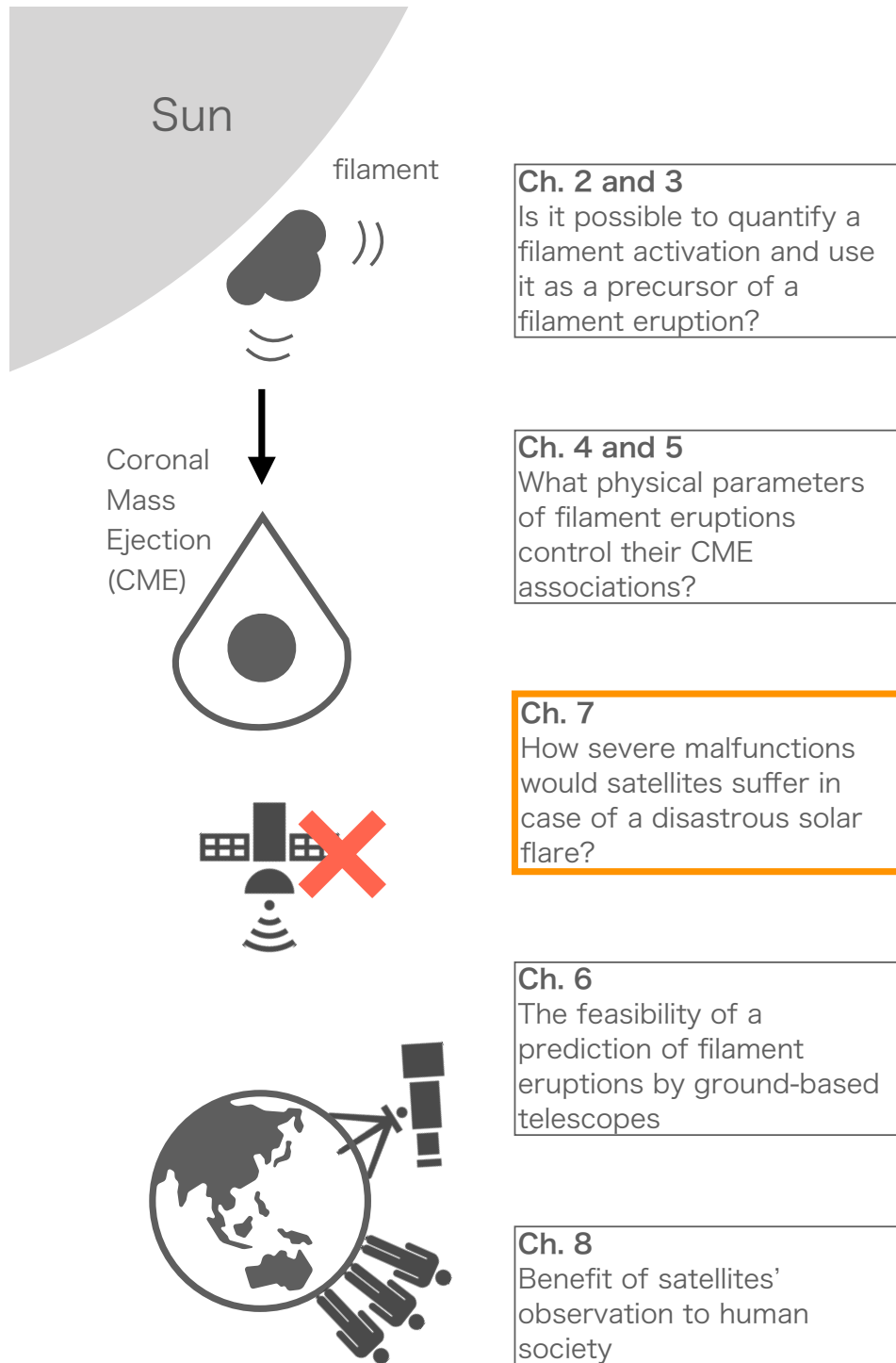observation to human
society

Figure 7.1: The graphical abstract of this dissertation (the orange rectangle corresponds to this Chapter).

magnetic reconnections) and release the energy of 10^{21}–10^{25} J in the various forms such as radiative energy, kinetic energy, and thermal and non-thermal energy [1]. Recently, it is pointed out that solar flares could bring various adverse effects on human society. Accompanied by solar flares, the intense electromagnetic waves in various wavelengths ranging from 10^{-1} Å (X-rays) to 10^{10} Å (radio), the huge bulk of plasma called Coronal Mass Ejection (CME) with its mass of 10^{11}–10^{13} kg [4], and energetic electrons and protons almost in the speed of light called Solar Energetic Particle (SEP) are often emitted or ejected. SEPs are the proton or electron whose energy ranges from a few keV to a few GeV driven by a magnetic reconnection during a solar flare (called Impulsive SEP event) or by a fast-large-scale CME shock wave (called Gradual SEP event) [11]. The electrons and protons in the near-Earth space are known to cause the various satellite malfunctions including electrostatic discharge, surface and internal charging and single event upsets. For the intensive review on the satellite anomalies, see Horne et al. (2013) [13] and Cannon et al. (2013) [14]. Moreover, highly-energetic protons can pose astronauts to the risk of radiation exposure.

The space assets are vulnerable to space weather effects, and various types of the anomalies can occur, associated with solar flare events. Figure 7.2 shows timestamps of the occurrence of satellite anomalies and temporal evolutions of some physical quantities related to space weather disturbances around the near-Earth space. Crosses and diamonds represent the satellite-anomaly events which occurred among Geostationary-orbit (GEO) satellites and Global Positioning System (GPS) satellites, respectively. For more information on the types and attributions of anomalies, see Figure 7.4. One can recognise that dozens of anomalies were detected after the peaks of the physical quantities. Several studies found relationships between the number of satellite anomalies and the physical quantities related to space weather. Choi et al. (2011) [136] found that there is a good correlation (correlation coefficient; c.c. > 0.9) between the number of satellite anomalies and Kp index (Kp index is a logarithmic expression of geomagnetic disturbance around the sub-auroral regions and a good proxy for the severity of geomagnetic disturbance). Pilipenko et al. (2006) [137] also showed fair correlations (c.c. = 0.2–0.6) between the satellite-anomaly rate defined as the ratio of the number of anomalies to that of the operational satellites and the fluxes of electron and proton within different energy ranges, Kp, and Dst indices (Dst index will be described in the following section).

Similar to other terrestrial disasters such as an earthquake, a low-frequency-high-impact solar disaster could also be anticipated. Maehara et al. and their colleagues [15–17] found that a "superflare", a flare whose energy is 10–1000 times larger than that ever observed on the Sun, could also occur on the solar-type and the sun-like stars by surveying stellar activities. They also found that the stellar superflares follow the similar power-law
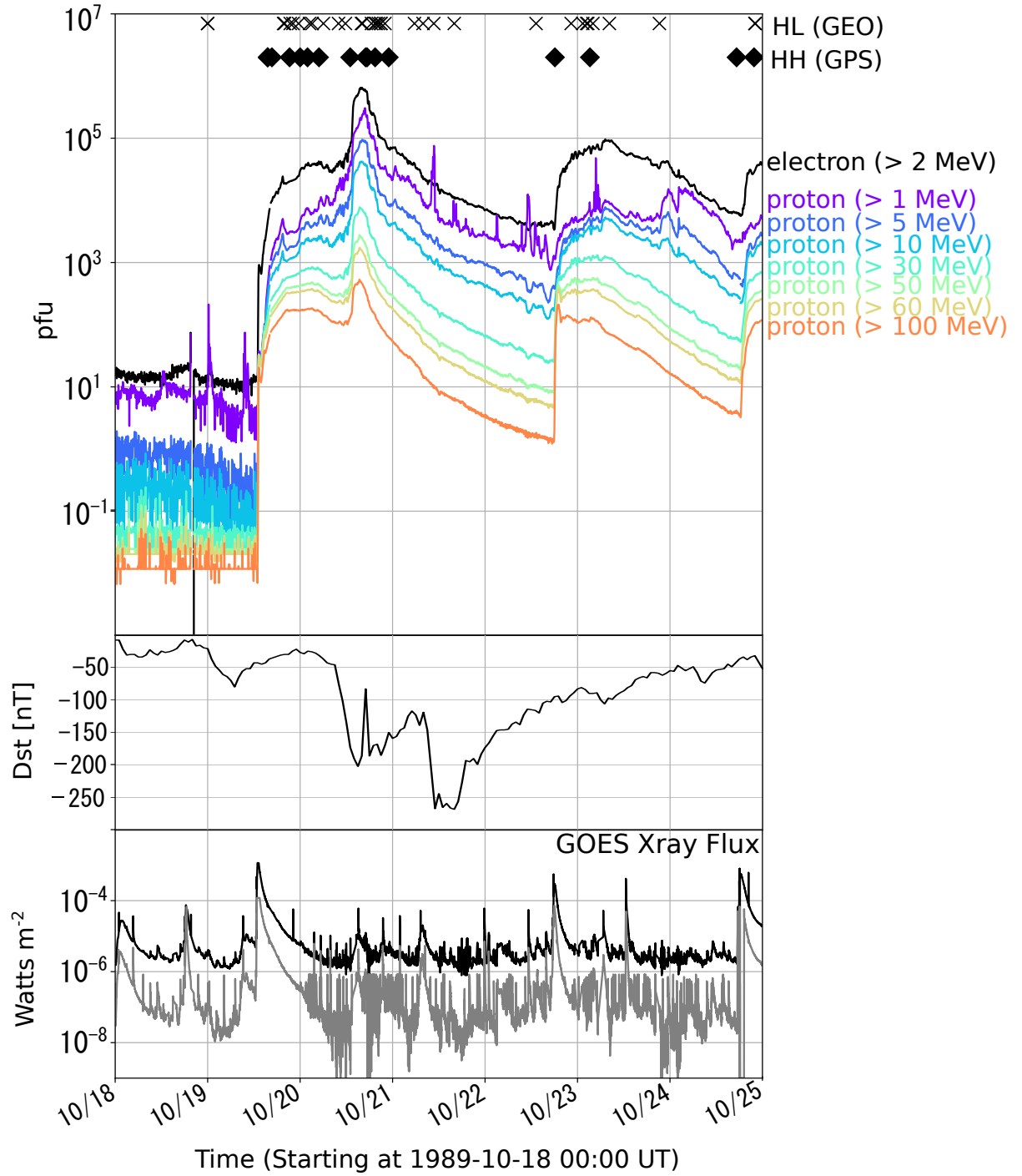
119

Figure 7.2: *Top to bottom*: Fluxes of an electron with its energy above 2 MeV, protons with seven different energies above 1, 5, 10, 30, 50, 60 and 100 MeV, the Dst index, and SXR between 1.0–8.0 Å (black) and 0.5–4.0 Å (grey) during October 18 to 25, 1989. Pfu, particle flux units, is equivalent to 1 str^{-1} cm^{-2} s^{-1} [135]. Crosses and diamonds represent satellite-anomaly events in high-altitude-low-inclination satellites (mostly GEO satellites) and high-altitude-high-inclination (mostly GPS), respectively. One can recognise that dozens of anomalies were detected at the peaks of the fluxes.

120

distribution between frequency and severity to the Sun. According to their studies, the expected frequency of X100 and X1000-class flares might be once in 200 and 1000 years, respectively. Moreover, indirect evidences of solar superflares have been reported and discussed in many studies from the theoretical and observational perspectives. Shibata et al. (2013) [20] conducted a simple theoretical calculation to assess the possibility whether the Sun can generate a large-enough sunspot to produce a superflare and concluded that it is possible to produce such a large sunspot that can initiate a X1000-class flare within one solar cycle ($\sim$11 years). From the observational point of view, Miyake et al. (2012, 2013) [21, 22] investigated the content of carbon-14 (^{14}C), the isotope of carbon-12, inside a Japanese tree ring. ^{14}C content in tree rings reflects its value in the atmosphere, and thus if its increase is observed, it should be the strong evidence of the enhancement of cosmic ray flux around the Earth. As a result, they found spiky sudden increases of ^{14}C content in 774 and in 994. Given that the origins of these proliferation are superflares, the former and latter events produced 50 times and 30 times larger amount of SEPs than one of the largest solar particle events on February 23, 1956, respectively [23].

However, to the best of our knowledge, few studies have focused on the assessment of the damage to artificial satellites in case of a disastrous superflare, although the assessments of socioeconomic impacts brought by "large" solar flares ($\sim$X10-class flares) have been widely researched [7, 14, 138, 139]. The main purpose of this study is, as the first assessment of the impact of a superflare, to discuss the possibility of satellite anomalies in case of X100- and X1000-class flares. In Section 7.1, we will describe the data set used in this analysis, including satellite anomaly database and physical quantities around the near-Earth environment. The methods and models of our analysis will also be presented. In Section 7.2, the results of our statistical analysis will be shown, and the implications from these results in case of a disastrous solar flare will be discussed in Section 7.3.

7.1 Data and Analysis

7.1.1 Database

To calculate the satellite-anomaly rate, which is the ratio of the number of anomalies to that of the operational satellites, we need both the data of satellite-anomaly reports and that of orbiting satellites. The data of satellite anomalies were obtained through Spacecraft Anomaly Data Base[†] maintained at National Oceanic and Atmospheric Administration National Centers for Environmental Information (NOAA NCEI) [140]. This database compiles miscellaneous information on satellite anomalies reported from seven

---

[†]https://www.ngdc.noaa.gov/stp/satellite/anomaly/satelliteanomaly.html

cooperation countries (Australia, Canada, Germany, India, Japan, United Kingdom, and the United States) from 1971 to 1996, including the universal and local time of anomaly, the spacecraft identification, orbit type, geographic latitude and longitude of sub-orbit point at anomaly start, altitude, anomaly type and anomaly diagnosis (the attribution of the anomaly). It should be noted that the anomaly-report contributions became smaller and stopped in the early 1990s, and hence, the anomaly rate after January 1, 1990, could be underestimated. Thus, we only used the anomaly reports until January 1, 1990, to calculate the satellite-anomaly rate in this study. In addition, generally speaking, the information on satellites contains high confidentiality, and the reports does not necessarily cover all the actual anomalies.

The number of operational spacecrafts used as a denominator of satellite-anomaly rate was counted from Satellite Catalog (SATCAT) [‡]. SATCAT provides useful information on all the Earth orbiting satellites including NORAD ID, which is a sequential 5-digit number assigned by the United States Space Command, satellite name, ownership, launch and decay date, inclination, and altitude. We defined the operational satellites at a certain day as those whose launch and decay date are before and after a certain day. In case a decay date was not reported for a satellite, it was assumed to be 20 years after the launch date. The number of the operational satellites owned by 14 countries (Australia, Canada, Germany, India, Japan, United Kingdom, the United States, Saudi Arabia, Brazil, People's Republic of China, ESA, International Telecommunication Satellite Organization, Indonesia, and France) was counted on the daily basis. All the anomalies in NOAA NCEI Spacecraft Anomaly Data Base were originated from these countries' satellites.

In this study, space environment was represented by SXR flux, electron and proton fluxes, and Dst index. All the flare events observed by the GOES were reported in NOAA NCEI website[§] from September 1975 to the present. On each flare event, start time, end time, peak time, location, and class of the flare were reported. SXR flux was obtained through conversion of the class of each flare. The fluxes of electron with its energy above 2 MeV and proton above seven different energies ($>1, 5, 10, 30, 50, 60$ and 100 MeV) were also retrieved from NCEI webpage[¶]. The data were available from January 1, 1986, to the present. Dst index [50] expresses the severity of the equatorial electric current ring in a unit of nT and is also widely chosen as the proxy of the geomagnetism. In this study, Dst index was used instead of Kp index [136] for the proxy of the global geomagnetism because Kp index may not be able to exhibit the severity of the extreme geomagnetic storm correctly. There is a rough correlation between Kp and Dst indices [141] and

---

[‡]https://celestrak.com/satcat/
[§]https://www.ngdc.noaa.gov/stp/space-weather/solar-data/solar-features/solar-flares/x-rays/goes/xrs/
[¶]https://satdat.ngdc.noaa.gov/sem/goes/data/avg/

the maximum Kp index, 9, roughly corresponds to -400 nT in Dst index. However, some studies showed that several past severe geomagnetic storms such as the 1989 event and the so-called Carrington event in 1859 [142], which is the most intense solar flare since modern telescopic observation started, reached under -400 nT in Dst [27, 143, 144]. Moreover, according to Vasyliūnas [145], the theoretical upper limit of Dst index could reach around -2500 nT, which should be adopted as the Dst value in case of a disastrous solar flare. The data of Dst index was taken from the Low Resolution OMNI data set[||] [146].

Hereafter, we call these indices (SXR flux, electron flux, proton flux with seven different energy ranges, and Dst index) as "space weather indices". In this study, simple linear regression between the satellite-anomaly rate and each space weather index for all the X-class flare events was conducted.

7.1.2 Data sampling

We classified the satellites and their anomalies in accordance with their orbits because the near-Earth space environment is physically quite different with respect to the altitude and inclination of orbits. Two types of orbits were then picked up. One is high-altitude-low-inclination (HL) orbit, in which a satellite is orbiting above 15,000 km and tilted less than 35 degree [147]. Most of the satellites in this orbit are composed of GEO satellites. The other is high-altitude-high-inclination (HH) orbit, in which a satellite is orbiting above 15,000 km and tilted larger than 55 degree. Almost all the HH satellites in this study are GPS satellites. In the forthcoming analysis, the satellite-anomaly rate of HL and HH satellites can be regarded as that of GEO and GPS satellites, respectively. As for low-earth-orbit (LEO) satellites, the number of anomaly reports was too tiny ($\sim$3 per month) to discuss the relationship between the satellite anomaly and each space weather index, compared to the number of orbiting satellites ($\sim$4000). Thus, in this study we will not consider LEO satellites.

Figure 7.3 shows the numbers of operational satellites and anomalies reported from HL satellites and HH satellites. Red and blue bars in the left panel show the numbers of the anomalies reported as Soft Error and those attributed to Single Event Upset, respectively. Figure 7.4 shows the histograms of the types and the attributions of HL satellites' anomalies. SE, PC, UNK, TE, ESDM, PF, HE, SEU, ESD, ECEMP, and RFI correspond to Soft Error, Phantom Command, Unknown, Telemetry Error, ElectroStatic Discharge Measured, Part Failure, Hard Error, Single Event Upset, ElectroStatic Discharge, Electron Caused ElectroMagnetic Pulse, and Radio Frequency Interference, respectively. SE and HE are defined as "recoverable bit flip type error" and "permanent chip damage or

---

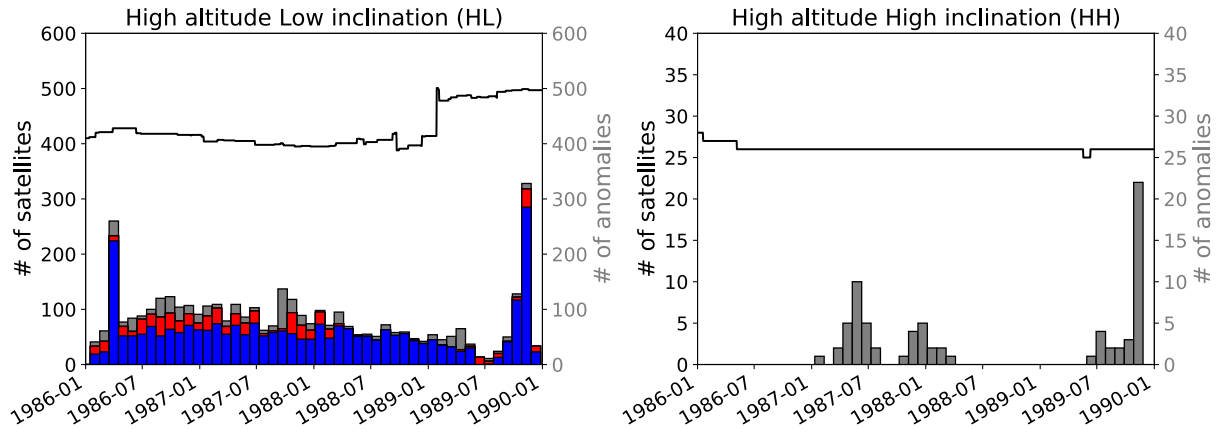[||]`https://cdaweb.sci.gsfc.nasa.gov/pub/data/omni/low\_res\_omni/`

Figure 7.3: The numbers of operational satellites (black line) and all the anomalies (grey bar) produced from NOAA NCEI Spacecraft Anomaly Data Base and SATCAT. Red and blue bars (overlaid) in the left panel show the number of Soft Error anomalies and that of Single-Event-Upset-attributed anomalies, respectively. The bin size of each bar is 30 days
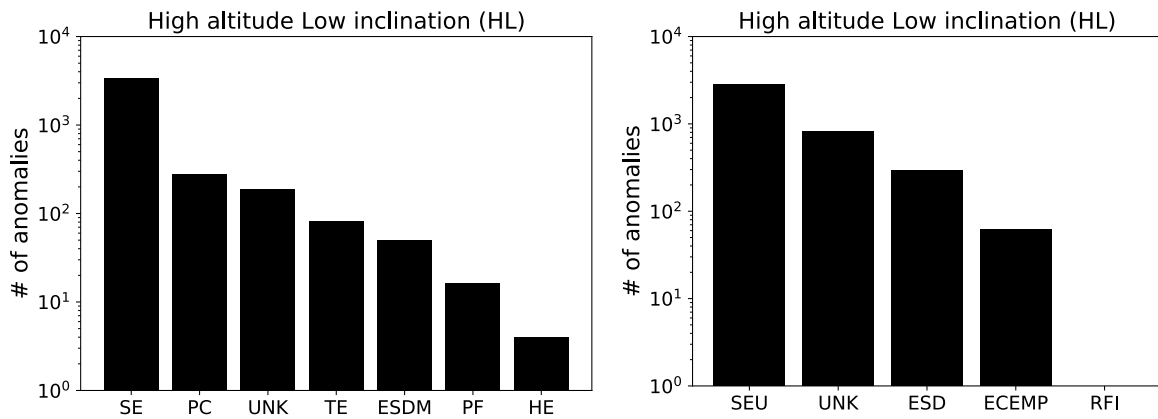

Figure 7.4: The numbers of anomalies in accordance with their types (left) and their attributions (right). Note that the y-axis is shown in a common log scale.

latch-up", respectively. For more details, access to the documentation for the anomaly data table**. From Figure 7.4, one can recognise that most of the reported anomalies of HL satellites were soft error and their attribution was single event upset. On the other hand, all the reported anomalies of HH satellites were soft error and their attributions were unknown. The numbers of operational HH satellites and their anomalies were quite small compared to HL satellites.

Here, the way of data sampling in this study will be explained. These are composed of two steps: event selection and N-days sampling. This procedure was conducted separately to both the cases of HL and HH satellites. First, all the X-class flare events from January 1, 1986, to January 1, 1990, were selected. The number of events was 90. Secondly, the author counted the number of satellite anomalies which took place over the following N days after the onset of each event in accordance with their types and attributions. At the same time, the average and maximum of space weather indices for the same duration were calculated as well. The sampling window, N, was chosen as an integer from 1 to 10. The number of anomalies was divided by that of operational satellites to produce a satellite-anomaly rate for each event.

7.1.3 Model

We used the ordinary least squares (OLS) method for single linear regressions. For each orbit type (HL or HH), single linear regression of the satellite-anomaly rate was conducted on one of 19 space weather indices (SXR peak flux, the average or the maximum flux of electron or proton with 7 different energy ranges, or the average or the maximum Dst index) with 10 different sampling windows.

To assume the upper limit of electron and proton fluxes in case of a solar superflare, we utilised the scaling law first proposed by Takahashi et al. (2016) [26]. They discussed the upper limit of the peak proton flux with its energy above 10 MeV on the basis of some simple physical assumptions and statistical relations among proton peak flux, Coronal Mass Ejection (CME) speed, and peak SXR flux of flares. They derived the scaling relation expressing the upper limit of proton peak flux, F_p, in terms of flare SXR peak flux, F_{sxr}, as

$$F_p = F_{p,0} \times F_{sxr}{}^{5/6},$$

where $F_{p,0}$ can be determined so that the upperlimit line passes the left-most data point. Figure 7.5 shows the way to determine the coefficient $F_{p,0}$ in case of proton peak flux with energy above 100 MeV. Here, we assumed that this scaling law could also hold for the protons within other energy ranges. For each energy range, we optimised $F_{p,0}$ one

---

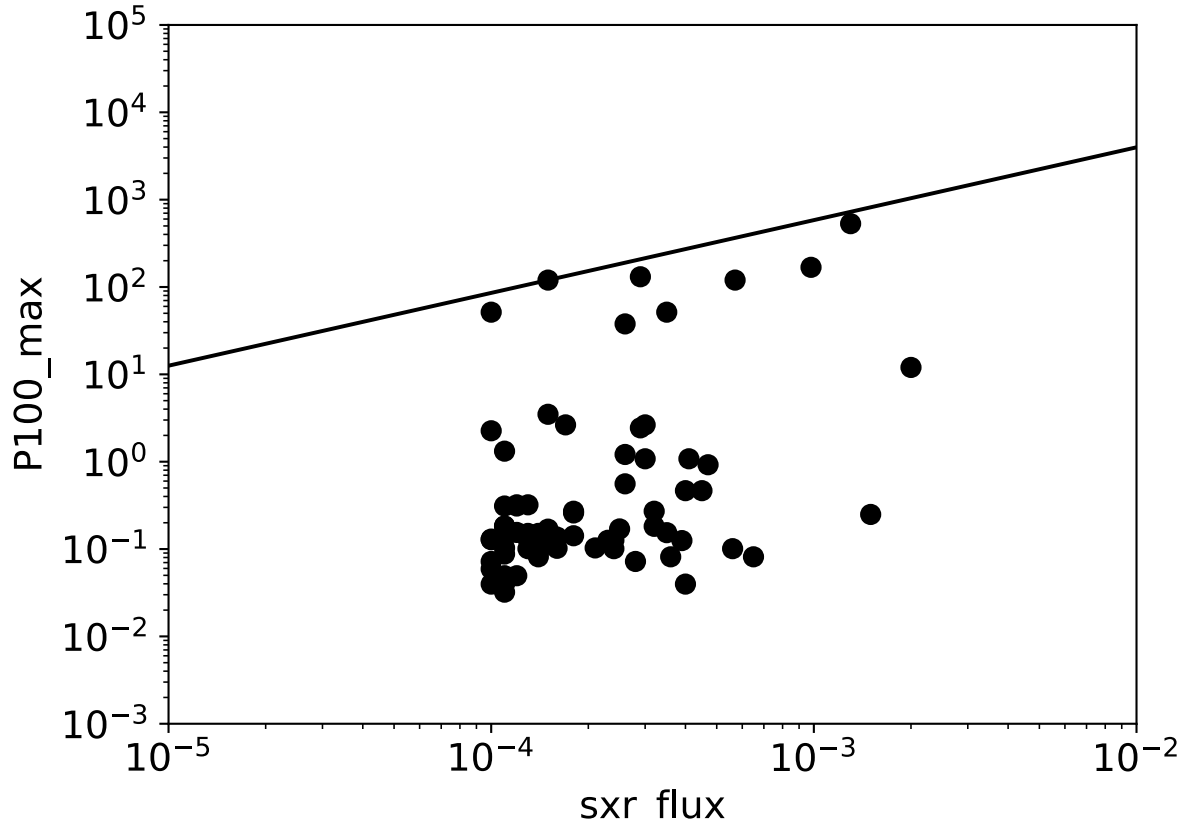**https://www.ngdc.noaa.gov/stp/satellite/anomaly/satelliteanomaly.html

Figure 7.5: Example of the method to determine $F_{p,0}$ in case of the proton peak flux with its energy higher than 100 MeV. The peak flux was determined as the 3-day maximum flux after the onset of a flare. Each black dot and a black line correspond to each flare event and the fitted line, respectively. In this case, the obtained $F_{p,0}$ was $10^{5.27}$.

by one to express the upper limit of the SEP flux in terms of peak SXR flux. Finally, by extrapolating these obtained relationships to the cases of X100- and X1000-class flare, which are equivalent to 0.01 and 0.1 W m^{-2}, respectively, we obtained the super-SEP fluxes. The upperlimit of the peak Dst index was assumed to be -2500 nT. This value was proposed by Vasyliūnas [145] on the basis of the physical assumption that the sum of the kinetic energy density of plasma in the magnetosphere and the energy density in the disturbed magnetic field should be limited by the pressure of the Earth dipole field at the equator.

7.2   Results

7.2.1   Case of HL(GEO) satellites

Figure 7.6 shows R^2 scores (also known as the coefficient of determination) of single linear regressions of HL (mostly GEO) satellites' all the reported anomalies on each space-weather index with 10 different sampling windows, and Figure 7.7 shows the fitting result for the best case. R^2 score is defined as below;

$$R^2 = 1 - \frac{\sum(y_{true} - y_{pred})^2}{\sum(y_{true} - \overline{y_{true}})},$$

where, y_{true} is an observation, y_{pred} is a predicted value by a model, and $\overline{y_{true}}$ is the average of the observations. In this study, y_{true} and y_{pred} correspond to the observed satellite-anomaly rates and those predicted by a single linear model, respectively. R^2 score is commonly used to assess the accuracy of a model, ranging from $-\infty$ to $+1$. If a model perfectly fits observations, R^2 becomes one, whilst if it cannot predict observations at all, R^2 goes to negative infinity. One can notice that proton integral flux with its energy higher than 100 MeV demonstrated high R^2 scores between 0.6 to 0.9, and the R^2 scores of SXR and Dst were less than 0.2. The highest R^2 score, 0.902, was obtained in the case of proton integral flux above 100 MeV averaged for 6 days from the onset of the flare.

Figure 7.8 show the same result as Figure 7.6 except that regression was conducted only for Soft-Error anomalies. Since most of the anomalies were composed of those of Soft-Error or Single-Event-Upset types as seen in Figure 7.3 and Figure 7.4, one can recognise that Soft-Error anomaly shows a very similar result to that of all the reported anomalies. The highest R^2 score in case of Soft-Error anomaly was 0.910 with 6-days averaged proton flux with energy above 100 MeV. Regressions for Phantom-Command and Telemetry-Error anomalies were also conducted and there were weak correlations around 0.3 (no figure). ElectroStatic Discharge Measured and Hard Error have no data
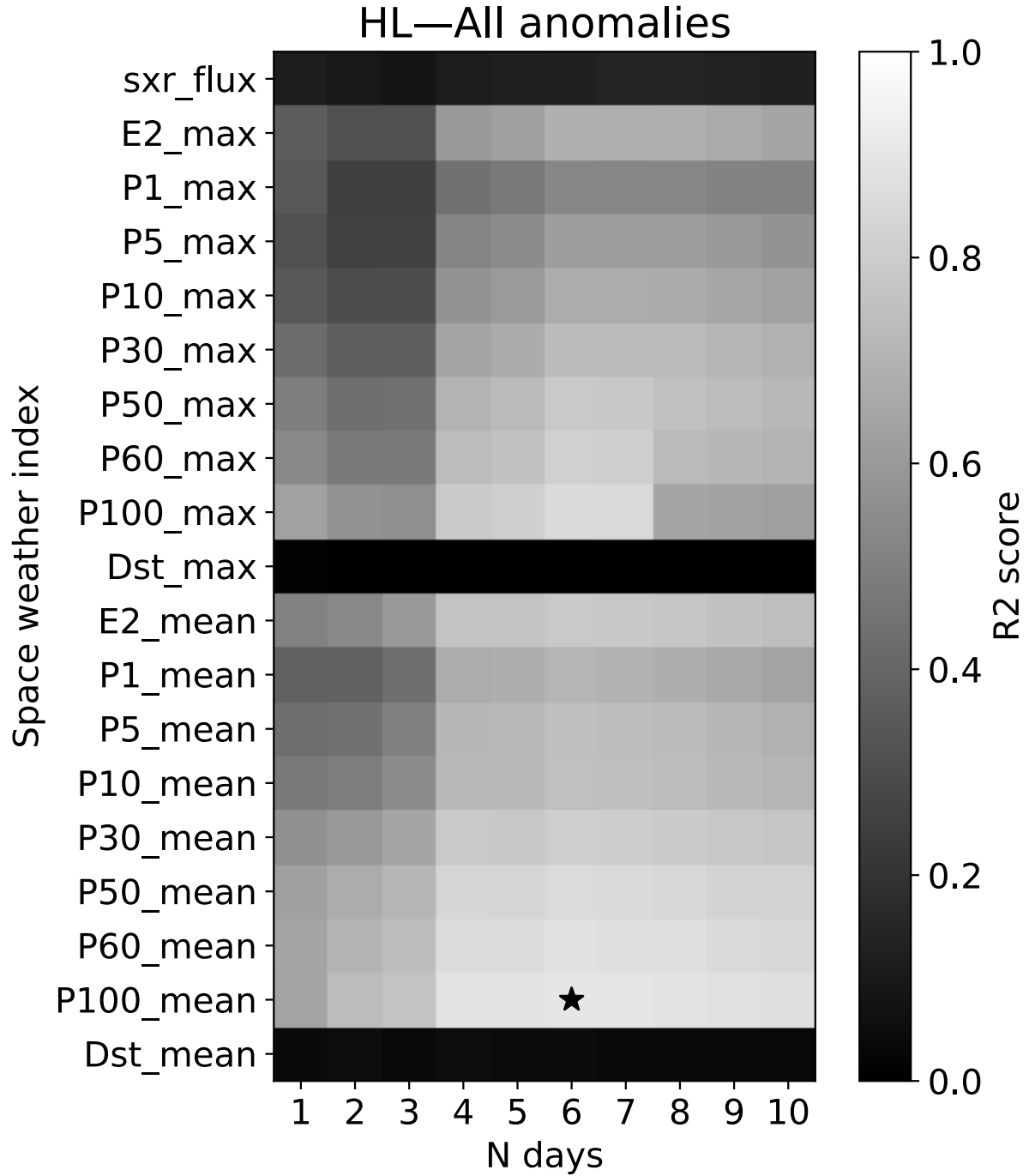
Figure 7.6: R^2 (coefficient of determination) scores of single linear regression of HL-satellites' all the reported anomalies on each space-weather index with 10 different sample windows. E2, P1, P5, P10, P30, P50, P60, and P100 correspond to electron integral flux with its energy > 2 MeV, proton integral fluxes with its energy > 1, 5, 10, 30, 50, 60 and 100, respectively. A star was set to the maximum R^2 score, 0.901.
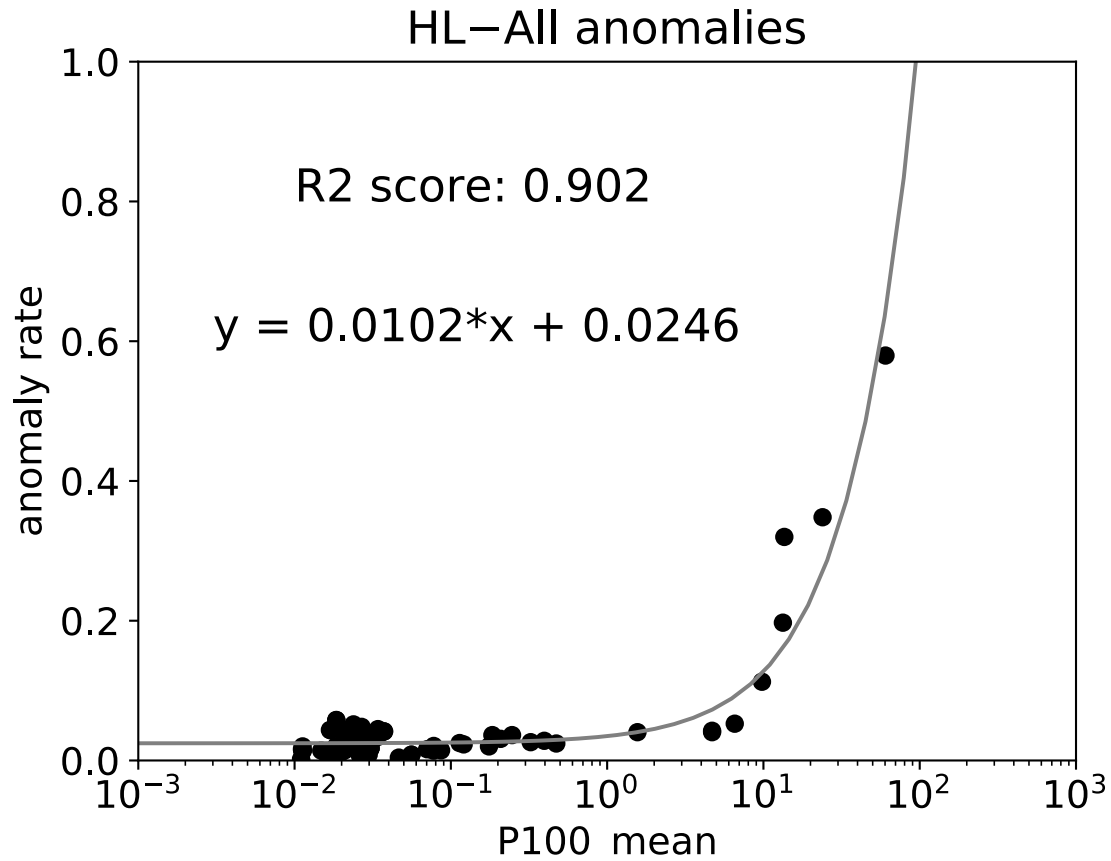
Figure 7.7: The result of single linear regression of 6-days averaged proton integral flux with its energy > 100 MeV to the anomaly rate (the total number of anomalies for 6 days divided by that of operational HL satellites). Black points and grey line correspond to events and fitted linear model, respectively. Note that the horizontal axis is shown in log scale.
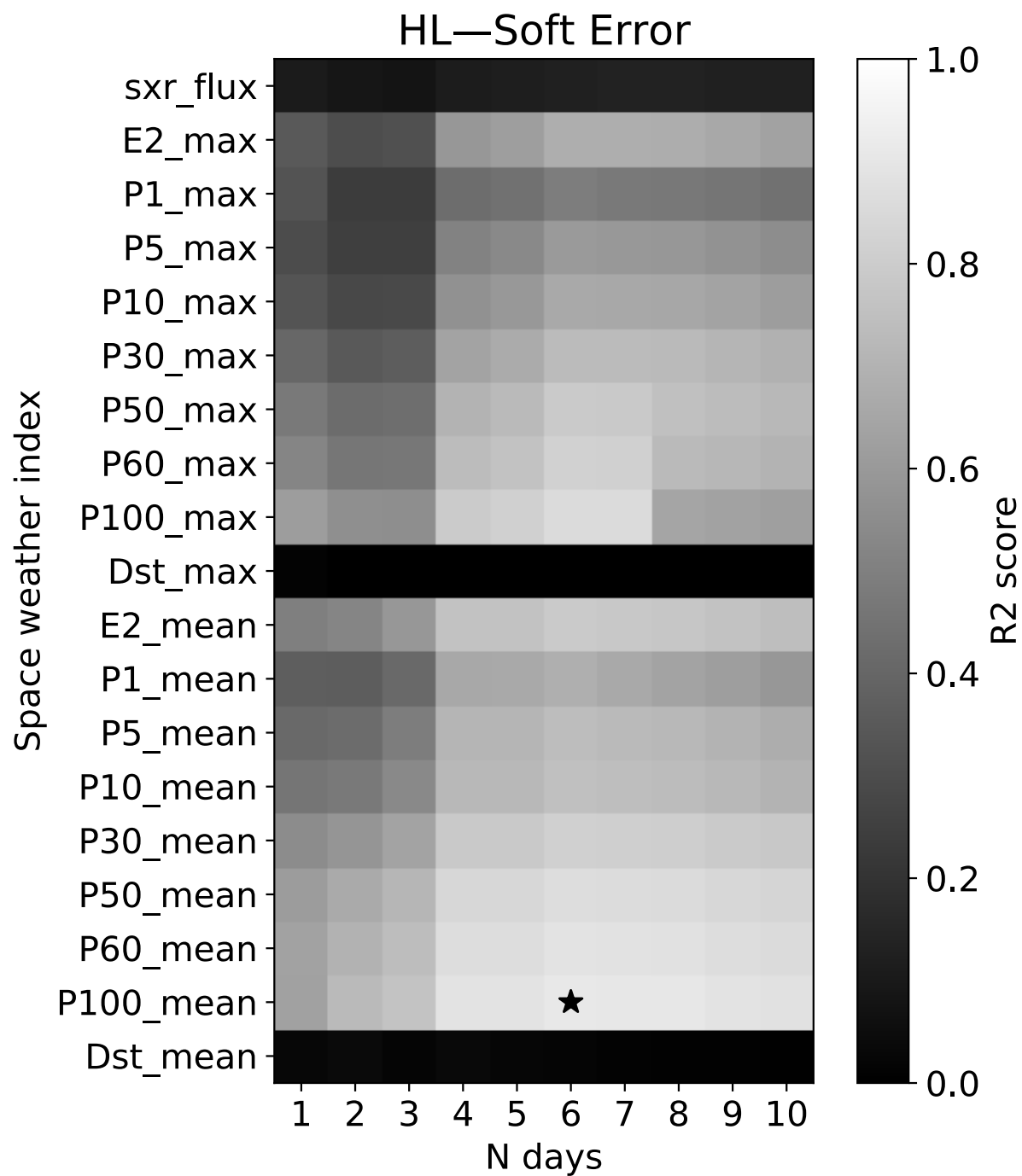
Figure 7.8: Same figure in Figure 7.6 except that only the anomalies reported as Soft Error were used for regression.

points to be fitted in this study, which means that these anomalies did not occur over 10 days after the onset of X-class flares. They may be attributed to other reasons. Part Failure has no correlation to any space-weather indices (R^2 score was almost zero).

Figure 7.9 shows the same result as Figure 7.6 except that regression was conducted only for Single-Event-Upset attributed anomaly. For the same reason stated above, we can recognise very similar distribution of R^2 score. The highest score was 0.894 with 6-days averaged > 100 MeV proton flux. ElectroStatic-Discharge-attributed anomaly shows weak correlation like PC and TE cases with R^2 score of < 0.4. Electron-Caused-ElectroMagnetic-Pulse-attributed anomaly have no data points to be fitted in this study.

7.2.2   Case of HH(GPS) satellites

Figure 7.10 shows the same result as Figure 7.6 except for the type of satellites' orbit, and Figure 7.11 shows the fitted result for the best case.   In this case, we fitted the satellite-anomaly rates calculated from all the anomaly reports from HH (mostly GPS) satellites. Note that in HH case, all the anomalies are classified as Soft-Error type and attributed to "unknown". One can recognise the similar distribution of R^2 score to that in case of HL. The highest score was 0.931 and obtained with 7-days averaged >100 MeV proton flux.

7.2.3   Prediction in case of a superflare

Now that single linear model for each type or attribution of anomaly and the possible upper limits of the space-weather indices in case of a solar superflare were obtained, one can estimate the satellite-anomaly rates in case of a superflare.

Before moving on to estimation, it should be noted that since Takahashi et al. (2016) [26] only discussed the upper limit of the peak, it is necessary to assume the upper limit of the average space-weather indices. Figure 7.12 shows the correlation between the 6-days average and maximum proton fluxes with a remarkably good correlation coefficient of 0.98. Thus, we assumed that the average super SEP fluxes should be proportional to the peak super SEP flux with a coefficient of 0.113.

Table 7.1 shows the best R^2 scores for anomaly types or attributions and the predicted satellite-anomaly rates in cases of X100- and X1000-class solar flares. In all the cases, the satellite-anomaly rates were best correlated with the 6-days or 7-days average proton flux with its energy above 100 MeV. The superflare-associated average proton fluxes > 100 MeV for X100- and X1000-class flares should be 4.49×10^2 and 3.06×10^3 pfu, respectively. As for HL satellites, the anomaly rates for X100- and X1000-class flares are predicted with very high R^2 score to be 4.62 and 31.3, respectively. These values are around 8 and 55
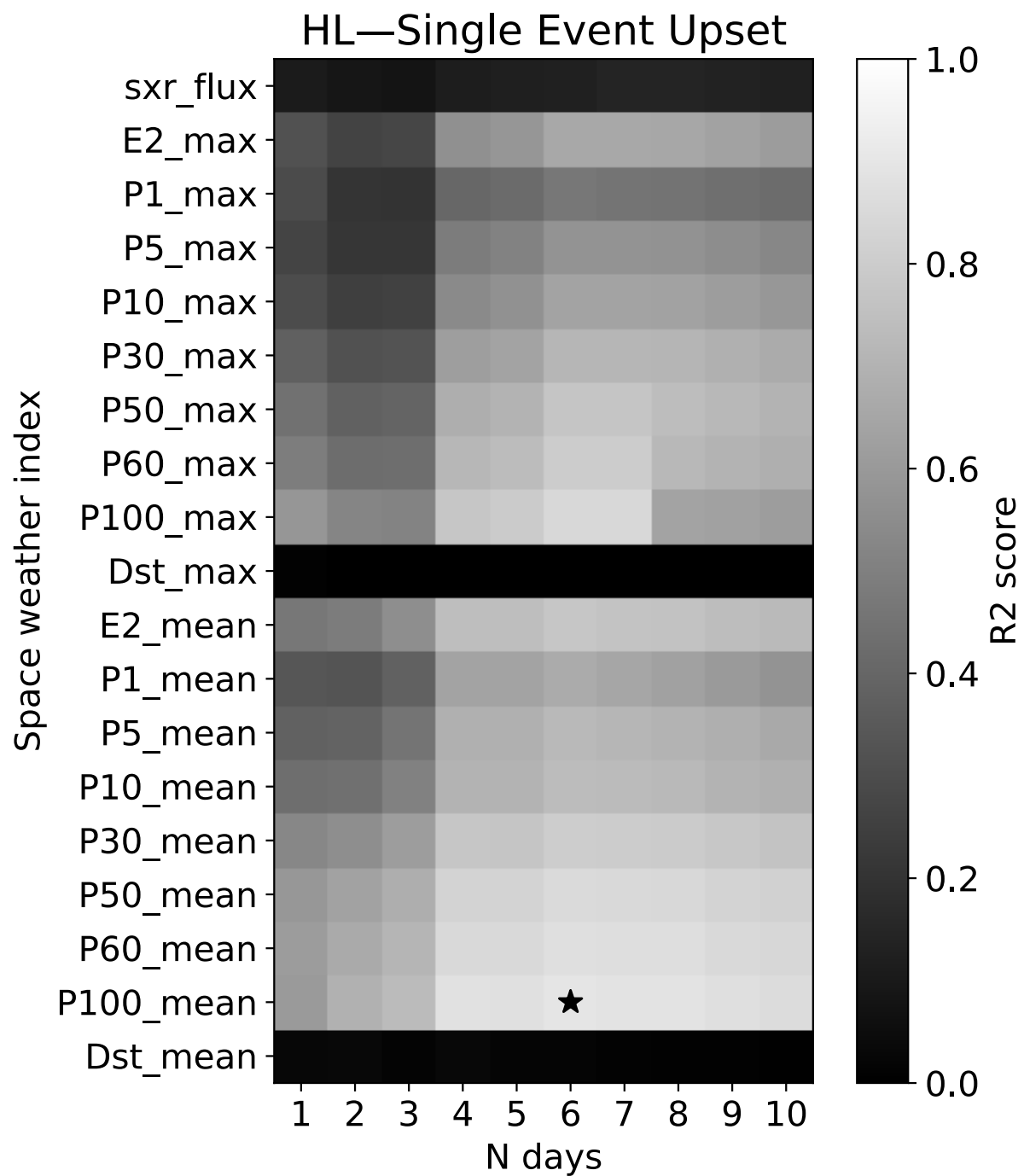
Figure 7.9: Same figure in Figure 7.6 except that only the anomalies attributed to Single Event Upset were used for regression.
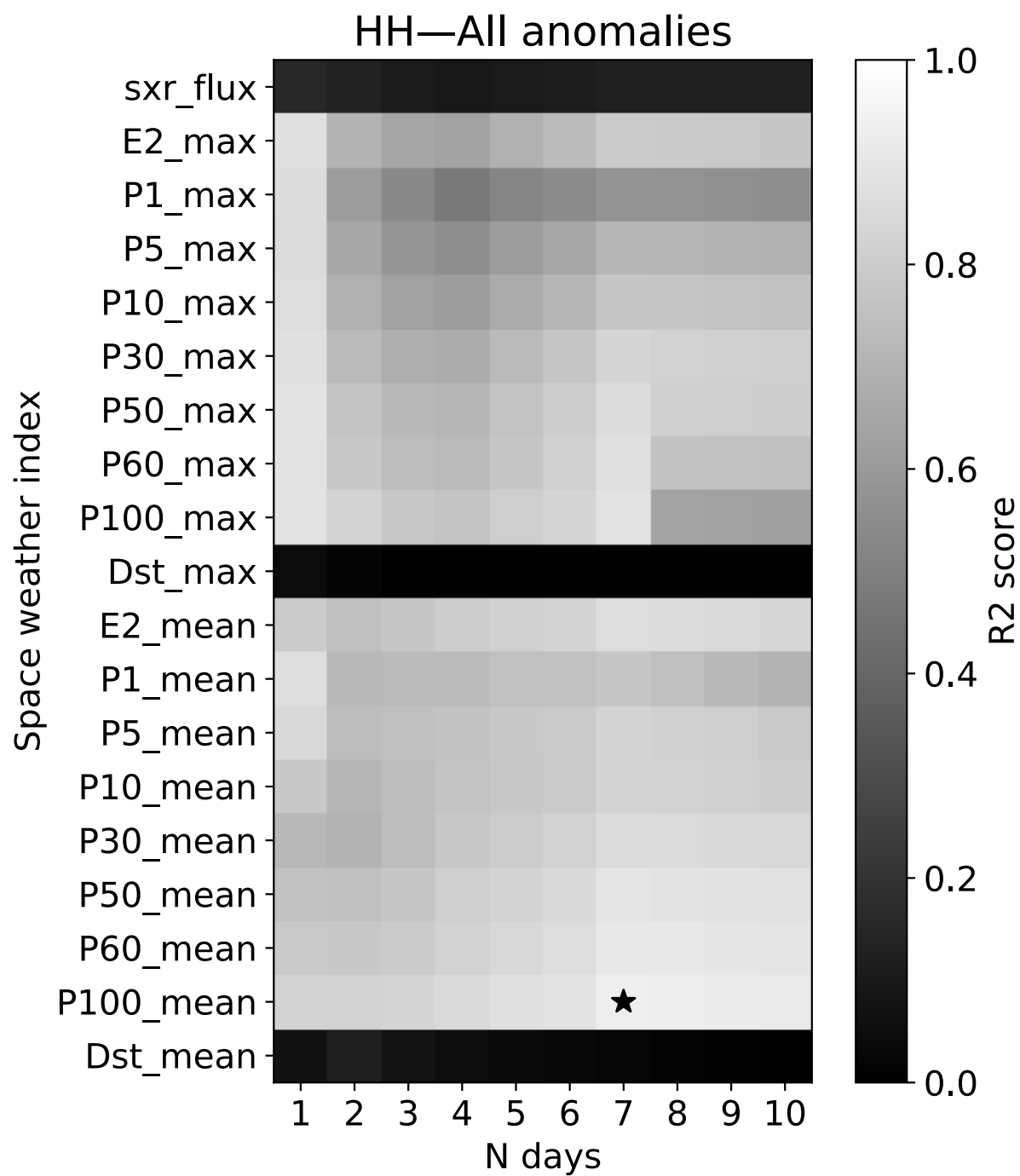
Figure 7.10: Same figure in Figure 7.6 except for the satellites' orbit of HH.
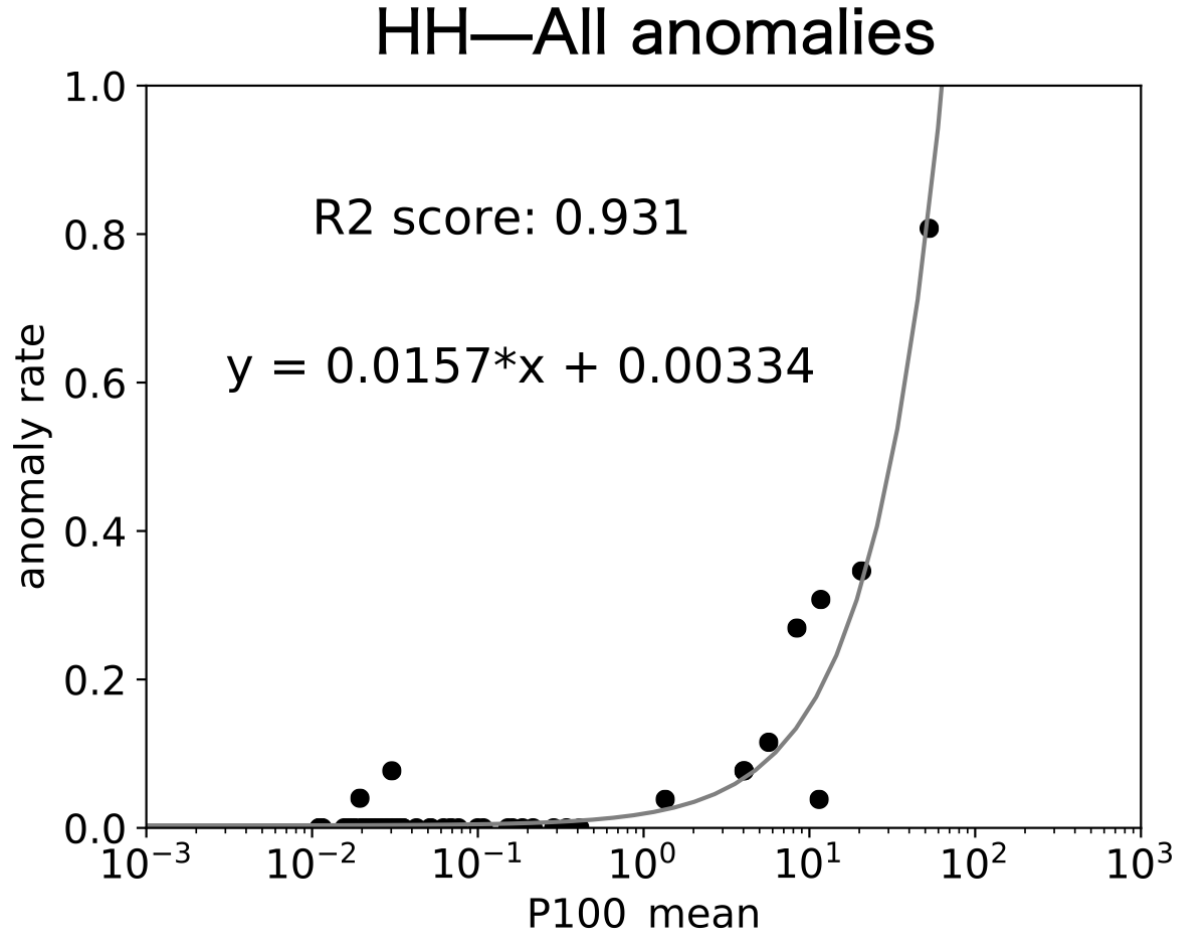
Figure 7.11: Same as the figure in Figure 7.7 except for the size of a sample window of 7 days and the satellites' orbit of HH.

Table 7.1: The best R^2 scores for anomaly types or attributions and the predictions of satellite-anomaly rate in cases of X100- and X1000-class solar flares.

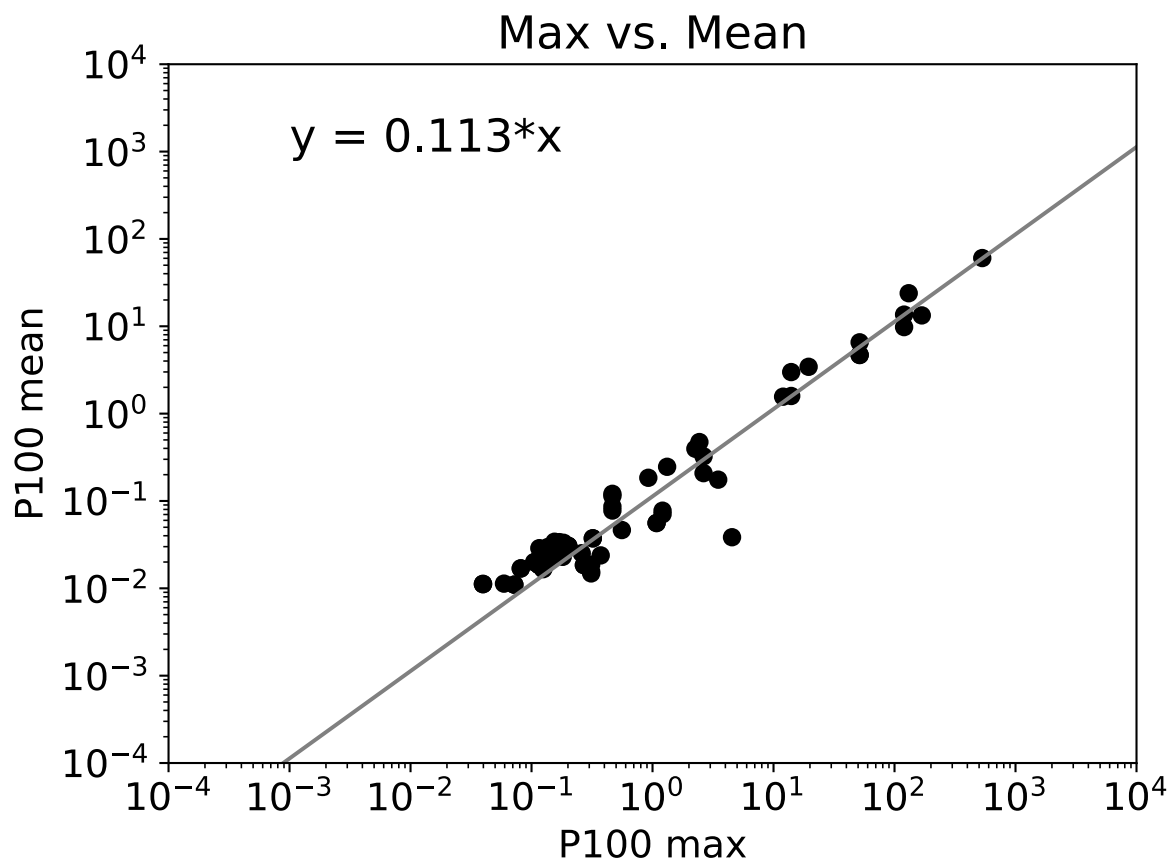| Orbit	Type or Attribution	R^2 score	Anomaly rate (X100)	Anomaly rate (X1000)
HL (GEO)	all	0.902	4.62	31.3
HL (GEO)	SE	0.910	4.57	31.0
HL (GEO)	SEU	0.895	4.22	28.6
HH (GPS)	all	0.931	7.07	48.1

Figure 7.12: Correlation between the 6-days average and maximum proton fluxes with its energy above 100 MeV. Each point corresponds to the X-class flare event taken into account in this study. Correlation coefficient is 0.98.

times larger than our worst case (the top-most event in Figure 7.7). The rates of Soft Error and Single Event Upset were 4.57 and 4.22 for X100-class flare and 31.0 and 28.6 for X1000-class flare, respectively. As for HH satellites, the estimated anomaly rates for X100- and X1000-class flares with the highest R^2 score are 7.07 and 48.1, respectively. These values are around 8 and 54 times larger than our worst case (the top-most event in Figure 7.11).

7.3   Summary and Discussion

In this study, for the purpose of evaluating the possible impact on satellite anomalies in case of a solar superflare, the authors conducted single linear regressions of satellite-anomaly rate on space-weather indices with different sampling windows in accordance with two orbits, high-altitude-low-inclination (HL, mostly GEO) and high-altitude-high-inclination (HH, mostly GPS) orbits. The satellite-anomaly rate was defined as the ratio of the total number of anomalies to that of operational satellites. The space-weather indices are taken as 19 different physical quantities, SXR peak flux, the average and maximum of electron flux with its energy above 2 MeV, proton fluxes with 7 different energy ranges, and Dst index. Sampling window for which to take average or maximum was chosen from 1 to 10 days. As a result, in case of HL satellites it was found that the satellite-anomaly rates for all the anomalies, SE, and SEU were correlated quite well (R^2 score > 0.9) to the 6-days average of proton flux with its energy higher than 100 MeV, and the other types and attributions of anomalies were weakly correlated. In case of HH satellites, the satellite-anomaly rate for all the anomalies are correlated, with the highest R^2 score of 0.931, to the 7-days average of proton flux with its energy higher than 100 MeV. Assuming the upper limit of the space-weather indices in case of X100- and X1000-class flares by following the discussion in Takahashi et al. (2016) [26] and Vasyliūnas (2011) [145], the predictions of the satellite-anomaly rates for X100- and X1000-class flares showed that SE and SEU on all the HL satellites could occur around 4–5 and 30 incidents per satellite, and SE on all the HH satellites could take place around 7 and 48 incidents per satellite, respectively. Our result suggests that in case of a superflare, it could be anticipated that all the satellites could suffer from anomalies, and the damages for X100- and X1000-class flares could be ∼8 and ∼54 times severer than the worst cases ever observed. Note that the estimation presented in this study is based on the satellite-anomaly data in the later 1980s, since when the satellite design should have been improved and become more tolerable. To assess the satellite-anomaly rate for the current satellite design, the recent satellite-anomaly data is necessary.

Belov et al. (2004) [148] carried out a statistical analysis of satellite-anomaly rates

based on multiple linear regression, on the basis of the same anomaly database (NOAA NCEI Spacecraft Anomaly Data Base), their own operational satellites' data (the number is $\sim$300) produced by various internet sources, and > 30 space weather parameters from 1987 to 1994. There are two differences between our and their studies. Firstly, they included the anomaly data around early 1990s which are excluded in this study because the anomalies were less reported due to small contribution from the cooperation countries during this period. Secondly, the definition of a satellite-anomaly rate is different. Their definition took it as the ratio of the number of daily anomalies to that of the satellites which experienced at least one anomaly from 1987 to 1994. On the other hand, our study took it as the ratio of the number of anomalies over the following 1–10 days after the onset of an X-class flare to that of the operational satellites in orbit at that time.

In their study, they proposed the models of satellite-anomaly rate given by

$$
\begin{aligned}
f_{HL} &= -54 + 1.4 \times 10^{-9} \left[E_2\right]_4^{1.2} + 0.83 \left[A_p\right]_5 + 0.19 \left[V_{sw}\right]_2 - 0.15 \left[B_z\right]_3 \\
&\quad + 1.1 \left[P_{100}\right]_1^{0.35} + 1.6 \left[P_{60}d\right]_1^{0.75} + 20 Sf + 15 Da_{10}, \text{and} \\
f_{HH} &= -85 + 6.5 \left[P_{100}\right]_1^{0.35} + 2.6 \left[P_{60}d\right]_1^{4.4} - 0.53 \left[\sum B_z\right]_4 + 14 \left[E_{ak}\right]_4 + 0.09 SSN_{365},
\end{aligned}
$$

where $[*]_n$ denotes the average of the * parameter over the past n-1 days, E_2 is the > 2 MeV electron fluence (fluence; the integrated flux over time expressed in 1 sr^{-1} cm^{-2} day^{-1}), A_p is Ap index (commonly used as a proxy of geomagnetic storm like Kp index), V_{sw} is the solar wind velocity, B_z is the Bz-component of interplanetary magnetic fields, $P_{60}d$ is > 60 MeV proton flux in 1 sr^{-1} cm^{-2} s^{-1}, P_{100} is > 100 MeV proton fluence in 1 sr^{-1} cm^{-2} day^{-1}, Sf is a seasonal factor ranging 1–3, Da_{10} is cosmic ray activity index, $\sum B_z$ is daily sum of B_z, E_{ak} is an energy injection to the magnetosphere, and SSN_{365} is annual average sunspot number (see Belov et al. (2004) [148] for more details). Correlation coefficients between their observations and predicted values by f_{HL} and f_{HH} were 0.39 and 0.70, respectively. In case of X100-class flares, the second term in f_{HL} and the third term in f_{HH} should have the order of 10^3 and 10^{13}, which are much higher than other parameters such as the first, third, fourth, fifth, eighth, and ninth terms in f_{HL} and the first, fourth, fifth, and sixth terms in f_{HH}. Neglecting these terms, one can obtain f_{HL} and f_{HH} in case of X100-class flares as $\sim$0.7 and $\sim$$10^9$ anomalies per day per satellite, respectively. The former value is comparable to our result, $\sim$0.5 anomalies per day per satellite, but the latter is unreasonably large. Note that this unreasonably large value of f_{HH} comes from the power of 4.4 in the third term.

In terms of disaster risk management, the current space weather prediction and monitoring system are constructed mainly based on the satellite-based data, which are vulnerable to space weather effects. This means that if a disastrous solar flare could happen and

most of the solar observational satellites should be broken, we could not prepare for the following solar eruptions in the current system. And thus, as complementary instruments, ground-based telescopes and the prediction methods based on them should be emphasised on to build a resilient space weather prediction and monitoring system [66, 91].

Chapter 8

Project Based Research

The author has carried out the following two projects undertaken at Special Research Project II and III in Graduate School of Advanced Integrated Studies in Human Survivability, Kyoto University: (1) Earth-observation data (EO data) for multidisciplinary research & consulting work, and (2) R&D for space-weather-prediction business. In this Chapter, the author reports the achievements of two projects, which are summarised as below; (1) A list of 184 publicly available EO data was compiled and made available on the web. We used them to plan a study of economic-activity estimation. In addition, the application to the consulting business was examined, and it was found to be difficult to apply in cases lacking spatial and geographical information. (2) We developed an algorithm that can predict geophysical quantity X related to space weather, which is crucial for satellite operations, 24 hours ahead with an error of 6.9%, through joint fundamental R&D with Company A.

8.1 Earth-Observation data for multidisciplinary research & consulting work

The purpose of this project is to provide solutions to problems that benefit society by using satellite Earth-observation data (EO data). In recent years, both the quality and quantity of satellites and EO data have increased, and the potential value of using them has been increasing. EO data as big data has three advantages: wide coverage of the entire globe, temporal homogeneity of observations at regular intervals for a long period of time, and various observation wavelengths. For example, the United Nations has been working on achieving the SDGs by using EO data [149–151].

In this context, by leveraging the skills to analyse the satellite imagery acquired through the researches in solar physics, we aim to provide insights for solutions to social
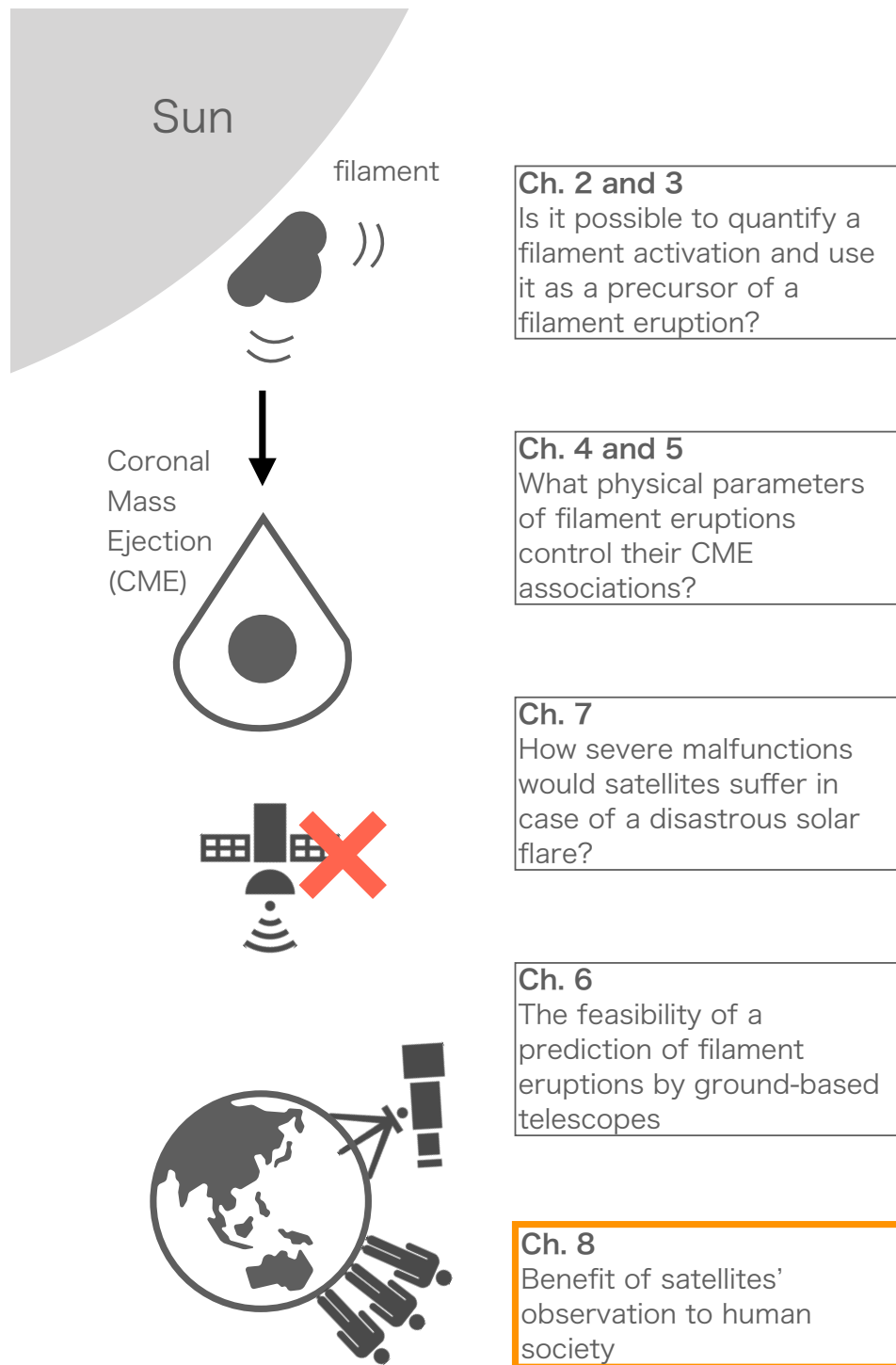
Sun

filament

Coronal Mass Ejection (CME)

Ch. 2 and 3
Is it possible to quantify a filament activation and use it as a precursor of a filament eruption?

Ch. 4 and 5
What physical parameters of filament eruptions control their CME associations?

Ch. 7
How severe malfunctions would satellites suffer in case of a disastrous solar flare?

Ch. 6
The feasibility of a prediction of filament eruptions by ground-based telescopes

Ch. 8
Benefit of satellites' observation to human society

Figure 8.1: The graphical abstract of this dissertation (the orange rectangle corresponds to this Chapter).

Figure 8.2: The layout of the website

problems. Specifically, we focused on (1) constructing EO data catalogue in Japanese, (2) multidisciplinary study using EO and geographical data, and (3) consulting work using EO data.

8.1.1 EO data catalogue in Japanese

I constructed and hosted a catalogue website of EO data available for free and for general and commercial use. The website was written in Japanese. There are several websites such as CEOS [152] and Google Earth Engine [153] that listed available EO data from all over the world in English, but there was no site that we could use in Japanese yet. Moreover, during the other activities described later, it is necessary to search for EO data that will contribute to the solution of the problem easily and quickly. Thus, as the first project, I created a catalogue of EO data available all over the world in Japanese.

By investigating Google Earth Engine [153], G-Portal [154], and NASA SEDAC [155], 184 data have been collected including satellite imagery and geographical information. Each element contains its name, observation period, spatial and temporal resolution, observation site, wavelength/frequency, what can be seen, and URL to access the data. It was hosted, and you can access the website at `http://www.gsais.kyoto-u.ac.jp/st/eo-database/`. Figure 8.2 shows the layout of the website.

8.1.2 Multidisciplinary study using EO and geographical data

Recently, the intensive studies have been conducted to estimate economic activities from satellite imagery and geographical information [156–159]. Jean et al. [156] utilised night light and day light satellite imagery for estimating daily consumptions in Nigeria, Tanzania, Uganda and Malawi by leveraging machine learning technique. As the second activity, through the joint research with Mr. Kazawa, we tried to conduct economic studies like those by leveraging EO data catalogue constructed in the previous subsection and geographical information. Mr. Kazawa has much expertise in economics and plays a key role in setting a hypothesis for the study and collecting data which could be used for verifying it. In contrast, I was involved in this project as a technical advisor and provided him with the knowledge of how to analyse data (e.g. how to implement machine learning, especially convolutional neural network).

As an achievement of this project, we successfully set the goal of this research. The objective of this joint study was to improve the accuracy of the estimation of economic activity indicators (e.g., GDP) in developed countries. In recent years, there have been widespread attempts to estimate indicators of economic activity using freely available EO data (especially nighttime light images) in developing countries [156, 157]. On the other hand, there have been few attempts to do the same in developed countries. If developed countries could predict indicators of economic activity with good accuracy, it would reduce the annual budget for statistical surveys. For example, in the case of Japan, the Ministry of Internal Affairs and Communications (MIC) conducts a nationwide statistical survey every year, and the budget for the survey is about 50 billion yen per year on average. In view of the above, it is a meaningful project to be able to accurately forecast economic activity indices in advanced countries

One of the possible reasons why EO data have not been used to predict economic activity indicators in developed countries is that the night-time light image is not a reliable indicator of income in developed countries, especially in urban areas, where the observed values in night-time light images (DN value) become saturated and cannot be used as a predictive feature (= explanatory variable). On the other hand, in recent years, some studies have been conducted to better predict economic activity indicators using data other than night light (e.g., vegetation data). Therefore, the use of EO data other than night-time light, such as vegetation data, may allow us to estimate economic activity indices for developed countries with better accuracy.

The current candidates of EO data, which could be the features of the forecast, include visible light, nocturnal light, vegetation data, aerosols, and geographical information such as the area of buildings. As for the model, we will examine multiple regression analysis, LASSO, Ridge, and decision trees.

		necessary for solution	publicly available EO data
spatial	resolution	X (masked due to confidentiality)	○ (> 2 m)
	coverage	X	○ (global)
temporal	resolution	◎ (< 1 day)	○ (~ 1 day)
	coverage	○	○
geographical information		X	○

Figure 8.3: Matrix of what publicly available EO data can benefit and what our case study needed for solution in terms of spatial, temporal, and geographical information.

8.1.3 Consulting work using EO data

The purpose of this activity is to practice leveraging EO data for actual consulting business using EO data catalogue. Thanks to the cooperation with Accenture Japan Ltd., one of the biggest consulting firms, there was an opportunity to participate in a working internship (`https://ceoc.or.jp/`), during which we are expected to propose a solution to the virtual client's issue by using the actual client's data on the basis of data-science methodologies. The given client's issue was to propose a better algorithm which optimises XX to the best state, which can benefit the client, than the current algorithm.

We achieved to understand the limit of applying EO data for the actual business. As far as using publicly available EO data, it will give us a precious insight only if spatial and geographical information is available for solution. In our case, temporal resolution was crucial for solution (< 1 day) and, even worse, spatial and geographical information was undisclosed due to confidentiality (see Figure 8.3). Thus, it was difficult to apply EO data effectively to provide the better algorithm to optimise XX[*].

---

[*]Due to confidentiality, some pieces of information are masked in this section.

8.2 Research and Development (R&D) for space-weather-prediction business

One of the major effects of space weather events on satellites is atmospheric drag on low earth orbit satellites [160]. The Earth's atmosphere is heated by various solar sources including EUV or UV radiation, Coronal Mass Ejections (CMEs), and solar winds, resulting in the expansion of the Earth's atmosphere. As a consequence, the neutral density of the atmosphere in low Earth orbit increases, and the altitude of the satellite decreases rapidly due to air drag. For example, Japan's X-ray astronomy satellite "ASCA" lost its attitude control due to aerodynamic drag during an X5.7-class flare on July 14, 2000, and re-entered the atmosphere on March 02, 2001 [161]. Thus, it is important for satellite operations to predict solar flares and the associated height variations of satellites.

In this project, collaborated with Company A[†], which is engaged in the research and development of space environment prediction, I developed a space weather forecasting system that will contribute to the prediction of satellite height variation. It has been reported by Organisation B that the satellite altitude variation can be accurately predicted by using the global average for the whole Earth of a certain physical quantity X. In this joint fundamental research and development project, we aimed to predict the global average of X 24 hours ahead of the time of the prediction.

8.2.1 Achievements

We achieved to predict the global average of X 24 hours ahead within an error of 6.9%. The error, δX, is defined here as

$$\delta X = \frac{\sqrt{\frac{1}{N} \sum_i^N \left(X_i^{true} - X_i^{pred} \right)^2}}{\frac{1}{N} \sum_i^N X_i^{true}},$$

where i and N are the index and the number of the events in our sample, X_i^{true} is the global average of the actually observed X for the event i, and X_i^{pred} is the predicted value for the event i. It corresponds to the Root Mean Squared Error between the predicted and actual values for the test data of the globally averaged X divided by the temporally and globally averaged X. In the remainder of this section, we discuss the hypothesis set-up, model, results, and future directions.

There are four major variations in the global mean X: (1) daily variation derived from the Earth's rotation period, (2) 27-day variation derived from the solar rotation period,

---

[†]Due to confidentiality, some pieces of information are masked in this section.

(3) seasonal variation, and (4) abrupt variation originated from solar flares and CMEs. We hypothesised that three of the four changes, (1), (2), and (3), are cyclical in nature and therefore could be predicted to some extent by autoregressive analysis based on past global average X.

The model used was Long Short-Term Memory (LSTM), a type of deep learning model, which is commonly used for time series prediction and natural language processing [162]. It is characterised by its ability to capture both short-term and long-term trends by using two types of values: hidden state, which captures short-term features, and cell state, which captures long-term features. As for the implementation, we utilised PyTorch library [163] written in Python. In the process of developing the model, we explored two points: the number of hidden layers and the number of past hours of global average X. The data used were global average X every two hours from 2000 to 2018 (83,203 examples in total), with 2015 (solar maximum period) and 2018 (solar minimum period) as test data (8,760 examples in total). For the training data (74,443 examples in total), instead of using the global average X as they are, we used a technique called rank Gaussian, which scales the order of values (ranks) to (-1,1) and maps them to a normal distribution with an inverse error function, in order to improve the accuracy. The implementation used here is the QuantileTransformer class in the pre-processing module, which is included in the scikit-learn library [164] in Python.

As a result, we were able to predict the global mean X within an error of 6.9% for all the test data. Figure 8.4 shows the predicted results for March 2015. The white line represents the actual global average X, the background colour represents the probability distribution of the global average X at a given point in time, and the red line represents the predicted value of the global average X (= the expected value for the probability distribution of the global average X). As can be seen from the figure, we successfully predicted the daily change in the global mean X (1 in the figure) and the long-term trend of the global mean X (3 in the figure). On the other hand, on 18 March, the predictions are far off: a large flare and fast CME (719 km s^{-1}) occurred on the Sun on 15 March, and an intense geomagnetic storm (geomagnetic disturbance index Dst ~ -200 nT) occurred at the Earth on 18 March. Therefore, it is inferred that physical quantities related to space weather, including X, were greatly disturbed during this period.

From these results, we can conclude that the hypothesis that the periodic changes in (1), (2) and (3) can be predicted from the past global mean X in an autoregressive manner is correct. In order to improve the accuracy of the prediction, a model that predicts the part that cannot be predicted auto-regressively, i.e., (4) solar flare-derived abrupt changes, should be constructed and combined with the model constructed in this study.
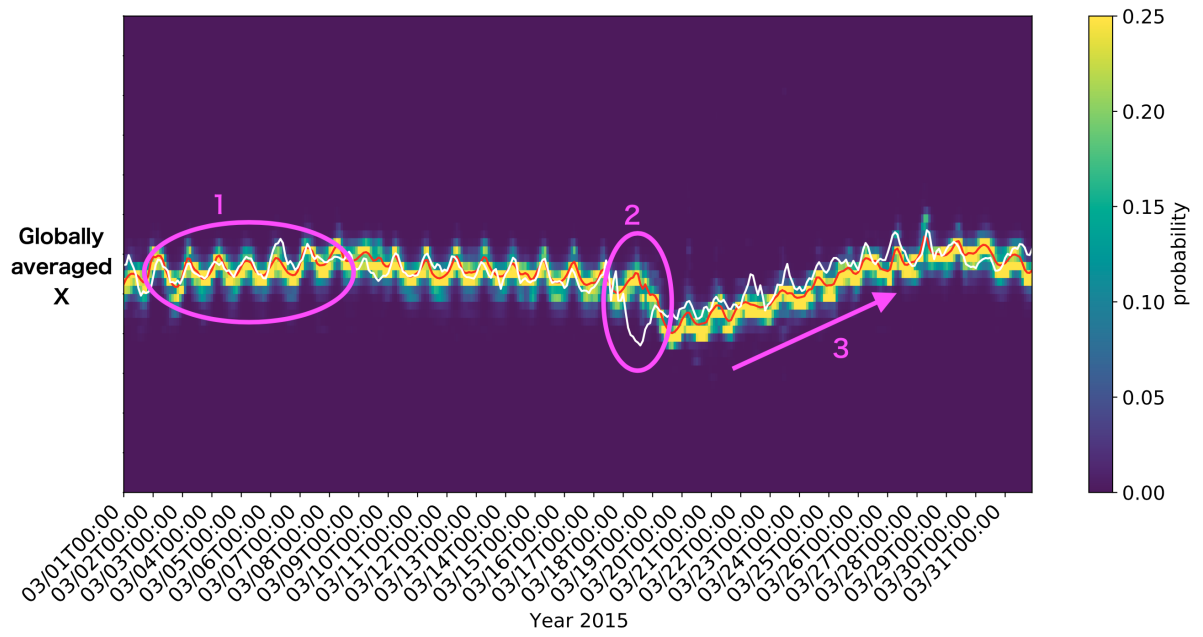
Figure 8.4: An example of the prediction on March, 2015. White line corresponds to the actual observation (globally averaged X). The background colour and red line display the probability distribution of the globally averaged X at a certain time and its expected value, respectively. One can recognise that the diurnal variation (1 in the figure) and long-term trend (3) were successfully estimated. However, we failed to predict the sudden disruption in the global average X due to a huge solar flare (2).

Summary & Conclusions

In this dissertation, the author studied the possibility and feasibility of space-weather prediction, especially the prediction of filament eruptions and CME occurrence, fully by the ground-based telescope, SMART/SDDI at Hida Observatory. The current major methodology of the prediction of solar eruptive phenomena depends on the observations by artificial satellites. However, it has been widely reported that artificial satellites are vulnerable to space weather. Moreover, the possibility of a disastrous solar flare has been intensively studied from the miscellaneous perspectives including the theoretical manner in magnetohydrodynamics, statistical studies of sun-like stars, investigating the content of the isotope, and the records in the ancient literature. Thus, if a disastrous solar flare should occur, and the majority of the satellites should suffer from loss of service, the predictability of succeeding solar flares should greatly weaken under the current situation. On the other hand, compared with artificial satellites, ground-based telescopes have little malfunctions by solar flares. Therefore, the possibility of the prediction and monitoring of solar eruptive phenomena on the basis of only the ground-based observations should be more studied as a backup.

In Chapter 2 and 3, the possibility of the prediction of filament eruptions was studied. The author and co-researchers first conducted a case study to investigate the predictability of a filament eruption on November 5, 2016. We found that the standard deviation of the LOS velocity distribution increased to 3–4 km s^{-1} 6 h prior to the eruption, compared with 2–3 km s^{-1} observed 21 h before the eruption. Thus, we concluded that the standard deviation of LOS velocity distribution could be used as the precursor of a filament eruption. Next, we further analysed other 11 events in the same manner and found that 9 out of 12 events exhibited Phase 1, during which the standard deviation of LOS velocity increased without significant changes in its average. Limited to robust estimations, our results suggest that we could predict the clearly observed filament eruptions with the lead time of 1.3 ± 0.47 h.

In Chapter 4 and 5, the possibility of predicting the occurrence of CMEs by the kinematics of filament eruptions was researched. We constructed "SMART/SDDI Filament Disappearance Catalogue," in which we listed almost all the filament eruptions observed

by the SDDI from May 2016 to June 2019 with miscellaneous information including the kinematics of filament eruptions. By investigating what physical parameters of filament eruptions determine their CME associations, we found that if the product of the maximum radial velocity normalised by 100 km s^{-1} and the filament length normalised by 100 Mm to the power of 0.96 is larger than 0.80, the filament will become a CME with a probability of 93%. Our findings suggest the importance of measuring the three-dimensional velocity of filament eruptions for the better prediction of CME occurrence.

In Chapter 6, with an introduction of Continuous H-Alpha Imaging Network (CHAIN) project, we argued the importance and feasibility of the prediction of solar eruptive phenomena based on ground-based telescopes.

In Chapter 7 and 8, the author examined the potential space-weather impacts on artificial satellites and their possible consequence. We assessed the potential impact on the artificial satellites in case of a disastrous solar flare. By taking simple linear regressions, we found that the 6-days averaged proton flux with its energy above 100 MeV showed a remarkably good correlation (R2 > 0.9) to the anomaly rate (the number of anomalies per satellite per flare event) of GEO satellites. This result implied that in case of 1-in-100-years and 1-in-1000-years solar flares, the GEO-satellite-anomaly rates should be $\sim$8 (1-in-100-years case) and $\sim$55 (1-in-1000-years case) times larger than the worst case ever observed.

In the final Chapter, for the objective of understanding the benefit of satellites' observation to human society, the author reported the outcomes of the following two projects; (1) Earth-observation data (EO data) for multidisciplinary research & consulting work, and (2) R&D for space-weather-prediction business. The achievements are summarised that (1) a list of 184 publicly available EO data was compiled, made available on the website, and used to plan a study of economic-activity estimation and a consulting business, and (2) we developed an algorithm that can predict geophysical quantity X related to space weather, which is crucial for satellite operations, 24 hours ahead with an error of 6.9%, through joint fundamental R&D with Company A.

Acknowledgement

Bibliography

[1] K. Shibata and T. Magara. Solar Flares: Magnetohydrodynamic Processes. <u>Living Reviews in Solar Physics</u>, 8:6, 2011.

[2] J. P. Delaboudinière, G. E. Artzner, J. Brunaud, A. H. Gabriel, J. F. Hochedez, F. Millier, X. Y. Song, B. Au, K. P. Dere, R. A. Howard, and et al. Eit: Extreme-ultraviolet imaging telescope for the soho mission. <u>Solar Physics</u>, 162(1–2):291–312, 1995.

[3] S. R. Kane. Impulsive (flash) Phase of Solar Flares: Hard X-Ray Microwave, EUV and Optical Observations. In Gordon Allen Newkirk, editor, <u>Coronal Disturbances</u>, volume 57, page 105, January 1974.

[4] P. F. Chen. Coronal Mass Ejections: Models and Their Observational Basis. <u>Living Reviews in Solar Physics</u>, 8:1, 2011.

[5] D. N. Baker, R. Balstad, J. M. Bodeau, E. Cameron, J. F. Fennell, G. M. Fisher, K. F. Forbes, P. M. Kintner, L. G. Leffler, W. S. Lewis, J. B. Reagan, A. A. Small III, T. A. Stansell, and L. Strachan. <u>Severe Space Weather Events–Understanding Societal and Economic Impacts: A Workshop Report</u>. The National Academies Press, Washington, D. C., 2008.

[6] H. Isobe, T. Takahashi, D. Seki, and Y. A. Yamashiki. Extreme solar flare as a catastrophic risk. <u>Jounal of Disaster Research</u>, under review.

[7] E. J. Oughton, A. Skelton, Richard B. Horne, Alan W. P. Thomson, and Charles T. Gaunt. Quantifying the daily economic impact of extreme space weather due to failure in electricity transmission infrastructure. <u>Space Weather</u>, 15:65–83, 2017.

[8] D. H. Boteler. Assessment of geomagnetic hazard to power systems in canada. <u>Natural Hazards</u>, 23(2):101–120, 2001.

[9] D. H. Boteler. A 21st century view of the march 1989 magnetic storm. <u>Space Weather</u>, 17(10):1427–1441, 2019.

[10] H. Schulte in den Bäumen, D. Moran, M. Lenzen, I. Cairns, and A. Steenge. How severe space weather can disrupt global supply chains. Natural Hazards and Earth System Sciences, 14(10):2749–2759, 2014.

[11] M. Desai and J. Giacalone. Large gradual solar energetic particle events. Living Reviews in Solar Physics, 13(3), 2016.

[12] R. B. Horne, S. A. Glauert, N. P. Meredith, D. Boscher, V. Maget, D. Heynderickx, and D. Pitchford. Space weather impacts on satellites and forecasting the earth's electron radiation belts with spacecast. Space Weather, 11(4):169–186, 2013.

[13] David F. Webb and Joe H. Allen. Spacecraft and ground anomalies related to the october-november 2003 solar activity. Space Weather, 2(3), 2004.

[14] P. Cannon, M. Angling, L. Barclay, C. Curry, C. Dyer, R. Edwards, G. Greene, M. Hapgood, R. Horne, D. Jackson, C. Mitchell, J. Owen, A. Richards, C. Rogers, K. Ryden, S. Saunders, M. Sweeting, R. Tanner, A. Thomson, and C. Underwood. Extreme space weather: impacts on engineered systems and infrastructure. Royal Academy of Engineering, London, 2013.

[15] H. Maehara, T. Shibayama, S. Notsu, Y. Notsu, T. Nagao, S. Kusaba, S. Honda, D. Nogami, and K. Shibata. Superflares on solar-type stars. Nature, 485:478–481, 2012.

[16] H. Maehara, T. Shibayama, Y. Notsu, S. Notsu, S. Honda, D. Nogami, and K. Shibata. Statistical properties of superflares on solar-type stars based on 1-min cadence data. Earth, Planets, and Space, 67(59), 2015.

[17] T. Shibayama, H. Maehara, S. Notsu, Y. Notsu, T. Nagao, S. Honda, T. T. Ishii, D. Nogami, and K. Shibata. Superflares on solar-type stars observed with kepler. i. statistical properties of superflares. The Astrophysical Journal Supplement Series, 209(5), 2013.

[18] Y. Notsu, H. Maehara, S. Honda, S. L. Hawley, James R. A. Davenport, K. Namekata, S. Notsu, Kai Ikuta, D. Nogami, and K. Shibata. Do kepler superflare stars really include slowly-rotating sun-like stars?—results using apo 3.5m telescope spectroscopic observations and gaia-dr2 data—. The Astrophysical Journal, 876(1), 2019.

[19] Soshi Okamoto, Yuta Notsu, Hiroyuki Maehara, Kosuke Namekata, Satoshi Honda, Kai Ikuta, Daisaku Nogami, and Kazunari Shibata. Statistical Properties of Super-

flares on Solar-type Stars: Results Using All of the Kepler Primary Mission Data. The Astrophysical Journal, 906(2):72, January 2021.

[20] K. Shibata, H. Isobe, A. Hillier, Arnab Rai Choudhuri, H. Maehara, T. T. Ishii, T. Shibayama, et al. Can superflares occur on our sun? Publications of the Astronomical Society of Japan, 65(49), 2013.

[21] F. Miyake, K. Nagaya, K. Masuda, and T. Nakamura. A signature of cosmic-ray increase in ad 774–775 from tree rings in japan. Nature, 486(7402):240–242, 2012.

[22] F. Miyake, K. Masuda, and T. Nakamura. Another rapid event in the carbon-14 content of tree rings. Nature Communications, 4(1), 2013.

[23] I. G. Usoskin and G. A. Kovaltsov. Occurrence of extreme solar particle events: Assessment from historical proxy data. The Astrophysical Journal, 757(1):92, 2012.

[24] A. Veronig, B. Vrsnak, M. Temmer, J. Magdalenic, and A. Hanslmeier. Statistical study of solar flares observed in soft x-ray, hard x-ray, and halpha emission. Hvar Observatory Bulletin, 25(1):39–48, 2001.

[25] M. Notsuki, T. Hatanaka, and W. Unno. A very unusual flare on february 23, 1956. Publications of the Astronomical Society of Japan, 8(1), 1956.

[26] T. Takahashi, Y. Mizuno, and K. Shibata. Scaling relations in coronal mass ejections and energetic proton events associated with solar superflares. The Astrophysical Journal Letters, 833(L8), 2016.

[27] H. Hayakawa, H. Tamazawa, Y. Uchiyama, Y. Ebihara, H. Miyahara, S. Kosaka, K. Iwahashi, and H. Isobe. Historical auroras in the 990s: Evidence of great magnetic storms. Solar Physics, 292(1), 2016.

[28] H. Hayakawa, K. Iwahashi, Y. Ebihara, H. Tamazawa, K. Shibata, D. J. Knipp, A. D. Kawamura, K. Hattori, K. Mase, I. Nakanishi, and H. Isobe. Long-lasting extreme magnetic storm activities in 1770 found in historical documents. The Astrophysical Journal, 850(2):L31, 2017.

[29] H. Hayakawa, Y. Ebihara, D. M. Willis, K. Hattori, A. S. Giunta, M. N. Wild, S. Hayakawa, S. Toriumi, Y. Mitsuma, L. T. Macdonald, K. Shibata, and S. M. Silverman. The great space weather event during 1872 february recorded in east asia. The Astrophysical Journal, 862(1):15, 2018.

[30] H. Hayakawa, Y. Ebihara, E. W. Cliver, K. Hattori, S. Toriumi, J. J. Love, N. Umemura, K. Namekata, T. Sakaue, T. Takahashi, and K. Shibata. The extreme space weather event in September 1909. Monthly Notices of the Royal Astronomical Society, 484(3):4083–4099, 2018.

[31] R. Kippenhahn and A. Schlüter. Eine Theorie der solaren Filamente (in German). Zeitschrift fur Astrophysik, 43(36–62):36, 1957.

[32] M. Kuperus and M. A. Raadu. The support of prominences formed in neutral sheets. Astronomy and Astrophysics, 31:189–193, 1974.

[33] H. R. Gilbert, T. E. Holzer, B. C. Low, and J. T. Burkepile. Observational interpretation of an active prominence on 1999 may 1. Astrophysical Journal, 549:1221–1230, 2001.

[34] S. Parenti. Solar prominences: Observations. Living Reviews in Solar Physics, 11(1):1–88, 2014.

[35] S. F. Smith and H. E. Ramsey. The Flare-Associated Filament Disappearance. Zeitschrift fur Astrophysik, 60:1–18, 1964.

[36] E. Tandberg-Hanssen. The Nature of Solar Prominences, volume 199 of Astrophysics and Space Science Library. Springer, Dordrecht, 1995.

[37] A. C. Sterling, R. L. Moore, and S. L. Freeland. Insights into filament eruption onset from solar dynamics observatory observations. The Astrophysical Journal, 731(L3):1–6, 2011.

[38] L. K. Harra, S. A. Matthews, and J. L. Culhane. Nonthermal Velocity Evolution in the Precursor Phase of a Solar Flare. Astrophysical Journal, 549:L245–L248, 2001.

[39] K. Ichimoto, T. T. Ishii, K. Otsuji, G. Kimura, Y. Nakatani, N. Kaneda, S. Nagata, S. UeNo, K. Hirose, D. Cabezas, and S. Morita. A New Solar Imaging System for Observing High-Speed Eruptions: Solar Dynamics Doppler Imager (SDDI). Solar Physics, 292:63, 2017.

[40] S. UeNo, S. Nagata, R. Kitai, H. Kurokawa, and K. Ichimoto. The development of filter vector magnetographs for the Solar Magnetic Activity Research Telescope (SMART). In Alan F. M. Moorwood and Masanori Iye, editors, Ground-based Instrumentation for Astronomy, volume 5492 of Society of Photo-Optical Instrumentation Engineers (SPIE) Conference Series, pages 958–969, 2004.

154

[41] B. Kliem and T. Török. Torus Instability. Physical Review Letters, 96(25):255002, 2006.

[42] G. Bateman. MHD Instabilities. The MIT Press, Cambridge, 1978.

[43] J. Feynman and S. F. Martin. The initiation of coronal mass ejections by newly emerging magnetic flux. Journal of Geophysical Research, 100:3355–3367, 1995.

[44] P. F. Chen and K. Shibata. An Emerging Flux Trigger Mechanism for Coronal Mass Ejections. Astrophysical Journal, 545:524–531, 2000.

[45] G. Del Zanna. The multi-thermal emission in solar active regions. Astronomy and Astrophysics, 558(A73):1–20, 2013.

[46] J. R. Lemen, A. M. Title, D. J. Akin, P. F. Boerner, C. Chou, J. F. Drake, D. W. Duncan, C. G. Edwards, F. M. Friedlaender, G. F. Heyman, N. E. Hurlburt, N. L. Katz, G. D. Kushner, M. Levay, R. W. Lindgren, D. P. Mathur, E. L. McFeaters, S. Mitchell, R. A. Rehse, C. J. Schrijver, L. A. Springer, R. A. Stern, T. D. Tarbell, J.-P. Wuelser, C. J. Wolfson, C. Yanari, J. A. Bookbinder, P. N. Cheimets, D. Caldwell, E. E. Deluca, R. Gates, L. Golub, S. Park, W. A. Podgorski, R. I. Bush, P. H. Scherrer, M. A. Gummin, P. Smith, G. Auker, P. Jerram, P. Pool, R. Soufli, D. L. Windt, S. Beardsley, M. Clapp, J. Lang, and N. Waltham. The Atmospheric Imaging Assembly (AIA) on the Solar Dynamics Observatory (SDO). Solar Physics, 275:17–40, 2012.

[47] P. H. Scherrer, J. Schou, R. I. Bush, A. G. Kosovichev, R. S. Bogart, J. T. Hoeksema, Y. Liu, T. L. Duvall, J. Zhao, A. M. Title, C. J. Schrijver, T. D. Tarbell, and S. Tomczyk. The Helioseismic and Magnetic Imager (HMI) Investigation for the Solar Dynamics Observatory (SDO). Solar Physics, 275:207–227, 2012.

[48] J. W. Harvey, J. Bolding, R. Clark, D. Hauth, F. Hill, R. Kroll, G. Luis, N. Mills, T. Purdy, C. Henney, D. Holland, and J. Winter. Full-disk Solar H-alpha Images From GONG. In AAS/Solar Physics Division Abstracts #42, volume 43 of Bulletin of the American Astronomical Society, page 17.45, 2011.

[49] G. E. Brueckner, R. A. Howard, M. J. Koomen, C. M. Korendyke, D. J. Michels, J. D. Moses, D. G. Socker, K. P. Dere, P. L. Lamy, A. Llebaria, M. V. Bout, R. Schwenn, G. M. Simnett, D. K. Bedford, and C. J. Eyles. The Large Angle Spectroscopic Coronagraph (LASCO). Solar Physics, 162:357–402, 1995.

[50] M. Nose, M. Sugiura, and T Kamei. Geomagnetic Dst index. doi:10.17593/14515-74000, 2015.

[51] H. V. Cane and I. G. Richardson. Interplanetary coronal mass ejections in the near-Earth solar wind during 1996-2002. Journal of Geophysical Research (Space Physics), 108(A4):1156, 2003.

[52] N. Gopalswamy, A. Lara, R. P. Lepping, M. L. Kaiser, D. Berdichevsky, and O. C. St. Cyr. Interplanetary acceleration of coronal mass ejections. Geophysical Research Letters, 27(2):145–148, 2000.

[53] B. Filippov. A filament eruption on 2010 october 21 from three viewpoints. Astrophysical Journal, 773(10):1–8, 2013.

[54] N. C. Joshi, A. K. Srivastava, B. P. Filippov, and P. Kayshap. Confined partial filament eruption and its reformation within a stable magnetic flux rope. Astrophysical Journal, 787(11):1–13, 2014.

[55] N. C. Joshi, T. Magara, and S. Inoue. Formation of a compound flux rope by the merging of two filament channels, the associated dynamics, and its stability. Astrophysical Journal, 795(4):1–15, 2014.

[56] H. Li, Y. Liu, and A. Elmhamdi. Relationship between distribution of magnetic decay index and filament eruptions. Astrophysical Journal, 830(132), 2016.

[57] A. R. Yeates. Potential Field Source Surface Solver. `https://github.com/antyeates1983/pfss`, 2017.

[58] A. A. van Ballegooijen, E. R. Priest, and D. H. Mackay. Mean field model for the formation of filament channels on the sun. Astrophysical Journal, 539:983–994, 2000.

[59] J. M. Beckers. A Study of the Fine Structures in the Solar Chromosphere. PhD thesis, University of Utrecht, 1964.

[60] T. Morimoto and H. Kurokawa. A Method for the Determination of 3-D Velocity Fields of Disappearing Solar Filaments. Publications of the Astronomical Society of Japan, 55:503–518, 2003.

[61] T. Morimoto and H. Kurokawa. Eruptive and Quasi-Eruptive Disappearing Solar Filaments and Their Relationship with Coronal Activities. Publications of the Astronomical Society of Japan, 55:1141–1151, 2003.

[62] T. Morimoto, H. Kurokawa, K. Shibata, and T. T. Ishii. Energetic relations between the disappearing solar filaments and the associated flare arcades. Publications of the Astronomical Society of Japan, 62(4):939–949, 2010.

[63] D. P. Cabezas, L. M. Martínez, Y. J. Buleje, M. Ishitsuka, J. K. Ishitsuka, S. Morita, A. Asai, S. UeNo, T. T. Ishii, R. Kitai, S. Takasao, Y. Yoshinaga, K. Otsuji, and K. Shibata. "Dandelion" Filament Eruption and Coronal Waves Associated with a Solar Flare on 2011 February 16. Astrophysical Journal, 836:33, 2017.

[64] T. Sakaue, A. Tei, A. Asai, S. UeNo, K. Ichimoto, and K. Shibata. Observational study on the fine structure and dynamics of a solar jet. ii. energy release process revealed by spectral analysis. Publications of the Astronomical Society of Japan, 70(6), 2018.

[65] D. Seki, K. Otsuji, H. Isobe, T. T. Ishii, T. Sakaue, and K. Hirose. Increase in the Amplitude of Line-of-sight Velocities of the Small-scale Motions in a Solar Filament before Eruption. Astrophysical Journal, 843:L24, 2017.

[66] D. Seki, K. Otsuji, H. Isobe, T. T. Ishii, K. Ichimoto, and K. Shibata. Small-scale motions in solar filaments as the precursors of eruptions. Publications of the Astronomical Society of Japan, 71(3):56(1–18), 2019.

[67] A. C. Sterling and R. L. Moore. Evidence for Gradual External Reconnection before Explosive Eruption of a Solar Filament. Astrophysical Journal, 602:1024–1036, 2004.

[68] H. Isobe and D. Tripathi. Large amplitude oscillation of a polar crown filament in the pre-eruption phase. Astronomy and Astrophysics, 449:L17–L20, 2006.

[69] T. E. Berger, R. A. Shine, G. L. Slater, T. D. Tarbell, A. M. Title, T. J. Okamoto, K. Ichimoto, Y. Katsukawa, Y. Suematsu, S. Tsuneta, B. W. Lites, and T. Shimizu. Hinode SOT Observations of Solar Quiescent Prominence Dynamics. Astrophysical Journal, 676:L89, 2008.

[70] T. Berger, P. Testa, A. Hillier, P. Boerner, B. C. Low, K. Shibata, C. Schrijver, T. Tarbell, and A. Title. Magneto-thermal convection in solar prominences. Nature, 472:197–200, 2011.

[71] A. Hillier, H. Isobe, K. Shibata, and T. Berger. Numerical Simulations of the Magnetic Rayleigh-Taylor Instability in the Kippenhahn-Schlüter Prominence Model. Astrophysical Journal, 736:L1, 2011.

[72] Andrew Hillier, Thomas Berger, Hiroaki Isobe, and Kazunari Shibata. NUMERICAL SIMULATIONS OF THE MAGNETIC RAYLEIGH-TAYLOR INSTABILITY IN THE KIPPENHAHN-SCHLÜTER PROMINENCE MODEL. i. FORMATION OF UPFLOWS. The Astrophysical Journal, 746(2):120, jan 2012.

[73] C. Chifor, H. E. Mason, D. Tripathi, H. Isobe, and A. Asai. The early phases of a solar prominence eruption and associated flare: a multi-wavelength analysis. Astronomy and Astrophysics, 458:965–973, 2006.

[74] R. L. Moore, A. C. Sterling, H. S. Hudson, and J. R. Lemen. Onset of the Magnetic Explosion in Solar Flares and Coronal Mass Ejections. Astrophysical Journal, 552:833–848, 2001.

[75] K. Kusano, Y. Bamba, T. T. Yamamoto, Y. Iida, S. Toriumi, and A. Asai. Magnetic Field Structures Triggering Solar Flares and Coronal Mass Ejections. Astrophysical Journal, 760(31):1–9, 2012.

[76] N. Ishiguro and K. Kusano. Double arc instability in the solar corona. The Astrophysical Journal, 843(2):101, 2017.

[77] A. H. McAllister, M. Dryer, P. McIntosh, H. Singer, and L. Weiss. A large polar crown coronal mass ejection and a "problem" geomagnetic storm: April 14-23, 1994. Journal of Geophysical Research, 101:13497–13516, 1996.

[78] H. Isobe, Y. Ebihara, A. D. Kawamura, H. Tamazawa, and H. Hayakawa. Intense geomagnetic storm during maunder minimum possibly by a quiescent filament eruption. The Astrophysical Journal, 887(1):7, 2019.

[79] A. C. Sterling, R. L. Moore, and L. K. Harra. Lateral Offset of the Coronal Mass Ejections from the X-flare of 2006 December 13 and Its Two Precursor Eruptions. Astrophysical Journal, 743:63, 2011.

[80] S. Gosain, B. Schmieder, P. Venkatakrishnan, R. Chandra, and G. Artzner. 3D Evolution of a Filament Disappearance Event Observed by STEREO. Solar Physics, 259:13–30, 2009.

[81] L. Ofman, T. A. Kucera, Z. Mouradian, and A. I. Poland. SUMER Observations of the Evolution and the Disappearance of a Solar Prominence. Solar Physics, 183:97–106, 1998.

[82] S. K. Antiochos, C. R. DeVore, and J. A. Klimchuk. A Model for Solar Coronal Mass Ejections. Astrophysical Journal, 510:485–493, 1999.

[83] T. Magara and S. Tsuneta. Hinode's Observational Result on the Saturation of Magnetic Helicity Injected into the Solar Atmosphere and Its Relation to the Occurrence of a Solar Flare. Publications of the Astronomical Society of Japan, 60:1181–1189, 2008.

[84] L. K. Harra, D. R. Williams, A. J. Wallace, T. Magara, H. Hara, S. Tsuneta, A. C. Sterling, and G. A. Doschek. Coronal Nonthermal Velocity Following Helicity Injection Before an X-Class Flare. Astrophysical Journal, 691:L99–L102, 2009.

[85] N. Gopalswamy, S. Yashiro, G. Michalek, G. Stenborg, A. Vourlidas, S. Freeland, and R. Howard. The SOHO/LASCO CME Catalog. Earth Moon and Planets, 104:295–313, 2009.

[86] S. Yashiro, N. Gopalswamy, G. Michalek, O. C. St. Cyr, S. P. Plunkett, N. B. Rich, and R. A. Howard. A catalog of white light coronal mass ejections observed by the SOHO spacecraft. Journal of Geophysical Research (Space Physics), 109(A7):A07105, 2004.

[87] J. Kubota and A. Uesugi. The vertical motion of matter in a prominence observed on May 7, 1984. Publications of the Astronomical Society of Japan, 38:903–909, 1986.

[88] E. W. Cliver, K. S. Balasubramaniam, N. V. Nitta, and X. Li. Great geomagnetic storm of 9 november 1991: Association with a disappearing solar filament. Journal of Geophysical Research: Space Physics, 114(A3):A00A20, 2009.

[89] J. A. Joselyn and P. S. McIntosh. Disappearing solar filaments: A useful predictor of geomagnetic activity. Journal of Geophysical Research: Space Physics, 86(A6):4555–4564, 1981.

[90] S. UeNo, K. Shibata, G. Kimura, Y. Nakatani, R. Kitai, and S. Nagata. CHAIN-project and installation of the flare monitoring telescopes in developing countries. Bulletin of the Astronomical Society of India, 35:697–704, 2007.

[91] D. Seki, S. UeNo, H. Isobe, K. Otsuji, D. P. Cabezas, K. Ichimoto, K. Shibata, and CHAIN team. Space Weather Prediction from the Ground: Case of CHAIN. Sun and Geosphere, 13(2):157–161, 2018.

[92] E. R. Priest and T. G. Forbes. Magnetic Field Evolution during Prominence Eruptions and Two-Ribbon Flares. Solar Physics, 126(2):319–350, 1990.

[93] T. Török and B. Kliem. Confined and Ejective Eruptions of Kink-unstable Flux Ropes. Astrophysical Journal Letters, 630(1):L97–L100, 2005.

[94] T. Sakurai. Magnetohydrodynamic interpretation of the motion of prominences. Publications of the Astronomical Society of Japan, 28(2):177–198, 1976.

[95] J. Liu, Y. Ye, C. Shen, Y. Wang, and R. Erdélyi. A New Tool for CME Arrival Time Prediction using Machine Learning Algorithms: CAT-PUMA. Astrophysical Journal, 855(2):109, 2018.

[96] N. Gopalswamy, A. Lara, S. Yashiro, M. L. Kaiser, and R. A. Howard. Predicting the 1-AU arrival times of coronal mass ejections. Journal of Geophysical Research, 106(A12):29207–29218, 2001.

[97] V. Domingo, B. Fleck, and A. I. Poland. The SOHO Mission: an Overview. Solar Physics, 162(1–2):1–37, 1995.

[98] W. Dean Pesnell, B. J. Thompson, and P. C. Chamberlin. The Solar Dynamics Observatory (SDO). Solar Physics, 275(1-2):3–15, 2012.

[99] G. R. Gapper, A. Hewish, A. Purvis, and P. J. Duffett-Smith. Observing interplanetary disturbances from the ground. Nature, 296(5858):633–636, 1982.

[100] T. Iju, M. Tokumaru, and K. Fujiki. Radial Speed Evolution of Interplanetary Coronal Mass Ejections During Solar Cycle 23. Solar Physics, 288(1):331–353, 2013.

[101] N. Gopalswamy, M. Shimojo, W. Lu, S. Yashiro, K. Shibasaki, and R. A. Howard. Prominence Eruptions and Coronal Mass Ejection: A Statistical Study Using Microwave Observations. Astrophysical Journal, 586(1):562–578, 2003.

[102] S. UeNo, K. Shibata, S. Morita, G. Kimura, A. Asai, R. Kitai, K. Ichimoto, S. Nagata, T. Ishii, Y. Nakatani, Y. Masashi, and et al. International Collaboration and Academic Exchange of the CHAIN Project in this Three Years (Period). Sun and Geosphere, 9:97–103, 2014.

[103] R. M. E. Illing and A. J. Hundhausen. Observation of a coronal transient from 1.2 to 6 solar radii. Journal of Geophysical Research: Space Physics, 90(A1):275–282, 1985.

[104] D. F Webb. Eruptive prominences and their association with coronal mass ejections. In JC. Vial and O. Engvold, editors, Solar prominences, volume 415 of Astrophysics and Space Science Library, pages 411–432. Springer, Cham, 2015.

[105] A. H. McAllister, H. Kurokawa, K. Shibata, and N. Nitta. A filament eruption and accompanying coronal field changes on november 5, 1992. Solar Physics, 169:123–149, 1996.

[106] K. Hori and J. L. Culhane. Trajectories of microwave prominence eruptions. Astronomy & Astrophysics, 382(2):666–677, 2002.

[107] H. Nakajima, M. Nishio, S. Enome, K. Shibasaki, T. Takano, Y. Hanaoka, C. Torii, H. Sekiguchi, T. Bushimata, S. Kawashima, et al. The nobeyama radioheliograph. Proceedings of the IEEE, 82(5):705–713, 1994.

[108] D. Seki, K. Otsuji, T. T. Ishii, K. Hirose, T. Iju, S. UeNo, D. P. Cabezas, A. Asai, H. Isobe, K. Ichimoto, and K. Shibata. SMART/SDDI Filament Disappearance Catalogue. Sun and Geosphere, 14(2):95–103, 2019.

[109] S. UeNo, S. Nagata, R. Kitai, and H. Kurokawa. Features of Solar Telescopes at the Hida Observatory and the Possibilities of Coordinated Observations with SolarB. In T. Sakurai and T. Sekii, editors, The Solar-B Mission and the Forefront of Solar Physics, volume 325 of Astronomical Society of the Pacific Conference Series, page 319, 2004.

[110] P. I. McCauley, Y. N. Su, N. Schanche, K. E. Evans, C. Su, S. McKillop, and K. K. Reeves. Prominence and Filament Eruptions Observed by the Solar Dynamics Observatory: Statistical Properties, Kinematics, and Online Catalog. Solar Physics, 290:1703–1740, 2015.

[111] M. Al-Omari, R. Qahwaji, T. Colak, and S. Ipson. Machine leaning-based investigation of the associations between cmes and filaments. Solar Physics, 262(2):511–539, 2010.

[112] H. R. Gilbert, T. E. Holzer, J. T. Burkepile, and A. J. Hundhausen. Active and eruptive prominences and their relationship to coronal mass ejections. The Astrophysical Journal, 537(1):503–515, 2000.

[113] RE. Fan, KW. Chang, CJ. Hsieh, XR. Wang, and CJ. Lin. Liblinear: A library for large linear classification. Journal of machine learning research, 9:1871–1874, 2008.

[114] K. M. Ashman, C. M. Bird, and S. E. Zepf. Detecting Bimodality in Astrometrical Datasets. The Astronomical Journal, 108:2348, 1994.

[115] Alexander L. Muratov and Oleg Y. Gnedin. MODELING THE METALLIC-ITY DISTRIBUTION OF GLOBULAR CLUSTERS. The Astrophysical Journal, 718(2):1266–1288, jul 2010.

[116] Nathan L Carlson, Madina R Sultanova, Sandanuwan P Kalawila Vithanage, Wayne A Barkhouse, Gihan L Ipita Kaduwa Gamage, Cody M Rude, and Omar López-Cruz. Globular cluster population of the HST frontier fields galaxy j07173724+3744224. Monthly Notices of the Royal Astronomical Society, 480(2):1956–1972, jul 2018.

[117] P. Heinzel, B. Schmieder, F. Fárník, P. Schwartz, N. Labrosse, P. Kotrč, U. Anzer, G. Molodij, A. Berlicki, E. E. DeLuca, and et al. Hinode,trace,soho, and ground-based observations of a quiescent prominence. The Astrophysical Journal, 686(2):1383–1396, 2008.

[118] H. R. Gilbert, L. E. Falco, T. E. Holzer, and R. M. MacQueen. Application of a New Technique for Deriving Prominence Mass from SOHO EIT Fe XII (19.5 nm) Absorption Features. The Astrophysical Journal, 641(1):606–610, 2006.

[119] S. Pojoga and T.S. Huang. On the sudden disappearances of solar filamentsand their relationship with coronal mass ejections. Advances in Space Research, 32(12):2641–2646, 2003.

[120] J. Jing, V. B. Yurchyshyn, G. Yang, Y. Xu, and H. Wang. On the Relation between Filament Eruptions, Flares, and Coronal Mass Ejections. The Astrophysical Journal, 614(2):1054–1062, 2004.

[121] C. J. Schrijver, K. Kauristie, A. D. Aylward, C. M. Denardini, S. E. Gibson, A. Glover, N. Gopalswamy, M. Grande, M. Hapgood, D. Heynderickx, N. Jakowski, V. V. Kalegaev, G. Lapenta, J. A. Linker, S. Liu, C. H. Mandrini, I. R. Mann, T. Nagatsuma, D. Nandy, T. Obara, T. Paul O'Brien, T. Onsager, H. J. Opgenoorth, M. Terkildsen, C. E. Valladares, and N. Vilmer. Understanding space weather to shield society: A global road map for 2015-2025 commissioned by COSPAR and ILWS. Advances in Space Research, 55:2745–2807, 2015.

[122] M. Steinegger, C. Denker, P. R. Goode, W. H. Marquette, J. Varsik, H. Wang, W. Otruba, H. Freislich, A. Hanslmeier, G. Luo, D. Chen, and Q. Zhang. The New Global High-Resolution Hα Network: First Observations and First Results. In A. Wilson, editor, The Solar Cycle and Terrestrial Climate, Solar and Space weather, volume 463 of ESA Special Publication, page 617, 2000.

[123] J. K. Ishitsuka, M. Ishitsuka, H. Trigoso Avilés, T. Sakurai, Y. Nishino, H. Miyazaki, K. Shibata, S. UeNo, K. Yumoto, and G. Maeda. A solar observing station for education and research in Peru. Bulletin of the Astronomical Society of India, 35:709–712, 2007.

[124] S. UeNo, K. Shibata, R. Kitai, K. Ichimoto, S. Nagata, H. Isobe, G. Kimura, Y. Nakatani, M. Kadota, T. T. Ishii, S. Morita, and K. Otsuji. The chain-project and installation of flare monitoring telescopes in developing countries. Data Science Journal, 8:S51–S58, 2009.

[125] S. UeNo, K. Shibata, K. Ichimoto, R. Kitai, S. Nagata, G. Kimura, and Y. Nakatani. Continuous H-alpha Imaging Network Project (CHAIN) with Ground- based Solar Telescopes for Space Weather Research. African Skies, 14:17, 2010.

[126] N. Seghouani. Un Observatoire dans la région des Aurès. African Skies, 14:44, 2010.

[127] J. K. Ishitsuka, A. Asai, S. Morita, R. Terrazas, D. P. Cabezas, V. Gutierrez, L. Martinez, Y. Buleje, R. Loayza, N. Nakamura, S. Takasao, Y. Yoshinaga, A. Hillier, K. Otsuji, K. Shibata, M. Ishitsuka, S. Ueno, R. Kitai, T. Ishii, K. Ichimoto, S. Nagata, and N. Narukage. Within the International Collaboration CHAIN: a Summary of Events Observed with Flare Monitoring Telescope (FMT) in Peru. Sun and Geosphere, 9:85–96, 2014.

[128] K. Nagashima, H. Isobe, T. Yokoyama, T. T. Ishii, T. J. Okamoto, and K. Shibata. Triggering Mechanism for the Filament Eruption on 2005 September 13 in NOAA Active Region 10808. Astrophysical Journal, 668:533–545, 2007.

[129] N. Narukage, T. T. Ishii, S. Nagata, S. UeNo, R. Kitai, H. Kurokawa, M. Akioka, and K. Shibata. Three Successive and Interacting Shock Waves Generated by a Solar Flare. Astrophysical Journal Letters, 684(1):L45, 2008.

[130] A. Asai, K. Shibata, T. T. Ishii, M. Oka, R. Kataoka, K. Fujiki, and N. Gopalswamy. Evolution of the anemone AR NOAA 10798 and the related geo-effective flares and CMEs. Journal of Geophysical Research (Space Physics), 114(A12):A00A21, 2009.

[131] Y. Zhang, R. Kitai, N. Narukage, T. Matsumoto, S. UeNo, K. Shibata, and J. Wang. Propagation of Moreton Waves. Publications of the Astronomical Society of Japan, 63:685, 2011.

[132] A. Asai, T. T. Ishii, H. Isobe, R. Kitai, K. Ichimoto, S. UeNo, S. Nagata, S. Morita, K. Nishida, D. Shiota, A. Oi, M. Akioka, and K. Shibata. First Simultaneous Observation of an Hα Moreton Wave, EUV Wave, and Filament/Prominence Oscillations. Astrophysical Journal Letters, 745(2):L18, 2012.

[133] T. T. Ishii, T. Kawate, Y. Nakatani, S. Morita, K. Ichimoto, and S. Masuda. High-Speed Imaging System for Solar-Flare Research at Hida Observatory. Publications of the Astronomical Society of Japan, 65:39, 2013.

[134] Y. Shen, K. Ichimoto, T. T. Ishii, Z. Tian, R. Zhao, and K. Shibata. A Chain of Winking (Oscillating) Filaments Triggered by an Invisible Extreme-ultraviolet Wave. Astrophysical Journal, 786(2):151, 2014.

163

[135] V. Kurt, A. Belov, H. Mavromichalaki, and M. Gerontidou. Statistical analysis of solar proton events. Annales Geophysicae, 22:2255, 2004.

[136] HS. Choi, J. Lee, KS. Cho, YS. Kwak, IH. Cho, YD. Park, YH. Kim, D. N. Baker, G. D. Reeves, and DK. Lee. Analysis of geo spacecraft anomalies: Space weather relationships. Space Weather, 9(S06001), 2011.

[137] V. Pilipenko, N. Yagova, N. Romanova, and J. Allen. Statistical relationships between satellite anomalies at geostationary orbit and high-energy particles. Advances in Space Research, 37:1192–1205, 2006.

[138] Abt Associates Inc. Social and Economic Impacts of Space Weather in the United States. https://www.weather.gov/media/news/SpaceWeatherEconomicImpactsReportOct-2017.pdf, 2017.

[139] S. Odenwald, James G., and William T. Forecasting the impact of an 1859-calibre superstorm on satellite resources. Advances in Space Research, 38:280–297, 2006.

[140] D. C. Wilkinson. National oceanic and atmospheric administration's space craft anomaly data base and exmaples of solar activity affecting spacecraft. Journal of Spacecraft and Rockets, 31(2):160, 1994.

[141] G. Rostoker. Effects of substorms on the stormtime ring current index dst. Annales Geophysicae, 18:1390–1398, 2000.

[142] R. C. Carrington. Description of a Singular Appearance seen in the Sun on September 1, 1859. Monthly Notices of the Royal Astronomical Society, 20(1):13–15, 1859.

[143] H. Hayakawa, F. R. Stephenson, Y. Uchikawa, Y. Ebihara, C. J. Scott, M. N. Wild, J. Wilkinson, and D. M. Willis. The celestial sign in the anglo-saxon chronicle in the 770s: Insights on contemporary solar activity. Solar Physics, 294(4), 2019.

[144] K. Hattori, H. Hayakawa, and Y. Ebihara. Occurrence of great magnetic storms on 6-8 March 1582. Monthly Notices of the Royal Astronomical Society, 487(3):3550–3559, 2019.

[145] V. M. Vasyliūnas. The largest imaginable magnetic storm. Journal of Atmospheric and Solar-Terrestrial Physics, 73:1444–1446, 2011.

[146] J. H. King and N. E. Papitashvili. Solar wind spatial scales in and comparisons of hourly wind and ace plasma and magnetic field data. Journal of Geophysical Research, 110(A02104), 2005.

[147] N. Iucci, A. E. Levitin, A. V. Belov, E. A. Eroshenko, N. G. Ptitsyna, G. Villoresi, G. V. Chizhenkov, et al. Space weather conditions and spacecraft anomalies in different orbits. <u>Space Weather</u>, 3(S01001), 2005.

[148] A. Belov, L. Dorman, N. Iucci, O. Kryakunova, and N. Ptitsyna. The relation of high and low-orbit satellite anomalies to different geophysical parameters. In D. Ioannis, editor, <u>Effects of Space Weather on Technology Infrastructure</u>, pages 147–164. Kluwer Academic Publishers, 2004.

[149] SM. Tam. Earth observations for official statistics–satellite imagery and geospatial data task team report. `https://unstats.un.org/bigdata/taskteams/satellite/UNGWG_Satellite_Task_Team_Report_WhiteCover.pdf`, 2017.

[150] S. Di Pippo. European global navigation satellite system and copernicus: Supporting the sustainable development goals. `https://www.unoosa.org/res/oosadoc/data/documents/2018/stspace/stspace71_0_html/st_space_71E.pdf`, 2018.

[151] EO4SDG Initiative. Earth Observations for the Sustainable Development Goals. `https://eo4sdg.org/`, Accessed on November 29, 2020.

[152] Committee on Earth Observation Satellites. `http://database.eohandbook.com/database/instrumenttable.aspx`, Accessed on November 29, 2020.

[153] Google Earth Engine. `https://developers.google.com/earth-engine/datasets/catalog`, Accessed on November 29, 2020.

[154] G-Portal. `https://gportal.jaxa.jp/gpr/`, Accessed on November 29, 2020.

[155] NASA Socioeconomic Data and Applications Center. `https://sedac.ciesin.columbia.edu`, Accessed on November 29, 2020.

[156] N. Jean, M. Burke, M. Xie, W. M. Davis, D. B. Lobell, and S. Ermon. Combining satellite imagery and machine learning to predict poverty. <u>Science</u>, 353(6301):790–794, 2016.

[157] S. Keola, M. Andersson, and O. Hall. Monitoring economic development from space: Using nighttime light and land cover data to measure economic growth. <u>World Development</u>, 66:322–334, 2015.

[158] D. Donaldson and A. Storeygard. The view from above: Applications of satellite data in economics. <u>Journal of Economic Perspectives</u>, 30(4):171–198, 2016.

[159] C. D. Elvidge, K. E. Baugh, S. J. Anderson, P. C. Sutton, and T. Ghosh. The night light development index (NLDI): a spatially explicit measure of human development from satellite data. Social Geography, 7(1):23–35, 2012.

[160] G. W. Prölss. Density perturbations in the upper atmosphere caused by the dissipation of solar wind energy. Surveys in Geophysics, 32(2):101–195, 2010.

[161] JAXA Institute of Space and Astronautical Science. ASCA. `https://www.isas.jaxa.jp/en/missions/spacecraft/past/asca.html`, Accessed on November 14, 2020.

[162] S. Hochreiter and J. Schmidhuber. Long short-term memory. Neural Computation, 9(8):1735–1780, 1997.

[163] A. Paszke, S. Gross, F. Massa, A. Lerer, J. Bradbury, G. Chanan, T. Killeen, Z. Lin, N. Gimelshein, L. Antiga, A. Desmaison, A. Kopf, E. Yang, Z. DeVito, M. Raison, A. Tejani, S. Chilamkurthy, B. Steiner, L. Fang, J. Bai, and S. Chintala. Pytorch: An imperative style, high-performance deep learning library. In H. Wallach, H. Larochelle, A. Beygelzimer, F. dAlché Buc, E. Fox, and R. Garnett, editors, Advances in Neural Information Processing Systems, volume 32, pages 8026–8037. Curran Associates, Inc., 2019.

[164] F. Pedregosa, G. Varoquaux, A. Gramfort, V. Michel, B. Thirion, O. Grisel, M. Blondel, P. Prettenhofer, R. Weiss, V. Dubourg, J. Vanderplas, A. Passos, D. Cournapeau, M. Brucher, M. Perrot, and É. Duchesnay. Scikit-learn: Machine learning in python. Journal of Machine Learning Research, 12(85):2825–2830, 2011.